

AD-A076 267

OHIO STATE UNIV COLUMBUS ELECTROSCIENCE LAB

F/G 4/1

TROPOSPHERIC WATER VAPOR ABSORPTION IN THE INFRARED WINDOW REGI--ETC(U)

AUG 79 M E THOMAS

DAAG29-77-C-0010

UNCLASSIFIED

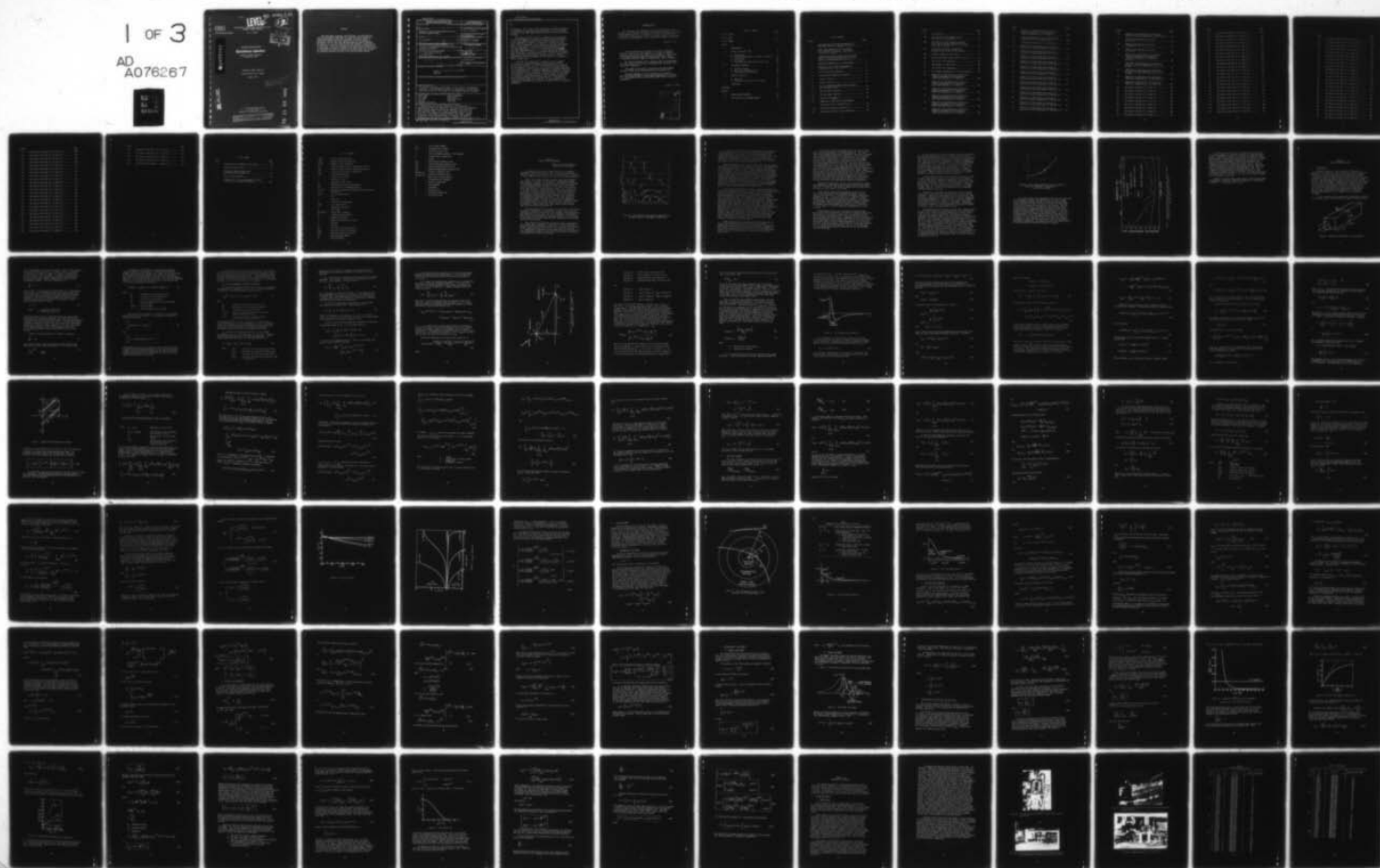
ESL-784701-5

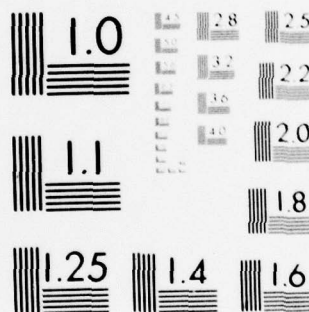
ARO-14702.4-6S

NL

1 OF 3

AD
A076267





MICROCOPY RESOLUTION TEST CHART
NATIONAL BUREAU OF STANDARDS-1963-A



The Ohio State University

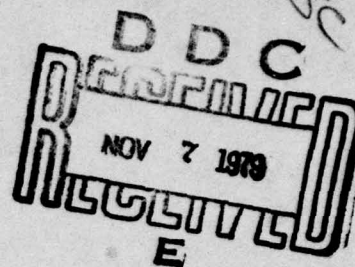
LEVEL

TROPOSPHERIC WATER VAPOR ABSORPTION IN THE
INFRARED WINDOW REGIONS

M. E. Thomas

ARO 14702.4-GS

19



AD A 076267

The Ohio State University

ElectroScience Laboratory

Department of Electrical Engineering
Columbus, Ohio 43212

TECHNICAL REPORT 784701-5

Contract DAAG-29-77-C-0010

August 1979

This document has been approved
for public release and sale; its
distribution is unlimited.

DDC FILE COPY

U. S. Army Research Office
P. O. Box 12211
Research Triangle Park, NC 27709

THE VIEW, OPINIONS, AND/OR FINDINGS CONTAINED IN THIS REPORT
ARE THOSE OF THE AUTHOR(S) AND SHOULD NOT BE CONSTRUED AS
AN OFFICIAL DEPARTMENT OF THE ARMY POSITION, POLICY, OR DE-
CISION, UNLESS SO DESIGNATED BY OTHER DOCUMENTATION.

79 11 05 008
62

NOTICES

When Government drawings, specifications, or other data are used for any purpose other than in connection with a definitely related Government procurement operation, the United States Government thereby incurs no responsibility nor any obligation whatsoever, and the fact that the Government may have formulated, furnished, or in any way supplied the said drawings, specifications, or other data, is not to be regarded by implication or otherwise as in any manner licensing the holder or any other person or corporation, or conveying any rights or permission to manufacture, use, or sell any patented invention that may in any way be related thereto.

UNCLASSIFIED

SECURITY CLASSIFICATION OF THIS PAGE (When Data Entered)

REPORT DOCUMENTATION PAGE		READ INSTRUCTIONS BEFORE COMPLETING FORM
1. REPORT NUMBER	2. GOVT ACCESSION NO.	3. RECIPIENT'S CATALOG NUMBER
4. TITLE (and Subtitle)		5. TYPE OF REPORT & PERIOD COVERED
TROPOSPHERIC WATER VAPOR ABSORPTION IN THE INFRARED WINDOW REGIONS.		Technical Report
7. AUTHOR(s)		6. PERFORMING ORG. REPORT NUMBER
M. E. Thomas		ESL-784701-5/
10. Michael E. Thomas		8. CONTRACT OR GRANT NUMBER(s)
		DAAG-29-77-C-0010
9. PERFORMING ORGANIZATION NAME AND ADDRESS		10. PROGRAM ELEMENT, PROJECT, TASK AREA & WORK UNIT NUMBERS
The Ohio State University ElectroScience Laboratory, Department of Electrical Engineering Columbus, Ohio 43212		12. 251
11. CONTROLLING OFFICE NAME AND ADDRESS		12. REPORT DATE
U. S. Army Research Office P. O. Box 12211 Research Triangle Park, N.C. 27709		August 1979
14. MONITORING AGENCY NAME & ADDRESS (if different from Controlling Office)		13. NUMBER OF PAGES
18. ARO		234
19. 14702.4-GS		15. SECURITY CLASS. (of this report)
		Unclassified
16. DISTRIBUTION STATEMENT (of this Report)		15a. DECLASSIFICATION/DOWNGRADING SCHEDULE
Approved for public release; distribution unlimited.		
17. DISTRIBUTION STATEMENT (of the abstract entered in Block 20, if different from Report)		
18. SUPPLEMENTARY NOTES		
The material contained in this report is also used as a dissertation submitted to the Department of Electrical Engineering, The Ohio State University as partial fulfillment for the degree Doctor of Philosophy.		
19. KEY WORDS (Continue on reverse side if necessary and identify by block number)		
Water vapor Laser propagation Line shape White cell CO ₂ laser Multi-pass cell CO laser Continuum Molecular absorption		
20. ABSTRACT (Continue on reverse side if necessary and identify by block number)		
→ Attenuation of infrared radiation in the troposphere is dominated by water vapor absorption. Most past work on the spectroscopy of water vapor has been on the analysis of the rotational and vibrational bands. As a result a thorough listing of line positions, line strengths and halfwidths exists today. Because of the weak "continuum" absorption in the water vapor windows centered at 10 and 4 microns, efforts to measure and model the continuum have not been as successful as efforts in the analysis →		

DD FORM 1 JAN 73 1473 EDITION OF 1 NOV 65 IS OBSOLETE

UNCLASSIFIED

SECURITY CLASSIFICATION OF THIS PAGE (When Data Entered)

402 251

JQB

20

of the bands. Yet a precise understanding of continuum absorption is important for long path energy transmission. For this reason the study of the water vapor windows has had a long and speculative history.

The purpose of this study is to demonstrate the importance of far wing phenomena in characterizing H_2O continuum absorption. A total line shape for water vapor-nitrogen interactions valid under tropospheric conditions is derived. The model is tested using a set of experimental room temperature H_2O continuum measurements of high quality. Using this data base parameters of the far wing component of the total line shape are determined from near band experimental data. Grating spectrometer measurements from 300 to 650 cm^{-1} are used to determine unknown far wing parameters of the pure rotational band of H_2O . CO and HF laser measurements taken in the 5 micron and 3 micron regions are used to determine the far wing parameters of the ν_2 and ν_1, ν_3 fundamental bands, respectively.

The total line shape model is applied to the millimeter, 10 μm , and 4 μm absorption windows with encouraging success. A significant increase in the self-broadening ability of H_2O over N_2 is predicted in the far wing. This allows the proper modeling of the absorption coefficient versus H_2O partial pressure dependence in all window regions. A negative temperature dependence is predicted by the model in the continuum. The observed rate of the temperature decrease is not predicted by the model, however the failings are related to approximations made on the interaction potentials and perturbation expansion of the Hamiltonians. Although the total line shape model has limitations, it does demonstrate the importance of considering far wings of absorption lines in continuum absorption.

ACKNOWLEDGMENTS

This report was also submitted to the Ohio State University as the Ph.D. dissertation of the author, Dr. Michael E. Thomas. The author's acknowledgment paragraph is reproduced below from the dissertation. I also wish to make particular note of the helpful contributions, both theoretical and experimental, of my colleague, Dr. Robert J. Nordstrom.

Ronald K. Long

I wish to express my gratitude to my advisor, Professor Ronald K. Long for his encouragement, criticisms, and helpful suggestions during the many stages of this research. Also I wish to recognize the many stimulating discussions with Dr. Robert J. Nordstrom, Professor Edward K. Damon and Dr. John C. Peterson.

Mr. Charles Boehnker and Mr. Stanley Taylor are acknowledged for their technical assistance in developing and improving vital experimental apparatus.

The author also recognizes the efforts of LaVerne Wemmer and Nancy Thomas during the preparation of the manuscript.

The work reported in this dissertation was supported in part by Contract DAAG29-77-C-0010 between Department of the Army, U. S. Army Research Office and The Ohio State University Research Foundation.

Michael E. Thomas

Accession For	
NTIS GAI	<input checked="checked" type="checkbox"/>
DEC TAB	<input type="checkbox"/>
Unann. used	<input type="checkbox"/>
Justification	
By	
Distribution/	
Availability Codes	
Dist	Availand/or special
A	

TABLE OF CONTENTS		Page
LIST OF FIGURES		iv
LIST OF TABLES		xii
LIST OF SYMBOLS		xiii
Chapter		
I	INTRODUCTION	1
II	THEORY OF SPECTRAL LINES	9
	A. Introduction	9
	B. Quantum Electrodynamics of Gases and Photons	12
	C. Line Strength	31
	D. Line Shape	44
	E. The Absorption Coefficient for H_2O in N_2	61
III	EXPERIMENTAL APPARATUS	74
	A. Frequency Probes	74
	B. White Type Absorption Cells	82
	C. Experimental Considerations	85
IV	ANALYSIS OF RESULTS	91
	A. Data Base	91
	B. Application of the Total Line Shape	95
V	CONCLUSIONS	135
REFERENCES		137
Appendix		
A	NORMALIZATION INTEGRALS	143
B	H_2O SPECTRA IN THE WINDOW REGIONS	148

LIST OF FIGURES

Figure		Page
1	Low resolution solar spectrum compared with laboratory spectra of atmospheric gasses.....	2
2	Water vapor absorption $C^0(\nu)$ at $T=296K$ as a function of frequency ν (wavelength λ) in the 8-12 μm region.....	6
3	Comparison of measured water vapor continuum at 25°C to Burch extrapolation for 14.3 torr water vapor buffered by 750 torr of air.....	7
4	Radiation transmission in a lossy medium.....	9
5	Binary collision and the classical path assumption, $R(t) = (R_0^2 + (vt)^2)^{1/2}$	15
6	The Intermolecular potential.....	18
7	Change of the integration variables.....	24
8	$f_1(\nu_0, T)$ versus T	41
9	$f_2(\nu_0, \nu)$ versus $\Delta\nu$	42
10	The correspondence between impact parameter and line shape region.....	45
11	The correlation function.....	46
12	The line shape function.....	47
13	The Voigt line shape.....	60
14	Comparison of $\frac{2\mu_1^2}{R^3}$ and kT in wavenumbers. The value of u_1 is 1.83×10^{18} esu cm.....	64
15	Plot of the Langevin function $L(x)$	65
16	Polarization of gases versus temperature.....	66

Figure		Page
17	$p(\nu)$ versus $\Delta\nu$	70
18a	Top view of CO laser showing output mirror and foil insulation.....	76
18b	Side view of CO laser showing uncovered invar rods at top and completely insulated invar rods at bottom.....	76
18c	One end of the CO laser plasma tube showing the electrode and glass bellow.....	77
18d	Brewster window with inlet ports.....	77
19	High voltage power supply control circuit.....	80
20	The 15.24 m cell experiment.....	84
21	Spot pattern on field mirror.....	86
22	The 10.785 m cell experiment.....	87
23	The frequency dependence of the far blue wing.....	99
24	Comparison of experimental and theoretical frequency dependence of the absorption coefficient from 300 cm^{-1} to 440 cm^{-1}	100
25	Comparison of experimental and theoretical frequency dependence of the absorption coefficient from 400 cm^{-1} to 650 cm^{-1}	101
26	Comparison of experimental and theoretical frequency dependence of the absorption coefficient from 930 cm^{-1} to 990 cm^{-1}	102
27	Comparison of experimental and theoretical frequency dependence of the absorption coefficient from 1040 cm^{-1} to 1090 cm^{-1}	103
28	Comparison of experimental and theoretical frequency dependence of the absorption coefficient from 1850 cm^{-1} to 2050 cm^{-1}	104
29	Comparison of experimental and theoretical frequency dependence of the absorption coefficient from 2470 cm^{-1} to 2870 cm^{-1}	105

Figure		Page
30	Comparison of experimental and theoretical frequency dependence of the absorption coefficient from 3400 cm^{-1} to 3800 cm^{-1}	106
31	Frequency dependence of the self-broadening coefficient for the different bands.....	108
32	Liquid water spectrum (8 cm^{-1} resolution).....	110
33	Comparison of experimental and theoretical H_2O partial pressure dependence at 337.9 cm^{-1}	112
34	Comparison of experimental and theoretical H_2O partial pressure dependence at 475.1 cm^{-1}	113
35	Comparison of experimental and theoretical H_2O partial pressure dependence at 611.4 cm^{-1}	114
36	Comparison of experimental and theoretical H_2O partial pressure dependence at 940.548 cm^{-1} ..	115
37	Comparison of experimental and theoretical H_2O partial pressure dependence at 944.194 cm^{-1} ..	116
38	Comparison of experimental and theoretical H_2O partial pressure dependence at 970.547 cm^{-1} ..	117
39	Comparison of experimental and theoretical H_2O partial pressure dependence at 974.547 cm^{-1} ..	118
40	Comparison of experimental and theoretical H_2O partial pressure dependence at 1053.924 cm^{-1} .	119
41	Comparison of experimental and theoretical H_2O partial pressure dependence at 1081.087 cm^{-1} .	120
42	Comparison of experimental and theoretical H_2O partial pressure dependence at 1880.348 cm^{-1} .	121
43	Comparison of experimental and theoretical H_2O partial pressure dependence at 1952.907 cm^{-1} .	122
44	Comparison of experimental and theoretical H_2O partial pressure dependence at 2003.165 cm^{-1} .	123
45	Comparison of experimental and theoretical H_2O partial pressure dependence at 3434.9994 cm^{-1} .	124

Figure		Page
46	Comparison of experimental and theoretical H ₂ O partial pressure dependence at 3788.2253 cm ⁻¹ .	125
47	Comparison of experiment and theory at 3.167 cm ⁻¹	126
48	Comparison of experiment and theory at 4.8333 cm ⁻¹	127
49	Comparison of experiment and theory at 7.667 cm ⁻¹	128
50	Comparison of experimental and theoretical frequency dependence of the absorption coefficient from 400 cm ⁻¹ to 650 cm ⁻¹ at 430 K.....	130
51	Comparison of experimental and theoretical H ₂ O partial pressure dependence at 440.1 cm ⁻¹ at 430K.....	131
52	Comparison of experimental and theoretical H ₂ O partial pressure dependence at 531.6 cm ⁻¹ at 430K.....	132
53	Comparison of experimental and theoretical temperature dependence of C _s at 944.1945 cm ⁻¹	133
54	Comparison of experimental and theoretical temperature dependence of C _s at 1203.0 cm ⁻¹	134
55	H ₂ O spectra from 850 cm ⁻¹ to 864 cm ⁻¹	149
56	H ₂ O spectra from 862 cm ⁻¹ to 876 cm ⁻¹	150
57	H ₂ O spectra from 874 cm ⁻¹ to 888 cm ⁻¹	151
58	H ₂ O spectra from 886 cm ⁻¹ to 900 cm ⁻¹	152
59	H ₂ O spectra from 898 cm ⁻¹ to 912 cm ⁻¹	153
60	H ₂ O spectra from 910 cm ⁻¹ to 924 cm ⁻¹	154
61	H ₂ O spectra from 920 cm ⁻¹ to 934 cm ⁻¹	155
62	H ₂ O spectra from 932 cm ⁻¹ to 946 cm ⁻¹	156
63	H ₂ O spectra from 944 cm ⁻¹ to 958 cm ⁻¹	157

Figure		Page
64	H ₂ O spectra from 956 cm ⁻¹ to 970 cm ⁻¹	158
65	H ₂ O spectra from 968 cm ⁻¹ to 982 cm ⁻¹	159
66	H ₂ O spectra from 980 cm ⁻¹ to 994 cm ⁻¹	160
67	H ₂ O spectra from 992 cm ⁻¹ to 1006 cm ⁻¹	161
68	H ₂ O spectra from 1004 cm ⁻¹ to 1018 cm ⁻¹	162
69	H ₂ O spectra from 1016 cm ⁻¹ to 1030 cm ⁻¹	163
70	H ₂ O spectra from 1028 cm ⁻¹ to 1042 cm ⁻¹	164
71	H ₂ O spectra from 1040 cm ⁻¹ to 1054 cm ⁻¹	165
72	H ₂ O spectra from 1052 cm ⁻¹ to 1066 cm ⁻¹	166
73	H ₂ O spectra from 1064 cm ⁻¹ to 1078 cm ⁻¹	167
74	H ₂ O spectra from 1076 cm ⁻¹ to 1090 cm ⁻¹	168
75	H ₂ O spectra from 1088 cm ⁻¹ to 1102 cm ⁻¹	169
76	H ₂ O spectra from 1100 cm ⁻¹ to 1114 cm ⁻¹	170
77	H ₂ O spectra from 1112 cm ⁻¹ to 1126 cm ⁻¹	171
78	H ₂ O spectra from 1124 cm ⁻¹ to 1138 cm ⁻¹	172
79	H ₂ O spectra from 1136 cm ⁻¹ to 1150 cm ⁻¹	173
80	H ₂ O spectra from 1148 cm ⁻¹ to 1162 cm ⁻¹	174
81	H ₂ O spectra from 1160 cm ⁻¹ to 1174 cm ⁻¹	175
82	H ₂ O spectra from 1172 cm ⁻¹ to 1186 cm ⁻¹	176
83	H ₂ O spectra from 1184 cm ⁻¹ to 1198 cm ⁻¹	177
84	H ₂ O spectra from 1196 cm ⁻¹ to 1210 cm ⁻¹	178
85	H ₂ O spectra from 1208 cm ⁻¹ to 1222 cm ⁻¹	179
86	H ₂ O spectra from 1220 cm ⁻¹ to 1234 cm ⁻¹	180
87	H ₂ O spectra from 1232 cm ⁻¹ to 1246 cm ⁻¹	181

Figure		Page
88	H ₂ O spectra from 1244 cm ⁻¹ to 1258 cm ⁻¹	182
89	H ₂ O spectra from 1256 cm ⁻¹ to 1270 cm ⁻¹	183
90	H ₂ O spectra from 1268 cm ⁻¹ to 1282 cm ⁻¹	184
91	H ₂ O spectra from 1800 cm ⁻¹ to 1814 cm ⁻¹	185
92	H ₂ O spectra from 1812 cm ⁻¹ to 1826 cm ⁻¹	186
93	H ₂ O spectra from 1824 cm ⁻¹ to 1838 cm ⁻¹	187
94	H ₂ O spectra from 1836 cm ⁻¹ to 1850 cm ⁻¹	188
95	H ₂ O spectra from 1848 cm ⁻¹ to 1862 cm ⁻¹	189
96	H ₂ O spectra from 1860 cm ⁻¹ to 1874 cm ⁻¹	190
97	H ₂ O spectra from 1872 cm ⁻¹ to 1886 cm ⁻¹	191
98	H ₂ O spectra from 1884 cm ⁻¹ to 1898 cm ⁻¹	192
99	H ₂ O spectra from 1896 cm ⁻¹ to 1910 cm ⁻¹	193
100	H ₂ O spectra from 1908 cm ⁻¹ to 1922 cm ⁻¹	194
101	H ₂ O spectra from 1920 cm ⁻¹ to 1934 cm ⁻¹	195
102	H ₂ O spectra from 1932 cm ⁻¹ to 1946 cm ⁻¹	196
103	H ₂ O spectra from 1944 cm ⁻¹ to 1958 cm ⁻¹	197
104	H ₂ O spectra from 1956 cm ⁻¹ to 1970 cm ⁻¹	198
105	H ₂ O spectra from 1968 cm ⁻¹ to 1982 cm ⁻¹	199
106	H ₂ O spectra from 1980 cm ⁻¹ to 1994 cm ⁻¹	200
107	H ₂ O spectra from 1992 cm ⁻¹ to 2006 cm ⁻¹	201
108	H ₂ O spectra from 2004 cm ⁻¹ to 2018 cm ⁻¹	202
109	H ₂ O spectra from 2016 cm ⁻¹ to 2030 cm ⁻¹	203
110	H ₂ O spectra from 2028 cm ⁻¹ to 2042 cm ⁻¹	204
111	H ₂ O spectra from 2040 cm ⁻¹ to 2054 cm ⁻¹	205

Figure		Page
112	H ₂ O spectra from 2500 cm ⁻¹ to 2514 cm ⁻¹	206
113	H ₂ O spectra from 2512 cm ⁻¹ to 2526 cm ⁻¹	207
114	H ₂ O spectra from 2524 cm ⁻¹ to 2538 cm ⁻¹	208
115	H ₂ O spectra from 2536 cm ⁻¹ to 2550 cm ⁻¹	209
116	H ₂ O spectra from 2548 cm ⁻¹ to 2562 cm ⁻¹	210
117	H ₂ O spectra from 2560 cm ⁻¹ to 2574 cm ⁻¹	211
118	H ₂ O spectra from 2584 cm ⁻¹ to 2598 cm ⁻¹	212
119	H ₂ O spectra from 2596 cm ⁻¹ to 2610 cm ⁻¹	213
120	H ₂ O spectra from 2608 cm ⁻¹ to 2622 cm ⁻¹	214
121	H ₂ O spectra from 2620 cm ⁻¹ to 2634 cm ⁻¹	215
122	H ₂ O spectra from 2632 cm ⁻¹ to 2646 cm ⁻¹	216
123	H ₂ O spectra from 2644 cm ⁻¹ to 2658 cm ⁻¹	217
124	H ₂ O spectra from 2656 cm ⁻¹ to 2670 cm ⁻¹	218
125	H ₂ O spectra from 2668 cm ⁻¹ to 2682 cm ⁻¹	219
126	H ₂ O spectra from 2680 cm ⁻¹ to 2694 cm ⁻¹	220
127	H ₂ O spectra from 2692 cm ⁻¹ to 2706 cm ⁻¹	221
128	H ₂ O spectra from 2704 cm ⁻¹ to 2718 cm ⁻¹	222
129	H ₂ O spectra from 2716 cm ⁻¹ to 2730 cm ⁻¹	223
130	H ₂ O spectra from 2728 cm ⁻¹ to 2742 cm ⁻¹	224
131	H ₂ O spectra from 2740 cm ⁻¹ to 2754 cm ⁻¹	225
132	H ₂ O spectra from 2752 cm ⁻¹ to 2766 cm ⁻¹	226
133	H ₂ O spectra from 2764 cm ⁻¹ to 2778 cm ⁻¹	227
134	H ₂ O spectra from 2776 cm ⁻¹ to 2790 cm ⁻¹	228
135	H ₂ O spectra from 2788 cm ⁻¹ to 2802 cm ⁻¹	229

Figure		Page
136	H ₂ O spectra from 2800 cm ⁻¹ to 2814 cm ⁻¹	230
137	H ₂ O spectra from 2812 cm ⁻¹ to 2826 cm ⁻¹	231
138	H ₂ O spectra from 2824 cm ⁻¹ to 2838 cm ⁻¹	232
139	H ₂ O spectra from 2836 cm ⁻¹ to 2850 cm ⁻¹	233
140	H ₂ O spectra from 2848 cm ⁻¹ to 2862 cm ⁻¹	234

LIST OF TABLES

Table		Page
1	Characteristics of Molecular Collisions.....	46
2	Observed CO Laser Lines.....	78
3	Nitrogen Broadened, Water Vapor Window Absorption Parameters.....	92
4	The Far Wing Parameters.....	96
5	Comparison of DF Laser Measurements by Mills to the Total Line Shape Calculations.....	107

LIST OF SYMBOLS

$a_o^\dagger(\bar{q})$	- photon creation operator
$a_o(\bar{q})$	- photon annihilation operator
$\bar{A}(\bar{r}, t)$	- Magnetic vector potential
$A_{u\ell}$	- Einstein coefficient for spontaneous emission
$B_{u\ell}$	- Einstein coefficient for stimulated emission
$B_{\ell u}$	- Einstein coefficient for absorption
$C(\tau)$	- correlation function
e	- charge of an electron
f	- frequency in H_z
g_k	- degeneracy of k^{th} state
H_{a1}	- Hamiltonian for absorbing molecule
H_b	- Hamiltonian for broadening molecule
$H_{a1p}(t)$	- Interaction Hamiltonian between absorbing molecule and photon
$H_c(t)$	- collision Hamiltonian
i	- $\sqrt{-1}$
I	- intensity
J	- rotational quantum number
$j(\nu)$	- line shape function
k	- absorption coefficient
ℓ	- path length
$\bar{M} = \langle u e \bar{r} \ell \rangle$	- dipole matrix element
M	- azimuthal quantum number
N	- number of molecules
n	- number of molecules per volume
p	- pressure
\bar{p}	- momentum
Q_{El}	- Electronic partition function
Q_{Vib}	- Vibrational partition function
Q_{Rot}	- Rotational partition function
\bar{Q}	- mean quadrupole moment
R_o	- impact parameter

\bar{R}	- mean octupole moment
$R(t)$	- intermolecular distance
s	- scattering coefficient
S	- time development operator, line strength
T	- transmittance, temperature
V	- volume
V_{DD}	- Dipole-dipole potential term
V_{DQ}	- Dipole-quadrupole potential term
V_{DO}	- Dipole-octupole potential term
V_{QQ}	- Quadrupole-Quadrupole potential term
$V_{\text{Inductive}}$	- Inductive potential term
$V_{\text{Dispersive}}$	- Dispersive potential term
$\bar{\alpha}$	- mean electric polarizability
α	- halfwidth at half maximum
ϵ	- emission coefficient
μ	- dipole moment
ν	- wavenumber
ρ	- density matrix
σ	- extinction coefficient
τ	- correlation time

CHAPTER I
"WATER, WATER EVERYWHERE"

Rhyme of the Ancient Mariner
- Samuel Taylor Coleridge

The importance of water is suggested by its considerable abundance on the surface of the earth. Its physical properties have been studied for a long time and it has proven to be a molecule of great complexity which gives water special and unique properties.

One of the largely unsolved problems concerning atmospheric water vapor is its effect on infrared (ir) propagation through the atmospheric windows. The propagation of radiation is affected by three major phenomena: absorption, scattering and turbulence. In the atmosphere water is primarily in its vapor phase; however water vapor clusters can form on particulates (i.e., clouds, fog) or ionized molecules. Attenuation of ir radiation by molecular water vapor is largely due to absorption. Water vapor clusters contribute to both absorption and scattering. Local heating of the atmosphere caused by water vapor absorption can contribute to turbulence or beam dispersion effects. An ideal approach to solving the propagation problem is to separate each phenomenon for independent study. To some extent this can be achieved. Under laboratory control, turbulence and particulate scattering can be minimized. However pure water vapor samples always contain some dimer and cluster formations [1].

Infrared absorption by the water vapor molecule is the dominant mechanism of atmospheric ir attenuation. Figure 1 shows the low resolution infrared transmittance of the atmosphere and demonstrates the importance of water vapor over other atmospheric constituents. Water vapor cluster attenuation caused by absorption and scattering is much smaller than water vapor molecular absorption in the strong absorption band regions.

This study will concentrate on the water vapor window absorption problem under tropospheric conditions. The main rotational and vibrational bands have been extensively characterized by Benedict, Calfee, Camy-Peyret and Flaud [2,3,4]. This work has resulted in a compendium of absorption line parameters maintained by AFGL [5]. This compendium represents a significant contribution to absorption calculations and is used in this study.

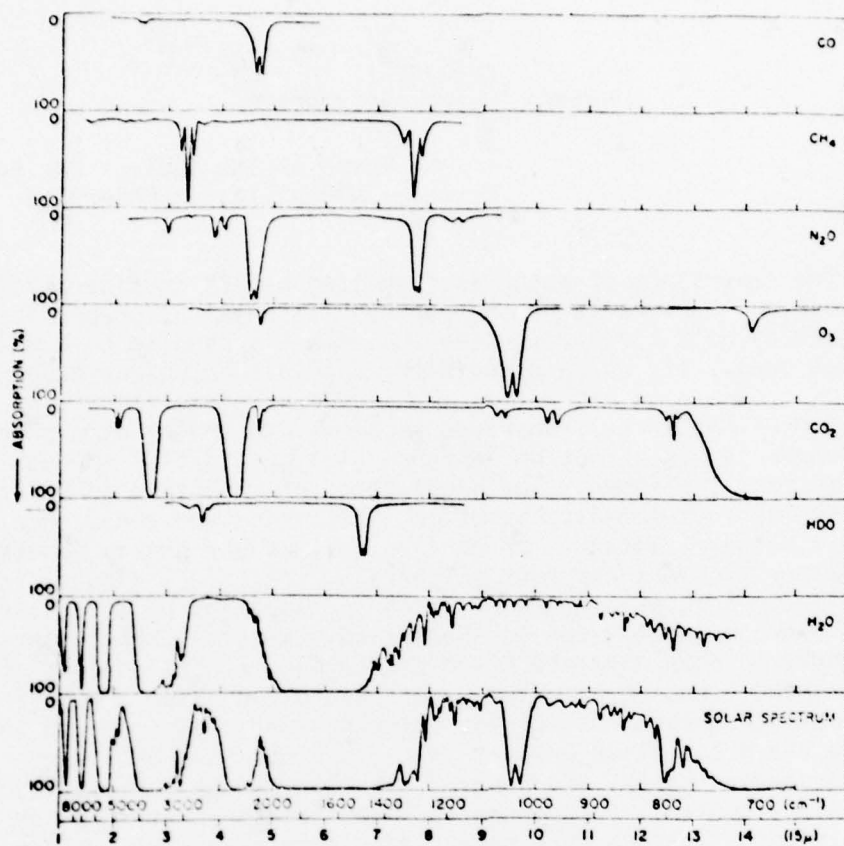


Figure 1. Low resolution solar spectrum compared with laboratory spectra of atmospheric gasses [6].

For general electro-optical system applications the strongly absorbing regions are not of interest; instead the regions of small attenuation are important. The infrared windows of the troposphere occur between 13 to 8 μm , 5 to 4.5 μm and 4.1 to 3.2 μm bounded by strong H_2O or CO_2 bands. The weak absorption which does occur in the window regions can be described as arising from two sources; local line and continuum absorption.

Weak absorption bands of CO_2 , HDO along with other H_2O absorption lines in the window regions comprise the local line contribution. The continuum contributes a slowly varying frequency dependence to the absorption. Elsasser [7], in 1938, recognized the existence of a continuum in the 13 to 8 μm window region which he attributed to the far wings of the strong nearby rotational and ν_2 vibrational bands of H_2O . Further verification of this nonlocal line absorption feature was provided by Yates and Taylor [8] who studied infrared attenuation along horizontal paths at sea level. Solar spectra studies also indicated continuum absorption in the 13 - 8 μm window [9,10,11]. The nature of the continuum based on these measurements was uncertain. It could be due to far wings of strong absorption bands or scattering and absorption by particulates.

In an effort to determine the cause of continuum absorption in the 13 to 8 μm window Bignell [12] in 1963 examined solar spectra while testing the atmosphere for aerosol amounts and studied CO_2 far wing contributions. He concluded that the amount of continuum absorption observed could not be accounted for by aerosol attenuation or far wings of CO_2 . An attempt was then made to model the continuum by far wings of the bordering H_2O bands. The important contribution from this initial work was the realization of the major water vapor contributions to the continuum. A second paper by Bignell [13] in 1970 described a careful examination of water vapor absorption in the window regions employing a multiple traversal absorption cell and grating spectrometer. Two important facts about the 13 - 8 μm window were observed namely a large ratio of water vapor self-to-foreign-gas broadening ability and a strong negative temperature dependence. Both of these results were not anticipated based on the far wing approaches of Bignell's 1963 paper. Also reported by Bignell was a similar but much weaker continuum absorption in the 4 μm region.

Further laboratory measurements performed by Burch [14,15] using a long path absorption cell and grating spectrometer examined the 10 μm and 4 μm regions in 1970 and 1971, respectively. Confirmation of the large self-to-foreign broadening dependence and negative temperature dependence were made in the 10 μm window region. The 4 μm continuum was more completely characterized and verified.

In recent years laser measurements have contributed a great deal to the understanding of continuum absorption. The stable high intensity monochromatic source provided by the laser alleviates some of the problems encountered in obtaining accurate long path absorption measurements which are characteristic of continuum (i.e., window) investigations. Initial CO_2 laser measurements by McCoy [16] in 1969 at $10.6 \mu\text{m}$ indicated the ratio of self-to-foreign broadening ability to be 200. The value inferred from line measurements is 5 [17]. This result confirmed the preliminary observations of Bignell's 1963 paper concerning the dominance of H_2O contributions to continuum absorption and provided a quantitative number for the self-to-foreign broadening ratio. Recent comprehensive studies at The Ohio State University [18,19,20] have extended the frequency range by examining many CO_2 laser lines using a stabilized laser with both a multiple traversal cell set to 1.5 kilometer path length and also with an optoacoustic spectrophone. The results further verify the general trend of large self to foreign broadening ratios and negative temperature dependence.

Arefev and Dianov-Klovov [21] have also examined the temperature dependence in the $10.6 \mu\text{m}$ region using a CO_2 laser and long path cell. A negative 1.7% change in absorption per degree Kelvin was observed, over a 284 to 353 K range.

From extended temperature measurements to 473 K using a laser diode operating at 1203 wavenumbers Montgomery [22] has observed that above 398 K a leveling of the negative temperature dependence occurs. To explain the result a competitive effect between dimer and far wing absorption was suggested. According to Montgomery, temperatures below 398 K dimer absorption dominates and above 398 K far wing absorption dominates. Because these measurements were made around $8 \mu\text{m}$, close to the ν_2 band of H_2O , it is not known if a similar temperature dependence will occur at $10 \mu\text{m}$.

Other popular lasers used in probing the continuum have been CO and DF which operate at the 5 and $4 \mu\text{m}$ regions respectively. Absorption at $5 \mu\text{m}$ features strong local line absorption along with continuum contributions [23]. Thus many of the special continuum characteristics are masked by comparable local line absorption. Recent measurements at White Sands [24] with a DF laser and 1.5 km path lengths show continuum absorption properties at $4 \mu\text{m}$ similar to those in the $10 \mu\text{m}$ region. An average self-to-foreign broadening ratio of around 90 has been measured. Thus it is possible that the $4 \mu\text{m}$ window continuum may be generated by the same phenomena as the $10 \mu\text{m}$ window.

Modeling efforts have not been totally successful in explaining the experimental observations. Attempts by Burch [14] to model measured absorption in the 8 - 12 μm region using the Lorentz line shape failed to predict the observed absorption magnitude, water vapor partial pressure dependence or temperature dependence. This computation used all absorption lines in the rotational and ν_2 bands of H_2O (i.e., no bound). Even though the validity of the Lorentz line shape does not extend beyond 5 - 10 cm^{-1} , the result has been a de-emphasis of far wing models in general. This has prompted the search for other mechanisms of continuum absorption. However, sophisticated far wing theories are being applied to the H_2O continuum by a few researchers.

A major candidate to describe continuum absorption has been the water vapor dimer [25,26]. The strength of this approach is the strong negative temperature dependence exhibited by dimer absorption. A similar candidate is the water vapor cluster [1,27] which extends the dimer concept to larger formations. Because monomer, dimer and cluster formations are present in any sample of water vapor it is difficult to determine the most important continuum mechanism involved.

Advanced far wing models are being used by Fomin and Zuev [28,29] to explain experimental measurements of the H_2O and CO_2 continua. Significant improvements over the Lorentz line shape far wing are demonstrated for the H_2O partial pressure dependence and frequency dependence. However a lack of detailed information on the nature of this (i.e., Fomin's) line shape formula make it difficult to properly evaluate its performance. Nonetheless, the success of their far wing approach has encouraged our efforts to develop a total line shape formula for H_2O .

The amplitude of the far wings of water vapor spectral lines are difficult to determine both theoretically and experimentally. Figures 2 and 3 show the frequency dependence of the 10 μm and 4 μm continuum regions respectively. The observed frequency dependence is consistent with a far wing extension of the bordering H_2O bands. The strong H_2O rotational band should dominate in the 10 μm region from the low frequency side as Figure 2 indicates. The 4 μm region exhibits more balance in the strength of the bordering bands. The ν_2 fundamental near 1600 cm^{-1} contributes from the low frequency side and the ν_1 and ν_3 fundamentals near 3700 cm^{-1} contribute from the high frequency side. A minimum at 2600 cm^{-1} occurs in the continuum due to the nearly equal strengths of the ν_2 and the ν_1 and ν_3 bands. Based on the frequency behavior of the H_2O continuum far wings must contribute some portion of the observed absorption, with perhaps dimer and cluster absorption accounting for the rest.

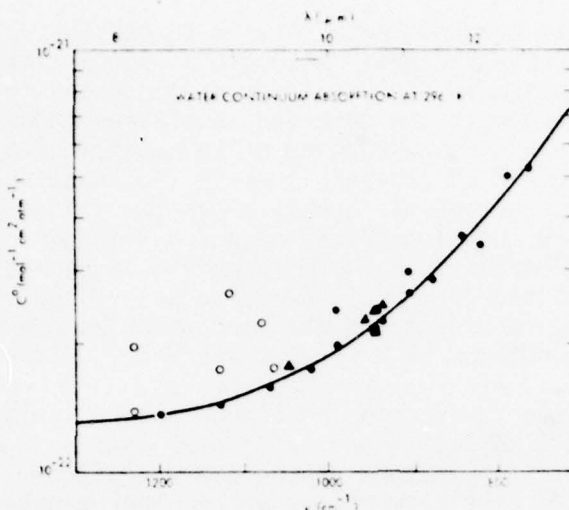


Figure 2. Water vapor absorption $C^0(v)$ at $T=296K$ as a function of frequency v (wavelength λ) in the 8-12 μm region.

Far wings of water vapor absorption lines are also significant in the fundamental bands. The H_2O spectrum in Figure 1 shows wing absorption underneath spectral structure at the band edges of the v_2 band at 5 μm and 7 to 8 μm . Far wings of absorption lines within the band can be studied in such regions. Once the nature of the far wings is determined in the near band region an extrapolation in frequency away from the band and into the windows can be performed. Thus the characteristics of far wing absorption can be determined in the window regions. To do this a proper model for far wing absorption must be developed and incorporated into a total line shape theory, from line center to far wing of a single absorption line. The total line shape must be normalized, thus insuring conservation of energy and proper magnitude of absorption. To achieve this goal an in depth analysis of the interactions of photons and gases is required.

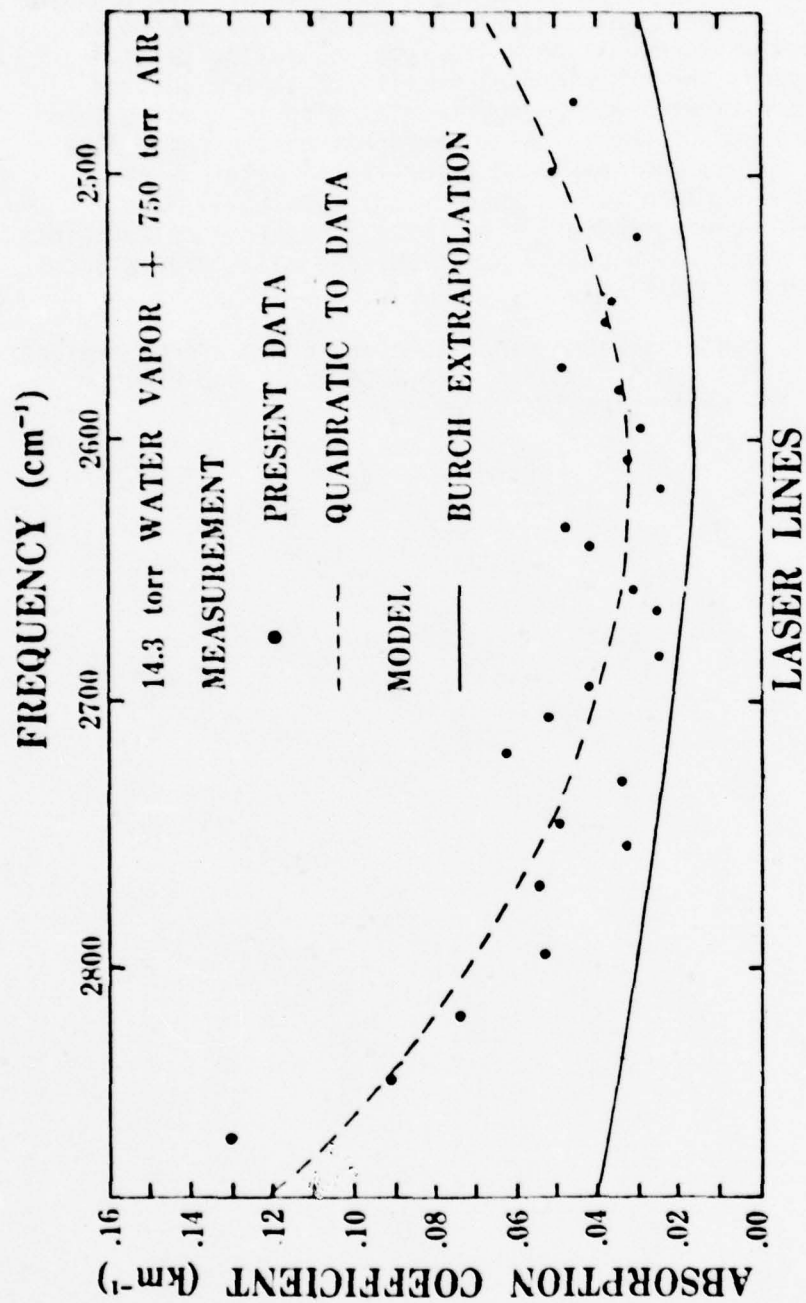


Figure 3. Comparison of measured water vapor continuum at 25°C to Burch extrapolation for 14.3 torr water vapor buffered by 750 torr of air.

The purpose of this study is to demonstrate the importance of far wing phenomena in characterizing H_2O continuum absorption. Chapter 2 attempts to develop a valid total line shape for water vapor-nitrogen interactions under tropospheric conditions. Chapter III describes the experimental apparatus and procedures used in making continuum measurements on White-type absorption cells. Chapter IV presents the experimental results of this study and a comprehensive review of other experimental efforts. Using this data base parameters of the far wing component of the total line shape are determined from near band experimental data. Then a comparison of experimental and theoretical results is made displaying remarkable agreement. The total line shape calculations are applied to the $4\ \mu\text{m}$, $5\ \mu\text{m}$, $10\ \mu\text{m}$, $17\ \mu\text{m}$, and millimeter windows under tropospheric conditions.

Appendix B contains water vapor spectra in the window regions from $850\ \text{cm}^{-1}$ to $1282\ \text{cm}^{-1}$, $1800\ \text{cm}^{-1}$ to $2054\ \text{cm}^{-1}$, and $2500\ \text{cm}^{-1}$ to $2862\ \text{cm}^{-1}$. The resolution is $.05\ \text{cm}^{-1}$.

CHAPTER II THEORY OF SPECTRAL LINES

A. Introduction

A general expression for the absorption coefficient is developed in this chapter. Section B derives a general expression from first principles containing line strength and line shape information. Section C develops the line strength resulting in a standard formula with some correction terms. Section D separately develops line shape expressions valid near line center and the far wing under the adiabatic assumption and binary collision approximation. Section E presents a technique for constructing the total line shape for $\text{H}_2\text{O}-\text{N}_2$ gaseous mixtures and a careful analysis of the intermolecular potential functions for $\text{H}_2\text{O}-\text{H}_2\text{O}$ and $\text{H}_2\text{O}-\text{N}_2$ collisions. Knowledge of the intermolecular potentials is crucial in predicting the far wing behavior of a line shape. The important equations of this chapter will be enclosed in rectangles.

In order to examine the attenuation of monochromatic radiation per unit path length, consider a medium (Figure 4) on which plane

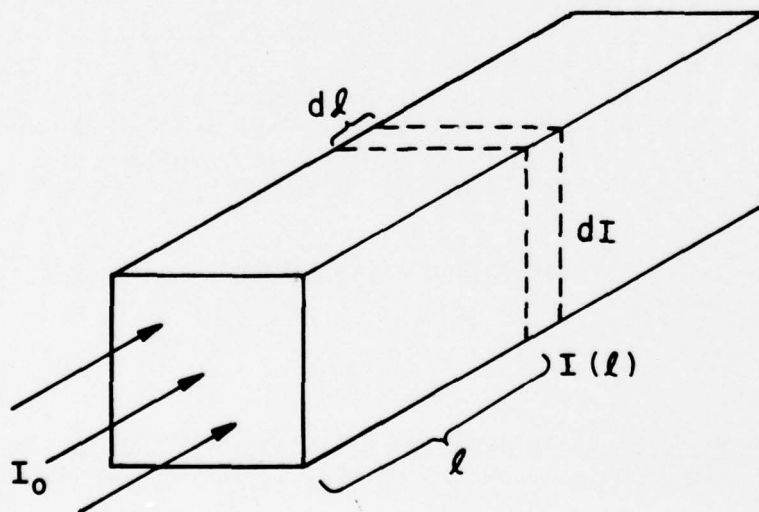


Figure 4. Radiation transmission in a lossy medium.

wave electromagnetic radiation is incident. Let "I" be the intensity at any point along the path and "ℓ" the path length. The medium is divided into a number of segments of length d perpendicular to the direction of the radiation. The change in intensity, dI, per unit length, dℓ, is proportional to some constant times the intensity plus another constant independent of intensity (for a homogeneous medium). This may be expressed as,

$$\frac{dI}{d\ell} = -\sigma I + \epsilon . \quad (1)$$

The parameter σ is the extinction coefficient and ϵ is the emission coefficient. In the following analysis the emission coefficient is not considered. The emission coefficient represents blackbody radiation of the medium and future arguments will justify its elimination. The physical processes which contribute to the extinction coefficient can be divided into two general classes, absorption and scattering. Thus,

$$\sigma = k + s \quad (2)$$

where k = absorption coefficient
 s = scattering coefficient.

The dominant coefficient will be determined by the nature of the medium and by the radiation frequency. This study is confined to gaseous media and the infrared spectrum. This condition basically eliminates scattering (because $a \ll \lambda$), which in the infrared becomes important for aerosols, clouds, fog, and various other particulates. As the next section will show, scattering is at least a two photon process where absorption can be a single photon interaction. In a perturbation expansion the single photon process will be favored.

Lambert's law for absorption of radiation is obtained,

$$\frac{dI}{d\ell} = -kI. \quad (3)$$

The solution of this simple differential equation leads to the definition of another important parameter, T, the transmittance.

$$T = e^{-k\ell} \quad (4)$$

where $T = \frac{I(\ell)}{I(0)} .$

The absorption coefficient, k , represents the molecular interaction with an electromagnetic field and other molecular systems, resulting in the absorption of a photon and the excitation of the absorbing molecular system. The analysis of such phenomena requires an understanding of molecular spectroscopy, quantum theory of radiation and intermolecular forces. For only one absorbing molecule and one perturbing foreign molecule the absorption coefficient may be functionally expressed as

$$k(M_a, M_f, \nu) = S_{lu}(M_a, \nu_0) j(\nu - \nu_0, M_a, M_f; \alpha(M_a, M_f, \nu_0)) \quad (5)$$

where

- M_a - represents the absorbing molecule
- M_f - represents the foreign molecule
- ν_0 - the linecenter wavenumber
- S_{lu} - the line strength for transition between l and u states
- $j(\Delta\nu; \alpha)$ - the line shape
- α - the half width at half maximum

Note that the line strength is a function of the absorbing molecule only (to first order). It is convenient to normalize $j(\Delta\nu; \alpha)$ by requiring,

$$\int_0^{\infty} k(M_a, M_f, \nu) d\nu = S_{lu}(M_a) \quad (6)$$

thus

$$\int_0^{\infty} j(\nu - \nu_0, M_a, M_f; \alpha(M_a, M_f, \nu_0)) d\nu = 1$$

The parameters M_a and M_f are themselves multi-variable functions of quantities affecting the properties of the associated molecular systems. They are used here to emphasize this fact and, having served their purpose, shall be eliminated from the notation and replaced by more explicit variables.

The description of the absorption coefficient, $k(\nu)$, can now be broken down into two parts, line strength and line shape function. These two quantities are natural choices for experimentally characterizing the absorption of a single line. Also the absorption line parameter compilation of AFGL [5] uses this formulation. Therefore the goal of the following theoretical development is to find standard mathematical forms of line strength and line shape.

B. Quantum Electrodynamics of Gases and Photons

In the quantum mechanical model representing gases and photons the Hamiltonian is complex; because of this, a careful description is necessary. The total Hamiltonian may be written

$$H_{\text{Tot}}(t) = H_{a_1} + H_b + H_p + H_{a_1p}(t) + H_c(t) \quad (7)$$

where

- H_{a_1} - Hamiltonian for the absorbing molecule
- H_b - Hamiltonian for the broadening molecule
- H_p - Hamiltonian for the photon field
- $H_{a_1p}(t)$ - Interaction Hamiltonian between absorbing molecule and photon field
- $H_c(t)$ - Collision Hamiltonian between absorbing molecule and broadening molecules.

Time dependent terms are explicitly indicated. Otherwise the separate Hamiltonians are time independent. The first three terms in the total Hamiltonian form the unperturbed or zero order Hamiltonian, H_0 . The last two form the interaction Hamiltonian. A description of each term in the total Hamiltonian follows.

H_{a_1} represents the absorbing molecule. In a gas sample many molecules will be of the same type; the subscript 1 indicates the absorbing molecules while all others are perturbers. The general unperturbed Hamiltonian for absorbing molecules is

$$H_a = H_{a\text{ROT}} + H_{a\text{VIB}} + H_{a\text{EL}} + H_{a\text{TRN}} \quad (8)$$

- where $H_{a\text{ROT}}$ - describes the rotational energy levels
- $H_{a\text{VIB}}$ - describes the vibrational energy levels
- $H_{a\text{EL}}$ - describes the electronic energy levels
- $H_{a\text{TRN}}$ - describes the translational energy of the total molecule.

H_{aTRN} will not be directly included in the analysis, but will be accounted for by properly averaging over velocities of the molecules.

H_b is a many-particle Hamiltonian representing all perturbing molecules. This includes foreign molecules and molecules of the same type as the absorber. It may be written

$$H_b = \sum_{j=2}^{N_a} H_{a_j} + \sum_{k=1}^K \sum_{m=1}^{N_k} H_{b_{km}} \quad (9)$$

N_a is the number of absorbing molecules, K is the number of types of foreign molecules, and N_k is the number of foreign molecules of the k th type. Each Hamiltonian is structured in the same way as Equation (8); that is the rotational, vibrational, electronic, and translational energies are represented.

H_p is the free space photon Hamiltonian. Many excellent texts discuss this term [31,32]. Simply stated, it is

$$H_p = \sum_{\vec{q}\sigma} \hbar\omega(\vec{q}) (a_{\vec{q}\sigma}^\dagger a_{\vec{q}\sigma} + \frac{1}{2}). \quad (10)$$

$a_{\vec{q}\sigma}^\dagger$ is the photon creation operator and $a_{\vec{q}\sigma}$ is the photon annihilation operator for a particular polarization σ and wavenumber \vec{q} corresponding to the angular frequency $\omega = \hbar|\vec{q}|$.

$H_{a1p}(t)$ is the interaction Hamiltonian between the absorbing molecule and photon field. It can be shown that [32]

$$H_{a1p}(t) = \left\{ -\frac{e}{2mc} (\vec{p} \cdot \vec{A}(\vec{r},t) + \vec{A}(\vec{r},t) \cdot \vec{p}) + \frac{e^2}{2mc^2} \vec{A}(\vec{r},t) \cdot \vec{A}(\vec{r},t) \right\} (u(t) - u(T)) \quad (11)$$

\vec{p} is the particle momentum operator. $\vec{A}(\vec{r},t)$ is the photon field magnetic vector potential operator.

$$\vec{A}(\vec{r},t) = \left(\frac{2\pi\hbar c}{qV} \right)^{1/2} \left\{ a_{\vec{q}\sigma}(\vec{q}) \vec{\epsilon}_{\vec{q}\sigma} e^{i[\vec{q} \cdot \vec{r} - \omega t]} + a_{\vec{q}\sigma}^\dagger(\vec{q}) \vec{\epsilon}_{\vec{q}\sigma}^* e^{-i[\vec{q} \cdot \vec{r} - \omega t]} \right\} \quad (12)$$

$\bar{\epsilon}_0$ is an orthonormal vector perpendicular to the free space photon propagation representing the polarization. T is the observation time or the time period during which the molecules and photons can interact.

$H_c(t)$ models the intermolecular potentials due to neighboring molecules surrounding the absorbing molecule. It is the least understood term in the Hamiltonian and yet when considering line shapes it is the most important. A general many-body expression can be written as

$$H_c(t) = \sum_{j=2}^{N_a} H_{a_j} a_1(t) + \sum_{k=1}^k \sum_{m=2}^{N_k} H_{b_{mk}} a_1(t) \quad (13)$$

Each term is a binary interaction of the external fields of the molecule. Figure 5 illustrates such an interaction. For mutual neutral molecules with permanent electrostatic potentials a single Hamiltonian in $H_c(t)$ may be written [33]

$$H_{b_{mk}} a_1(R(t); \bar{r}_{mk}, \bar{r}_1) = \langle V_{\text{Electrostatic}} + V_{\text{Magnetostatic}} \rangle_{\text{Rot}} \\ - V_{\text{Dispersive}} - V_{\text{Inductive}} + V_{\text{Repulsive}} \quad (14)$$

$R(t)$ is the intermolecular distance between two moving molecules. The quantities \bar{r}_{mk}, \bar{r}_1 locate the charged particles in the internal molecular coordinate system for the broadener and the absorber, respectively. The magnetostatic potential function is significantly smaller than the electrostatic potential so it is ignored. A brief description of the potential terms will be given.

A multipole expansion of the electrostatic potential is

$$V_{\text{Electrostatic}} = \frac{V_{DD}(\bar{r}_{mk}, \bar{r}_1)}{R^3(t)} + \frac{V_{DQ}(\bar{r}_{mk}, \bar{r}_1)}{R^4(t)} + \frac{V_{DQ}(\bar{r}_{mk}, \bar{r}_1) + V_{QQ}(\bar{r}_{mk}, \bar{r}_1)}{R^5(t)} \\ + \dots \quad (15)$$

where

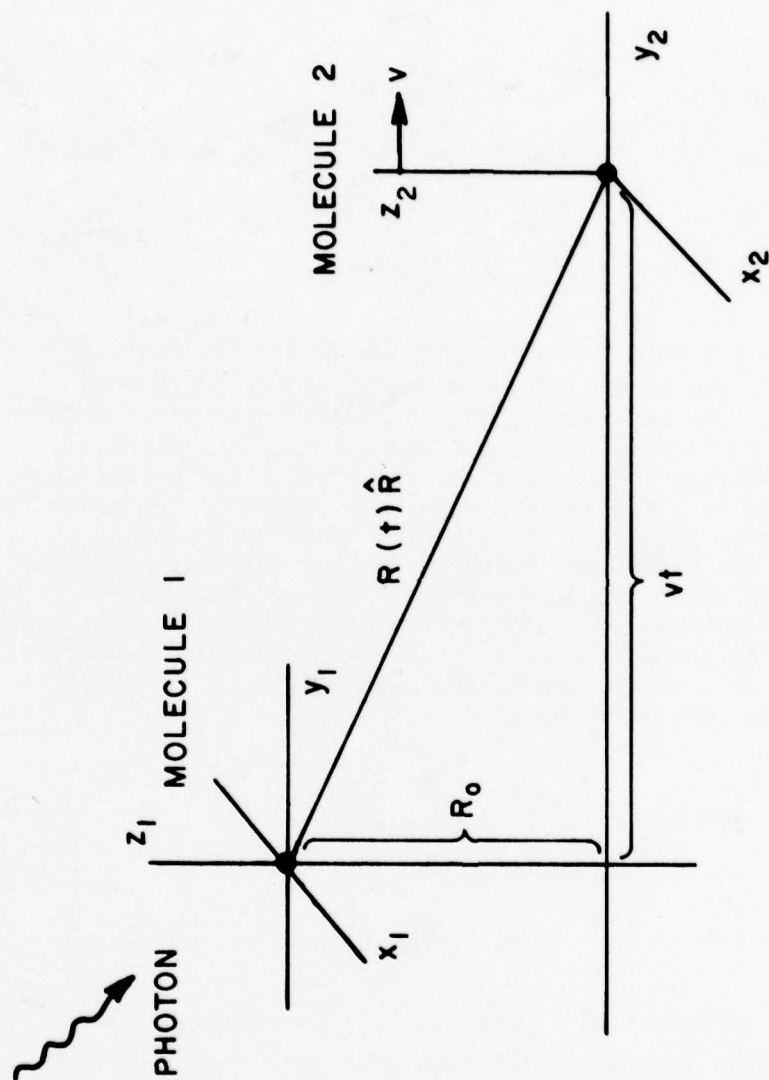


Figure 5. Binary collision and the classical path assumption, $R(t) = (R_0^2 + (vt)^2)^{1/2}$.

- $V_{DD}(\bar{r}_{mk}, \bar{r}_1)$ - Dipole-dipole interaction term
 $V_{DQ}(\bar{r}_{mk}, \bar{r}_1)$ - Dipole-quadrupole interaction term
 $V_{DO}(\bar{r}_{mk}, \bar{r}_1)$ - Dipole-octupole interaction term
 $V_{QQ}(\bar{r}_{mk}, \bar{r}_1)$ - Quadrupole-quadrupole interaction term

and

$$\begin{aligned}
 V_{DD}(\bar{r}_{mk}, \bar{r}_1) &= \mu_{mk} \mu_1 f(\Omega_{mk}, \Omega_1) \\
 V_{DQ}(\bar{r}_{mk}, \bar{r}_1) &= \mu_{mk} \bar{Q}_1 g_1(\Omega_{mk}, \Omega_1) + \bar{Q}_{mk} \mu_1 g_2(\Omega_{mk}, \Omega_1) \\
 V_{DO}(\bar{r}_{mk}, \bar{r}_1) &= \mu_{mk} \bar{R}_1 h_1(\Omega_{mk}, \Omega_1) + \bar{R}_{mk} \mu_1 h_2(\Omega_{mk}, \Omega_1) \\
 V_{QQ}(\bar{r}_{mk}, \bar{r}_1) &= \bar{Q}_{mk} \bar{Q}_1 i(\Omega_{mk}, \Omega_1)
 \end{aligned}$$

μ_{mk} and μ_1 are the dipole moments of broadener and absorber, respectively. \bar{Q} is the mean quadrupole moment and \bar{R} is the mean octupole moment. The functions of Ω_{mk} and Ω_1 represent the angular dependence of the potential functions and whether the potential function is attractive or repulsive at the generalized orientation angles Ω_{mk} and Ω_1 in a space-fixed coordinate system. The molecules are rotating during the collision with the amount of rotation observed during the collision depending on the collision duration time. The forces induced by the electrostatic potential will always try to orient the molecules in a minimum energy configuration resulting in a net attractive force. An average over this rotation is performed to account for the molecule's ability to achieve this preferred orientation; it is denoted by $\langle \rangle_{Rot}$.

$$\langle V_{E1} \rangle_{Rot} = \frac{\int d\Omega V_{E1} e^{-V_{E1}/kT} p(\Omega_0, t_d, f_{mk}^R, f_1^R)}{\int d\Omega e^{-V_{E1}/kT} p(\Omega_0, t_d, f_{mk}^R, f_1^R)} \quad (16)$$

where $d\Omega$ is the differential element for all orientation angles and $p(\Omega_0, t_d, f_{mk}^R, f_1^R)$ is a pulse function with unit amplitude and pulse duration depending on Ω_0 , the initial orientation, t_d , the collision duration time and f_{mk}^R and f_1^R , the rotational frequencies of the broadening molecule and absorbing molecule, respectively.

For collisions with large impact parameters the collision duration time is very brief, thus

$$\langle V_E \rangle_{\text{Rot}} \sim V_E \quad (17)$$

For collisions with small impact parameters the electrostatic potentials can be so strong that it is no longer a small perturbation to the rotational motion. This happens in the formation of liquids and solids. The molecule's ability to rotate is inhibited as it takes a relatively fixed orientation. Thus the average over rotations breaks down. In fact the formulation of the unperturbed Hamiltonian is no longer valid. This is an important point for water vapor and will be discussed in more detail later.

Not all molecules have permanent dipole moments, and thus other types of long range potentials are of interest. The most important are induction and dispersion, both with leading terms of the form $R^{-6}(t)$. Induction potentials, $V_{\text{Inductive}}$, represent the interaction of a permanent electric multipole of one molecule with an induced electric multipole of another molecule with perhaps no permanent multipole. The resulting potential is attractive. Dispersion potentials arise from the random motion (within the bounds of the uncertainty principle) of electrons about the nuclei generating instantaneous multipoles. These brief multipoles can induce multipoles in other molecules resulting in an attractive potential. For a detailed description of these potentials see Margenau and Kestner [33]. Approximate forms are given below [34].

$$V_{\text{Inductive}} = - \frac{[\mu_1^2 \bar{\alpha}_{mk} + \mu_{mk}^2 \bar{\alpha}_1]}{R^6(t)} \quad (18)$$

$$V_{\text{Dispersive}} = - \frac{\bar{\alpha} e^2 \langle r^2 \rangle}{2 R^6(t)} \quad (19)$$

where

$\bar{\alpha}$ - mean electric polarizability

e - charge of an electron.

The discussion of $H_c(t)$ thus far has involved the long range potentials. Intuitively, these are the most important potentials

to consider for gases. The short range potentials, $V_{\text{Repulsive}}$, are repulsive in nature such as experienced by the electron clouds of very close molecules. The combination of the long range attractive potentials and the short range repulsive potentials determine intermolecular bonds which result in possible polymer formations. In some gases the dimer is by far the most common polymer. Knowledge of bond lengths and strengths are helpful in determining the nature of intermolecular potentials for small separations (2-7 Å). Figure 6 shows the form of a general intermolecular potential.

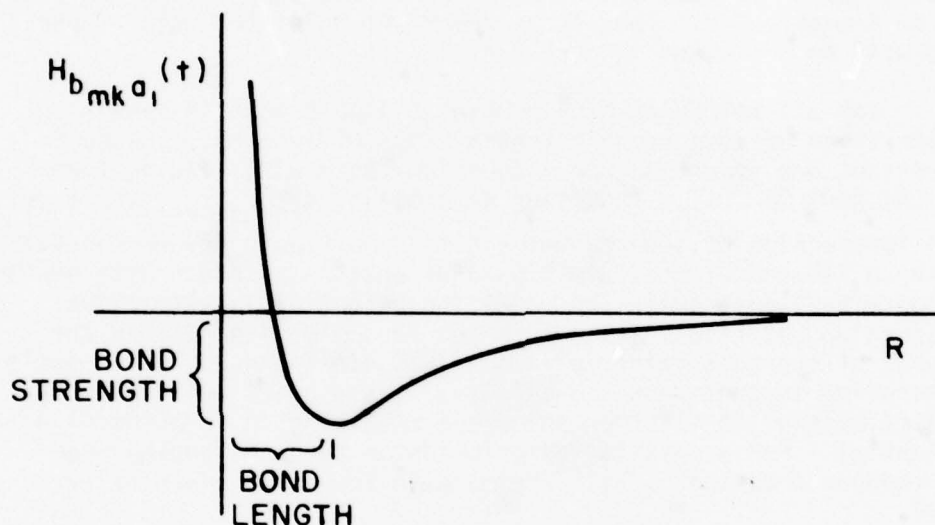


Figure 6. The intermolecular potential

The development of spectral line intensity by Anderson, Tsao and Curnutte [35,36] will be followed to obtain a transition rate of the system. The probability that the system will change from an initial state $|s^i(t)\rangle$ to some final state $\langle s^f(t)|$ is

$$P_{i \rightarrow f} = |\langle s^f(t) | s^i(t) \rangle|^2 \quad (20)$$

The zero order eigenfunction of the system is a product of the eigenfunctions corresponding to each individual zero order Hamiltonian composing the total quantum system.

$$|s(t)\rangle = |a_1(t)a_2(t)\dots a_{N_a}(t)b_{11}(t)\dots b_{km}(t)\dots b_{KN_k}(t)\dots n_{q\sigma}(t)\dots\rangle \quad (21)$$

The notation follows from the definition of the Hamiltonians. The time dependence of the initial and final eigenstates can be characterized by the appropriate time-development operator (scattering operator)

$$|s^i(t)\rangle = S_{\text{Tot}}(t) |s^i\rangle \quad (22)$$

and

$$\langle s^f(t) | = \langle s^f | S_{\text{oc}}^{-1}(t). \quad (23)$$

A convenient form for the operators of concern is

$$S_{\text{Tot}}(t) = e^{-\frac{1}{i\hbar} \int_0^t H_{\text{Tot}}(t') dt'} \quad (24)$$

$$S_{\text{oc}}^{-1}(t) = e^{\frac{-1}{i\hbar} \int_0^t H_{\text{oc}}(t') dt'} \quad (25)$$

where $H_{\text{oc}}(t) = H_0 + H_c(t)$.

$H_c(t)$ lacks only the interaction between field and particle since the final state comes after the photon interaction. Therefore,

$$P_{i \rightarrow f} = |\langle s^f | S_{\text{oc}}^{-1}(t) S_{\text{Tot}}(t) | s^i \rangle|^2. \quad (26)$$

Let

$$V(t) = S_{\text{oc}}^{-1}(t) S_{\text{Tot}}(t) \quad (27)$$

then

$$i\hbar \dot{V}(t) = (S_{\text{oc}}^{-1}(t) H_{a,p}(t) S_{\text{oc}}(t)) V(t) \quad (28)$$

where the relations

$$i\hbar S_{oc}^{-1}(t) = - S_{oc}^{-1}(t) H_{oc}(t)$$

$$i\hbar S_{Tot}(t) = H_{Tot}(t) S_{Tot}(t)$$

have been used. Equation (27) leads to

$$V(t) = \exp \left\{ \frac{1}{i\hbar} \int_0^t S_{oc}^{-1}(t') H_{a_1p}(t') S_{oc}(t') dt' \right\} . \quad (29)$$

A perturbation expansion of the above result gives

$$V(t) = 1 + \sum_{n=1}^{\infty} \frac{1}{(i\hbar)^n} \int_0^t dt' \int_0^{t'} dt'' \dots \int_0^{t^{(n-1)}} dt^{(n)} (S_{oc}^{-1}(t') H_{a_1p}(t') S_{oc}(t')) \\ (S_{oc}^{-1}(t'') H_{a_1p}(t'') S_{oc}(t'')) \dots (S_{oc}^{-1}(t^{(n)}) H_{a_1p}(t^{(n)}) S_{oc}(t^{(n)})) . \quad (30)$$

Terms for $n \geq 2$ represent multiple photon processes such as Raman scattering, Rayleigh scattering, second harmonic generation, etc. For the Photon density levels and frequencies of interest these higher order terms are unimportant. $V(t)$ to first order is

$$V(t) = 1 + \frac{1}{i\hbar} \int_0^t dt' S_{oc}^{-1}(t') H_{a_1p}(t') S_{oc}(t') . \quad (31)$$

Recall also that $H_{a_1p}(t)$ contains two terms, one involving a single photon interaction ($\bar{P} \circ \bar{A}$) and the other a two photon process ($\bar{A} \circ \bar{A}$). For the same reasons as above only the $\bar{P} \circ \bar{A}$ term needs to be retained. Also, because the eigenstate has the particle and photon states independent of one another the interaction Hamiltonian can be written using Equations (11) and (12) as follows,

$$\begin{aligned}
H_{a_1 p}(t) = & \left(-\frac{e}{cm}\right) \left(\frac{2\pi\hbar c}{qV}\right)^{1/2} (a_{\sigma}(\bar{q}) \bar{p} \cdot \bar{\epsilon}(\bar{q}) e^{i\bar{q}\cdot\bar{r}}) e^{-i\omega t} \\
& + \left(\frac{2\pi\hbar c}{qV}\right)^{1/2} (a_{\sigma}^{\dagger}(\bar{q}) \bar{p} \cdot \bar{\epsilon}^*(\bar{q}) e^{-i\bar{q}\cdot\bar{r}}) e^{i\omega t} (u(t) - u(T))
\end{aligned} \quad (32)$$

$$H_{a_1 p}(t) = \left[H_{a_1 p}^{ab} e^{-i\omega t} + H_{a_1 p}^{em} e^{i\omega t} \right] (u(t) - u(T)). \quad (33)$$

Equation (33) has two parts, one for absorption and one for emission of a photon. For absorption the matrix element becomes

$$\langle s^f | V^{ab}(t) | s^i \rangle = \frac{1}{i\hbar} \int_0^T dt' \langle s^f | S_{oc}^{-1}(t') H_{a_1 p}^{ab} S_{oc}(t') | s^i \rangle e^{-i\omega t'} \quad (34)$$

and for emission

$$\langle s^f | V^{em}(t) | s^i \rangle = \frac{1}{i\hbar} \int_0^T dt' \langle s^f | S_{oc}^{-1}(t) H_{a_1 p}^{em} S_{oc}(t') | s^i \rangle e^{i\omega t'}. \quad (35)$$

The zero order part of the time development operator is removed by observing

$$S_{oc}(t) | s^i \rangle = \exp\left(\frac{1}{i\hbar} E_i t\right) S_c(t) | s^i \rangle \quad (36)$$

$$\langle s^f | S_{oc}^{-1}(t) = \exp\left(\frac{-1}{i\hbar} E_f t\right) \langle s^f | S_c^{-1}(t). \quad (37)$$

Also, using $\hbar\omega_0 = E_f - E_i$ and $\Delta\omega = \omega - \omega_0$ the matrix elements become

$$\langle s^f | V^{ab}(t) | s^i \rangle = \frac{1}{i\hbar} \int_0^T dt' e^{-i\Delta\omega t'} \langle s^f | S_c^{-1}(t') H_{a_1 p}^{ab} S_c(t') | s^i \rangle \quad (38)$$

and

$$\langle s^f | V^{em}(t) | s^i \rangle = \frac{1}{i\hbar} \int_0^T dt' e^{i\Delta\omega t'} \langle s^f | S_c^{-1}(t') H_{a_1 p}^{em} S_c(t') | s^i \rangle. \quad (39)$$

It is only necessary to analyze Equation (38) since the emission matrix element will develop analogously. This is a manifestation of detailed balancing.

Substituting Equation (38) into Equation (26) yields

$$P_{i \rightarrow f} = \frac{1}{\hbar^2} \left| \int_0^T dt' e^{-i\Delta\omega t'} \langle s^f | S_c^{-1}(t') H_{a_1 p}^{ab} S_c(t') | s^i \rangle \right|^2. \quad (40)$$

The general probability, P , is obtained by summing $P_{i \rightarrow f}$ over the final states and averaging over the initial states

$$P = \left\langle \sum_f P_{i \rightarrow f} \right\rangle_i. \quad (41)$$

The probability of a transition becomes

$$P = \frac{1}{\hbar^2} \int_0^T dt' \int_0^T dt'' e^{-i\Delta\omega(t''-t')} \text{Tr} \left[\rho_0 S_c^{-1}(t') H_{a_1 p}^{ab} S_c(t') S_c^{-1}(t'') H_{a_1 p}^{ab} S_c(t'') \right] \quad (42)$$

where ρ_0 is the density matrix generated by the initial states. Since the operators in a trace can be cyclically permuted the trace in Equation (42) becomes

$$\text{Tr} \left[\rho_0 H_{a_1 p}^{ab} (S_c^{-1}(t'') S_c(t')) H_{a_1 p}^{ab} (S_c(t'') S_c^{-1}(t')) \right].$$

It is convenient to observe that

$$\begin{aligned} S_c^{-1}(t'') S_c(t') &= S_c^{-1}(\tau) \quad \text{and} \\ S_c(t'') S_c^{-1}(t') &= S_c(\tau) \end{aligned} \quad (43)$$

where $\tau = t'' - t'$. Tsao and Curnutte [36] maintain these relations to be true when averaged over all molecular collision paths. This simplifies the trace to the form

$$\text{Tr} \left[\rho_0 H_{a1p}^{ab} S_c^{-1}(\tau) H_{a1p}^{ab} S_c(\tau) \right] . \quad (44)$$

Let

$$F(\tau) = e^{-i\Delta\omega\tau} \text{Tr} \left[\rho_0 H_{a1p}^{ab} S_c^{-1}(\tau) H_{a1p}^{ab} S_c(\tau) \right] . \quad (45)$$

Note that $F(\tau) = F^*(-\tau)$ (where * denotes complex conjugate) and transform the variables of integration from t'' and t' to τ and t' . Figure 7 illustrates this change of variables. Therefore,

$$P = \frac{1}{\hbar^2} \left[\int_0^T d\tau F(\tau) \int_0^{T-\tau} dt' + \int_{-T}^0 d\tau F(\tau) \int_{|\tau|}^T dt' \right]$$

or

$$P = \frac{2}{\hbar^2} \text{Re} \int_0^T d\tau (T-\tau) F(\tau) . \quad (46)$$

For a cw probe photon field the observation time is extremely long compared to interaction times.

It is assumed therefore that $T \gg \tau$ and P becomes

$$P = \frac{2T}{\hbar^2} \text{Re} \int_0^T d\tau F(\tau) . \quad (47)$$

The assumption that $T \gg \tau$ will in practice become invalid for 100 picosecond or less pulse durations of the photon field (i.e., $T < 10^{-10}$ seconds). The transition rate, Γ , is the probability

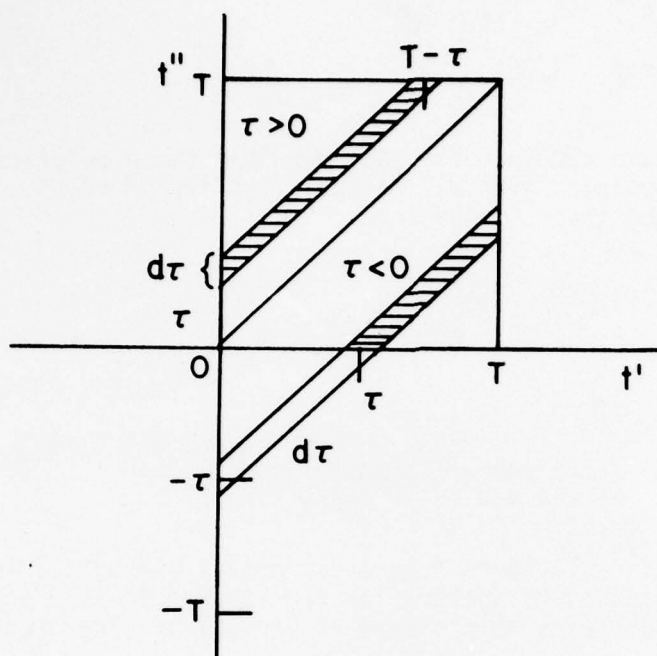


Figure 7. Change of the integration variables.

of observing a transition per unit of time or $\Gamma = \frac{P}{T}$. The transition is between two energy levels designated upper and lower. For absorption, the lower energy is the initial state. Thus the transition rate can be written Γ_{lu} , and Equation (47) becomes

$$\Gamma_{lu} = \frac{2}{\hbar^2} \operatorname{Re} \int_0^\infty d\tau e^{-i\Delta\omega\tau} \operatorname{Tr} \left[\rho_0 H_{a_1 p}^{ab} S_c^{-1}(\tau) H_{a_1 p}^{ab} S_c(\tau) \right] \quad . \quad (48)$$

The observation time has been extended to infinity with very little loss in accuracy. Equation (48) forms the basis for many modern line shape theories [37,38,39,40,41] which have followed the work of Anderson, Tsao, and Curnutte.

Equation (48) is written in a very compact form and will be expanded by summing over the initial states of the trace and a complete set of final states, i.e.

$$\Gamma_{lu} = \frac{2}{\pi^2} \operatorname{Re} \int_0^\infty d\tau e^{i\Delta\omega\tau} \sum_{\substack{a_l, J_l, M_l \\ s_l^b \\ q_l, \sigma_l}} \frac{1}{g_l} \rho_l \rho_{s_l^b} \rho_p \sum_{\substack{a_u, J_u, M_u \\ s_u^b \\ q_u, \sigma_u}} \quad (49)$$

$$\langle a_l J_l M_l s_l^b n_{q\sigma l} | H_{a_1 p}^{ab} | a_u J_u M_u s_u^b n_{q\sigma u} \rangle \langle a_u J_u M_u s_u^b n_{q\sigma u} | S_c^{-1}(\tau) H_{a_1 p}^{ab} S_c(\tau) | a_l J_l M_l s_l^b n_{q\sigma l} \rangle$$

- where
- $g_l = 2J_l + 1$ - degeneracy of lower level
 - $\frac{1}{g_l} \rho_l = \rho_{\text{Vib}} \rho_{\text{Rot}}$ - density matrix over vibrational and rotational states
 - ρ_p - density matrix for the photon field
 - $\rho_{s_l^b}$ - density matrix over vibrational and rotational states of broadening molecule.

The "a" quantum numbers represent all other quantum numbers necessary to describe the absorbing molecule besides the rotational quantum numbers J and M. s_l^b and s_u^b represent all states and necessary quantum numbers for the broadening molecules. To abbreviate the notation let $l = a_l J_l M_l$ and $u = a_u J_u M_u$ and, realizing $H_{a_1 p}^{ab}$ is independent of s_l^b or s_u^b , we have

$$\Gamma_{lu} = \frac{2}{\pi^2} \operatorname{Re} \left[\sum_{\substack{a_l J_l \\ a_u J_u}} \rho_l \frac{1}{g_l} \sum_{\substack{m_l, m_u \\ q_l, \sigma_l}} \sum_{q_l \sigma_l} \rho_p \langle n_{q\sigma l} | H_{a_1 p}^{ab} | u n_{q\sigma u} \rangle \sum_{\substack{s_u^b \\ s_l^b}} \rho_{s_l^b} \delta_{s_l^b s_u^b} \int_0^\infty d\tau e^{-i\Delta\omega\tau} \langle u s_u^b n_{q\sigma u} | S_c^{-1}(\tau) H_{a_1 p}^{ab} S_c(\tau) | l s_l^b n_{q\sigma l} \rangle \right]. \quad (50)$$

Reducing the sums for nontrivial matrix elements

$$\Gamma_{lu} = \frac{2\pi}{\hbar^2} \text{Re} \left\{ \sum_{a_\ell, J_\ell} \rho_\ell \frac{1}{g_\ell} \sum_{M_\ell, M_u} \sum_{q_\ell, \sigma_\ell} \rho_p \langle \ell n_{q\sigma\ell} | H_{a_1 p}^{ab} | u n_{q\sigma u} \rangle \sum_b \rho_{s^b} \right. \\ \left. \times \int_0^\infty d\tau e^{-i\Delta\omega\tau} \langle u s^b n_{q\sigma u} | S_c^{-1}(\tau) H_{a_1 p}^{ab} S_c(\tau) | \ell s^b n_{q\sigma\ell} \rangle \right\}. \quad (51)$$

The subscripts "u" and "l" have been dropped from s^b and s^b in the above formula since the Kronecker- δ requires $\ell=u$. By inserting unit operators between the time development operators and the interaction Hamiltonian $H_{a_1 p}^{ab}$ the following relation is obtained

$$\langle u s^b n_{q\sigma u} | S_c^{-1}(\tau) H_{a_1 p}^{ab} S_c(\tau) | \ell s^b n_{q\sigma\ell} \rangle = \\ \sum_{u', s^{b'}} \langle u s^b n_{q\sigma u} | S_c^{-1}(\tau) | u' s^{b'} n'_{q\sigma u} \rangle \langle u' s^{b'} n'_{q\sigma u} | H_{a_1 p}^{ab} | \ell' s^{b'} n'_{q\sigma\ell} \rangle \\ \sum_{\substack{n'_{q\sigma u} \\ s^{b''} n'_{q\sigma\ell}}} \\ \times \langle \ell' s^{b''} n'_{q\sigma\ell} | S_c(\tau) | \ell s^b n_{q\sigma\ell} \rangle. \quad (52)$$

Since S_c is independent of the photon field and $H_{a_1 p}^{ab}$ is independent of the broadening molecules $s^{b'} = s^{b''}$, $n'_{q\sigma\ell} = n_{q\sigma\ell}$, and $n'_{q\sigma u} = n_{q\sigma u}$.

Further the adiabatic assumption [36,37] is made requiring $u=u'$, $s^b = s^{b'}$, and $\ell=\ell'$. Therefore, Equation (52) becomes

$$\langle u s^b | S_c^{-1}(\tau) | u s^b \rangle \langle u n_{q\sigma u} | H_{a_1 p}^{ab} | \ell n_{q\sigma\ell} \rangle \langle \ell s^b | S_c(\tau) | \ell s^b \rangle. \quad (53)$$

Substituting this result into Equation (51) we obtain,

$$\Gamma_{\ell u} = \frac{2\pi}{\hbar^2} \sum_{a_{\ell}, J_{\ell}} \rho_{\ell} \frac{1}{g_{\ell}} \sum_{M_{\ell} M_u} \sum_{q_{\ell} \sigma_{\ell}} \rho_p \langle \ell n_{q\sigma u} | H_{a_1 p}^{ab} | \ell n_{q\sigma \ell} \rangle^2 \frac{\text{Re}}{\pi} \int_0^{\infty} d\tau e^{-i\Delta\omega\tau} \\ \times \sum_b \rho_{s^b} \langle u s^b | S_c^{-1}(\tau) | u s^b \rangle \langle \ell s^b | S_c(\tau) | \ell s^b \rangle. \quad (54)$$

Now examine a single matrix element of the time development operator in terms of each collision Hamiltonian between the absorber and all broadeners

$$\langle \ell s^b | S_c(\tau) | \ell s^b \rangle = \langle \ell s^b | \prod_{j=2}^{N_a} S_{ca_1 a_j} \prod_{k=1}^{N_1} S_{ca_1 b_{k1}} \dots \prod_{n=1}^{N_k} S_{ca_1 b_{nk}} | \ell s^b \rangle. \quad (55)$$

Assuming binary collisions,

$$\langle \ell s^b | S_c(\tau) | \ell s^b \rangle = \langle \ell s^a | S_{ca_1 a} | \ell s^a \rangle^{N_a-1} \langle \ell s^{b_1} | S_{ca_1 b_1} | \ell s^{b_1} \rangle^{N_1} \dots \\ \dots \langle \ell s^{b_k} | S_{ca_1 b_k} | \ell s^{b_k} \rangle^{N_k}. \quad (56)$$

$S_{ca_1 a}$, $S_{ca_1 b_1}$, ..., $S_{ca_1 b_k}$ represent quantities averaged over velocity and impact parameter, and summed over collisional events. Analogously, it can be stated,

$$\langle u s^b | S_c^{-1}(\tau) | u s^b \rangle = \langle u s^a | S_{ca_1 a} | u s^a \rangle^{N_a-1} \langle u s^{b_1} | S_{ca_1 b_1} | u s^{b_1} \rangle^{N_1} \dots \\ \dots \langle u s^{b_k} | S_{ca_1 b_k} | u s^{b_k} \rangle^{N_k}. \quad (57)$$

The sum over broadening states in Equation (54) can be expanded to be

$$\sum_b \rho_{sb} \langle u_s^b | S_c^{-1}(\tau) | u_s^b \rangle \langle \ell_s^b | S_c(\tau) | \ell_s^b \rangle =$$

$$\left(\sum_a \rho_{sa} \langle \langle u_s^a | S_{ca_1a}^{-1}(\tau) | u_s^a \rangle \langle \ell_s^a | S_{ca_1a}(\tau) | \ell_s^a \rangle \rangle_{R_0, v, t_0}^{N_a} \dots \dots \right.$$

$$\left. \times \left(\sum_{b_k} \rho_{sb_k} \langle \langle u_s^{b_k} | S_{ca_1b_k}^{-1}(\tau) | u_s^{b_k} \rangle \langle \ell_s^{b_k} | S_{ca_1b_k}(\tau) | \ell_s^{b_k} \rangle \rangle_{R_0, v, t_0}^{N_k} \right) \right) .$$

(58)

The symbol $\langle \rangle_{R_0, v, t_0}$ indicates the average over impact parameter and velocity and sum over collision events. It is written mathematically, for arbitrary A,

$$\langle A \rangle_{R_0, v, t_0} = \frac{1}{V} 8\pi^{1/2} \left(\frac{\pi}{2kT} \right)^{3/2} \int_0^\infty v^3 dv e^{-(\mu v^2/kT)} \int_{R_{Min}}^\infty R_0 dR_0 \sum_{t_0} A$$

(59)

where

- V - volume
- μ - reduced mass of binary system
- T - temperature
- k - Boltzmann's constant.

Also because $N_a \gg 1$ then $N_a - 1 \sim N_a$ this fact is used in Equation (58). It is convenient to define

$$\begin{aligned}
c_{a_1 a}(\tau) &= \sum_s \rho_s^a \langle \langle u s^a | S_{ca_1 a}^{-1}(\tau) | u s^a \rangle \langle l s^a | S_{ca_1 a}(\tau) | l s^a \rangle \rangle_{R_0, v, t_0} \\
&\vdots \\
c_{a_1 b_k}(\tau) &= \sum_{s_k} \rho_{s_k}^{b_k} \langle \langle u s^{b_k} | S_{ca_1 b_k}^{-1}(\tau) | u s^{b_k} \rangle \langle l s^{b_k} | S_{ca_1 b_k}(\tau) | l s^{b_k} \rangle \rangle_{R_0, v, t_0} .
\end{aligned}$$

Then

$$\begin{aligned}
\sum_b \rho_s^b \langle u s^b | S_c^{-1}(\tau) | u s^b \rangle \langle l s^b | S_c(\tau) | l s^b \rangle &= C(\tau) \\
&= c_{a_1 a}^N(\tau) c_{a_1 b_1}^N(\tau) \dots c_{a_1 b_k}^N(\tau) . \quad (60)
\end{aligned}$$

The transition rate can then be written

$$\begin{aligned}
\Gamma_{lu} &= \sum_{a_l J_l} \rho_l \left(\frac{2\pi}{\hbar^2} \frac{1}{g_l} \sum_{M_u, M_l} \sum_{q_l, \sigma_l} \rho_p \left| \langle u n_{q\sigma u} | H_{a_1 p}^{ab} | l n_{q\sigma l} \rangle \right|^2 \right. \\
&\quad \left. \times \left\{ \operatorname{Re} \frac{1}{\pi} \int_0^\infty d\tau e^{-i\Delta\omega\tau} C(\tau) \right\} \right) . \quad (61)
\end{aligned}$$

For no external perturbations except for photon interactions, $H_c(t)=0$. Then $C(\tau)=1$ and

$$\operatorname{Re} \frac{1}{\pi} \int_0^\infty d\tau e^{-i\Delta\omega\tau} = \delta(\Delta\omega) .$$

The transition rate takes on the familiar form of Fermi's Golden Rule.

$$\Gamma_{lu} = \sum_{a_l J_l} \rho_l \left(\frac{2\pi}{\hbar} \frac{1}{g_l} \sum_{M_u, M_l} \sum_{q_l, \sigma_l} \rho_p \left| \langle u n_{q_l} | H_{a_l p}^{ab} | l n_{q_l \sigma_l} \rangle \right|^2 \delta(E_u - E_l - \hbar\omega) \right). \quad (62)$$

The sums over a_l and J_l simply add the effects of all possible transitions. The term in parenthesis in Equation (62) leads to the absorption contribution to the line strength for a single transition. To complete the line strength emission processes must be included. The transition rate for emission is ($H_c(t)=0$)

$$\Gamma_{ul} = \sum_{a_u J_u} \frac{\rho_u}{g_u} \left(\frac{2\pi}{\hbar} \sum_{M_u, M_l} \sum_{q_u, \sigma_u} \rho_p \left| \langle u n_{q_u} | H_{a_l p}^{em} | l n_{q_u \sigma_u} \rangle \right|^2 \delta(E_u - E_l + \hbar\omega) \right). \quad (63)$$

The frequency dependence of the transition rate is contained in the integral expression and this becomes the line shape for collision-broadened lines. Thus

$$j_c^R(\omega) = \frac{1}{\pi} \operatorname{Re} \int_0^\infty d\tau e^{-i\Delta\omega\tau} C(\tau). \quad (64)$$

$C(\tau)$ is interpreted as an autocorrelation function between the state of the atom at $\tau=0$ and at time τ . It is symmetric about $\tau=0$, monotonically decaying as time increases. Using the symmetric property of $C(\tau)$, Equation (64), can be re-expressed as

$$j_c^R(\omega) = \frac{\text{Re}}{2\pi} \int_{-\infty}^{\infty} d\tau e^{-i\omega\tau} e^{i\omega_0\tau} C(\tau)$$

$$= \text{Re } F^{-1} \left\{ e^{i\omega_0\tau} C(\tau) \right\} . \quad (65)$$

Thus, $j_c^R(\omega)$ and $e^{i\omega_0\tau} C(\tau)$ are Fourier transform pairs. To generalize the concept further, let $j_c^I(\omega)$ be the Hilbert transform companion of $j_c^R(\omega)$. Define

$$j_c(\omega) = F^{-1} \left\{ e^{i\omega_0\tau} C(\tau) \right\} = j_c^R(\omega) + i j_c^I(\omega) . \quad (66)$$

$j_c^I(\omega)$ represents refractive index effects of the collision process. Because the interest of this study is centered upon line shapes (refractive index changes are small for gases) the superscript R will be dropped and the line shape function will be denoted by

$$j_c(\omega) = \text{Re } F^{-1} \left\{ e^{i\omega_0\tau} C(\tau) \right\} . \quad (67)$$

The line strength and line shape equations will be developed separately in the following sections.

C. The Line Strength

The line strength of a particular transition (fixed a_ℓ, J_ℓ) will now be considered. For a medium in thermal equilibrium the rate of transitions from particular upper to lower energy states and lower to upper energy states must be equal, i.e.

$$\left(\frac{dN_{q\sigma}}{dt} \right)_{\text{absorbed}} = \left(\frac{dN_{q\sigma}}{dt} \right)_{\text{emitted}} . \quad (68)$$

$N_{q\sigma}$ is the photon occupation number, that is, the number of photons with wavenumber q and polarization σ . The quantities in Equation (68) are related to the transition rate by

$$\left(\frac{dN_{q\sigma}}{dt}\right)_{\text{abs}} = n_a \Gamma_{\ell u} \quad \text{and} \quad (69)$$

$$\left(\frac{dN_{q\sigma}}{dt}\right)_{\text{em}} = n_a \Gamma_{u\ell} \quad \text{where} \quad (70)$$

n_a is the total number of absorbing molecules per volume. Using Equations (62) and (63) for fixed a_ℓ, J_ℓ the above relations are written,

$$n_a \Gamma_{\ell u} = n_{a\ell} \frac{2\pi}{\hbar} \frac{1}{g_\ell} \sum_{M_u, M_\ell} \sum_{q_\ell, \sigma_\ell} \rho_p \left| \langle u n_{q\sigma u} | H_{a,p}^{ab} | \ell n_{q\sigma \ell} \rangle \right|^2 \delta(E_u - E_\ell - \hbar\omega) \quad (71)$$

and

$$n_a \Gamma_{u\ell} = n_{au} \frac{2\pi}{\hbar} \frac{1}{g_u} \sum_{M_u, M_\ell} \sum_{q_\ell, \sigma_\ell} \rho_p \left| \langle u n_{q\sigma u} | H_{a,p}^{em} | \ell n_{q\sigma \ell} \rangle \right|^2 \delta(E_u - E_\ell + \hbar\omega) \quad (72)$$

where $n_{a\ell}$ and n_{au} are the number of absorbing molecules in the lower and upper energy level, respectively. To obtain the standard form for the line strength, the matrix element in Equation (71) and Equation (72) is assumed to be independent of the sum over initial photon states. This is usually a good approximation but breaks down for pure rotational transitions and a correction factor will be introduced to handle this situation. Since

$$\sum_{q_\ell, \sigma_\ell} \rho_p = 1$$

Equations (71) and (72) become

$$n_a \Gamma_{lu} = n_{al} \frac{2\pi}{\hbar} \frac{1}{g_l} \sum_{\substack{M_u, M_l \\ q_u, \sigma_u}} |\langle u n_{q\sigma u} | H_{a1p}^{ab} | l n_{q\sigma l} \rangle|^2 \delta(E_u - E_l - \hbar\omega) \quad (73)$$

and

$$n_a \Gamma_{lu} = n_{au} \frac{2\pi}{\hbar} \frac{1}{g_u} \sum_{\substack{M_a, M_l \\ q_u, \sigma_u}} |\langle u n_{q\sigma u} | H_{a1p}^{em} | l n_{q\sigma l} \rangle|^2 \delta(E_u - E_l + \hbar\omega) \quad (74)$$

Combining the above equations with Equation (68) results in the Einstein relation. A brief outline of how this comes about follows.

To simplify the mathematical expressions, Equations (73) and (74) are compressed to the form

$$n_a \Gamma_{lu} = n_{al} \frac{1}{g_l} \sum_{\substack{M_u, M_l \\ q_u, \sigma_u}} \Gamma'_{lu; q_u, \sigma_u} \quad (75)$$

and

$$n_a \Gamma_{lu} = n_{au} \frac{1}{g_u} \sum_{\substack{M_u, M_l \\ q_u, \sigma_u}} \Gamma'_{ul; q_u, \sigma_u} \quad (76)$$

Substituting in Equation (32) for the interaction Hamiltonians the primed transition rates can be written

$$\begin{aligned} \Gamma'_{lu; q_u, \sigma_u} = \frac{2\pi}{\hbar} \left| -\frac{e}{cm} \left(\frac{2\pi\hbar c}{qv} \right)^{1/2} \langle n_{q\sigma u} | a_{\sigma}(\bar{q}) | n_{q\sigma l} \rangle \langle u | \bar{p} \cdot \bar{\epsilon}_{\sigma} e^{i\bar{q} \cdot \bar{r}} | l \rangle \right|^2 \\ \times \delta(\hbar(\omega_0 - \omega)) \end{aligned} \quad (77)$$

and

$$\Gamma'_{ul;q_u,\sigma_u} = \frac{2\pi}{\hbar} \left| -\frac{e}{cm} \left(\frac{2\pi\hbar c}{qv} \right)^{1/2} \langle n_{q\sigma u} | a_{\sigma}^{\dagger}(\bar{q}) | n_{q\sigma l} \rangle \langle u | \bar{p} \cdot \bar{\epsilon}_{\sigma}^* e^{-i\bar{q} \cdot \bar{r}} | l \rangle \right|^2 \times \delta(\hbar(\omega_0 + \omega)) . \quad (78)$$

The above expressions are reduced using

$$\begin{aligned} \langle n_{q\sigma u} | a_{\sigma}(\bar{q}) | n_{q\sigma l} \rangle &= \sqrt{N_{q\sigma l}} \delta_{N_{q\sigma u}, N_{q\sigma l}-1} , \\ \langle n_{q\sigma u} | a_{\sigma}^{\dagger}(\bar{q}) | n_{q\sigma l} \rangle &= \sqrt{N_{q\sigma l}+1} \delta_{N_{q\sigma u}, N_{q\sigma l}+1} , \\ e^{i\bar{q} \cdot \bar{r}} &\sim 1 \quad \text{the dipole approximation and} \\ \langle u | \bar{p} | l \rangle &= im\omega \langle u | \bar{r} | l \rangle = \frac{im\omega}{e} \bar{M} . \end{aligned}$$

Thus

$$\Gamma'_{lu;q_u,\sigma_u} = N_{q\sigma l} \frac{4\pi^2 \omega^2}{\hbar^2 v^2 c^2} \bar{M}^2 \bar{\epsilon}_{\sigma_u}^* \delta(\omega_0 - \omega) \quad (79)$$

and

$$\Gamma'_{ul;q_u,\sigma_u} = (N_{q\sigma l} + 1) \frac{4\pi^2 \omega^2}{\hbar^2 v^2 c^2} \bar{M}^2 \bar{\epsilon}_{\sigma_u}^* \delta(\omega_0 + \omega) . \quad (80)$$

The sum over the final photon states is approximated by

$$\sum_{q_u, \sigma_u} \rightarrow \sum_{\sigma_u} \frac{V}{(2\pi)^3} \int q^2 dq d\Omega_q .$$

The primed transition rates become

$$\Gamma'_{lu} = N_{q\sigma l} \frac{8\pi\omega_0^3}{3 \hbar c^3} |\bar{M}|^2 \quad (81)$$

and

$$r'_{ul} = (N_{qu} + 1) \frac{8\pi\omega_0^3}{3hc^3} |\bar{M}|^2 \quad (82)$$

The sums over the final photon states effectively result in an average over the random orientations of the molecules and are only valid for random orientations between the photon field and dipoles. Substituting Equations (81) and (82) into (75) and (76) we obtain

$$n_a \Gamma_{lu} = n_{al} N_{qu} A_{ul} \frac{g_u}{g_l} \quad \text{and} \quad (83)$$

$$n_a \Gamma_{ul} = n_{au} (N_{qu} + 1) A_{ul} \quad (84)$$

where $A_{ul} = \frac{8\pi\omega_0^3}{3hc^3} \frac{1}{g_u} \sum_{M_u, M_l} |\bar{M}|^2$ is the Einstein A coefficient.

Using Equation (68) the thermal equilibrium relation is obtained

$$n_{al} (N_{qu} A_{ul} \frac{g_u}{g_l}) = n_{au} (N_{qu} A_{ul} + A_{ul}) \quad (85)$$

The Einstein B coefficients are obtained by defining

$$B_{ul} = \frac{\pi^2 c^3}{h \omega_0^3} A_{ul} = \frac{2\pi^2}{3h^2} \frac{1}{g_u} \sum_{M_u, M_l} |\bar{M}|^2,$$

$$B_{lu} = \frac{g_u}{g_l} B_{ul}$$

and

$$u(\omega_0) = \frac{h\omega_0^3}{\pi^2 c^3} N_{qu}$$

where $u(\omega_0)$ is the intensity of incident radiation. Equation (85) is now written in the familiar form of the Einstein relation [42]

$$n_{al} u(\omega_0) B_{lu} = n_{au} (u(\omega_0) B_{ul} + A_{ul}). \quad (86)$$

Consider an incident radiation field of frequency ω_0 upon this medium in thermal equilibrium. The radiation field will upset the balance between absorption and emission, giving rise to induced transitions, n_{tr} , in unit time per unit volume,

$$n_{tr} = (n_{al} u(\omega_0) B_{lu} - n_{au} [u(\omega_0) B_{ul} + A_{ul}]). \quad (87)$$

Because spontaneous emission is essentially isotropic and induced emission and absorption are in the same direction as the incident radiation, the spontaneous emission contribution in the direction of incident radiation is small and will be ignored. Therefore,

$$n_{tr} = n_{al} u(\omega_0) B_{lu} - n_{au} u(\omega_0) B_{ul}. \quad (88)$$

Substituting for the Einstein B coefficients

$$n_{tr} = \left(\frac{n_{al}}{g_l} - \frac{n_{au}}{g_u} \right) \frac{2\pi}{3\hbar^2} \sum_{M_u, M_l} |\bar{M}|^2 u(\omega_0). \quad (89)$$

Using a Maxwell-Boltzmann population distribution, n_{tr} becomes

$$n_{tr} = \frac{n_a}{g_l} \frac{2\pi}{3\hbar^2} \sum_{M_u, M_l} |\bar{M}|^2 (1 - e^{-\hbar\omega_0/kT}) u(\omega_0) \quad (90)$$

where	$\frac{n_{al}}{g_l}$	=	$\frac{n_a e^{-E_l/kT}}{Q_{El} Q_{Vib} Q_{Rot}}$
	Q_{El}	=	Electronic partition function
	Q_{Vib}	=	Vibrational partition function
	Q_{Rot}	=	Rotational partition function
	E_l	=	$E_{El} + E_{Vib} + E_{Rot}$: lower energy level
	g_l	=	$g_{El} g_{Vib} g_{Rot}$

Recalling Lambert's law

$$\frac{dI}{d\ell} = -kI,$$

and multiplying both sides by a differential of frequency yields

$$-\frac{dI}{d\ell} d\omega = kI d\omega. \quad (91)$$

Recall that the spectral intensity $I = cu(\omega)$ represents the incident energy per area and also that the negative change in intensity per length over an incremental band of frequencies is equal to the net number of transitions induced by the radiation field in unit time per unit volume times the energy contained in that incremental band of frequencies. Thus,

$$\begin{aligned} dn_{tr}(\omega) \hbar\omega &= -\frac{dI}{d\ell} d\omega \\ &= k c u(\omega) d\omega. \end{aligned} \quad (92)$$

Integrating both sides

$$n_{tr} \hbar\omega_0 = c \int_0^{\infty} k(\omega) u(\omega) d\omega. \quad (93)$$

If $k(\omega)$ is nonzero over an incremental frequency range where $u(\omega)$ is slowly varying (blackbody approximation) or if $u(\omega)$ represents a monochromatic source (laser approximation) where $\omega_{laser} \approx \omega_0$ then,

$$\begin{aligned} n_{tr} \frac{\hbar\omega_0}{cu(\omega_0)} &= \int_0^{\infty} k(\omega) d\omega \\ &= S_{lu}. \end{aligned} \quad (94)$$

S_{lu} is the line strength of a particular transition as defined by Equation (6). The above equation is valid for broadband or laser sources. Substituting Equation (90) for n_{tr} , the desired expression for the line strength is obtained,

$$S_{lu} = n_a \frac{e^{-E_l/kT}}{Q_{El} Q_{Vib} Q_{Rot}} \frac{2\pi\omega_0}{3c\hbar} \sum_{M_u, M_l} |\bar{M}|^2 (1 - e^{-\hbar\omega_0/kT}) \quad (95)$$

From the ideal gas law, the number of absorbing molecules is

$$n_a = \frac{P_a}{kT} \quad .$$

Using this fact and converting from radian frequency to wavenumbers, ν , the line strength becomes

$$S_{lu} = \frac{P_a}{kT} \frac{8\pi^3}{3h} \frac{\nu_0}{Q_{El} Q_{Vib} Q_{Rot}} \frac{e^{-E_l/kT}}{\sum_{M_u, M_l} |\bar{M}|^2 (1 - e^{-hc\nu_0/kT})} \quad (96)$$

The line strength at a standard temperature and pressure is denoted as

$$S_{lu}^0 = \frac{P_{ao}}{T_o} \frac{8\pi^3}{3h} \frac{\nu_o}{Q_{El}^0 Q_{Vib}^0 Q_{Rot}^0} \frac{e^{-E_l/kT_o}}{\sum_{M_u, M_l} |\bar{M}|^2 (1 - e^{-hc\nu_o/kT_o})} \quad (97)$$

At any temperature and pressure,

$$S_{lu} = S_{lu}^0 \left(\frac{T_o P_o}{P_a T} \right) \frac{Q_{El}^0 Q_{Vib}^0 Q_{Rot}^0}{Q_{El} Q_{Vib} Q_{Rot}} \frac{e^{E_l \left(\frac{T - T_o}{kTT_o} \right)}}{(1 - e^{-hc\nu_o/kT})} \quad (98)$$

For the AFGL listing $T = 296k$ and $p_{ao} = 1 \text{ atm}$. Also the basic definition of the absorption coefficient is different for the AFGL listing from that defined in Equation (3). To convert between the AFGL line strength (denoted as S_{lu}^0) and the line strength defined by Equation (96), use

$$S_{lu}^0 = 0.733926 \times 10^{22} \left(\frac{p_a}{760} \right) \frac{1}{T} S_{lu}^{0'} \quad (99)$$

For mid to near infrared ($\nu > 1000 \text{ cm}^{-1}$) near-line-center calculations the line strength defined by Equation (96) works very well. However for pure rotational transitions corrections to the line strength must be made.

The first correction for rotational transitions originates from the molecule's ability to align its dipole to the electric vector of the photon field. If the sum over initial photon states had been kept at the beginning of the development in this section the correction factor to the line strength would have been included. This correction is basically the Van Vleck-Weisskopf line shape [43,44] which includes a $\frac{\omega}{\omega_0}$ factor multiplying the Lorentz line shape. This correction only applies to near line center of a transition [43] since the impact approximation was made.

The second correction pertains to the Maxwell-Boltzmann population distribution where the energy levels are not fixed. This accounts for population changes in the shifted energy levels and how they will affect the population difference for that transition. Let ΔE_l and ΔE_u represent these level shifts of the lower and upper energy states respectively. Then using

$$\frac{N_{al}}{q_l} = \frac{N_a}{Q} e^{-(E_l + \Delta E_l)/kT}$$

and

$$\frac{N_{au}}{q_u} = \frac{N_a}{Q} e^{-(E_u + \Delta E_u)/kT}$$

gives a correction factor of

$$e^{-\Delta E_l/kT} \frac{(1 - e^{-\nu hc/kT})}{(1 - e^{-\nu_0 hc/kT})} \quad (100)$$

The value of ΔE_l is in practice unknown. Near line center modeling attempts by Farmer [45] to predict water vapor rotational band absorption ignores this term ($\Delta E_l \ll kT$).

The resulting correction to the standard line strength equation becomes

$$S_{lu}^{Cor} = \begin{cases} \frac{\nu}{\nu_0} \frac{(1-e^{-hc\nu/kT})}{(1-e^{-hc\nu_0/kT})} & \text{near line center} \\ e^{-\Delta E_l/kT} \frac{(1-e^{-hc\nu/kT})}{(1-e^{-hc\nu_0/kT})} & \text{far wing} \end{cases} \quad (101)$$

The line strength for far-infrared lines ($\nu < 1000 \text{ cm}^{-1}$) becomes

$$S_{lu} = \begin{cases} S_{lu}^0 \frac{T_0^{p_a}}{T_0^{p_{ao}}} \frac{Q_{El}^0 Q_{Vib}^0 Q_{Rot}^0}{Q_{El}^0 Q_{Vib}^0 Q_{Rot}^0} e^{E_l \left(\frac{T-T_0}{kT_0} \right)} \frac{(1-e^{-hc\nu_0/kT})}{(1-e^{-hc\nu_0/kT_0})} \frac{\nu}{\nu_0} \frac{(1-e^{-hc\nu/kT})}{(1-e^{-hc\nu_0/kT})} & \text{near line center} \\ S_{lu}^0 \frac{T_0^{p_a}}{T_0^{p_{ao}}} \frac{Q_{El}^0 Q_{Vib}^0 Q_{Rot}^0}{Q_{El}^0 Q_{Vib}^0 Q_{Rot}^0} e^{E_l \left(\frac{T-T_0}{kT_0} \right)} \frac{(1-e^{-hc\nu_0/kT_0})}{(1-e^{-hc\nu_0/kT_0})} e^{-\Delta E_l/kT} \frac{(1-e^{-hc\nu/kT})}{(1-e^{-hc\nu_0/kT})} & \text{far wing.} \end{cases} \quad (102)$$

Figures 8 and 9 show the population difference factors

$$\text{and } \begin{cases} f_1(\nu_0, T) = \frac{(1-e^{-hc\nu_0/kT})}{(1-e^{-hc\nu_0/kT_0})} \\ f_2(\nu_0, \nu) = \frac{(1-e^{-hc\nu/kT})}{(1-e^{-hc\nu_0/kT})} \end{cases}$$

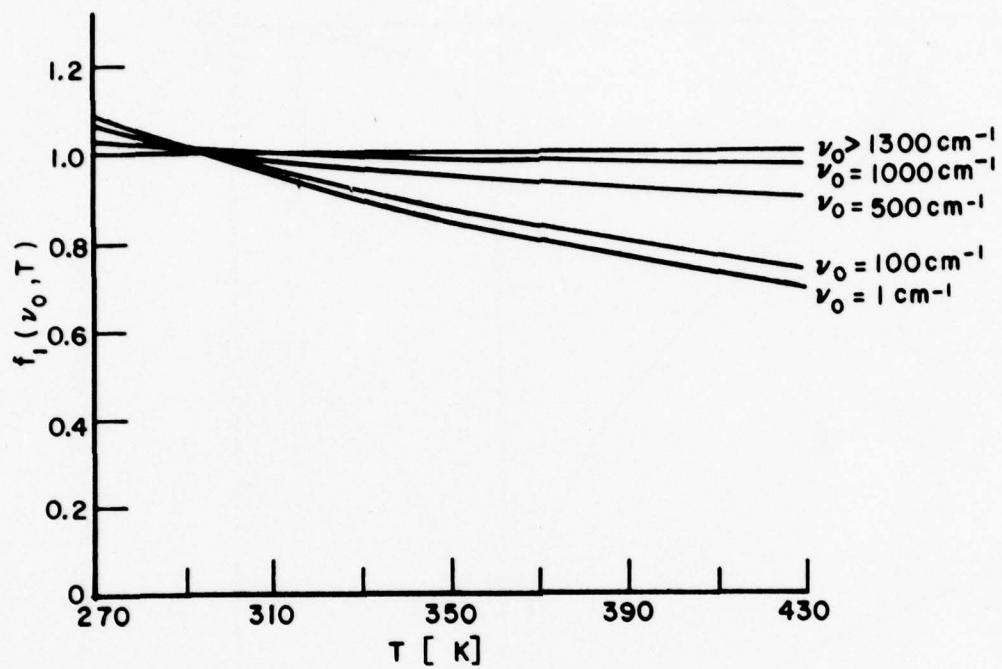


Figure 8. $f_1(v_0, T)$ versus T .

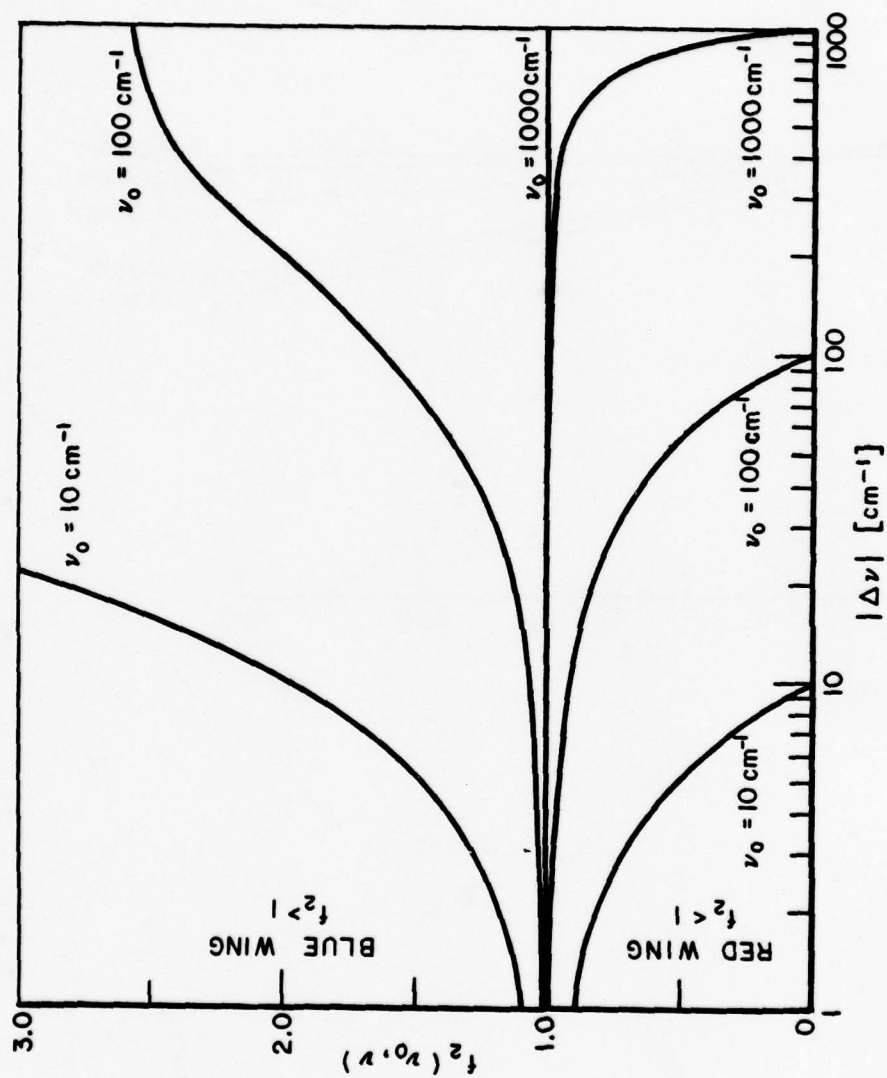


Figure 9. $f_2(\nu_0, v)$ versus Δv .

become unity for $\nu_0 > 1000$ wavenumbers. Figure 8 illustrates the negative temperature dependence of $f_1(\nu_0, T)$ for different values of ν_0 . Figure 9 demonstrates the importance of $f_2(\nu_0, \nu)$ in the blue wing ($f_2 > 1$, $\nu - \nu_0 = \Delta\nu > 0$) and red wing ($f_2 < 1$, $\Delta\nu < 0$) for different values of ν_0 .

To summarize the results of this section the line strength will be presented in four limits, greater than and less than 1000 cm^{-1} , near line center and far wing. Notice that some of the corrections to the line strength are frequency dependent and by definition belong to the line shape function.

$$S_{lu} = \left\{ \begin{array}{ll} \left. \begin{array}{l} S_{lu}^0 \frac{T_0 p_a}{T p_{a0}} \frac{Q_{El}^0 Q_{Vib}^0 Q_{Rot}^0}{Q_{El} Q_{Vib} Q_{Rot}} e^{\frac{E_l(T-T_0)}{kT_0}} \frac{(1-e^{-h\nu_0/kT})}{(1-e^{-h\nu_0/kT_0})} \\ \text{near line center} \end{array} \right\} \nu_0 > 1000 \text{ cm}^{-1} \\ \left. \begin{array}{l} S_{lu}^0 \frac{T_0 p_a}{T p_{a0}} \frac{Q_{El}^0 Q_{Vib}^0 Q_{Rot}^0}{Q_{El} Q_{Vib} Q_{Rot}} e^{\frac{E_l(T-T_0)}{kT_0}} \frac{(1-e^{-h\nu_0/kT})}{(1-e^{-h\nu_0/kT_0})} \frac{\nu}{\nu_0} \frac{(1-e^{-h\nu/kT})}{(1-e^{-h\nu_0/kT})} \\ \nu_0 < 1000 \text{ cm}^{-1} \end{array} \right\} \\ \left. \begin{array}{l} S_{lu}^0 \frac{T_0 p_a}{T p_{a0}} \frac{Q_{El}^0 Q_{Vib}^0 Q_{Rot}^0}{Q_{El} Q_{Vib} Q_{Rot}} e^{\frac{E_l(T-T_0)}{kT_0}} \frac{(1-e^{-h\nu_0/kT})}{(1-e^{-h\nu_0/kT_0})} e^{-\Delta E_l/kT} \\ \text{far wing} \end{array} \right\} \nu_0 > 1000 \text{ cm}^{-1} \\ \left. \begin{array}{l} S_{lu}^0 \frac{T_0 p_a}{T p_{a0}} \frac{Q_{El}^0 Q_{Vib}^0 Q_{Rot}^0}{Q_{El} Q_{Vib} Q_{Rot}} e^{\frac{E_l(T-T_0)}{kT_0}} \frac{(1-e^{-h\nu_0/kT})}{(1-e^{-h\nu_0/kT_0})} \frac{(1-e^{-h\nu/kT})}{(1-e^{-h\nu_0/kT})} e^{-\Delta E_l/kT} \\ \nu_0 < 1000 \text{ cm}^{-1} \end{array} \right\} \end{array} \right.$$

(103)

D. The Line Shape

The most general classification of line shapes is that of homogeneous and inhomogeneous broadening. Homogeneous broadening means that all molecules have the same basic line shape characteristics. That is if a line shape is observed for a collection of molecules the same line shape will be observed for each molecule. Examples are natural broadening (radiation damping) and collision broadening. Inhomogeneously broadened lines represent a collection of frequency shifted homogeneously broadened lines. Thus each molecule's line shape may be completely different from the total line shape of a collection of molecules. Examples are Doppler broadening, non-uniform electric and magnetic fields in Stark and Zeeman effects, inhomogeneities in a medium and crystalline strains and defects.

1. Homogeneous line shape

The Fourier transform relationship of Equation (67) typifies homogeneous line shapes. This is easily demonstrated using the time-bandwidth product of Fourier transform theory.

$$\Delta\tau \Delta\omega = 1.$$

Thus the width of a line is the same for all molecules.

The line shape and correlation function are divided into three regions pertaining to near-line, intermediate, and far-wing. Separate conditions determined by the collisional dynamics characterize each region. Figure 10 illustrates the effects of collisions at different ranges between the broadening and absorbing molecule. The lines labeled 1 and 2 represent possible collisional paths. Table 1 lists the characteristics of collisions in each region. These conditions will be applied to the correlation function to extract the form of the correlation function to be applied to the near line center and far wing regions. Figure 11 shows a general correlation function and where the different types of broadening will dominate. The functional form of the line shape is correspondingly broken down into three parts.

$$\begin{aligned} j_c(\omega) &= \text{Re } F^{-1} \left\{ e^{i\omega_0\tau} C_{FW}(\tau) \right\} + F^{-1} \left\{ e^{-i\omega_0\tau} C_{IW}(\tau) \right\} \\ &\quad + F^{-1} \left\{ e^{-i\omega_0\tau} C_{NLC}(\tau) \right\} \\ &= j_{cFW}(\omega) + j_{cIW}(\omega) + j_{cNLC}(\omega). \end{aligned} \quad (104)$$

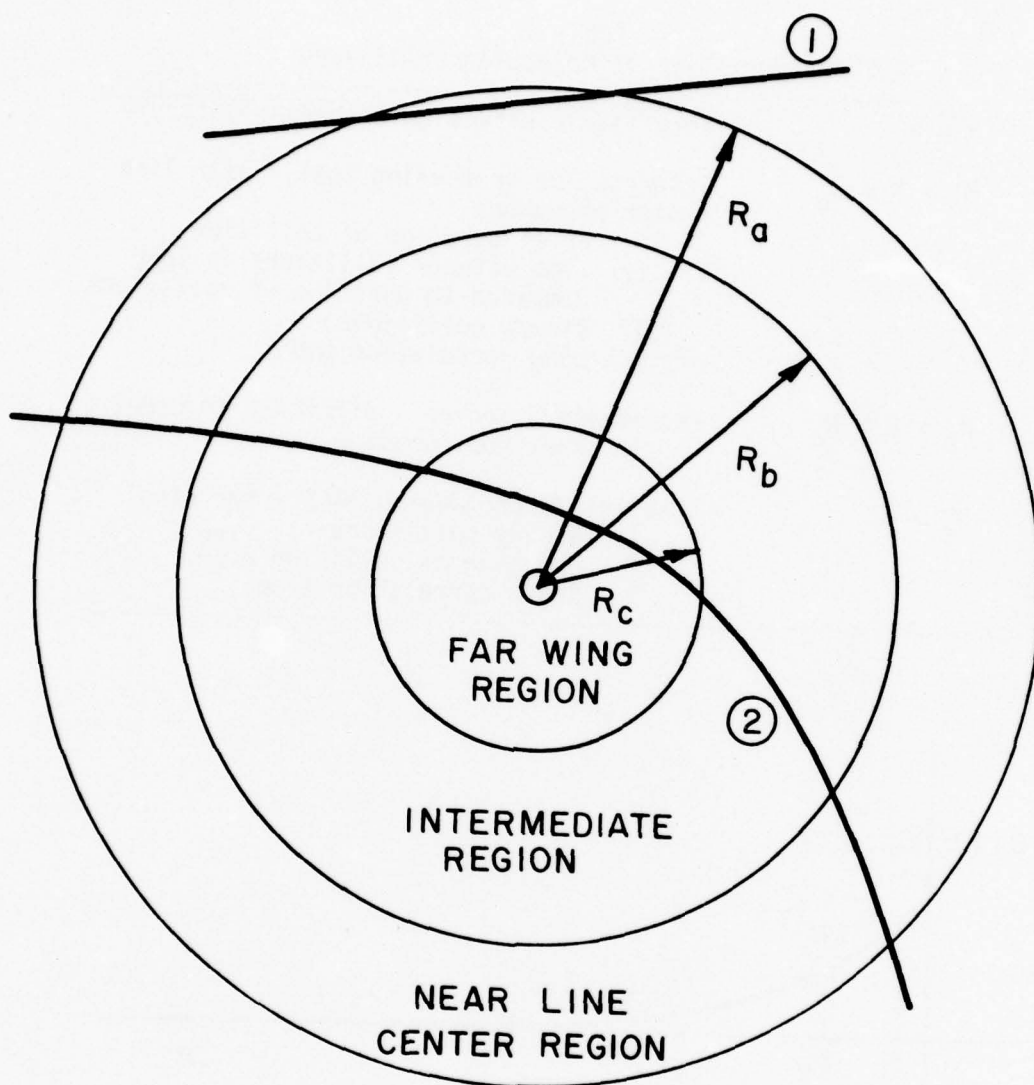


Figure 10. The correspondence between impact parameter and line shape region.

Table 1
Characteristics of Molecular Collisions

$R > R_a$	Very little effect on absorbing molecule
$R_a > R > R_b$	Interruption broadening [46] - near line center phenomena <ol style="list-style-type: none"> 1. Brief duration of collision 2. Time between collisions is long compared to duration of collisions 3. Binary collisions 4. Long correlation time
$R_b > R > R_c$	Intermediate region - difficult to model <ol style="list-style-type: none"> 1. Many body problem
$R_c > R$	Statistical broadening [46] - far wing <ol style="list-style-type: none"> 1. Binary collisions 2. Duration of collision $\sim \frac{2R}{v}$ 3. Short correlation time

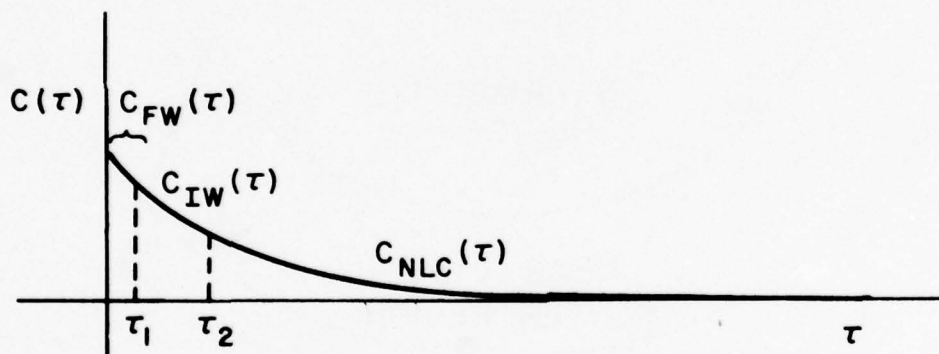


Figure 11. The correlation function.

$j_{CFW}(\omega)$ describes the far wing line shape. $j_{CIW}(\omega)$ describes the intermediate wing line shape. $j_{CNLC}(\omega)$ describes the near line center shape. The subscripts therefore represent the frequency regions over which the line shape function will apply. This is illustrated in Figure 12. The goal of this section is

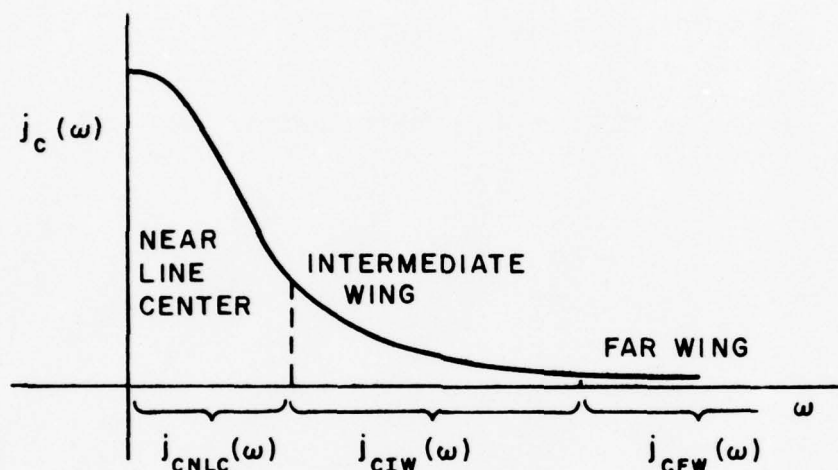


Figure 12. The line shape function.

to find the line shape functions for near line center, intermediate wing, and far wing. The near line center and far wing cases are tractable but the intermediate wing is not. It will be determined by a mixing of the near line center and far wing line shape functions.

a. Interruption broadening

Table 1 lists the conditions for interruption or impact broadening. These will be applied to a general correlation function, $C_{a_1b}(\tau)$, which describes the interactions between the absorbing molecule and some broadener. Since the interaction time is brief we will reexamine the change in the correlation function for a small change in time. Begin with Equation (58)

$$C_{a_1b}(\tau+d\tau) = \sum_b \rho_s^b \langle \langle u_s^b | S_{ca_1b}^{-1}(\tau+d\tau) | u_s^b \rangle \langle l_s^b | S_{ca_1b}(\tau+d\tau) | l_s^b \rangle \rangle_{R_0, v, t_0} \quad (105)$$

Define

$$S_{ca_1b}(\tau+d\tau) = S_c(\tau \rightarrow \tau+d\tau) S_c(\tau) \quad (106)$$

where
$$S_c(\tau \rightarrow \tau+d\tau) = \exp\left(\frac{1}{i\hbar} \int_{t_0}^{\tau_0+d\tau} H_{ca_1b}(t) dt\right)$$

and t_0 - time at which a collision occurs.

Therefore,

$$C_{a_1b}(\tau+d\tau) = \sum_b \rho_b \langle\langle us^b | S_{ca_1b}^{-1}(\tau \rightarrow \tau+d\tau) | us^b \rangle \langle ls^b | S_{ca_1b}(\tau \rightarrow \tau+d\tau) | ls^b \rangle \rangle_{R_0, v, t_0} \quad (107)$$

$$\times \langle\langle us^b | S_{ca_1b}^{-1}(\tau) | us^b \rangle \langle ls^b | S_{ca_1b}(\tau) | ls^b \rangle \rangle_{R_0, v, t_0} .$$

To obtain the separate averages in the above equation it is assumed the events at τ and $\tau+d\tau$ are independent [36]. Because $S_{ca_1b}(\tau)$ is averaged over orientation and does not change vibrational and electronic states for near line center phenomena, it is independent of the sum over the quantum numbers of the broadening molecule. The general correlation function can be written

$$C_{a_1b}(\tau) = \langle\langle us^b | S_{ca_1b}^{-1}(\tau) | us^b \rangle \langle ls^b | S_{ca_1b}(\tau) | ls^b \rangle \rangle_{R_0, v, t_0} . \quad (108)$$

Using this result and Equation (107) we have

$$C_{a_1b}(\tau+d\tau) = C_{a_1b}(\tau) \langle\phi(\tau \rightarrow \tau+d\tau)\rangle_{R_0, v, t_0} \quad (109)$$

where

$$\phi(\tau \rightarrow \tau+d\tau) = \sum_b \rho_b \langle us^b | S_{ca_1b}^{-1}(\tau \rightarrow \tau+d\tau) | us^b \rangle \langle ls^b | S_{ca_1b}(\tau \rightarrow \tau+d\tau) | ls^b \rangle .$$

Examine a single collision event at time τ to $\tau+d\tau$ or equivalently t_0 to $t_0+d\tau$ and the corresponding change in the correlation function

$$\frac{d C_{a_1 b}(\tau)}{d\tau} = \sum_{t_0}^{\tau+d\tau} \int_{\tau}^{\tau+d\tau} d\tau \frac{C'_{a_1 b}(\tau)}{d\tau} . \quad (110)$$

$C'_{a_1 b}(\tau)$ indicates that no sum over collision times is performed.

After evaluating the integral the following differential equation is obtained

$$\frac{d C_{a_1 b}(\tau)}{C_{a_1 b}(\tau)} = - d\tau \langle 1 - \phi(\tau + \tau + d\tau) \rangle_{R_0, v} . \quad (111)$$

Let

$$\sigma_{a_1 b} = \langle 1 - \phi(\tau + \tau + d\tau) \rangle_{R_0, v}$$

then

$$C_{a_1 b}(\tau) = C_{a_1 b}(0) e^{-\sigma_{a_1 b} \tau} ; \quad C_{a_1 b}(0) = 1. \quad (112)$$

Extracting the volume term in Equation (59) and writing the average over velocity and impact parameter as

$$\langle \rangle_{R_0, v} \rightarrow \frac{1}{V} \langle \rangle_{R_0, v}$$

leads to

$$C_{a_1 b}^{N_b}(\tau) = e^{-n_b \sigma_{a_1 b} \tau} . \quad (113)$$

The term $n_b \sigma_{a_1 b}$ represents the magnitude of the collisional perturbations. For $n_b \sigma_{a_1 b}$ small the absorbing molecule will remain correlated to its $\tau=0$ state longer than for $n_b \sigma_{a_1 b}$ large. In

the frequency domain it is related to the halfwidth at half maximum as verified by the Fourier transform of the correlation function. Let the halfwidth be denoted by

$$\alpha_{a_1b} = \alpha_{a_1b}^r + i\alpha_{a_1b}^i = n_b \sigma_{a_1b}^r + i n_b \sigma_{a_1b}^i$$

where α^r and α^i correspond to the real and imaginary parts of $n_b \sigma_{a_1b}$. Using Equation (104) the near line center line shape becomes

$$j_{\text{CNLC}}(\omega) = \frac{1}{\pi} \frac{\alpha_{a_1b}^r}{(\omega - \omega_0 + \alpha_{a_1b}^i)^2 + (\alpha_{a_1b}^r)^2} \quad \text{where} \quad (114)$$

$\alpha_{a_1b}^r$ is the halfwidth at half maximum and $\alpha_{a_1b}^i$ is the line shift.

The next step in the analysis is to solve for σ_{a_1b} . First, examine

$$S_{c_{a_1b}}(\tau \rightarrow \tau + d\tau) = e^{-i\eta} \quad (115)$$

where

$$\eta = \frac{1}{\hbar} \int_{t_0}^{t_0 + d\tau} dt H_{c_{a_1b}}(t) \rightarrow \frac{1}{\hbar} \int_{-\infty}^{\infty} dt H_{c_{a_1b}}(t) \quad (116)$$

The extension of the limits of integration is valid since the collision interactions drop off rapidly for increasing intermolecular distance. σ_{a_1b} can now be written

$$\sigma_{a_1b} = \sum_b \rho_s^b \langle 1 - \langle u_s^b | e^{i\eta} | u_s^b \rangle \langle \ell_s^b | e^{-i\eta} | \ell_s^b \rangle \rangle_{R_0, v} \quad (117)$$

where $\sum_b \rho_s^b = 1$ has been used. A perturbation expansion on the time development operation can now be carried out, that is

$$\begin{aligned} \langle \ell_s^b | e^{-i\eta} | \ell_s^b \rangle &= 1 - i \langle \ell_s^b | \eta | \ell_s^b \rangle - \frac{1}{2} \langle \ell_s^b | \eta^2 | \ell_s^b \rangle + \dots \\ &= 1 - i\eta_\ell - \frac{1}{2} \eta_\ell^2 + \dots \end{aligned} \quad (118)$$

To second order in η_k , σ_{a_1b} becomes

$$\sigma_{a_1b} = \sum_b \rho_{sb} \left\langle \frac{1}{2}(\eta_k^2 + \eta_u^2) + \eta_u \eta_k \right\rangle_{R_{0,v}} - i \sum_b \rho_{sb} \langle \eta_u - \eta_k \rangle_{R_{0,v}} \quad (119)$$

This is a form similar to that obtained by Anderson [35]. η , has been evaluated by Mizushima [47] using for the collision Hamiltonian the intermolecular potentials of the general form

$$H_{ca_1b}(\tau) = \frac{V_j}{R(t)^{mj}} \quad \text{and} \quad R(t) = (R_0^2 + (vt)^2)^{1/2} \quad \text{and}$$

$$\eta = \frac{V_j}{\hbar} \frac{1}{v R_0^{mj-1}} \pi \frac{\Gamma(mj-1) 2^{2-mj}}{\left[\Gamma\left(\frac{mj}{2}\right) \right]^2} \quad (120)$$

Of interest to this study is the temperature dependence of the halfwidth. This can be easily computed for the first order Anderson theory. One notes that

$$\eta \propto \frac{1}{v} \rightarrow \sigma_{a_1b} \propto \frac{1}{v^2} = \bar{v} \propto \sqrt{T} \quad \text{where}$$

\bar{v} is the mean thermal velocity. Using $n_b = \frac{p_b}{kT}$ the temperature dependence of the halfwidth is

$$\sigma_{a_1b} \propto \frac{1}{\sqrt{T}} \quad (121)$$

This is the standard dependence used in AFGL tape [5] computations. It is not however what is sometimes observed [48,49]. As more terms in the perturbation expansion are included the temperature dependence will be modified.

Two basic broadening mechanisms can result in the modulation of the line center-frequency, energy level shifts and phase shifts of the eigenstates. These are analogous to frequency modulation and phase modulation. Anderson's theory accounts for both effects yet needs higher order terms. Another popular theory is the phase

shift approximation [47,50] which considers only phase modulation but to all orders. To see how the phase shift approximation comes about, consider once again the perturbation expansion of Equation (118)

$$\langle \ell s^b | e^{-i\eta} | \ell s^b \rangle = 1 + (-i \langle \ell s^b | \eta | \ell s^b \rangle) + \frac{1}{2!} (i^2 \langle \ell s^b | \eta^2 | \ell s^b \rangle) + \frac{1}{3!} (\dots) \dots$$

Examine

$$\begin{aligned} \langle \ell s^b | \eta^2 | \ell s^b \rangle &= \sum_{\ell' s^b} \langle \ell s^b | \eta | \ell' s^b \rangle \langle \ell' s^b | \eta | \ell s^b \rangle \\ &= \langle \ell s^b | \eta | \ell s^b \rangle^2 + \sum_{\substack{\ell' s^b \\ \ell s^b}} \langle \ell s^b | \eta | \ell' s^b \rangle \langle \ell' s^b | \eta | \ell s^b \rangle . \end{aligned} \quad (122)$$

For the second term to exist the operator η must initially be changing the eigenstate to some virtual state then back to the stationary eigenstate. This describes an energy level shift or frequency modulation. The first term in Equation (122) indicates no change in eigenstate but may produce a phase change, or phase shift. To make the phase shift approximation simply ignore the second term. Then

$$\langle \ell s^b | e^{-i\eta} | \ell s^b \rangle = e^{-i\eta_\ell} \quad (123)$$

where $\eta_\ell = \langle \ell s^b | \eta | \ell s^b \rangle$ so that

$\sigma_{a_1 b}$ now becomes

$$\sigma_{a_1 b} = \sum_b \rho_{s^b} \langle 1 - e^{i(\eta_u - \eta_\ell)} \rangle_{R_0, v} . \quad (124)$$

Letting $\phi = \eta_u - \eta_\ell$ we may write

$$o_{a_1 b}^r = \sum_b \rho_{s_b} \langle 1 - \cos \phi \rangle_{R_0, v}$$

or

$$= \sum_b \rho_{s_b} \frac{2^{\frac{m_j+3}{2}} \Gamma(\frac{2m_j-3}{m_j-1})}{(m_j-1) \frac{2}{m_j-1}} \left\{ \begin{matrix} \Gamma(-\frac{2}{m_j-1}) \cos(\frac{\pi}{m_j-1}) & m_j \neq 3 \\ \frac{\pi}{2} & m_j = 3 \end{matrix} \right\} \left(\frac{k}{2\mu} \right)^{\frac{m_j-3}{2}} \\ \times \left[\frac{\Gamma(\frac{m_j-1}{2})}{\Gamma(\frac{m_j}{2})} \right]^{2/m_j-1} \left[\langle u s_b | v_j | u s_b \rangle - \langle s_b | v_j | s_b \rangle \right]^{2/m_j-1}.$$

This may be written in a more compact form as

$$= \sum_b \rho_{s_b} \delta_j \tau^{\frac{m_j-3}{2m_j-2}}. \quad (125)$$

Similarly the line shift term becomes

$$o_{a_1 b}^i = \sum_b \rho_{s_b} \langle \sin \phi \rangle_{R_0, v} \\ \text{or} \\ = \sum_b \rho_{s_b} \delta_j \tan\left(\frac{\pi}{m_j-1}\right) \tau^{\frac{m_j-3}{2m_j-2}}. \quad (126)$$

For dipole-dipole interactions the temperature dependence of the halfwidth becomes

$$\alpha_{a_1 b} \propto \frac{1}{T}. \quad (127)$$

For dipole-quadrupole interactions

$$\alpha_{a_1 b} \propto \frac{1}{T^{1.83}}. \quad (128)$$

The total near-line-center line shape becomes

$$j_{\text{CNLC}}(\omega) = \text{Re } F^{-1} \left\{ e^{i\omega_0 \tau} C_{\text{NLC}}(\tau) \right\}$$

or

$$= \text{Re } F^{-1} \left\{ e^{i\omega_0 \tau} e^{-\alpha_{a_1} \tau} e^{-\alpha_{a_1 b_1} \tau} \dots e^{-\alpha_{a_1 b_k} \tau} \right\}$$

which leads to

$$j_{\text{CNLC}}(\omega) = \frac{1}{\pi} \frac{\alpha^r}{(\omega - \omega_0 + \alpha^i)^2 + (\alpha^r)^2} \quad (129)$$

where

$$\alpha^r = \alpha_{a_1}^r + \alpha_{a_1 b_1}^r + \dots + \alpha_{a_1 b_k}^r$$

$$\alpha^i = \alpha_{a_1}^i + \alpha_{a_1 b_1}^i + \dots + \alpha_{a_1 b_k}^i$$

b. Statistical broadening

The far wing and to a lesser extent the line center regions of the true line shape are affected by statistical broadening processes. Strong collisions caused by close encounters dominate this situation. Because no perturbation expansion can be used, the phase shift approximation will be applied. The phase shift term, η , (see Equation (116)) can be written as

$$\eta = \frac{1}{\hbar} \int_{t_0}^{t_0 + \tau} dt \frac{v_j}{R(t)^{m_j}} \quad (130)$$

The major contribution of the phase term comes in the region $t_0 < \frac{R_0}{v}$ [51], where

$$v_n = \frac{v_j}{\hbar} \frac{1}{v R_0^{m_j - 1}} \begin{cases} \frac{\Gamma(m_j - 1)^2}{\Gamma(\frac{m_j}{2})^2} \frac{v}{R_0} \tau & m_j - \text{even} \\ \frac{v}{R_0} \tau & m_j = 3 \end{cases} \quad (131)$$

Again consider a general correlation function

$$C_{a,b}^{N_b}(\tau) = \left[\sum_b \rho_b \frac{1}{V} \langle \langle u_s^b | e^{i\eta_l | u_s^b} \rangle \langle l_s^b | e^{-i\eta_l | l_s^b} \rangle \rangle_{R_0, v, t_0} \right]^{N_b}$$

or

$$C_{a,b}^{N_b}(\tau) = \left[1 + \frac{n_b \sum_b \rho_b \langle e^{i(\eta_u - \eta_l)} - 1 \rangle_{R_0, v, t_0}}{N_b} \right]^{N_b}$$

thus

$$C_{a,b}^{N_b}(\tau) = \exp(-n_b \sum_b \rho_b \langle 1 - e^{i(\eta_u - \eta_l)} \rangle_{R_0, v, t_0}) \quad (132)$$

The sum over t_0 is converted to an integral which gives its major contribution between $-\frac{R_0}{v}$ and $\frac{R_0}{v}$, that is

$$\langle 1 - e^{i(\eta_u - \eta_l)} \rangle_{R_0, v, t_0} = \left\langle \int_{-\frac{R_0}{v}}^{\frac{R_0}{v}} dt_0 (1 - e^{i(\eta_u - \eta_l)}) \right\rangle_{R_0, v}$$

or

$$\langle 1 - e^{i(\eta_u - \eta_l)} \rangle_{R_0, v, t_0} = \left\langle \frac{2R_0}{v} (1 - e^{i(\eta_u - \eta_l)}) \right\rangle_{R_0, v} \quad (133)$$

Evaluating the real and imaginary parts separately we have

$$\left\langle \frac{2R_0}{v} (1 - \cos(\eta_u - \eta_\ell)) \right\rangle_{R_0, v} =$$

$$= \frac{4\pi}{m_j} \left(\frac{\tau}{\hbar} \right)^{3/m_j} (v_{ju} - v_{j\ell})^{3/m_j} \begin{cases} \xi_j^{3/m_j} \Gamma(-\frac{3}{m_j}) \cos(\frac{3}{2m_j}) & m_j - \text{even} \\ \frac{\pi}{2} & m_j = 3 \end{cases}$$

which may be written compactly as

$$\left\langle \frac{2R_0}{v} (1 - \cos(\eta_u - \eta_\ell)) \right\rangle_{R_0, v} = \gamma_j \tau^{3/m_j} \quad (134)$$

where

$$v_{ju} = \langle u s^b | v_j | u s^b \rangle$$

$$v_{j\ell} = \langle \ell s^b | v_j | \ell s^b \rangle$$

$$\xi_j = \frac{\Gamma(m_j - 1) 2^{2 - m_j}}{[\Gamma(\frac{m_j}{2})]^2}.$$

Similarly for the line shift term

$$\left\langle \frac{2R_0}{v} \sin(\eta_u - \eta_\ell) \right\rangle_{R_0, v} =$$

$$= \frac{4\pi}{m_j} \left(\frac{\tau}{\hbar} \right)^{3/m_j} (v_{ju} - v_{j\ell})^{3/m_j} \begin{cases} \xi_j^{3/m_j} \Gamma(-\frac{3}{m_j}) \sin(\frac{3\pi}{2m_j}) & m_j - \text{even} \\ \frac{\pi}{2} & m_j = 3 \end{cases}$$

or in a compact form

$$\left\langle \frac{2R_0}{v} \sin(\eta_u - \eta_\ell) \right\rangle_{R_0, v} = \epsilon_j \tau^{3/m_j} \quad (135)$$

The general correlation function can now be written

$$C_{a,b}^{N_b}(\tau) = e^{-n_b \sum_s \rho_{s,b} (\gamma_j + i\epsilon_j) \tau^{3/m_j}} \quad (136)$$

Under the far wing approximation $\Delta\omega \gg (\epsilon_j)^{m_j/3}$ so that the line shift term can be ignored. The far wing line shape for the general correlation function becomes

$$j_{CFW}(\omega) = \text{Re} \int_0^\infty e^{i\omega_0 \tau} e^{-\lambda_{bj} \tau^{3/m_j}} d\tau$$

where $\lambda_{bj} = n_b \sum_s \rho_{s,b} \gamma_j$

Writing the decaying exponential function in a power series, an asymptotic expansion can be obtained

$$j_{CFW}(\omega) = \frac{1}{\pi} \text{Re} \left[\sum_{s=0}^{\infty} \frac{(\lambda_{bj})^s}{s!} \frac{1}{(i\Delta\omega)^{1+3s/m_j}} \Gamma\left(1 + \frac{3s}{m_j}\right) \right] \quad (138)$$

The temperature dependence of the term $n_a \gamma_j$ is

$$n_a \gamma_j \propto \frac{1}{T} (V_j(T))^{3/m_j} \quad (139)$$

The far wing frequency dependence for the leading term in the expansion is

$$j_{CFW}(\omega) \propto \frac{1}{(\Delta\omega)^{1+3/m_j}} \quad (140)$$

The total far wing line shape becomes

$$\begin{aligned}
j_{CFW}(\omega) &= \text{Re } F^{-1} \left\{ e^{i\omega_0 \tau} C_{FW}(\tau) \right\} \\
\text{or} \\
&= \text{Re } F^{-1} \left\{ e^{i\omega_0 \tau} e^{-\lambda_a \tau^{3/m_a}} e^{-\lambda_{b_1} \tau^{3/m_1}} e^{-\lambda_{b_2} \tau^{3/m_2}} \dots e^{-\lambda_{b_k} \tau^{3/m_k}} \right\}.
\end{aligned}
\tag{141}$$

Which, after performing the Fourier transform, becomes

$$j_{CFW}(\omega) = \frac{1}{\pi} \text{Re} \left[\sum_{s=0}^{\infty} \sum_{t_1}^{\infty} \dots \sum_{t_k}^{\infty} \frac{(\lambda_a^s \lambda_{b_1}^{t_1} \lambda_{b_2}^{t_2} \dots \lambda_{b_k}^{t_k}) \Gamma\left(\frac{3s}{m_a} + \frac{3t_1}{m_1} + \dots + \frac{3t_k}{m_k} + 1\right)}{s! t_1! \dots t_k! (i\Delta\omega)^{\frac{3s}{m_a} + \frac{3t_1}{m_1} + \dots + \frac{3t_k}{m_k} + 1}} \right].
\tag{142}$$

In the very far wing only the leading terms will be necessary.

It is important to mention another statistical theory which does not use the phase shift (phase modulation) approximation by Fomin and Tvorogov [41]. However a perturbation expansion only to second order is used. The resulting statistical line shape contains the phase shift approximation formula multiplied by another factor. This new term can be interpreted as a level shift (frequency modulation) correction factor to the phase shift approximation result. Since energy level shifts are an important part of far wing phenomena, the correction term will also be important. A simplified expression for the level shift correction term is

$$\exp\left(-\frac{G_j}{T} (\Delta\nu)^{(m_j-1)/m_j} \omega_j^{2/3}\right).
\tag{143}$$

where $G_j = \mu \omega_j$, μ is the reduced mass and ω_j is a parameter which decreases as ω_j increases. Also G_j does vary with the vibrational quantum number.

2. Inhomogeneous line shapes

a. Doppler line shape

The random kinetic motion of molecules causes a Doppler shift of the homogeneously broadened line shape. Molecules with different velocities will experience different frequency shifts so that a new total line shape results, called the inhomogeneous Doppler profile.

The analysis of this effect begins with Doppler's equation

$$v = (c-v_0)v_0 \rightarrow v = \frac{c(v_0-v)}{v_0} \quad (144)$$

and the Maxwell-Boltzmann distribution

$$f_{MB}(E) = e^{-E/kT} \quad (145)$$

Using the kinetic energy $E = \frac{1}{2} mv^2$ and Equations (144) and (145) we have

$$f_{MB}(v-v_0) = e^{-\frac{Mc^2}{2kTv_0^2} (v-v_0)^2} \quad (146)$$

where M is the mass of the absorbing molecule. This represents the probability distribution of the shifted frequencies due to velocity components of the molecules parallel to the incident photon field. Enforcing the normalizing condition

$$\int_0^{\infty} j_D(v-v_0) dv = 1$$

we have

$$j_D(v-v_0) = \frac{(\ln 2)^{1/2}}{\alpha_D \sqrt{\pi}} e^{-\frac{(v-v_0)^2 (\ln 2)}{\alpha_D^2}} \quad (147)$$

where $\alpha_D = \left(\frac{2kT \ln 2}{Mc^2}\right)^{1/2}$ ν_0 is the halfwidth at half intensity.

b. Voigt line shape

The Doppler line shape assumes the shifted homogeneous line shapes are delta functions, which is not strictly true but a good approximation in many cases such as low total gas pressures. The broadened natural line shape is always present in any experiment and in problems of atmospheric importance, collision broadening is present.

Figure 13 illustrates the shifted collision broadened homo-

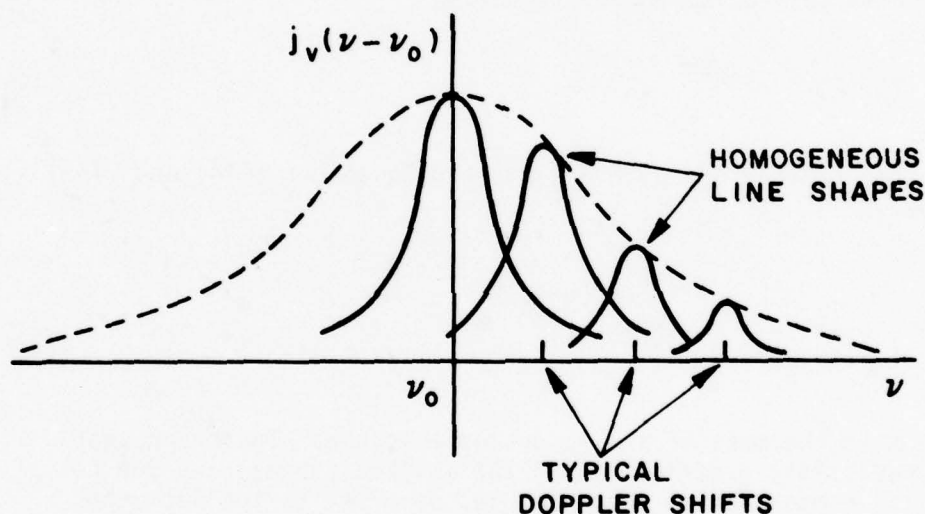


Figure 13. The Voigt line shape.

geneous line shape weighted by a Gaussian (Doppler) distribution. This process can be thought of as a convolution of a homogeneous line shape through a Doppler profile. Thus

$$j_v(\nu - \nu_0) = \int_{-\infty}^{\infty} j_H(\nu - \nu'; \alpha_H) j_D(\nu' - \nu_0; \alpha_D) d\nu' \quad (148)$$

$j_H(v-v_0)$ and α_H are the homogeneous line shape and its corresponding halfwidth, respectively. The resulting line shape is called the Voigt line shape.

The homogeneous line shape that is often used is the Lorentz profile. Substituting in Lorentz and Doppler line shape the Voigt profile becomes,

$$j_v(v-v_0) = \frac{\alpha_H}{\alpha_D \pi^{3/2}} (\ln 2) \int_{-\infty}^{\infty} \frac{e^{-y^2}}{(\xi-y)^2 + a^2} dy \quad (149)$$

where

$$y = \frac{v'-v_0}{\alpha_D} (\ln 2)^{1/2}$$

$$\xi = \frac{v-v_0}{\alpha_D} (\ln 2)^{1/2}$$

$$a = \frac{\alpha_H}{\alpha_D} (\ln 2)^{1/2} .$$

E. The Absorption Coefficient for H₂O in N₂

This section combines the results of sections C and D to form the absorption coefficient particular to the H₂O-N₂ absorption problem. Initially the line strength and line shape will be developed separately.

The discussion of the H₂O-N₂ line shape must begin with the nature of the intermolecular potential functions. As mentioned in Section B of this chapter the intermolecular potentials are not completely understood. This is especially true concerning the nature of strong collisions which form the statistical line shape [34]. Therefore a careful analysis concentrating on the essential features of the interaction is required. The general form of the intermolecular potential Hamiltonian for H₂O-H₂O collisions, H_{ba1} , and for N₂-H₂O collisions, H_{ba1} , become, using Equation (14) through Equation (19),

$$H_{aa_1} = \left\langle \frac{\mu_1^2 f}{R^3(t)} + \frac{\mu_1 \bar{Q}_1 g_1 + \mu_1 \bar{Q}_1 g_2}{R^4(t)} + \frac{\bar{Q}_1^2 i + \mu_1 R_1 h_1 + \mu_1 R_1 h_2}{R^5(t)} + \dots \right\rangle_{\text{Rot}} - \frac{2 \mu_1^2 \bar{\alpha}_1 + \frac{1}{2} \bar{\alpha}_1 e^2 \langle r_1^2 \rangle}{R^6(t)} + V_{\text{Rep1}} \quad (150)$$

$$H_{ba_1} = \left\langle \frac{\mu_1 \bar{Q}_2 g}{R^4(t)} + \dots \right\rangle_{\text{Rot}} - \frac{2 \mu_1 \bar{\alpha}_2 + \frac{1}{2} \bar{\alpha}_1 e^2 \langle r_2^2 \rangle}{R^6(t)} + V_{\text{Rep2}} \quad (151)$$

The subscripts 1 and 2 represent H_2O and N_2 terms, respectively. Next the potential functions will be considered for interruption and statistical type collisions.

The short collision times characteristic of interruption broadening allow the approximation of Equation (17) (i.e., $\langle V_{E1} \rangle \approx V_{E1}$) to be made. Based on the modeling success of Benedict and Kaplan [52,53] only the leading terms in the interaction potentials need be retained. Therefore, for near line center phenomena the interaction Hamiltonians become

$$H_{aa_1} \approx \frac{\mu_1^2}{R^3(t)} f \quad (152)$$

and

$$H_{ba_1} \approx \frac{\mu_1 \bar{Q}_2}{R^4(t)} g \quad (153)$$

Collisions contributing to statistical broadening may or may not require the weighted rotational average, $\langle \rangle_{\text{Rot}}$. This can be determined by examining the collision duration time and time of rotation of the molecule. Based on the average thermal velocities and impact parameters for strong collisions for H_2O - H_2O and N_2 - H_2O collisions order of magnitude estimates for the collision duration time can be obtained. The result is

$$t_d \approx \frac{2R_0}{\bar{v}} \begin{cases} \sim 10^{-12} & \text{for H}_2\text{O-H}_2\text{O} \\ \sim 10^{-13} - 10^{-12} & \text{for N}_2\text{-H}_2\text{O} \end{cases} \quad (154)$$

Typical period of rotation times for N_2 range between 10^{-10} to 10^{-11} sec and for H_2O range between 10^{-11} to 10^{-13} sec. These numbers are based on the molecular moments of inertia and a representative range of J-numbers. Water vapor however can effectively rotate faster due to its distortions. It is well known that the rotational motion of water vapor requires high order perturbation theory [4]. This necessity is a manifestation of the ease with which the water molecule will distort.

Based on the above arguments the weighted rotational average, $\langle \dots \rangle_{\text{Rot}}$, is important for H_2O-H_2O collisions and the approximation of Equation (17) can be used for N_2-H_2O collisions in the statistical limit. Thus, for far wing phenomena, the interaction Hamiltonians become (retaining only leading terms)

$$H_{aa_1} \approx \left\langle \frac{\mu_1^2}{R^3(t)} f \right\rangle_{\text{Rot}} - \frac{2\mu_1^2 \bar{\alpha}_1 + \frac{1}{2} \bar{\alpha}_1 e^2 \langle r_1^2 \rangle}{R^6(t)} \quad (155)$$

and

$$H_{ba_1} \approx \frac{\mu_1 \bar{Q}_2}{R^4(t)} \quad (156)$$

Eisenberg and Kauzmann [34] list the statistical average of $(\mu_1^2/R^3(t))f$ for rotating molecules to be

$$\left\langle \frac{\mu_1^2}{R^3(t)} f \right\rangle_{\text{Rot}} = - \frac{2\mu_1^4}{3kTR^6(t)} \quad (157)$$

under the condition that

$$\frac{2\mu_1^2}{kTR^3(t)} \ll 1.$$

Figure 14 is a plot of $2\mu_1^2/R^3(t)$ versus kT and shows that Equation

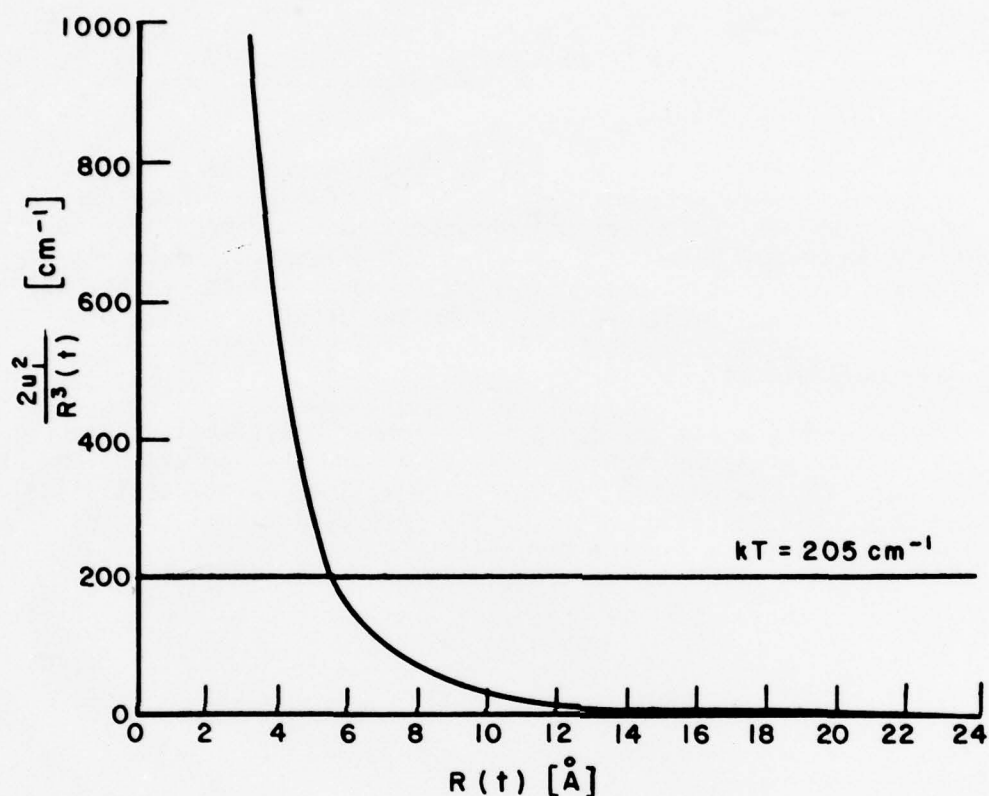


Figure 14. Comparison of $\frac{2\mu_1^2}{R^3}$ and kT in wavenumbers.

The value of μ_1 is 1.83×10^{-18} esu cm.

(157) will generally be valid. It will break down for very close collisions which contribute to the very far wing. Since contributions of far wings out to 1000 cm^{-1} from line center are of interest to this study, it is important to examine the statistical average of the dipole-dipole term for

$$\frac{2\mu_1^2}{kTR^3(t)} > 1.$$

This can be done by recognizing the analogy between Equation (16) and orientational polarizability calculations [54]. Thus,

$$\left\langle \frac{\mu_1^2}{R^3(t)} f \right\rangle_{\text{Rot}} = \frac{\mu_1^2}{R^3(t)} L(x) \quad (158)$$

where $L(x)$ the Langevin function and $x = 2\mu_1^2/R^3(t)$. Figure 15

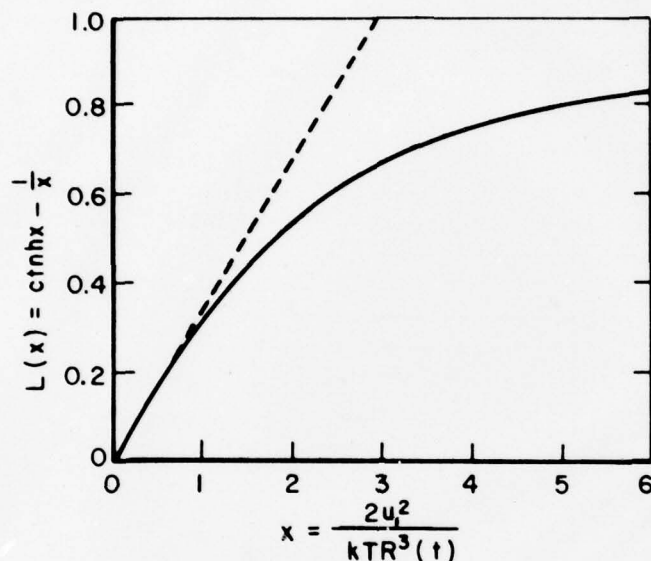


Figure 15. Plot of the Langevin function $L(x)$.

is a plot of $L(x)$. As x increases above 1 the curve becomes non-linear requiring higher powers in x .

Because of the complex nature of $\left\langle \frac{\mu_1^2}{R^3(t)} f \right\rangle_{\text{Rot}}$ for $\frac{2\mu_1^2}{R^3(t)} > 1$

and its limited range of importance (3 to 6 Å; bonding occurs at 2.8 Å) Equation (157) will be used. It is recognized that temperature and frequency dependent correction terms may be required in the very far wing. Under this approximation, the $\text{H}_2\text{O}-\text{H}_2\text{O}$ interaction Hamiltonian becomes

$$H_{aa_1} = - \left(\frac{2\mu_1^4}{3kT} + 2\mu_1^2 \bar{\alpha}_1 + \frac{1}{2} \alpha_1 e^2 \langle r_1^2 \rangle \right) \frac{1}{R^6(t)} \quad (159)$$

or in a more useful form

$$H_{aa_1} = - \left\{ \frac{\mu_1^2}{3kT} + \bar{\alpha}_1 + \left(\frac{1}{4} \frac{e^2 \langle r_1^2 \rangle}{\mu_1^2} \right) \bar{\alpha}_1 \right\} \frac{2\mu_1^2}{R^6(t)} \quad (160)$$

where the term

$$\frac{\mu_1^2}{3kT} + \left(1 + \frac{1}{4} \frac{e^2 \langle r_1^2 \rangle}{\mu_1^2} \right) \bar{\alpha}_1$$

represents a general polarizability for H_2O . The quantity $\frac{\mu_1^2}{3kT}$ is the orientational polarizability and the remaining expression is the electronic polarizability. Figure 16 [55] demonstrates the dominance

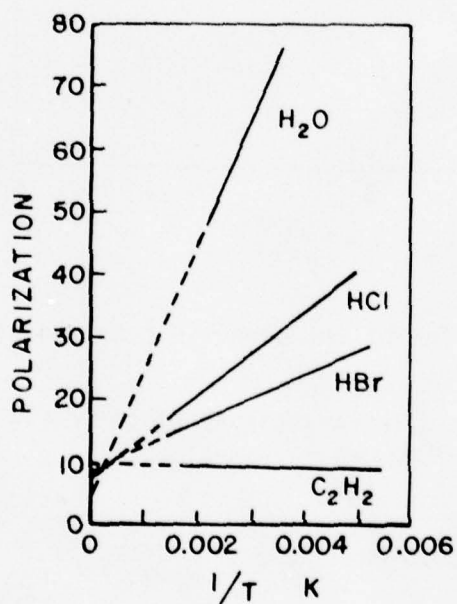


Figure 16. Polarization of gases versus temperature.

of orientational polarizability over electronic polarizability since the orientational polarizability is the only temperature dependent term in Equation (160). Based on this, the H_2O-H_2O interaction Hamiltonian is written

$$\boxed{H_{aa_1} = - \frac{2\mu_1^4}{3kTR^6(t)}} \quad (161)$$

The near line center and far wing line shapes now follow from Equations (129) and (142),

$$j_{\text{CNLC}}(\nu) = \frac{1}{\pi} \frac{\alpha^r}{(\nu - \nu_0)^2 + (\alpha^r)^2} \quad (162)$$

and

$$j_{\text{CFW}}(\nu) = \frac{1}{\pi} \left(\frac{.6266 \lambda_{a6}}{|\nu - \nu_0|^{1.5}} + \frac{.8491 \lambda_{b4}}{|\nu - \nu_0|^{1.75}} \right) \quad (163)$$

where

$$\alpha^r = \alpha_0^r \left(\frac{296}{T} \right)^{.83} \left[B \left(\frac{296}{T} \right)^{.17} p_a + p_b \right] \quad (164)$$

$$\alpha_0^r \left(\frac{296}{T} \right)^{.83} p_b = \alpha_{a_1 b}^r$$

$$B = \frac{\alpha_{a_1 a}^r}{\alpha_{a_1 b}^r}$$

p_a - absorber pressure

p_b - broadner pressure

T - temperature

$$\lambda_{a6} = \frac{p_a}{kT} \sum_b \rho_{sb} \frac{4\pi}{6\ell} \left(\frac{1}{h} (v_{6u} - v_{6\ell}) \right)^{1/2} \epsilon_6^{1/2} \Gamma(-\frac{1}{2}) \cos(\frac{\pi}{4})$$

or

$$\boxed{\lambda_{a6} = A_1(\nu) \left(\frac{296}{T} \right)^{1.5} p_a} \quad (165)$$

$$\lambda_{b4} = \frac{p_b}{kT} \sum_s \rho_{sb} \frac{4\pi}{h} (v_{4u} - v_{4l})^{3/4} \epsilon_4^{3/4} \Gamma(-\frac{3}{4}) \cos(\frac{3\pi}{8})$$

$$\lambda_{b4} = A2(v, J) \left(\frac{296}{T} \right) p_b \quad (166)$$

Because of the statistical averaging over rotations the H_2O-H_2O interaction potential matrix elements for strong collisions are independent of angle and not a function of the J quantum number. However $A1(v)$ will be different for every vibrational band, identified by the general vibrational quantum v representing both upper and lower levels. For N_2-H_2O collisions the statistical average was not performed; thus $A2(v, J)$ is a function of the vibrational and rotational quantum numbers involved. Since the potential function for near line center and far wing phenomena are the same, the J -dependence of $A2(v, J)$ can be expressed in terms of the J -dependence of α_0 . Using Equations (125) and (134), $A2(v, J)$ becomes

$$A2(v, J) = A2(v) (19.919) \left(\frac{\alpha_0^r}{.07} \right)^{1.125} \quad (167)$$

where .07 represents a mean value for α_0^r . $A1(v)$ and $A2(v)$ will be experimentally determined because of the complex nature of the terms and uncertainty of the interaction potentials. α_0 will be obtained from the AFGL line listing [5] and a B of 5 [30] will be used.

Equations (162) and (163) describe only parts of the total line shape. As section D indicates the intermediate wing region is unknown. Thus, the development of a total line shape must take a semi-empirical course. The construction of the total line shape will follow the guidelines listed below.

1. The total line shape is smooth everywhere.
2. The total line shape is normalizable.
3. The near line center and far wing forms must dominate under the appropriate frequency limits.
4. The intermediate wing region is to some extent a mixing of interruption and statistical broadening mechanisms.

The first step is to make Equation (163) a bounded function for all $(\nu - \nu_0)$. Varanasi et al [56] have developed a line shape which accomplishes this and produces the statistical frequency dependence in the far wing. It is

$$j(\nu) = \frac{1}{\pi} \left(\frac{\eta}{2} \sin \frac{\pi}{\eta} \right) \frac{\alpha^{\eta-1}}{|\Delta\nu|^\eta + \alpha^\eta}, \quad \Delta\nu = \nu - \nu_0. \quad (168)$$

Using this result and normalizing the far wing line shape to one (i.e., $\int_0^\infty j_{\text{CFW}}(\nu) d\nu = 1$) Equation (163) becomes

$$j_{\text{CFW}}(\nu) = \frac{1}{\pi} \left[\frac{.3198 \lambda_{a6}}{|\Delta\nu|^{1.5 + (\lambda_{a6})^3}} + \frac{.4334 \lambda_{b4}}{|\Delta\nu|^{1.75 + (\lambda_{b4})^{7/3}} \right]. \quad (169)$$

To construct the total line shape the concepts developed in the introduction to Section D will be followed. By choosing band pass and band stop filters (centered at ν_0) with slow fall off, mixing of the interruption and statistical line shapes respectively can be achieved in the intermediate region. The total line shape is written

$$j_c(\nu) = N(j_{\text{CNLC}}(\nu) p(\nu) + j_{\text{CFW}}(\nu)(1-p(\nu))) \quad (170)$$

where N is the normalization constant determined by

$$\int_0^\infty d\nu j_c(\nu) = 1$$

and $p(\nu)$ is a band pass filter function about ν_0 . Since $p(\nu)$ cannot be predicted with the present theory it must be chosen empirically. To insure a smooth joining of the interruption and statistical line shapes the derivative of $p(\nu)$ at $\nu = \nu_0$ and $\nu = \nu_0 \pm a$ is required to be zero. Where "a" is the frequency which represents the cut-off of the window function in the frequency domain. Also it is desirable for $p(\nu)$ to be a well known and easily integrated function. This will be helpful in the determination of N , the

normalization constant. Based on these guidelines $p(v)$ has been chosen to be

$$p(v) = \begin{cases} \frac{1}{2} + \frac{1}{2} \cos \frac{\pi}{5} \Delta v & |\Delta v| < 5 \text{ cm}^{-1} \\ 0 & |\Delta v| \geq 5 \text{ cm}^{-1} \end{cases} \quad (171)$$

where $a=5 \text{ cm}^{-1}$. Figure 17 is a plot of $p(v)$. As the figure

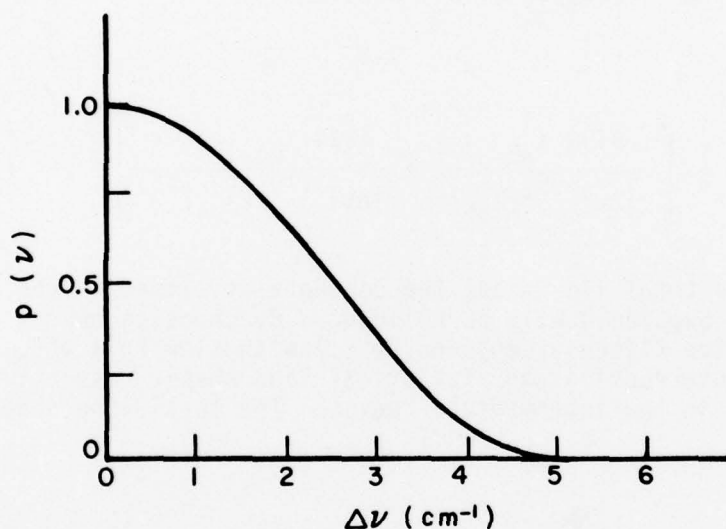


Figure 17. $p(v)$ versus Δv

illustrates the band pass filter function, $p(v)$, is virtually unity a few halfwidths from line center. This allows the interruption line shape to dominate near line center as it should. Similarly the stop band filter function ($1-p(v)$) allows the statistical (far wing) line shape to dominate beyond 5 cm^{-1} (50 to 100 halfwidths from line center). Thus a total line shape has been constructed which satisfies the four guidelines outlined earlier.

An important correction to the statistical line shape is the level shift correction term given by Equation (143). Applying this term to Equation (169) we obtain,

$$j_{\text{CFW}}(\nu) = \frac{1}{\pi} \left[\frac{.3198 \lambda_{a6}}{|\Delta\nu|^{1.5} + (\lambda_{a6})^3} \exp(-G_{a6}(\nu)\sqrt{\Delta\nu}) + \frac{.4334 \lambda_{b4}}{|\Delta\nu|^{1.75} + (\lambda_{b4})^{7/3}} \exp(-G_{b4}(\nu)\sqrt{\Delta\nu}) \right] . \quad (172)$$

The $\Delta\nu$ dependence in the exponential correction terms are slightly different from the term derived by Fomin [41] ($m_i=6 \Rightarrow |\Delta\nu|^{.55}$; $m_i=4 \Rightarrow |\Delta\nu|^{.5}$). Both $\Delta\nu$'s are taken here to the one-half power to simplify the normalization calculations. The reduced mass for $\text{H}_2\text{O}-\text{H}_2\text{O}$ collisions is less than the reduced mass for $\text{H}_2\text{O}-\text{N}_2$ collisions. Also, from Equation (143)

$$\omega_{04} > \omega_{06}$$

and therefore

$$G_{a6}(\nu) < G_{b4}(\nu) . \quad (173)$$

The "G" parameters are functions of the vibrational quantum numbers. The temperature dependence of the "G" parameters is

$$\boxed{\begin{aligned} G_{a6}(\nu) &= G_a(\nu) \left(\frac{296}{T}\right)^{.67} \\ G_{b4}(\nu) &= G_b(\nu) \left(\frac{296}{T}\right)^{.67} \end{aligned}} . \quad (174)$$

To determine the line strength for water vapor, the partition function ratios, $S_{\ell u}^0$, E_ℓ and ν_0 in Equation (102) must be obtained. $S_{\ell u}^0$, E_ℓ and ν_0 will be taken from the AFGL line compilation [5].

The vast majority of the H_2O molecules will be in the electronic ground state, therefore

$$\frac{Q_{E1}^0}{Q_{E1}} = 1 . \quad (175)$$

The vibrational partition function varies only slightly over the temperature range of the troposphere and can be assumed constant.

$$\frac{Q_{\text{Vib}}^0}{Q_{\text{Vib}}} \approx 1. \quad (176)$$

The rotational partition function for H_2O is very important. For an asymmetric top [57] the rotational partition function ratio becomes

$$\frac{Q_{\text{Rot}}^0}{Q_{\text{Rot}}} = \left(\frac{T}{T_0}\right)^{1.5}. \quad (177)$$

The total absorption coefficient for $\text{H}_2\text{O}-\text{N}_2$ mixtures can be written

$$k(\nu) = \sum_i k_i(\nu) = \sum_{\ell u} S_{\ell u}(\nu) j_c(\nu). \quad (178)$$

The summation is over all water vapor transitions. The line strength in Equation (103) contains frequency dependent terms which belong to the line shape in order to satisfy Equation (6). Therefore using Equations (103), (162), (170), (172), (175), (176), and (177) the $\text{H}_2\text{O}-\text{N}_2$ absorption coefficient becomes

$$k(\nu) = \sum_{\ell u} S_{\ell u} N(j_{\text{CNLC}}(\nu)p(\nu) + j_{\text{CFW}}(\nu)(1-p(\nu))) \quad (179)$$

where

$$S_{lu} = S_{lu}^0 \frac{T_0 p_a}{T p_{a0}} \left(\frac{T_0}{T} \right)^{1.5} e^{\frac{T-T_0}{kT_0}} \frac{(1-e^{-hc\nu_0/kT})}{(1-e^{-hc\nu_0/kT_0})} \quad (180)$$

$$j_{CNLC}(\nu) = \begin{cases} \frac{1}{\pi} \frac{\nu}{\nu_0} \frac{(1-e^{-h\nu c/kT})}{(1-e^{-h\nu_0 c/kT})} \frac{\alpha^r}{((\Delta\nu)^2 + (\alpha^r)^2)} & \nu_0 < 1000 \text{ cm}^{-1} \\ \frac{1}{\pi} \frac{\alpha^r}{(\Delta\nu)^2 + (\alpha^r)^2} & \nu_0 > 1000 \text{ cm}^{-1} \end{cases} \quad (181)$$

$$j_{CFW}(\nu) = \begin{cases} \frac{1}{\pi} \frac{(1-e^{-h\nu c/kT})}{(1-e^{-h\nu_0 c/kT})} \left[\frac{.3198 \lambda_{a6} e^{-G_{a6}\sqrt{\Delta\nu}}}{|\Delta\nu|^{1.5+\lambda_{a6}^3}} + \frac{.4334 \lambda_{b4} e^{-G_{b4}\sqrt{\Delta\nu}}}{|\Delta\nu|^{1.75+\lambda_{b4}^{7/3}}} \right] & \nu_0 < 1000 \text{ cm}^{-1} \\ \frac{1}{\pi} \left[\frac{.3198 \lambda_{a6} e^{-G_{a6}\sqrt{\Delta\nu}}}{|\Delta\nu|^{1.5+\lambda_{a6}^3}} + \frac{.4334 \lambda_{b4} e^{-G_{b4}\sqrt{\Delta\nu}}}{|\Delta\nu|^{1.75+\lambda_{b4}^{7/3}}} \right] & \nu_0 > 1000 \text{ cm}^{-1} \end{cases} \quad (182)$$

The normalization constant, N, is determined by the equation

$$N^{-1} = \int_0^{\infty} j_{CNLC}(\nu) p(\nu) d\nu + \int_0^{\infty} j_{CFW}(\nu) (1-p(\nu)) d\nu. \quad (183)$$

The solution of the above equation as a function of the different line shape parameters is presented in Appendix A.

CHAPTER III EXPERIMENTAL APPARATUS

This chapter describes the experimental equipment used to obtain the data of Chapter IV. All measurements have been taken on one of two long-path multiple-traversal absorption cells using a CO laser, a CO₂ laser or a Fourier transform interferometer as probes. The combination of laser and Fourier transform spectroscopy techniques provides a more complete experimental environment.

A. Frequency Probes

1. The CO laser

Lasing action in liquid nitrogen (LN₂) cooled CO lasers has been observed from 5 μ m to 8 μ m corresponding to the 1-0 to 36-35 vibrational bands [58]. Due to our interest in the 5 μ m atmospheric window, the range of operation of The Ohio State University CO laser was optimized for operation on the lower vibrational bands.

The resonant cavity structure follows the design of Charles Freed [59]. A black granite-Invar structure supports the optics and plasma tube and provides a stable open loop optical system. The four, 1 inch diameter Invar rods, which are thermally and acoustically shielded, define the length spacing between the 2 inch thick black granite end plates. Figures 18a and 18b show a top and side view respectively of the Invar structure. The figures illustrate the different stages of insulation, acoustic, thermal, and radiation shield. Aluminum clamps are used to secure the output mirror end plate and Invar cross pieces (used to support the plasma tube and liquid nitrogen fill system). The grating end plate is fastened to the Invar rods by half inch stainless steel bolts. The output mirror endplate is 9" x 10-12" and the grating end plate is 9" x 12-1/2".

The resonant cavity optical system contains a spherical output mirror of 5 meter radius of curvature and a gold coated grating mounted externally to the plasma tube. The spacing between the mirror and grating is 1.63 meters producing an output spot size of 2.2 mm and a beam waist of 1.87 mm. The grating can be easily rotated with a micrometer adjustment making the laser line-selectable. A piezoelectric-driven output mirror mount provides the necessary adjustments for optimum output power and open loop stability.

The plasma tube design is based on work by Djeu [60]. The plasma is composed of a N_2 -He-CO-Xe mixture at a total pressure of 7 torr. The tube has high voltage electrodes at each end with the ground electrode at the center of the tube. Figure 18c shows one end of the uninsulated plasma tube with an electrode. The outer 4" diameter pyrex tube forms the liquid nitrogen (LN_2) reservoir. The inner 15 mm diameter pyrex glass tube contains the plasma and high voltage nickel electrodes. The inner tube has a glass bellows at each end to ease the strain created between the inner and outer tubes when LN_2 is present. The electrodes are 1" long and approximately 1" outer diameter and 0.35" inner diameter with six equally spaced 1/16" rods on the front face. The electrodes not only provide the high electric field needed to generate a plasma, but also serve to resist flow of the CO molecules in the active LN_2 cooled section to the passive outer section. Thus ground state CO absorption is reduced to allow operation of the laser in the lower (2-1 and 1-0) vibrational bands. The electrical connection to the nickel electrodes also serves as a gas line for the N_2 -CO-Xe mixture feeding the plasma. Helium is introduced in the warm passive section of the tube and serves as a flush for unexcited CO as well as part of the active media. Figure 18d shows the inlet ports; the top port goes to the high voltage electrode and the side port is for the helium. The gases are then evacuated at the center port near the grounded electrode. Also shown is an end heater which warms the exterior tubes to prevent moisture condensation on the CaF_2 Brewster windows. The inlet lines from the flowmeters to the inlet ports on the tube are 1/16" inner diameter; this discourages gas breakdown in the inlet lines and makes the plasma more stable.

Liquid nitrogen CO lasers have the danger of ozone explosions if the discharge is initiated with ozone present. Ozone is produced by dissociation of CO in the plasma, and explosions can be a problem when the discharge goes out but the high voltage remains on. Normally, the plasma is generated before LN_2 is introduced in the reservoir. For safe operation a control circuit was constructed that senses the state of the plasma (on or off) and if the plasma de-energizes the high voltage power supply and LN_2 fill control are also turned off automatically. Figure 19 displays the circuit schematic for this system. Since the OSU CO laser does not use O_2 in the active media as other systems do, the O_3 formation problem is greatly reduced. Thus, with reasonable care safe operation of the laser can be accomplished.

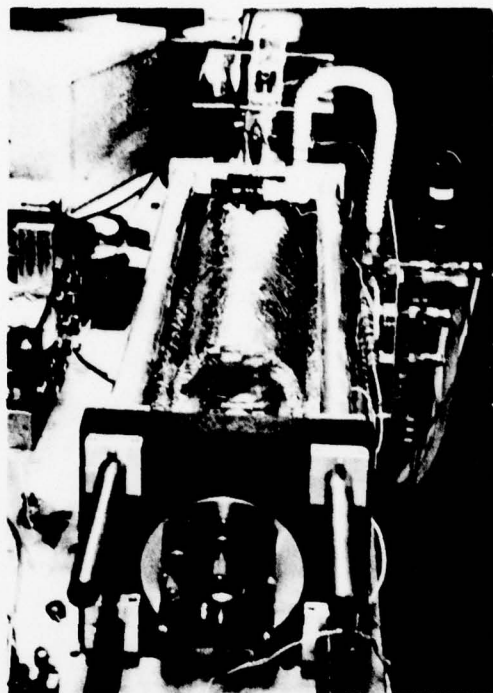


Fig. 18a. Top view of CO Laser showing output mirror and foil insulation.

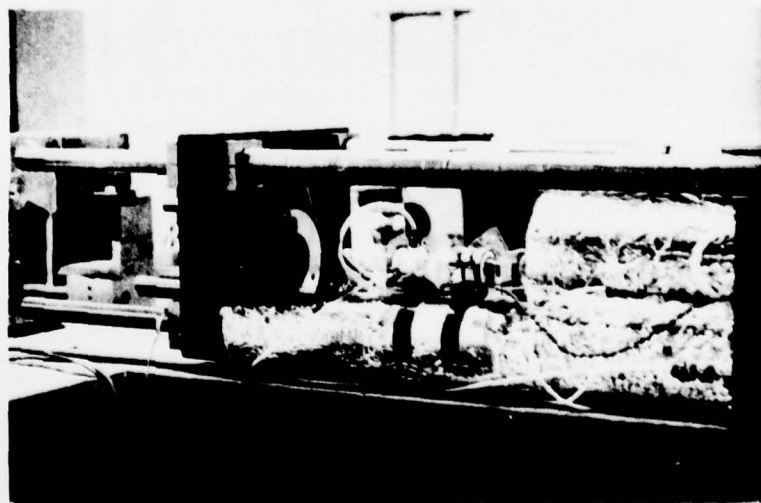


Fig. 18b. Side view of CO Laser showing uncovered invar rods at top and completely insulated invar rods at bottom.

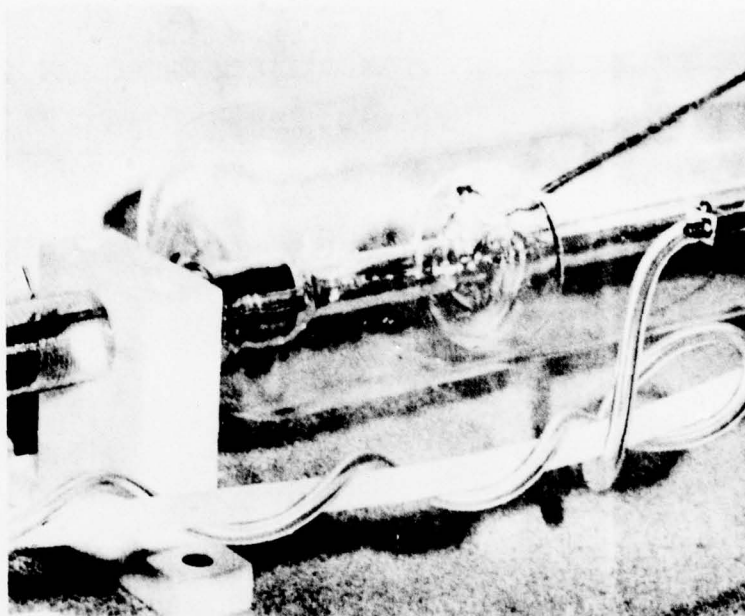


Fig. 18c. One end of the CO Laser plasma tube showing the electrode and glass bellow.

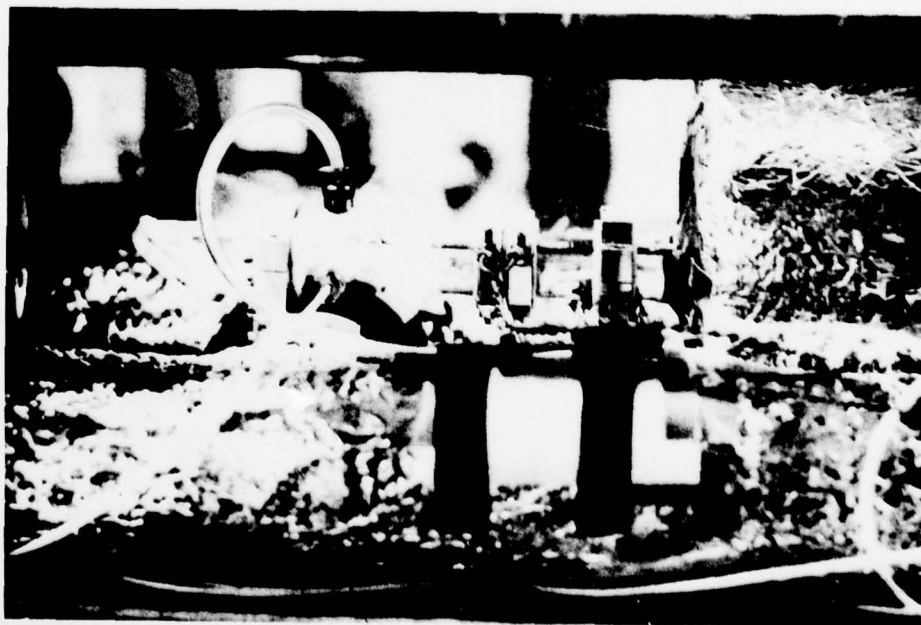


Fig. 18d. Brewster window with inlet ports.

Table 2
Observed CO Laser Lines

Line	ID	$\nu_0(\text{cm}^{-1})$	Typical Power (mw)
2-1	P(9)	2081.258	2
	P(10)	2077.140	5
	P(11)	2072.987	5
	P(12)	2068.802	7
3-2	P(7)	2063.225	1
	P(8)	2059.209	2
	P(9)	2055.159	10
	P(10)	2051.075	20
	P(11)	2046.958	20
	P(12)	2042.808	22
	P(13)	2038.624	25
	P(14)	2034.4075	20
	P(15)	2030.158	5
	P(7)	2037.124	5
4-3	P(8)	2033.143	10
	P(9)	2029.128	10
	P(10)	2025.080	10
	P(11)	2020.998	40
	P(12)	2016.882	25
	P(13)	2012.734	30
	P(14)	2008.552	25
	P(15)	2004.337	25
	P(16)	2000.090	20
5-4	P(7)	2011.093	5
	P(8)	2007.147	15
	P(9)	2003.167	15
	P(10)	1999.154	90
	P(11)	1995.107	90
	P(12)	1991.026	50
	P(13)	1986.913	40
	P(14)	1982.766	60
	P(15)	1978.586	20
	P(16)	1974.374	20
6-5	P(6)	1989.010	1
	P(7)	1985.133	6
	P(8)	1981.222	30
	P(9)	1977.277	40
	P(10)	1973.299	60
	P(11)	1969.287	60
	P(12)	1965.242	40
	P(13)	1961.163	60
	P(14)	1957.051	60
	P(15)	1952.907	50
	P(16)	1948.729	50
	P(17)	1944.519	30

Table 2 (Continued)

Line	ID	$\nu_0(\text{cm}^{-1})$	Typical Power (mw)
7-6	P(6)	1963.088	3
	P(7)	1959.246	20
	P(8)	1955.370	30
	P(9)	1951.460	50
	P(10)	1947.517	60
	P(11)	1943.540	50
	P(12)	1939.529	100
	P(13)	1935.486	60
	P(14)	1931.409	40
	P(15)	1927.299	15
8-7	P(6)	1937.239	10
	P(7)	1933.432	25
	P(8)	1929.592	10
	P(9)	1925.717	25
	P(10)	1921.808	25
	P(11)	1917.866	25
	P(12)	1913.891	25
	P(13)	1909.883	20
	P(14)	1905.841	20
	P(15)	1901.766	10
	P(16)	197.659	1
	P(17)	1893.519	1
9-8	P(6)	1911.467	3
	P(7)	1907.695	10
	P(8)	1903.889	10
	P(9)	1900.049	25
	P(10)	1896.176	30
	P(11)	1892.269	30
	P(12)	1888.328	25
	P(13)	1884.355	20
	P(14)	1880.348	20
	P(15)	1876.309	20
	P(16)	1872.236	15
10-9	P(6)	1885.771	4
	P(7)	1882.034	15
	P(8)	1878.263	20
	P(9)	1870.620	40

AD-A076 267

OHIO STATE UNIV COLUMBUS ELECTROSCIENCE LAB

F/G 4/1

TROPOSPHERIC WATER VAPOR ABSORPTION IN THE INFRARED WINDOW REGI--ETC(U)

AUG 79 M E THOMAS

DAAG29-77-C-0010

UNCLASSIFIED

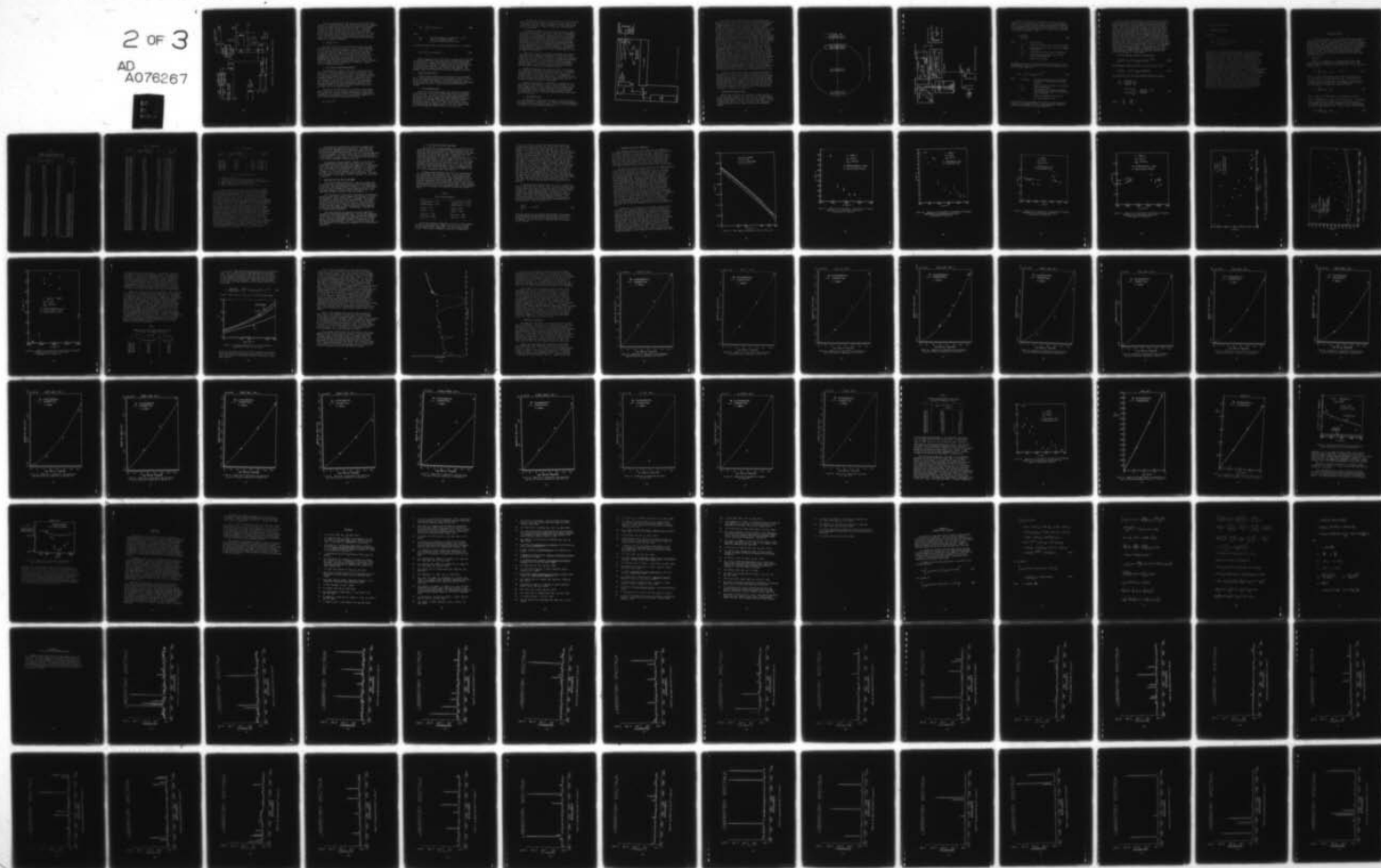
ESL-784701-5

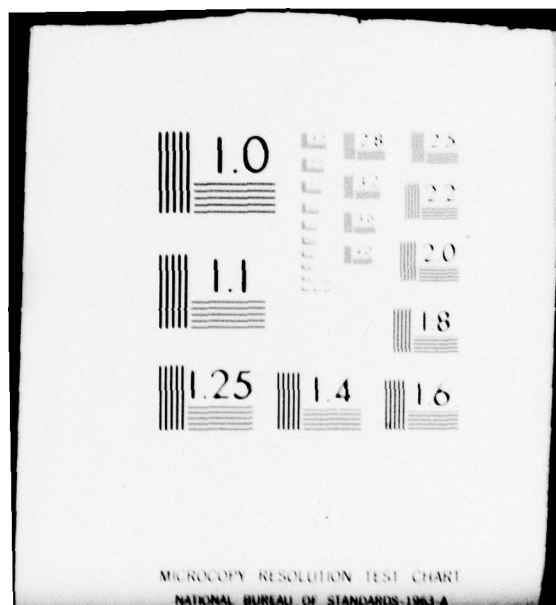
ARO-14702.4-GS

NL

2 OF 3

AD
A076267





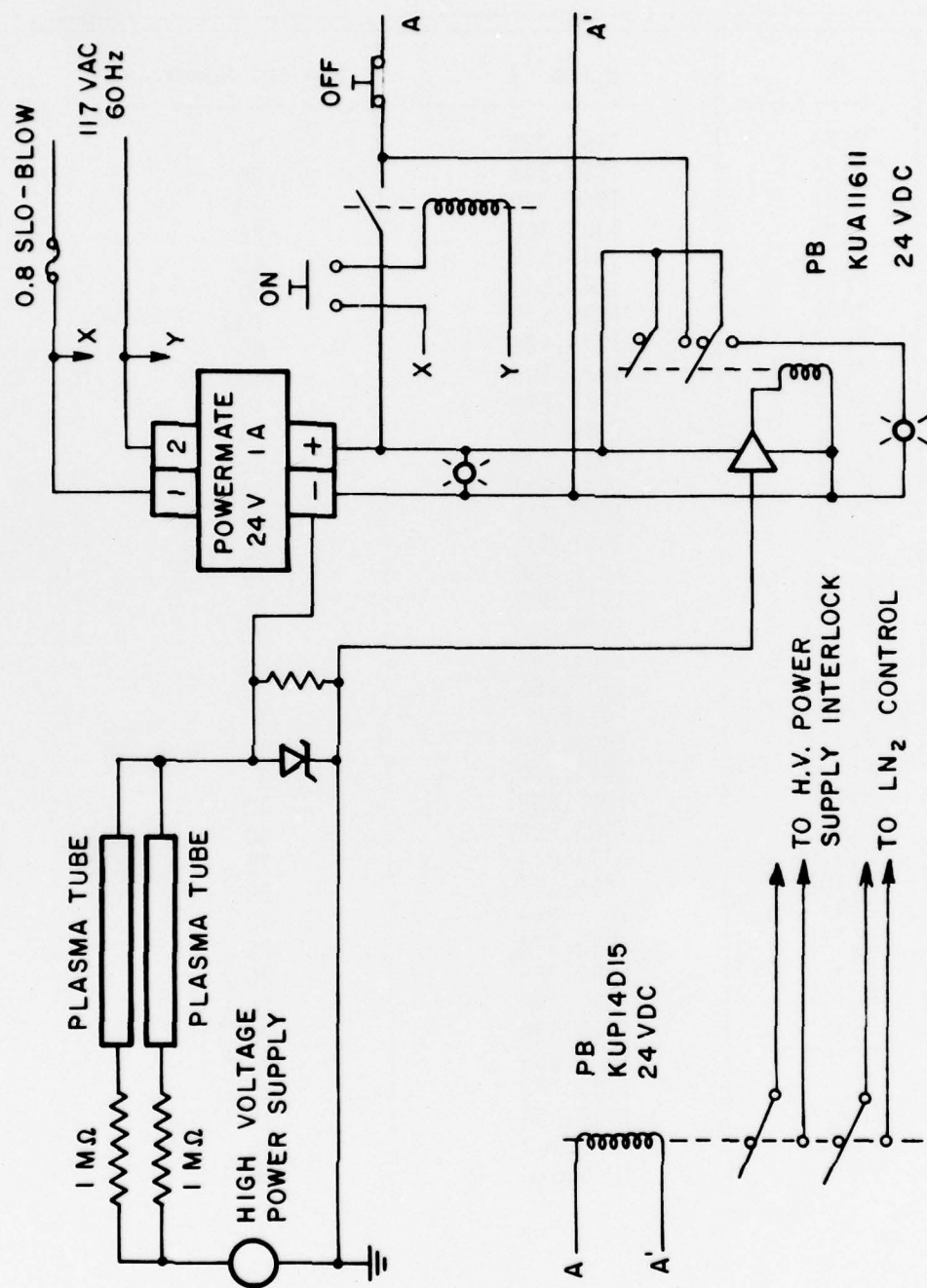


Figure 19. High voltage power supply control circuit.

Single line operation has been observed on 82 CO transitions from the 2-1 vibrational band to the 10-9 vibrational band. Research efforts have emphasized the low vibrational bands and no attempt was made to achieve output beyond the 10-9 band. It should be possible to extend the range of the present laser by two more vibrational bands. Outfitting the laser with different output mirrors and gratings would extend the output range to 8 μm . Table 2 lists the lines observed to date, along with a nominal output power. The CO laser presently operates with good (1%) short term stability in frequency and power.

2. The CO₂ Laser

The CO₂ laser used in the experiments has been previously described [18]. Briefly, the laser is a GTE Sylvania model 948 CO₂ laser plasma tube with a modified resonant cavity. The laser is also electronically stabilized by sensing plasma impedance fluctuations caused by changes in the gain of the system [61]. A feedback signal to the PZT cavity length-controller maintains optimum mirror separation. Lasing action on 23 transitions in the 00⁰₁-10⁰₀ (10 μm) vibrational band and 20 transitions in the 00⁰₁-02⁰₀ (9 μm) vibrational band has been observed. This effectively covers a frequency region from 930 cm^{-1} to 1085 cm^{-1} , ideally suited for 10 μm window studies.

3. The Fourier Transform Spectrometer

The monochromatic outputs of the laser sources prevent the observation of the total spectral response of a molecule. The addition of a Nicolet 7199 Fourier transform spectrometer expands the experimental capability of this study. The continuous spectral coverage from 800 cm^{-1} to 5000 cm^{-1} with a resolution of 0.05 cm^{-1} (0.035 cm^{-1} for spectra of limited bandwidth) provided by the instrument allows the close examination of local absorption line and near band wing features of absorbing molecules. The frequency response of the LN₂ cooled HgCdTe detector determines the lower limit of the spectral range.

The heart of the spectrometer is a Michelson interferometer with a fixed mirror in one arm and a moving mirror in the other. The moving mirror intensity modulates a broadband collimated beam and produces an interferogram, $I(\delta)$, which can be thought of as a sum of single monochromatic interference patterns,

$$B(\nu) \cos(2\pi\nu\delta)$$

i.e.

$$I(\delta) = \int_0^{\infty} B(\nu) \cos(2\pi\nu\delta) d\nu \quad (184)$$

where

- $B(\nu)$ - amplitude component at frequency ν in cm^{-1}
- $\delta=2L$ - optical retardation length
- L - distance traveled by moving mirror.

To obtain the spectrum $B(\nu)$ a Fourier transform of $I(\delta)$ is taken

$$B(\nu) = 2 \int_0^{\infty} I(\delta) \cos(2\pi\nu\delta) d\delta \quad (185)$$

Modern computers and the fast Fourier transform (FFT) algorithm by Cooley and Tukey [62] have made Fourier transform spectroscopy a practical tool. However the digitization of the interferogram and finite optical retardation lengths limit the resulting spectrum in resolution and bandwidth. To perform the FFT and other data manipulations the system includes a Nicolet 1180 computer. The computer handles up to one-half million point (complex) transforms.

B. White Absorption Cells

Two White-type absorption cells have been used in the experiments, a 15.24 meter base path cell constructed in the early sixties and a 10.785 meter base path cell just recently completed. Experience with the older absorption cell has prompted many improvements in the 10.785 meter cell. A brief description of these cells follows.

1. The 15.24 meter cell

This cell was first described by Long [63] and more recently by Peterson [18]. The cell is a steel pipe, 0.607 m in diameter, and 16.15 m long. The walls of the cell were honed smooth during construction in order to reduce water vapor adsorption effects. The mirrors are aluminum-coated pyrex with a measured reflectivity of 97.1% at 5 μm and radii of curvature of 15.24 meters which determines the mirror separation. The entrance and exit windows are currently BaF_2 half-degree wedges. A six inch diffusion pump and 100 cfm mechanical pump are used for cell evacuation.

The long path lengths (1-1.5 km) required for accurate measurements of the weak water vapor absorption at CO_2 and certain low-vibrational CO laser frequencies prompted a careful study of the 15.24 m cell stability. Several problems were identified and are discussed below.

The optical alignment of the cell was sensitive to changes in the internal pressure. The output beam would shift upwards by 3 mm at a 1 km path length as the cell's pressure was changed from vacuum to one atmosphere. Nonuniformities of the windows, the mirrors, and the detector then resulted in fluctuations in the output beam's signal level resulting in a high noise level on the data. To solve this problem the background measurement (usually taken with the cell evacuated) was taken with the cell at the same pressure as the sample measurements. This procedure has the additional benefit of ratioing out absorption effects of contaminants in the buffer gas if the same gas supply is used throughout the experiment.

Vibrations of the cell caused by vacuum pump and building vibrations (i.e., compressors switching on and off etc.) also changed the mirror alignment in the cell. Because typical measurements take an entire day it was difficult to complete successfully a long-path experiment. By vibrationally isolating all pumps and the mixing fans inside the cell the vibration problem was greatly reduced. To best avoid building noise the experiments were performed during off hours whenever possible.

Another problem which had a major effect on the experiment was nonuniform reflectivity of the mirror surfaces. Oil deposits and particulates collected on the mirrors over several years in a random fashion. Thus any change in the cell alignment had a dramatic effect on the output signal level. The problem was solved by recoating the mirrors and by using a 100 mw Argon laser to maintain alignment throughout the experiment.

Figure 20 illustrates the experimental arrangement for the CO and CO_2 laser measurements. Irises 1 and 2 were used to verify the alignment of the ir lasers against the Argon alignment laser. A BaF_2 beamsplitter was used to direct part of the laser energy to a reference detector. Mirrors mounted on kinematic mounts are labeled KM. The focal lengths of spherical mirrors are listed next to the mirrors.

2. The 10.785 m cell

The 10.8 meter cell which will now be described was designed by Professor Edward K. Damon [64]. Dr. Robert J. Nordstrom conceived the unique optical system which couples the lasers and interferometer to the optical system of the absorption cell.

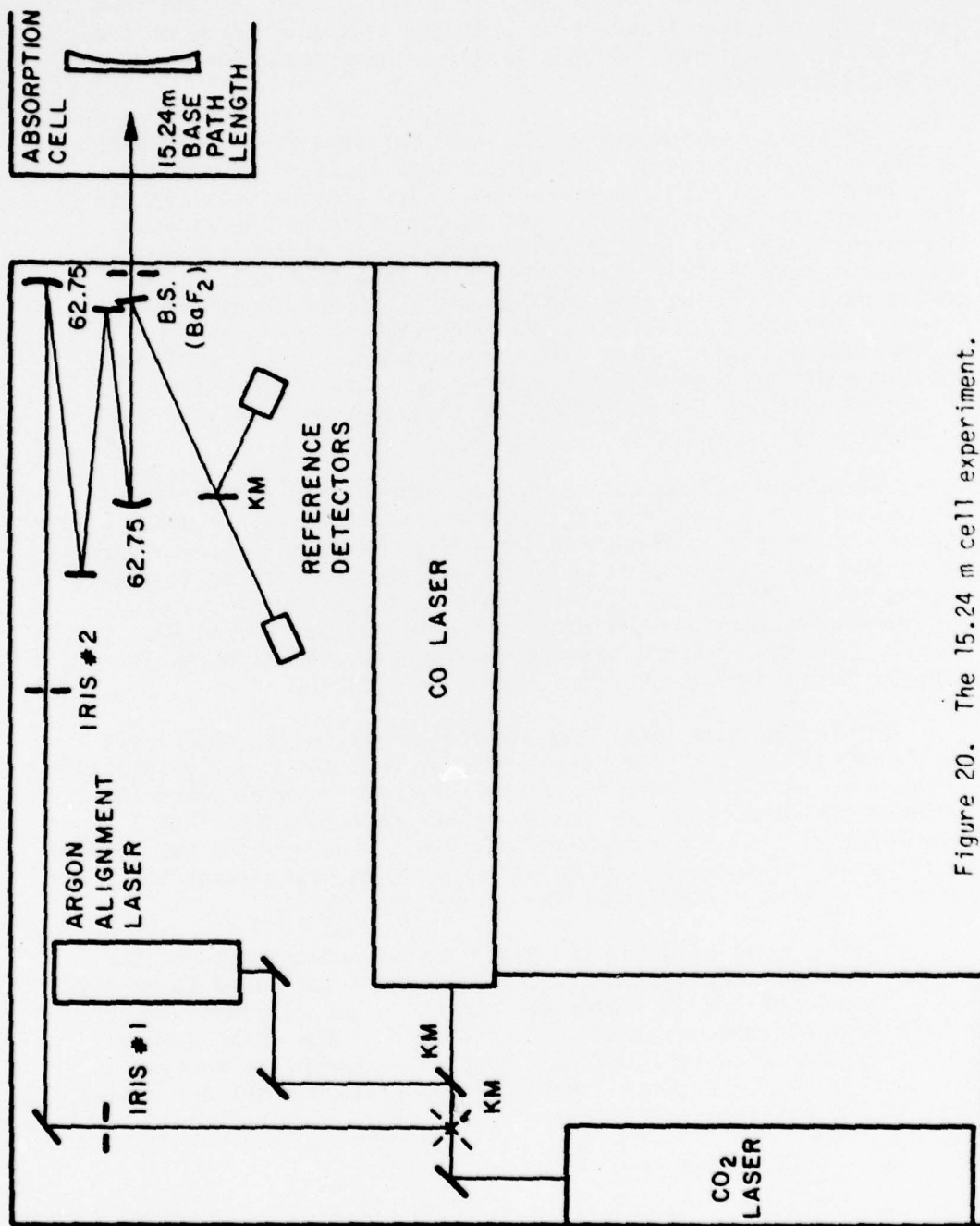


Figure 20. The 15.24 m cell experiment.

The 10.785 m cell features many design improvements over the 15.24 m cell. The internal cell mirrors are mounted externally through vacuum bellows in order to reduce the pressure dependent alignment problem of the older cell and to maintain a constant mirror separation over a wide temperature range of the cell. The mirrors are microprocessor controlled by stepper motors allowing great ease in changing or correcting the cell alignment. They are gold coated with a reflectivity of 98.6% at $10.6\mu\text{m}$, and have a radius of curvature of 10.785 m. The improved optical design of the 10.785 m cell features longer path lengths, improved spatial stability, and reduced aberration effects [65,66] over the standard White type design [67]. Figure 21 illustrates the spot arrangement on the field mirror of the new cell. Spot number 5 would typically be the output spot on a White type system. Instead it is fed back into the optical system generating two additional rows of spots. Path lengths of 1.8 km with laser sources and 1 km with a broadband source have been achieved on the new cell. The cell and optical tables are rigidly coupled and vibrationally isolated from the building. The new cell is constructed of 304 stainless steel with a smooth interior finish to reduce adsorption effects and to allow a wider variety of gases to be studied (e.g. ozone). Buffer gases are introduced uniformly along the cell. This method has greatly reduced gas mixing times in the new cell over the mixing time in the older 15.24 m cell. The two cells have similar vacuum systems except the 10.785 m cell has a Key Vacuum Product coaxial foreline trap model CFT-300 to reduce oil backstreaming of the mechanical pump. The new cell is also temperature controlled from -60°C to 60°C with a length uniformity of 1°C . This in fact was the principal reason for designing the new cell.

Figure 22 illustrates the total experimental system of the 10.785 m cell facility. The enclosures labeled source, FTIR, transfer optics, and detectors represent sealed boxes which house the indicated equipment. The labels S and W in the optical path of the blackbody source represent the source image and the FTIR beamsplitter image to be imaged on the field and focusing mirrors of the absorption cell, respectively. The sliding mirror in the detector box can be inserted into the cell output optical path to test the alignment of the optical system. The notation used in Figure 22 is the same as Figure 20.

C. Experimental Considerations

White type absorption cells represent an important part of the experimental apparatus presently used for the measurement of weak absorption coefficients. Also, the spectrophone, another sensitive experimental tool, requires calibration which is usually accomplished by White cell data. Because of their importance a detailed discussion of the nature of White cell experiments follows.

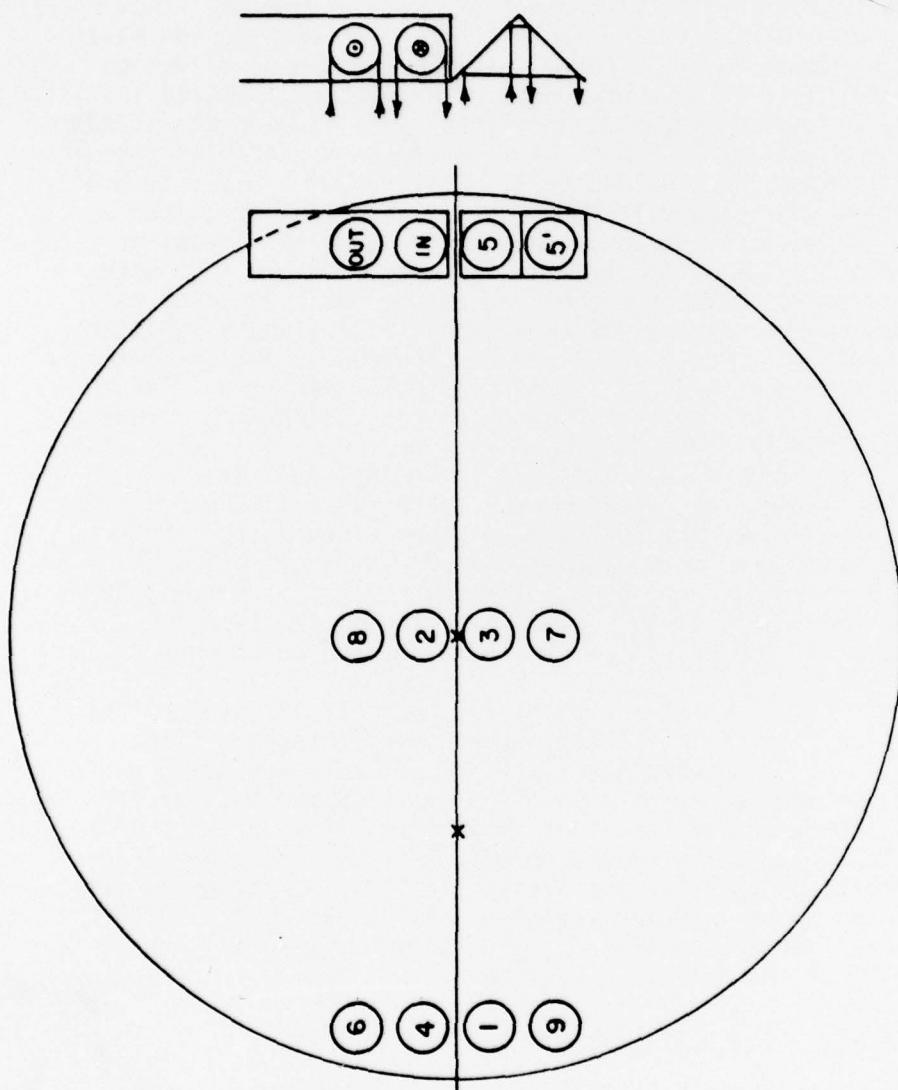


Figure 21. Spot pattern on field mirror.

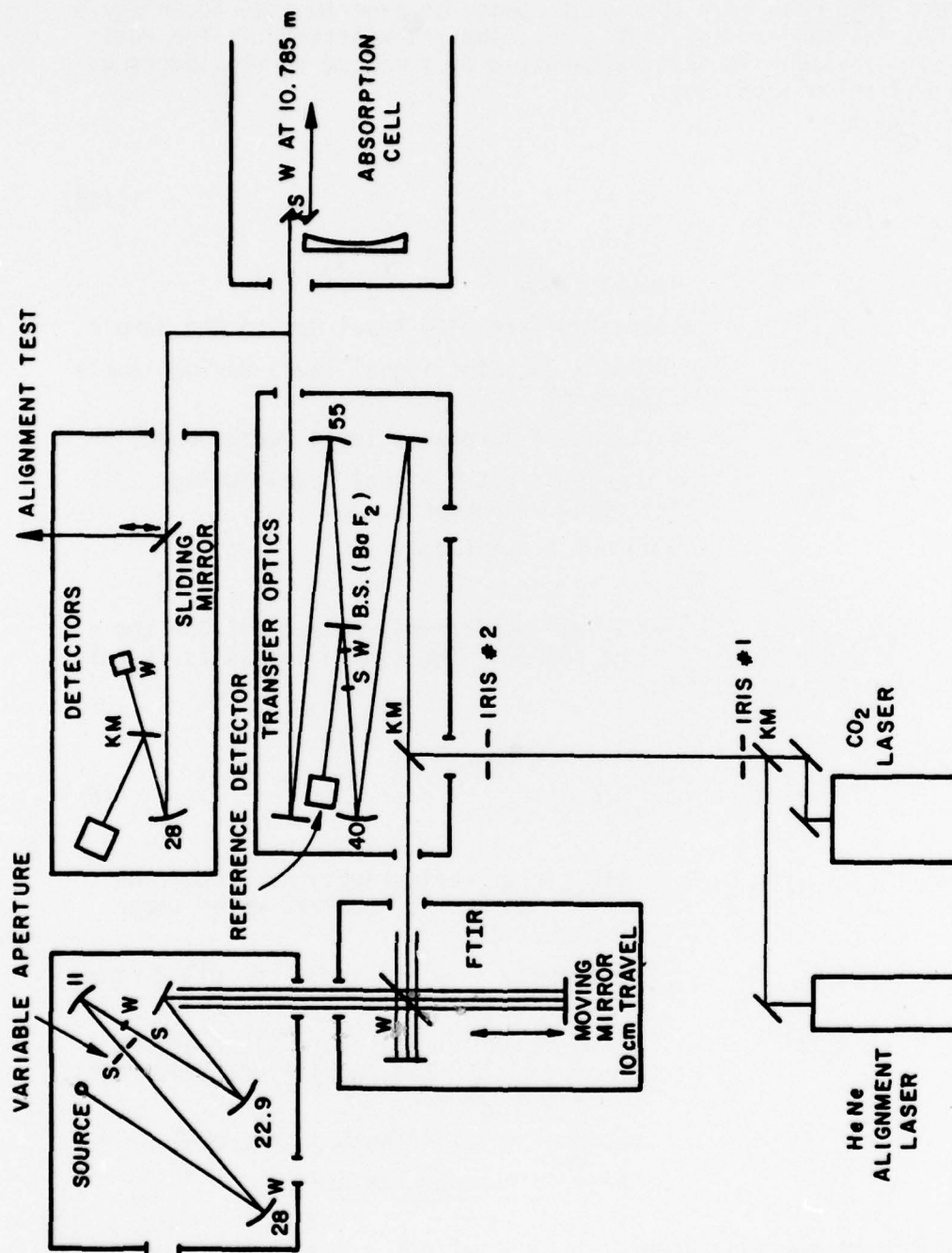


Figure 22. The 10.785 m cell experiment.

White cells measure the transmittance through a medium as opposed to a spectrophone which directly measures the absorption effect. This can give the spectrophone an experimental advantage for transmittances above 90% [68]. The transmittance is the ratio of the radiation intensity attenuated by a medium to the unattenuated radiation intensity. Thus,

$$T = \frac{I_S(n)/I_{RS}}{I_B(n)/I_{RB}} \quad (186)$$

where

- T - transmittance
- $I_S(n)$ - attenuated intensity level due to the sample
- I_{RS} - reference detector signal level during sample measurement
- $I_B(n)$ - unattenuated intensity level (background)
- I_{RB} - reference detector signal level during background measurement.
- n - number of traversals.

I_{RS} and I_{RB} scale $I_S(n)$ and $I_B(n)$ respectively to account for the different power levels of the source. The sample intensity, $I_S(n)$, can be further expressed as

$$I_S(n) = I_{OS} R^r(x, y, p_{H_2O}) K_S(t) e^{-kn\ell_0} \quad (187)$$

where

- $R(x, y, p_{H_2O})$ - the mirror reflectivity as a function of the mirror surface and water vapor pressure
- I_{OS} - intensity level at input to cell during sample measurement
- $K_S(t)$ - time dependent intensity fluctuations caused by windows, amplifiers, detectors, mirror drift etc.
- r - number of reflections inside cell
- ℓ_0 - base path length of cell.

To eliminate the time dependent fluctuations a time average over a number of measurements is taken. Two experimental techniques can be used to accomplish this averaging process.

Since the mirror reflectivity is a function of the position on the mirror surface and cell vibrations can cause mirror drift which misaligns the cell and changes the position of the spots on the field mirror, intensity variations in the output beam can result. Path differencing [69] averages over the mirror surface by changing the path length while keeping the sample fixed and averages over window, detector, etc. noise by taking many measurements at each path length. Another approach used at The Ohio State University maintains the cell alignment throughout an experiment by using optical lasers to account for the drift of the cell mirrors. By greatly reducing the mirror drift problem no average over the mirror surface is required. Figures 20 and 22 show the alignment lasers and irises 1 and 2 which are used to verify alignment of the cell before each measurement sequence. Also the output spot from the cell is monitored to test the cell mirror alignment before each measurement sequence. The average over the other noise sources is accomplished by averaging 400 data points with a 45 millisecond interval taken on a computer-controlled data acquisition system for a fixed sample.

The time averaged intensity is expressed as

$$\langle I_s(n) \rangle_t = I_{os} R^r(x, y, p_{H_2O}) \langle K_s(t) \rangle_t e^{-kn\ell_o} \quad (188)$$

The background intensity signal is similarly written, ($k=0$)

$$\langle I_B(n) \rangle_t = I_{oB} R^r(x, y, p_{H_2O}=0) \langle K_B(t) \rangle_t \quad (189)$$

Using Equation (186) the time averaged transmittance becomes

$$\begin{aligned} \langle T \rangle_t &= \frac{\langle I_s(n) \rangle_t}{\langle I_B(n) \rangle_t} \frac{I_{RB}}{I_{RS}} \\ &= \frac{R^r(x, y, p_{H_2O})}{R^r(x, y, p_{H_2O}=0)} \frac{\langle K_s(t) \rangle_t}{\langle K_B(t) \rangle_t} e^{-kn\ell_o} \end{aligned} \quad (190)$$

where $\frac{I_{os}}{I_{oB}} \cdot \frac{I_{RB}}{I_{RS}} = 1.$

Proper time averaging requires

$$\langle K_S(t) \rangle_t = \langle K_B(t) \rangle_t .$$

Therefore,

$$\langle T \rangle_t = \frac{R^r(x, y, p_{H_2O})}{R^r(x, y, p_{H_2O}=0)} e^{-kn\ell_0} . \quad (191)$$

To obtain the true absorption coefficient, k , (see Equation (4)) the mirror reflectivity must be the same in vacuum (or dry gaseous mixture) as it is with water vapor present at any pressure. This point has proven to be a major obstacle in obtaining the true absorption coefficient. Water vapor is adsorbed by the mirrors forming a very thin film (~ 1 micron [70]). The thickness of the film will depend on mirror temperature and pressure of water vapor in the cell. Therefore the effect on mirror reflectivity also depends on temperature and pressure. The reduction of mirror reflectivity by water vapor will also be frequency dependent. Interference effects become more important as the wavelength approaches the film thickness (i.e., R decreases as ν increases). Absorption and refractive index effects exhibit an irregular frequency dependence since they are related to resonance phenomena [71]. Burch et al [14] reported in 1967 that water vapor adsorption did not cause major difficulties at room temperature with 10 torr water vapor and 36 reflections. However, Burch has recently reported [72] that the $4 \mu\text{m}$ region has major water vapor adsorption problems. Further the 10.785 m cell at OSU has 110 to 150 reflections and typically has more than 10 torr water vapor for long path experiments. Thus, water vapor adsorption effects are important in particular at $4 \mu\text{m}$ and to a lesser extent at $10 \mu\text{m}$.

CHAPTER IV ANALYSIS OF RESULTS

A considerable amount of infrared window water vapor absorption data has been collected over the past ten years at The Ohio State University and elsewhere. Measurements of room temperature nitrogen-broadened water vapor absorption made during this study and collected during experimental programs at other laboratories will be presented. The total line shape expression developed in Chapter II will then be used in conjunction with the AFGL line listing [5] to model the measured data. The results of the modeling demonstrate the importance of far wing line shape contributions to the water vapor continuum absorption.

A. Data Base

Table 3 is a compendium of nitrogen-broadened water vapor window absorption parameters at room temperature (296 K). The general form for the absorption coefficient which is used to present the data [14] is

$$k(\nu) = \frac{p_a}{RT} (C_N p_{N_2} + C_S p_a) \quad [\text{km}^{-1}], \quad (192)$$

where C_S is the self-broadening coefficient for water vapor, C_N is the nitrogen broadening coefficient, p_{N_2} is the pressure of nitrogen in torr, p_a is the water vapor partial pressure in torr, R is the ideal gas constant, and T is the temperature in Kelvin. The equation can be conveniently rewritten to obtain

$$k(\nu) = \frac{C_N}{RT} p_a (p_{N_2} + B p_a) \quad (193)$$

where $B = \frac{C_S}{C_N}$ is the dimensionless self-broadening coefficient.

Table 3 lists $\frac{C_N}{RT}$ and B at many different frequencies. One exception to the formula (Equation (193)) must be made for 1957.050 cm^{-1} since the CO laser line at this frequency is within the halfwidth of a local water absorption line. In this case the formula becomes

$$k(\nu) = \frac{C_N}{RT} p_a (p_{N_2} - B p_a). \quad (194)$$

Table 3

Nitrogen Broadened, Water Vapor
Window Absorption Parameters

$\nu(\text{cm}^{-1})$	$C_N/RT \times 10^5 (\frac{\text{km}^{-1}}{\text{torr}^2})$	B	Laser Line ID
337.9	656.7	10.5	a
366.0	165.2	25.4	a
389.0	124.9	26.9	a
411.0	60.1	45.0	a
433.7	68.7	35.6	a
439.0	68.7	35.0	a
448.8	50.2	43.6	a
475.1	67.4	27.4	a
482.6	71.2	23.6	a
498.0	23.7	55.2	a
531.6	14.4	70.8	a
559.2	8.67	86.6	a
579.0	23.5	30.7	a
597.0	11.5	56.2	a
611.4	5.24	95.9	a
629.0	5.80	84.6	a
934.894	0.36	330.0	P(30),b
936.804	0.32	343.6	P(28),b
938.688	0.498	195.7	P(26),b
940.548	0.571	171.5	P(24) [†] ,b
942.383	0.759	114.8	P(22),b
944.194	0.257	340.1	P(20) [†] ,b
945.980	0.164	549.5	P(18),b
951.192	0.308	264.6	P(12),b
952.881	0.331	251.2	P(10),b
969.140	0.041	2133.4	R(10)*,b
970.547	1.761	35.1	R(12),b
971.930	1.091	107.3	R(14)*,b
973.288	0.837	95.2	R(16)*,b
974.622	0.903	80.6	R(18),b
977.214	0.768	98.0	R(22),b
980.913	0.163	467.3	R(28),b
1048.661	0.555	120.9	P(18) [†] ,b
1050.441	0.730	86.9	P(16) [†] ,b
1052.196	0.674	99.0	P(14) [†] ,b
1053.924	0.588	138.6	P(12) [†] ,b
1073.278	0.401	213.2	R(12)*,b
1077.303	0.583	113.2	R(18),b
1079.852	0.167	414.9	R(22)*,b
1081.087	0.564	131.2	R(24),b
1082.296	0.546	105.6	R(26) [†] ,b
1854.933	42.9	7.6	10-9 P(14),c

Table 3 (continued)

$\nu(\text{cm}^{-1})$	$C_N/RT \times 10^5 (\frac{\text{km}^{-1}}{\text{torr}^2})$	B	Laser Line ID
1880.348	26.7	16.1	9-8 P(14) ,c
1905.840	38.9	9.9	8-7 P(14) ,c
1927.299	23.4	10.4	7-6 P(15) ,c
1931.409	17.2	8.2	7-6 P(14) ,c
1948.729	19.7	13.3	6-5 P(16) ,c
1952.907	10.5	15.2	6-5 P(15) ,c
1957.050	44.7	3.8	6-5 P(14) ,c
1970.129	16.8	13.6	5-4 P(17) ,c
1974.374	4.88	26.6	5-4 P(16) ,c
1978.586	4.45	21.5	5-4 P(15) ,c
2003.165	5.04	7.25	5-4 P(9) ,c
2004.337	5.21	4.4	4-3 P(15) ,c
2012.733	6.65	5.5	4-3 P(13) ,c
2025.079	4.95	5.2	4-3 P(10) ,c
2029.128	2.20	8.75	4-3 P(9) ,c
2038.625	5.34	6.5	3-2 P(13) ,c
2471.243	0.26	54.3	3-2 P(11) ,d
2496.720	0.25	44.6	3-2 P(10) ,d
2521.769	0.233	37.3	3-2 P(9) ,d
2546.373	0.221	32.1	3-2 P(8) ,d
2553.951	0.216	31.4	2-1 P(11) ,d
2570.522	0.210	29.7	3-2 P(7) ,d
2580.095	0.204	29.7	2-1 P(10) ,d
2594.197	0.198	30.3	3-2 P(6) ,d
2605.806	0.191	32.1	2-1 P(9) ,d
2617.386	0.186	34.5	3-2 P(5) ,d
2631.066	0.179	38.6	2-1 P(8) ,d
2640.075	0.175	42.0	3-2 P(4) ,d
2655.863	0.168	50.2	2-1 P(7) ,d
2665.218	0.165	55.2	1-0 P(10) ,d
2680.178	0.157	67.1	2-1 P(6) ,d
2691.608	0.152	78.1	1-0 P(9) ,d
2703.998	0.146	90.9	2-1 P(5) ,d
2717.538	0.141	107.5	1-0 P(8) ,d
2727.308	0.137	121.9	2-1 P(4) ,d
2742.997	0.132	144.9	1-0 P(7) ,d
2750.093	0.128	158.7	2-1 P(3) ,d
2767.968	0.123	192.3	1-0 P(6) ,d
2792.434	0.116	250.0	1-0 P(5) ,d
2816.380	0.110	312.5	1-0 P(4) ,d
2839.791	0.102	400.0	1-0 P(3) ,d
2862.646	0.099	476.2	1-0 P(2) ,d
3434.9994	13.3	5.00	2-1 P(8) ,e

Table 3 (Continued)

$\nu(\text{cm}^{-1})$	$C_N/RT \times 10^5 (\frac{\text{km}^{-1}}{\text{torr}^2})$	B	Laser Line ID
3483.6522	69.0	8.20	2-1 P(7) ,e
3531.1747	476.7	3.91	2-1 P(6) ,e
3577.5002	532.8	6.30	2-1 P(5) ,e
3644.1454	429.4	5.00	1-0 P(7) ,e
3693.4226	1542.3	4.34	1-0 P(6) ,e
3788.2253	203.4	8.92	1-0 P(4) ,e

Sources of experimental data.

- a. Gryvnak and Burch [73]
- b. Peterson, Thomas, Nordstrom, Damon and Long [20]
- c. Long, Damon, Nordstrom, Peterson, Thomas and Sherman [23]
- d. Watkins, White, Bower and Sojka [24]
- e. Watkins, Spellicy, White, Sojka, Bower [76]

The values from 337.9 to 629.0 cm^{-1} are taken from Burch [73] who used a grating spectrometer and a White-type absorption cell. The values from 934.894 cm^{-1} to 1082.296 cm^{-1} represent the 00⁰1-10⁰0 and 00⁰1-02⁰0 CO₂ laser line measurements taken at The Ohio State University [20]. The asterisk in the laser line identification column indicates the measurement using The Ohio State University differential spectrophone [20]; the remainder of The Ohio State University measurements were determined using the 15.24 m White cell [20]. The complete set of spectrophone measurements show excellent agreement with the White cell data [18]. Further verification of the listed values designated by a dagger (†) in the laser line identification column has been achieved through a recently completed remeasurement program using the newly completed 10.785 m cell which was described in the last chapter. The data from 1854.933 cm^{-1} to 2038.625 cm^{-1} are CO laser measurements also taken at The Ohio State University [23,74] on the 15.24 m cell. The parameters of the last seven CO laser lines were obtained with the CO laser described in Chapter III. The values from 2471.243 cm^{-1} to 2862.646 cm^{-1} are DF laser measurements performed by the Atmospheric Sciences Laboratory [24,75]. The HF laser measurements from 3434.9994 cm^{-1} to 3788.2253 cm^{-1} were also performed by the Atmospheric Sciences Laboratory [76].

The magnitude of absorption at a particular frequency can be inferred from the magnitude of C_N/RT and B . The water vapor partial pressure dependence of the absorption coefficient can be determined from the magnitude of B . For B small ($\sim 5-10$) the k versus p_v dependence is nearly linear and for B large the dependence is nearly parabolic. The table clearly shows the characteristics of the different frequency regions. The interpretation and modeling of this data is the topic of the next section.

To complement the monochromatic frequency listing of Table 3, broadband spectral data of pure water vapor have also been taken using the Nicolet FTIR system (see Chapter II). The portions of this spectrum in the window regions from 850 cm^{-1} to 1282 cm^{-1} , 1800 cm^{-1} to 2054 cm^{-1} , and 2500 cm^{-1} to 2862 cm^{-1} are presented in Appendix B. This FTIR spectrum is for a sample of 12 torr pure water vapor at 296 K and 323.5 meters path length. The local line structure in the windows is clearly indicated. The resolution is 0.05 cm^{-1} .

B. Application of the Total Line Shape

This section contains three parts. The first examines the far wing "A" and "G" parameters and the normalization coefficient of the total line shape developed in Chapter II. The determination of the "A" and "G" parameters allows the application of the total line shape formulas to the water vapor continuum problem. This application becomes the topic of the next two parts.

Part two presents a comparison of experimental and theoretical absorption coefficients versus frequency and H_2O partial pressure. The agreement is good, from which it is concluded that far wings can explain the observed H_2O continuum absorption. The window regions studied are the $4\text{ }\mu\text{m}$, $5\text{ }\mu\text{m}$, $10\text{ }\mu\text{m}$, $17\text{ }\mu\text{m}$ and millimeter. The general success of the model in predicting absorption in all the H_2O infrared windows is further evidence of the correctness of the total line shape approach. Shortcomings in the model are also recognized and discussed.

Part three presents the observed and modeled temperature dependence of the absorption coefficient. The far wing expression for the total line shape features a negative temperature dependence which is required if agreement with experiment is to be obtained. However the rate of the negative temperature dependence is less than observed experimentally. This is explained by recognizing the inadequacies of the temperature dependence of the intermolecular potentials.

1. Parameters of the total line shape

The "A" and "G" far wing parameters of the total line shape (Equation (182)) will be determined from experimental data. To avoid any complicating effects (i.e., dimer absorption) the experimental data are taken from "near-band" regions where far wing contributions from the band dominate. Furthermore, this allows the determination of the far wing contribution in the 12-8 μm and 4 μm window regions. Figure 1 shows 15 μm , 5 μm and 3 μm to be near-band regions for H_2O absorption. The 15 μm and longer wavelength data by Burch [72] are used to obtain the line shape parameters for the rotational band. The 5 μm CO laser results are used to determine the parameters for the ν_2 fundamental band. The 3 μm HF laser results are used to obtain the parameters for the ν_1 and ν_3 fundamental bands (see Table 3).

A computer program applying the total line shape equations and employing the AFGL absorption line listing for water vapor was used to model the experimental data. The parameters were determined by trial and error until a good representation of the near band experimental data was obtained. The success of this technique removed the need for more sophisticated fitting routines. Further, considering the limitations of the model, a more accurate determination of the "A" and "G" parameters would not be meaningful. The "A" and "G" parameters for the main H_2O bands are listed in Table 4.

Table 4

The Far Wing Parameters

$A1(\text{Rotational}) = 2.35$	$G_a(\text{Rotational}) = 0.065$
$A2(\text{Rotational}) = 0.18$	$G_b(\text{Rotational}) = 0.115$
$A1(\nu_2) = 1.73$	$G_a(\nu_2) = 0.07$
$A2(\nu_2) = .153$	$G_b(\nu_2) = 0.084$
$A1(\nu_1, \nu_3) = 1.95$	$G_a(\nu_1, \nu_3) = .045$
$A2(\nu_1, \nu_3) = 0.165$	$G_b(\nu_1, \nu_3) = .088$

Using the equations of Appendix A and the far wing parameters of Table 4, the normalization coefficient, N , can be evaluated for the different water vapor bands. For water vapor-nitrogen mixtures under general tropospheric conditions of temperature

and pressure and for $\nu > 100 \text{ cm}^{-1}$ the normalization coefficient is equal to one within one percent. At less than 100 cm^{-1} the normalization coefficient is less than one (i.e., $\nu = 18.6 \text{ cm}^{-1}$, $N = 0.95$). Since most of the water vapor spectral lines are above 100 cm^{-1} , N is generally equal to one. The total line shape contains a normalized near-line-center line shape (Equation (181)). When multiplied by the p-function it represents 98% to 96% of the area under the total line shape, very close to what the near-line-center area would be if no p-function were used. Therefore, the total line shape as constructed for the different bands does not modify the emphasis of the near line center line shapes commonly used (the Lorentz line shape for $\nu > 1000 \text{ cm}^{-1}$ and the modified Van Vleck-Weisskopf [45] line shape for $\nu < 1000 \text{ cm}^{-1}$). This is an important point because previous modeling attempts in the $5 \mu\text{m}$ region [74] have used super-Lorentz line shapes which enhance the wings of the local lines while ignoring the far wings of strong lines in the heart of the ν_2 fundamental band. To maintain normalization the absorption at line center must decrease by a significant amount (10-15%). This distorts the true total line shape since the Lorentz line shape does model near line center phenomena (Chapter II Section D). The line shape developed in this study avoids this problem.

To reduce the long computer time of an all line calculation requires two conditions to be met. One is a bound (frequency range) in which absorption lines are considered about a central frequency) of 1500 cm^{-1} . Larger bounds produce no significant change. Note that previous workers with the Lorentz line shape have used a bound of only 20 cm^{-1} which apparently was selected to minimize computer time rather than from any physical principles. Also our program performs a test on the absorption line intensity to eliminate the many weak lines which do not have appreciable far wing absorption. The test criteria is

$$\frac{S_{lu}^0 \alpha_0^r}{(\Delta\nu)^2} < 1 \times 10^{-28} \quad (195)$$

where S_{lu}^0 and α_0^r are read directly from the AFGL listing and $\Delta\nu$ is the frequency difference between the absorption line and the frequency location for which the absorption coefficient is to be computed. If Equation (195) is satisfied then the absorption line is ignored.

2. Frequency and pressure dependence

The frequency dependence of the statistical line shape far wing (Equation (182)) is illustrated in Figure 23 for the rotational, ν_2 and (ν_1, ν_3) bands of nitrogen broadened H_2O . Comparison to the Lorentz line shape is also made. The figure shows the statistical far wing to be greater than the Lorentz far wing until around 1000 cm^{-1} (this intersection point decreases with pressure) from line center where the exponential factor in the statistical line shape causes a drop below the Lorentz far wing. Thus the total line shape (Equation (179)) can be technically termed sub-Lorentzian.

The results of the application of the total line shape determined for each band are presented in Figures 24 thru 30. Recall that figures 24, 25, 28 and 30 represent the near band data from which the "A" and "G" parameters were determined. Figures 26, 27 and 29 represent the window regions and show remarkable agreement with experimental data. This is a strong indication that far wings of the water vapor fundamental bands play an important role in continuum absorption. Discrepancies in the data comparison can be attributed to experimental error, inaccurate parameters on the AFGL [5] listing, and breakdown of the line shape model. Perhaps the most serious breakdown of the model occurs in the $10\text{ }\mu\text{m}$ window region, which is dominated by the rotational band. Collisional interactions resulting in line distortions 600 to 800 cm^{-1} from line center are not small perturbations to the pure rotational motion of the molecule which will typically have energy levels from 0 to a few hundred wavenumbers (see Chapter 2, Section B). Thus the model of the far wings for the rotational band is not strictly valid. However, the results in the $10\text{ }\mu\text{m}$ region are surprisingly good and perhaps this is not a serious problem. Also, the inability to achieve a reasonably good fit to the HF data makes the "A" and "G" parameters for the ν_1, ν_3 bands questionable.

Random errors in the absorption line shape parameters (line position, line strength, halfwidth, etc.) tend to average out in the far wing continuum region because hundreds of absorption lines are contributing simultaneously. However local line contributions do not have this property. Appendix B contains spectra from 850 to 2862 cm^{-1} of the window regions studied. The local line structure is clearly indicated and a correlation can be found between strong local line contributions and data discrepancies in many cases. The problem of properly characterizing nearby absorption lines relative to some frequency of concern may not only pertain to the standard line shape parameters (i.e., line strength, halfwidth and line position). Since line positions are usually obtained from low pressure samples of pure water vapor modeling attempts at a total pressure of one atmosphere may require

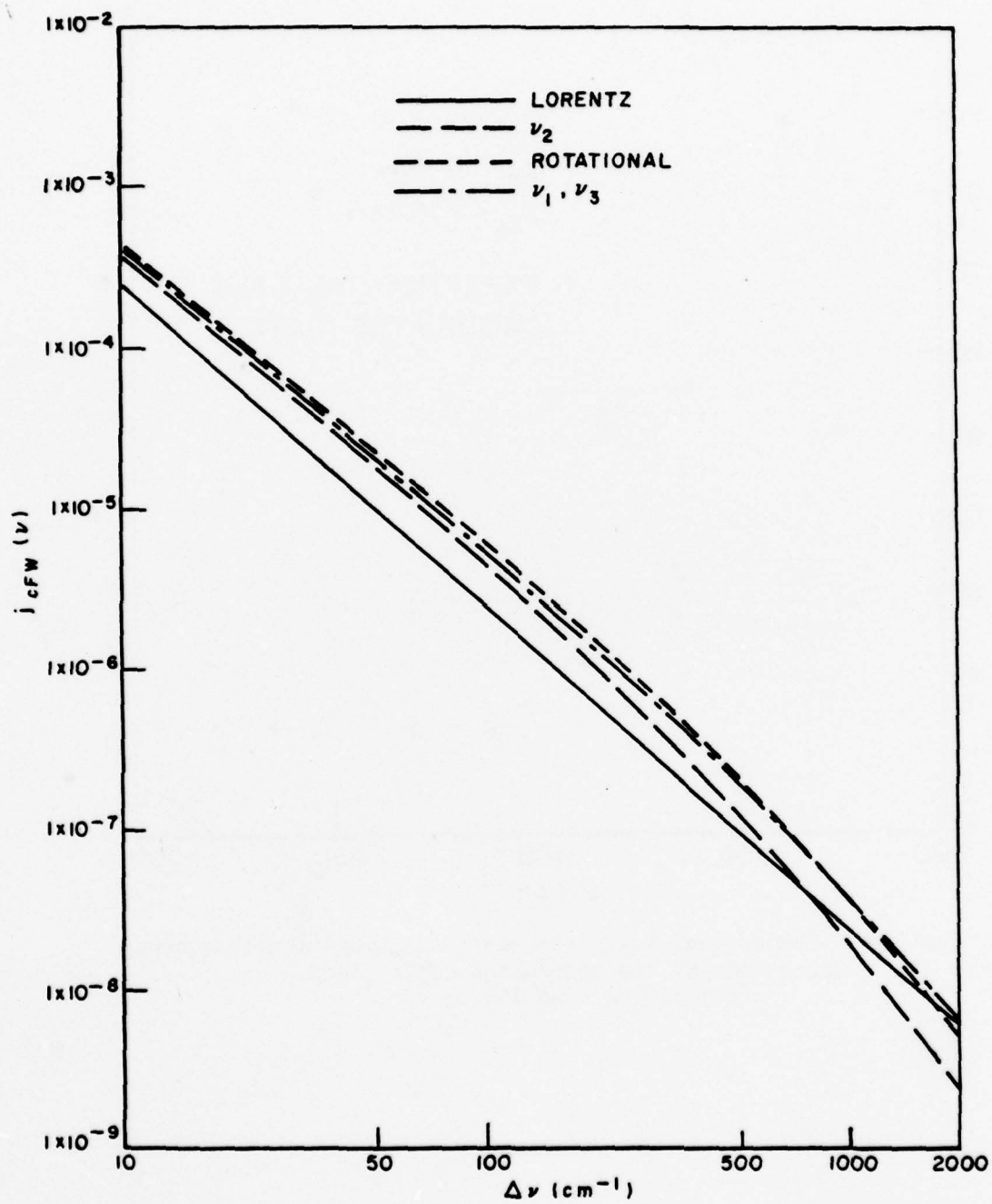


Figure 23. The frequency dependence of the far blue wing.

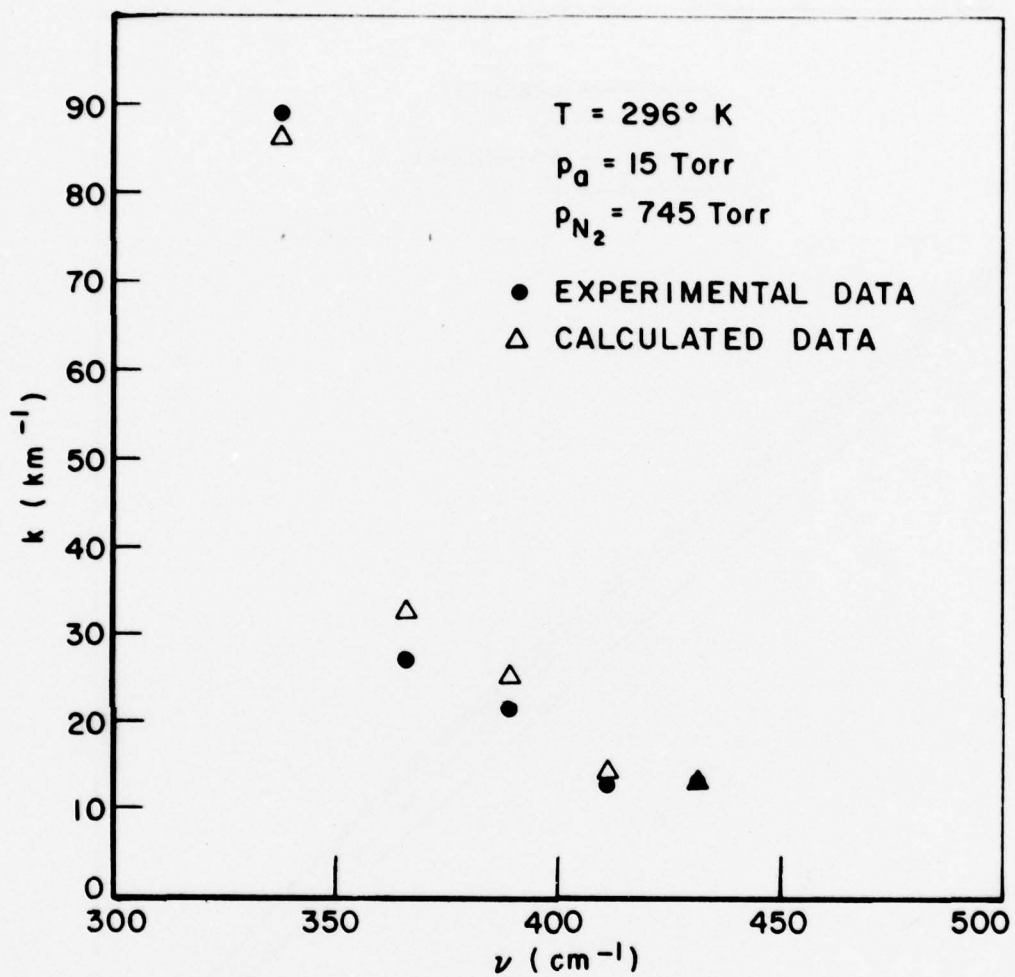


Figure 24. Comparison of experimental and theoretical frequency dependence of the absorption coefficient from 300 cm^{-1} to 440 cm^{-1} .

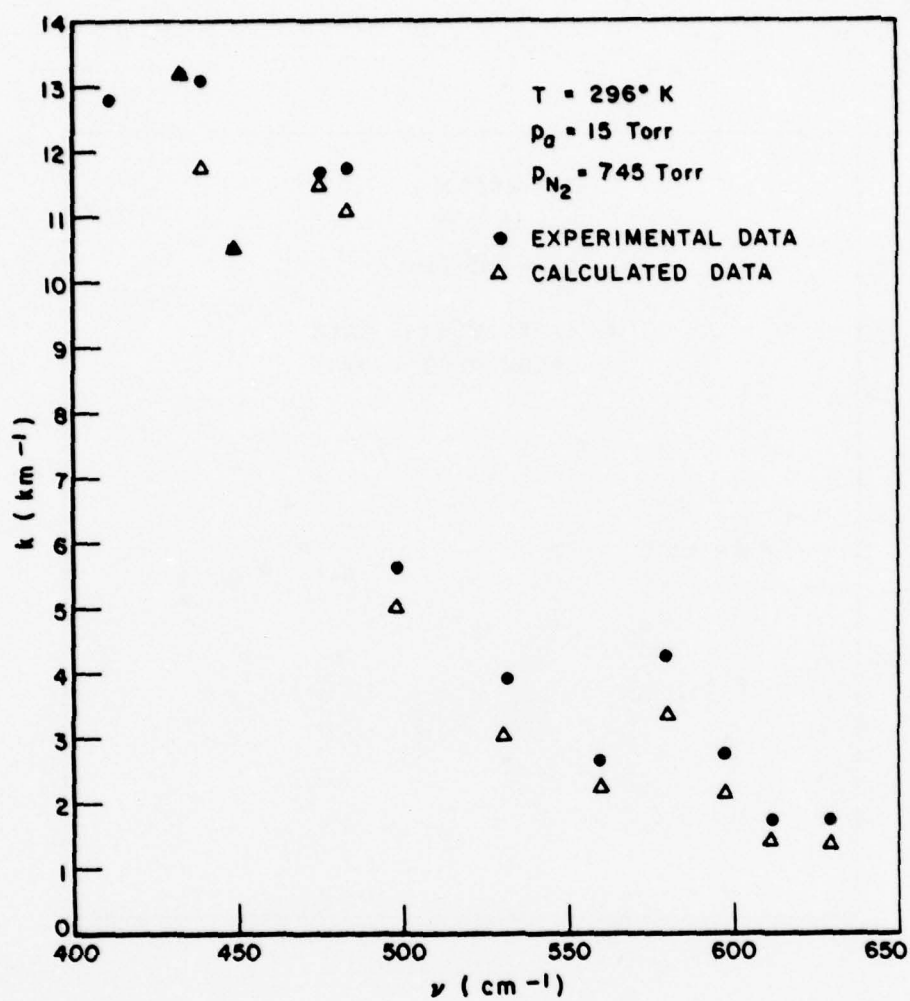


Figure 25. Comparison of experimental and theoretical frequency dependence of the absorption coefficient from 400 cm^{-1} to 650 cm^{-1} .

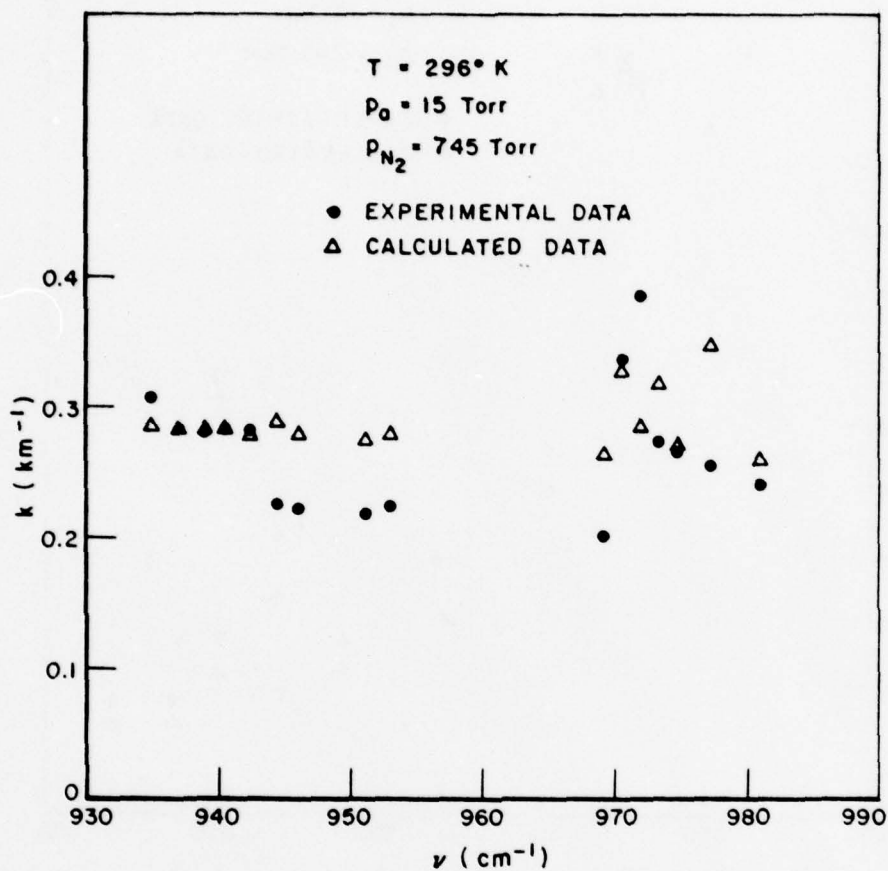


Figure 26. Comparison of experimental and theoretical frequency dependence of the absorption coefficient from 930 cm^{-1} to 990 cm^{-1} .

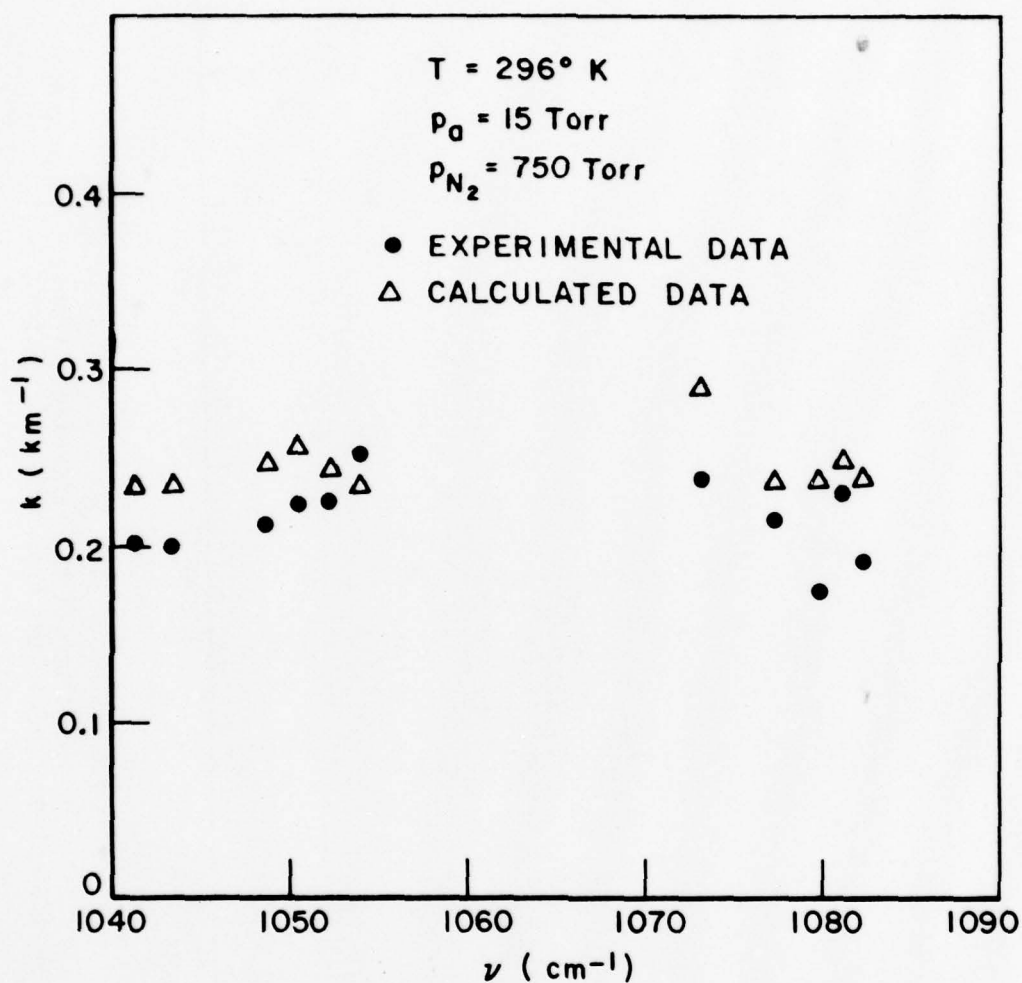


Figure 27. Comparison of experimental and theoretical frequency dependence of the absorption coefficient from 1040 cm^{-1} to 1090 cm^{-1} .

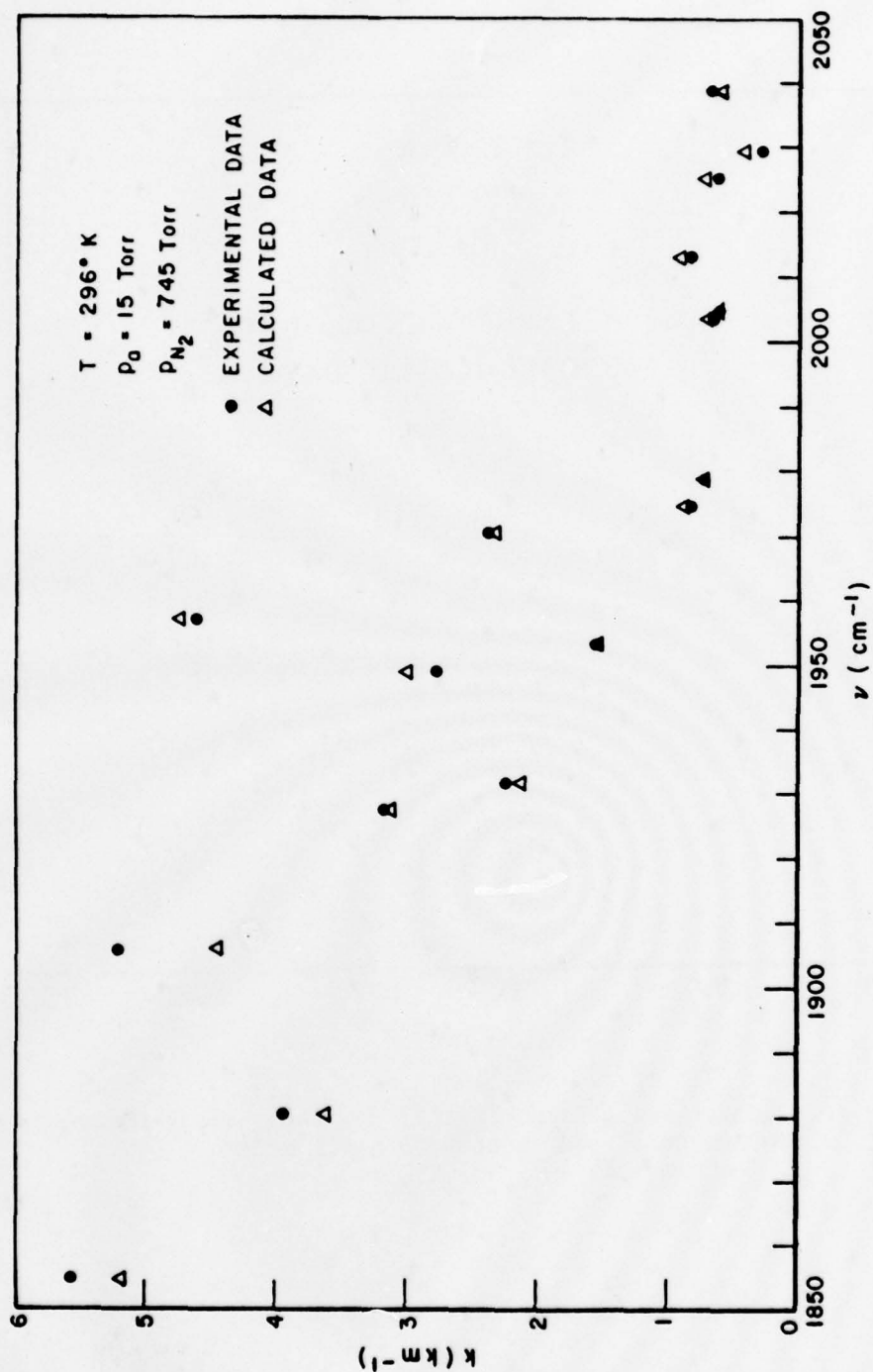


Figure 28. Comparison of experimental and theoretical frequency dependence of the absorption coefficient from 1850 cm^{-1} to 2050 cm^{-1} .

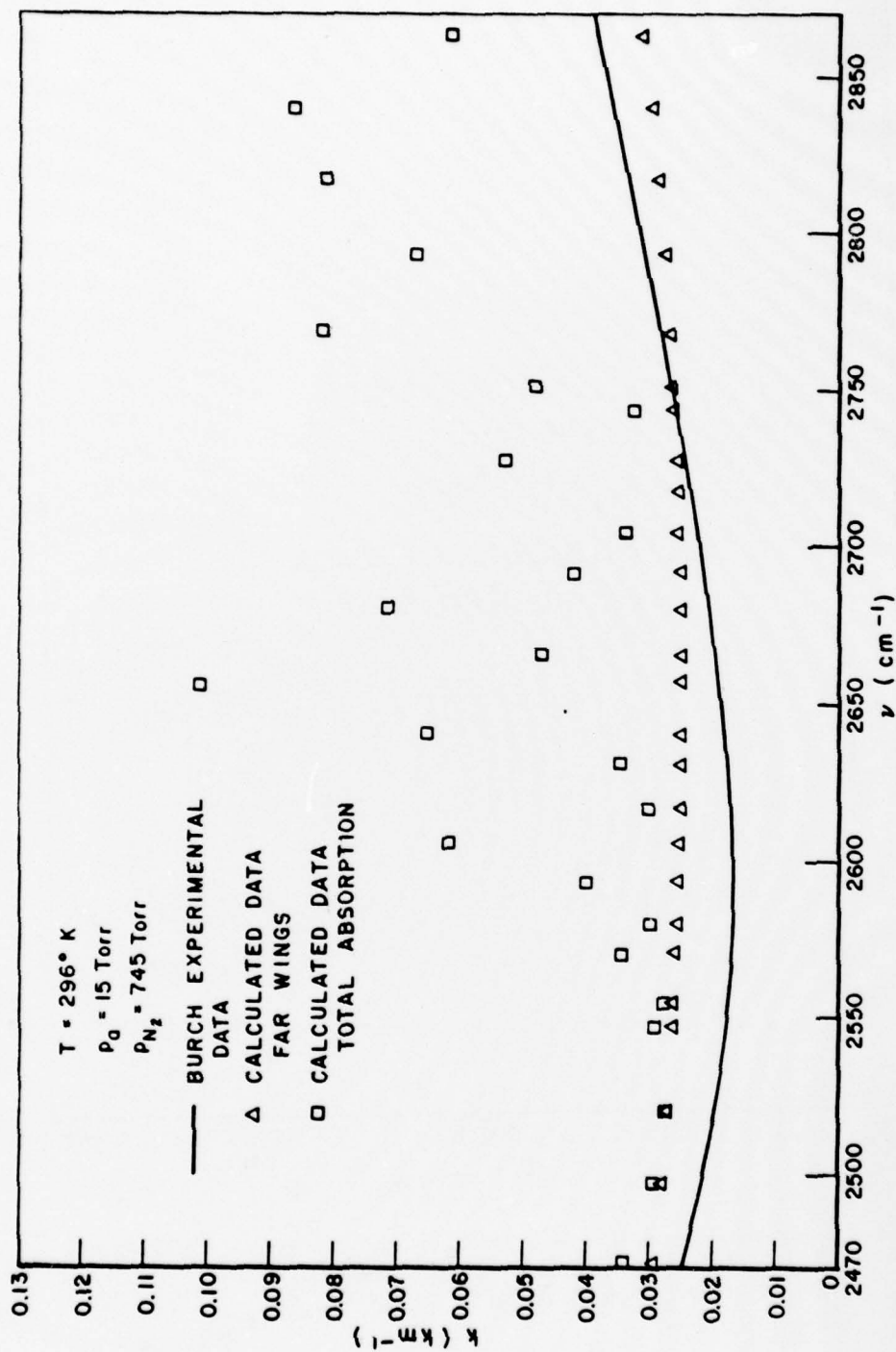


Figure 29. Comparison of experimental and theoretical frequency dependence of the absorption coefficient from 2470 cm^{-1} to 2870 cm^{-1} .

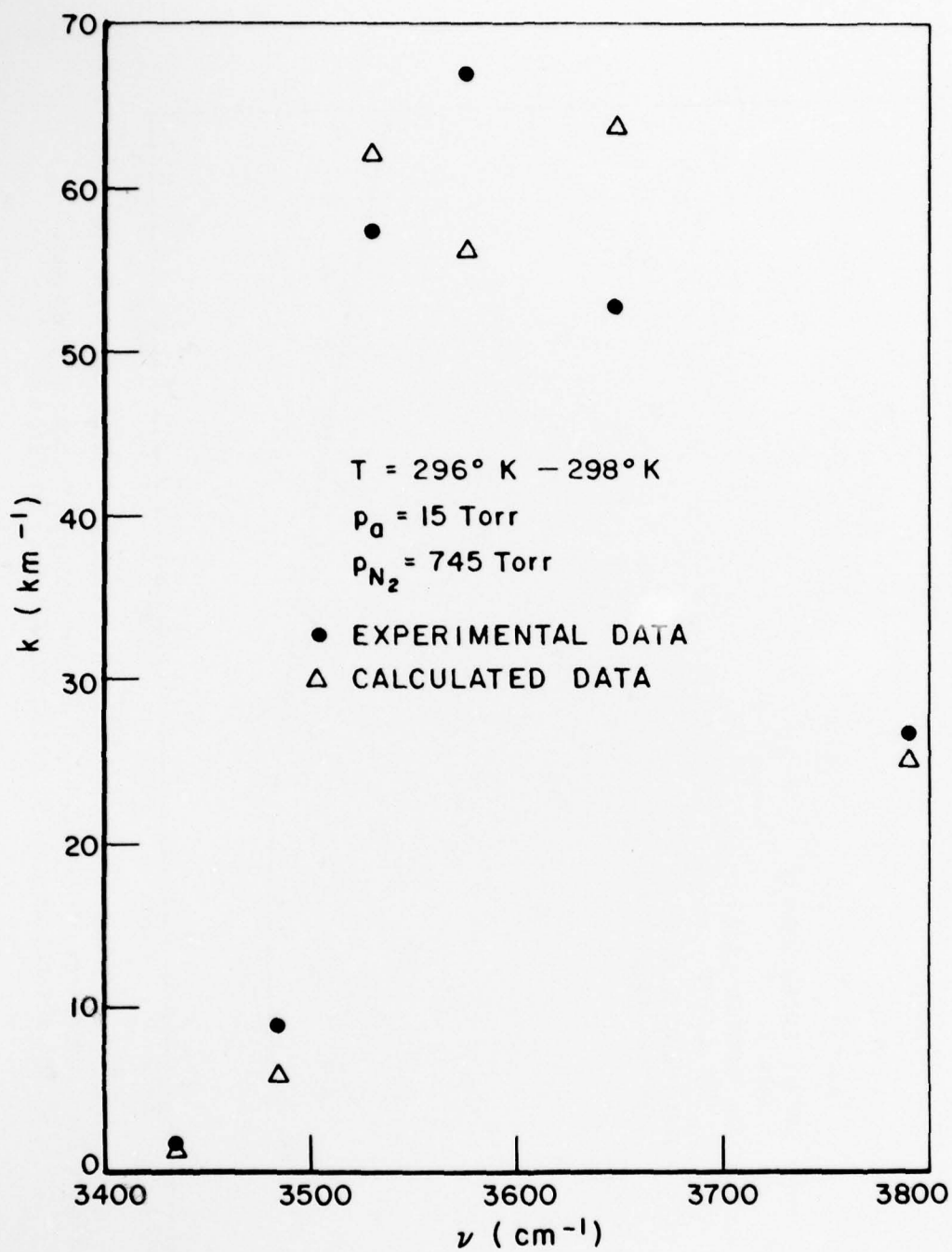


Figure 30. Comparison of experimental and theoretical frequency dependence of the absorption coefficient from 3400 cm⁻¹ to 3800 cm⁻¹.

the consideration of pressure shifts. This effect is described in Chapter II, Section D (see Equation (126)). The pressure or line shift is similar to the halfwidth (pressure and temperature dependence) except smaller in magnitude. In fact line shifts are usually ignored because it is a small effect. However even a small change in line position of a local absorption line can have significant effects on the absorption characteristics at a monochromatic frequency. This is especially true if the probe frequency is within two halfwidths of the line center position. This condition is quite often satisfied in the near band regions.

Figure 29 illustrates the 4 μm window region. The calculated data points are of two types. One set represents the total amount of absorption, local line and far wing contributions. The other set represents only far wing absorption. Comparison to experimental measurements by Burch [15] is made showing reasonable agreement with the far wing calculations. Since Burch made measurements where local line contributions were minimal, only far wing contributions are represented. Table 5 compares experimental DF laser measurements by Mills [77] to calculations using the total line shape of this study. The measurements include local line contributions and the modeling agrees quite well in every case. The DF laser measurements [24] listed in Table 3 are generally higher than measurements made by Burch and Mills. A comparison between the measurements of Burch and ASL is made in Figure 3. As emphasized in Chapter III, White cell measurements in this region are very difficult and discrepancies between experimenters are expected. However, the measurements by Burch and Mills and the far wing calculations show good consistency.

Table 5

Comparison of DF laser measurements by Mills
to the total line shape calculations.

$T = 296 \text{ K}$ $p_a = 14.3 \text{ Torr}$ $P_{N_2} = 745.7 \text{ Torr}$

ν	Calculated (km^{-1})	Mills (km^{-1})
2546.373	.027	.031
2570.522	.032	.035
2594.197	.037	.057
2631.066	.033	.038
2655.863	.103	.103
2680.178	.067	.075

The water vapor partial pressure dependence of the absorption coefficient is characterized by the magnitude of B in Equation (193). For B small (5-10) the linear term will dominate and for B large (100-200) the quadratic term will dominate. The curves of the absorption coefficient versus water vapor partial pressure can vary from linear to parabolic. Using the far wing formula of the total line shape (Equation (182)) an expression for B can be obtained

$$B = \frac{.3198}{.4334} \frac{A_1(\nu)}{A_2(\nu, J)} \left(\frac{296}{T}\right)^{.5} \exp((G_{b4} - G_{a6})\sqrt{\Delta\nu}) (\Delta\nu)^{1/4}. \quad (196)$$

Figure 31 shows a plot of B versus $\Delta\nu$ for the different bands.

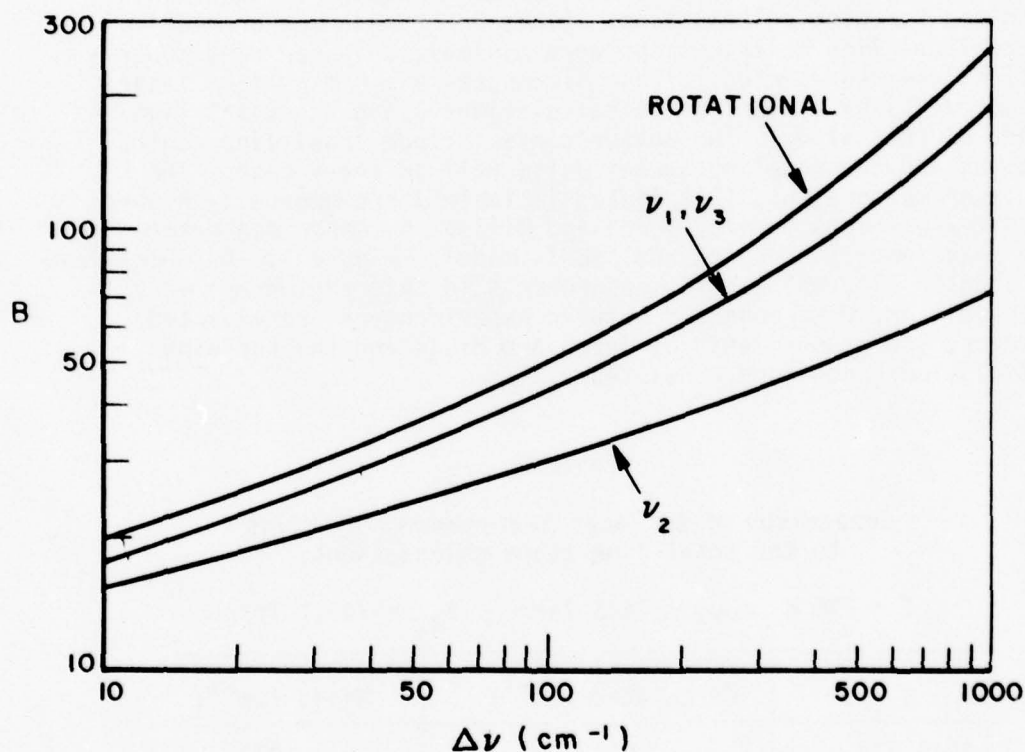


Figure 31. Frequency dependence of the self-broadening coefficient for the different bands.

Notice that the choice of the "A" and "G" parameters has produced larger B values for the rotational and ν_1, ν_3 bands than the ν_2 band. This feature is consistent with what is observed in liquid water spectra.

Since liquids are composed of closely spaced molecules (relative to a gas) the nature of the collisions will always be in the statistical domain. Thus liquid spectra provide an opportunity to examine general features of the statistical line shape as well as the physics of close collisions. Figure 32 is a plot of a liquid water spectrum from 800 to 4800 cm^{-1} . It shows the corresponding fundamental bands of the gas phase, the ν_2 bending mode and ν_1, ν_3 stretching modes. Two other vibrational bands also appear. The librational band, ν_2 , around 800 cm^{-1} on the plot is caused by the hindered rotational motion of the H_2O molecules [34]. The association band, ν_A , at 2050 cm^{-1} is caused by the hindered translational - rotational motion of the H_2O molecules [34]. The perturbation of the rotational motion of H_2O is represented by the average over orientations $\langle \nu \rangle_{\text{rot}}$ as discussed in Chapter II, Section B. It is clear from the H_2O liquid spectrum that this is an important consideration. Further the band strength of the ν_1, ν_3 band is significantly larger than the ν_2 band as opposed to the gas phase where they are more nearly equal. This suggests that strong collisions perturb the stretching motion of H_2O more than the bending motion. This fact explains the different magnitudes of B for the ν_2 and ν_1, ν_3 bands in the statistical wing. The rotational band is also greatly perturbed by the strong collisions and therefore has large B values similar to the ν_1, ν_3 bands.

Table 3 lists experimental B values at many frequencies. Notice that as the frequency increases away from the rotational and ν_2 bands B increases as one would expect. At 337.9 cm^{-1} B is 10.5 then increases to 200-300 in the 10 μm window. The fluctuation in B indicated by Table 3 to small values at unexpected frequencies can be explained by local line effects. Since near line center B is 5 this will decrease the effective B that is observed. Notice also that in the 4 μm window region B is lower on the side closest to the ν_2 band. This is consistent with the observation that B will be smaller for ν_2 band than the ν_1, ν_3 bands.

As an example the effective value of B determined from least squares fitting calculated points to Equation (193) for the 00⁰₁-10⁰₀ P(20) laser line position is 123. This number represents a weighted average of B values from many absorption lines. The major contributing lines from the rotational band are centered around 200 cm^{-1} and therefore from Figure 31 the B value for these lines is approximately between 170 and 200. The resulting B value is less than this because of contributions from the ν_2 band (see Figure 31) and local lines which have smaller B values.

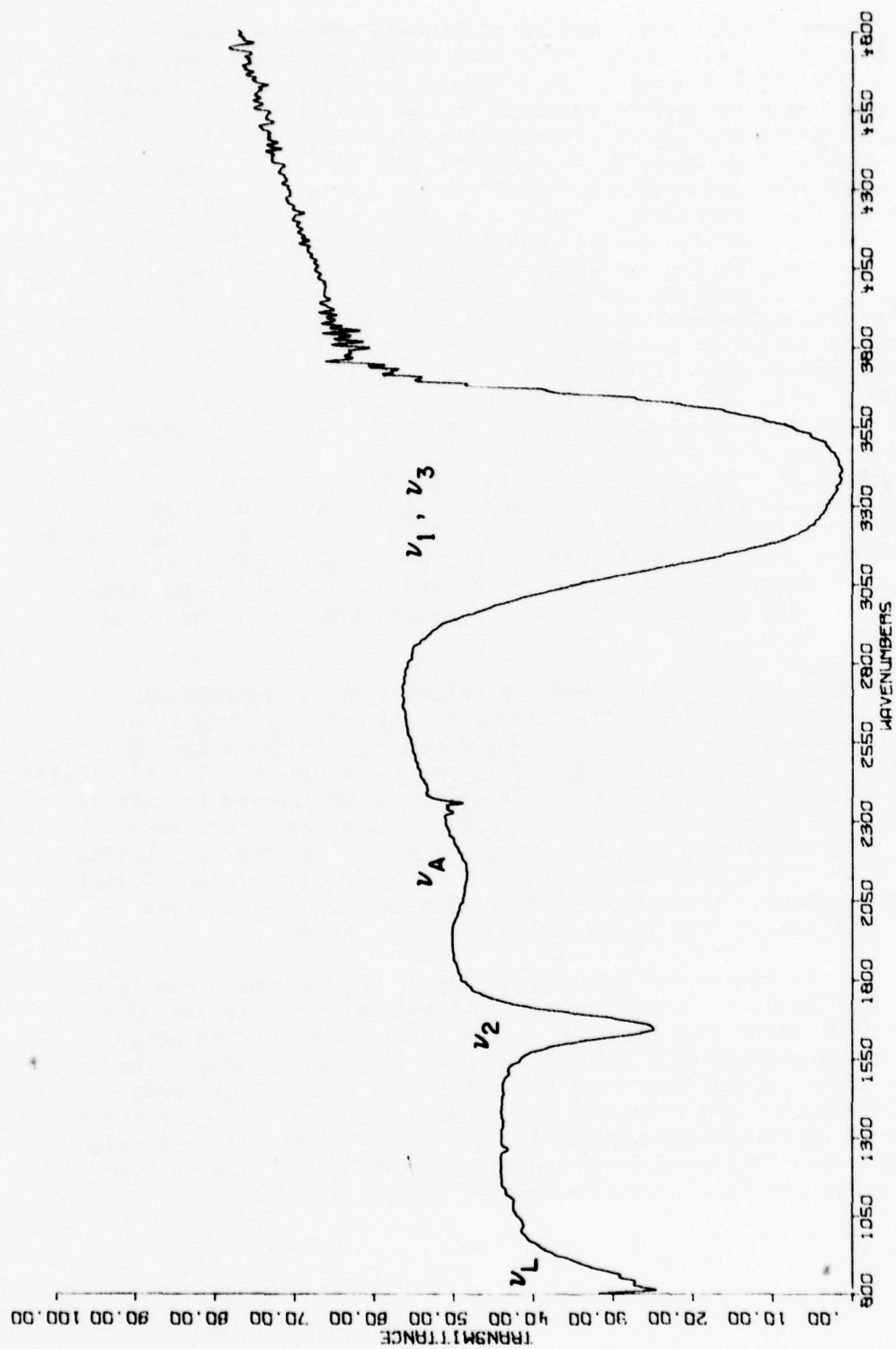


Figure 32. Liquid water spectrum (8 cm⁻¹ resolution).

The success of the model in predicting the proper water vapor partial pressure dependence of the absorption coefficient is demonstrated by Figures 33 thru 46. The plots are of nitrogen-broadened water vapor absorption at 296⁰K and 760 Torr total pressure. The solid curve is the theoretical prediction and the boxes are experimental data points. The frequency of the absorption is labeled on each plot. The frequency locations selected for the plots have good magnitude agreement between theory and experiment emphasizing the models ability to predict the pressure dependence.

The millimeter and submillimeter spectral regions in the troposphere also exhibit continuum absorption [78]. The total line shape model should also work in this region. Figures 47 thru 49 represent window absorption at millimeter frequencies. The solid curves are theoretical calculations and the squares are experimental data points taken from Bastin [78]. The lack of experimental data in this region makes it impossible to characterize this region more completely. The model predicts the absorption magnitude fairly well at 7.667 cm⁻¹ but shows increasing relative absorption as the frequency decreases. This general trend can be caused by improper frequency dependence of the rotational band red wing as it goes to 0 cm⁻¹. A strong candidate for this problem is the symmetric structure of the statistical line shape (Equation (169)). The asymmetry of distortion of a low lying rotational energy level in a vibrational potential well should produce an asymmetric line shape. The total line shape model used in this study does not account for this.

3. Temperature dependence

The temperature dependence of continuum absorption has been a difficult problem. As pointed out in Figure 14 close collisions which generate the far wings violate the approximation made on the interaction potential. Thus it can be expected that the temperature dependence in the far wing will not be totally valid. The problem is further complicated for the rotational band far wings because of the breakdown in the perturbation expansion as discussed previously. A correction to the self-broadening coefficient of the rotational band lines is used in the model. However no modification to the temperature dependent factors in the total line shape equations governing the vibrational bands has been used.

Table 5 lists the C_N/RT and B experimental coefficients [73] for the water vapor absorption coefficient at 430 K from 430.0 cm⁻¹ to 629.0 cm⁻¹. The values of B in this frequency region are on the average a factor of 5 smaller than the corresponding B values in Table 3. The temperature dependence of B indicated in Equation (196) does not account for this. Since this region is dominated by far wing behavior and it is recognized that the

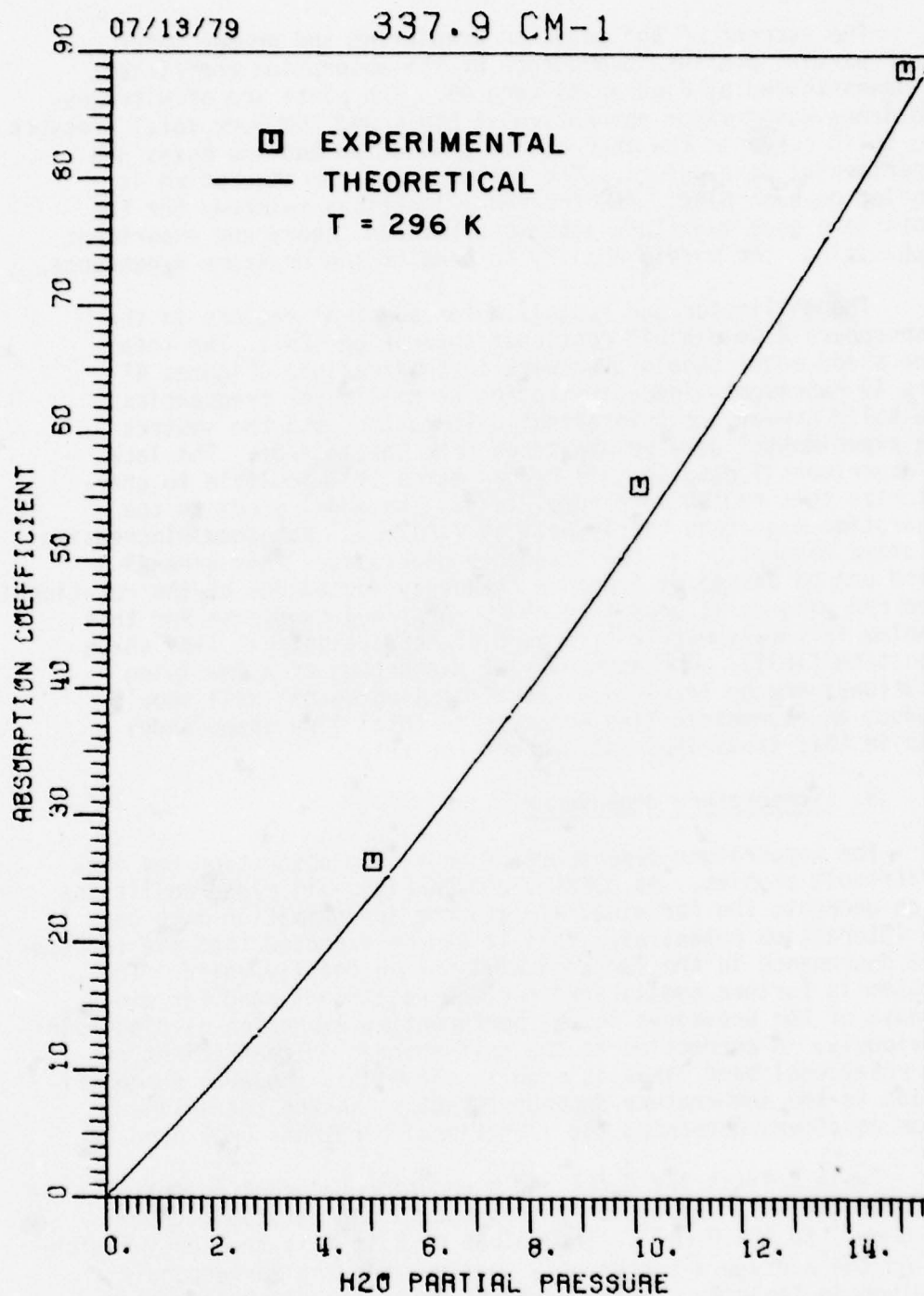


Figure 33. Comparison of experimental and theoretical H_2O partial pressure dependence at 337.9 cm^{-1} .

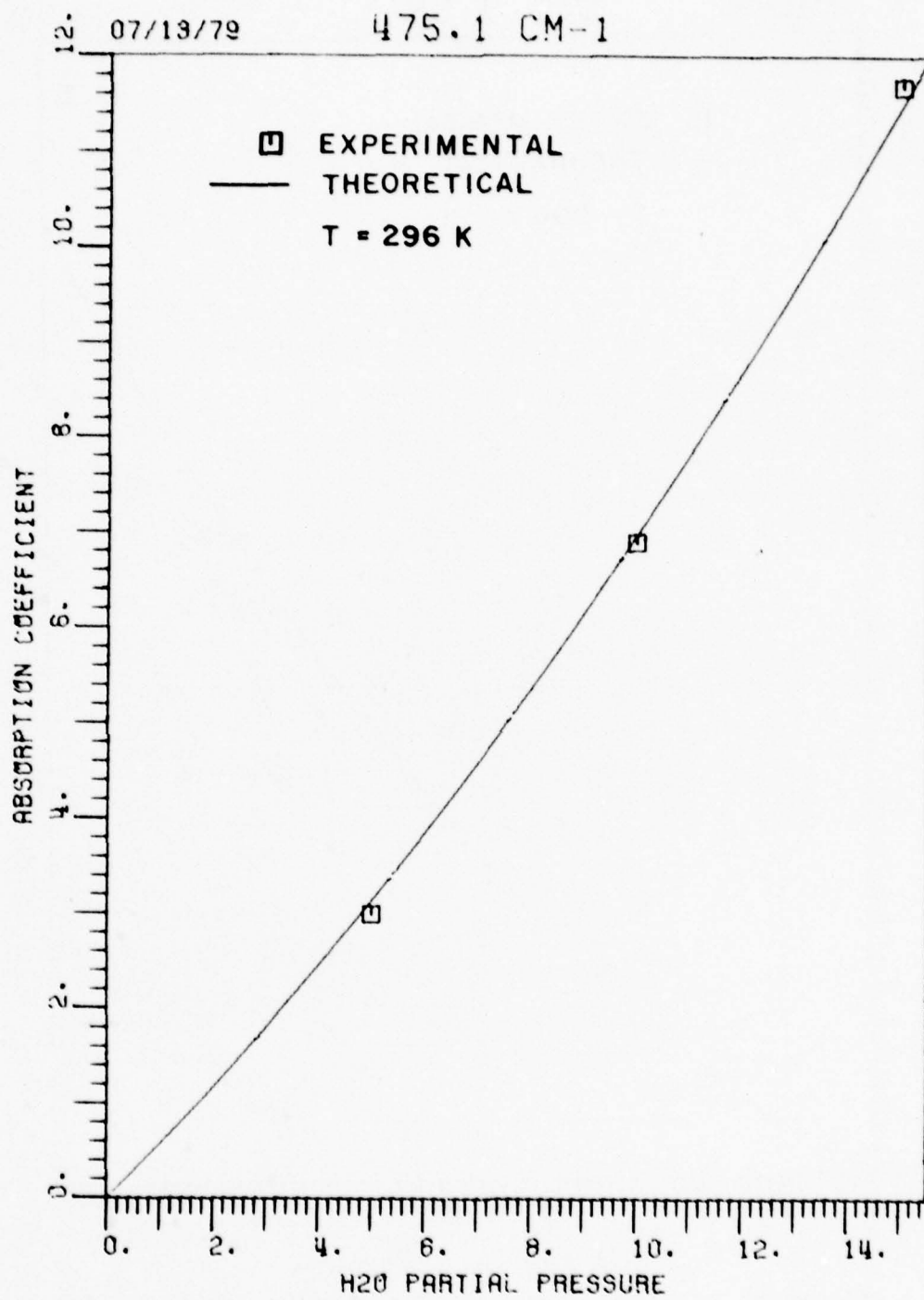


Figure 34. Comparison of experimental and theoretical H₂O partial pressure dependence at 475.1 cm⁻¹.

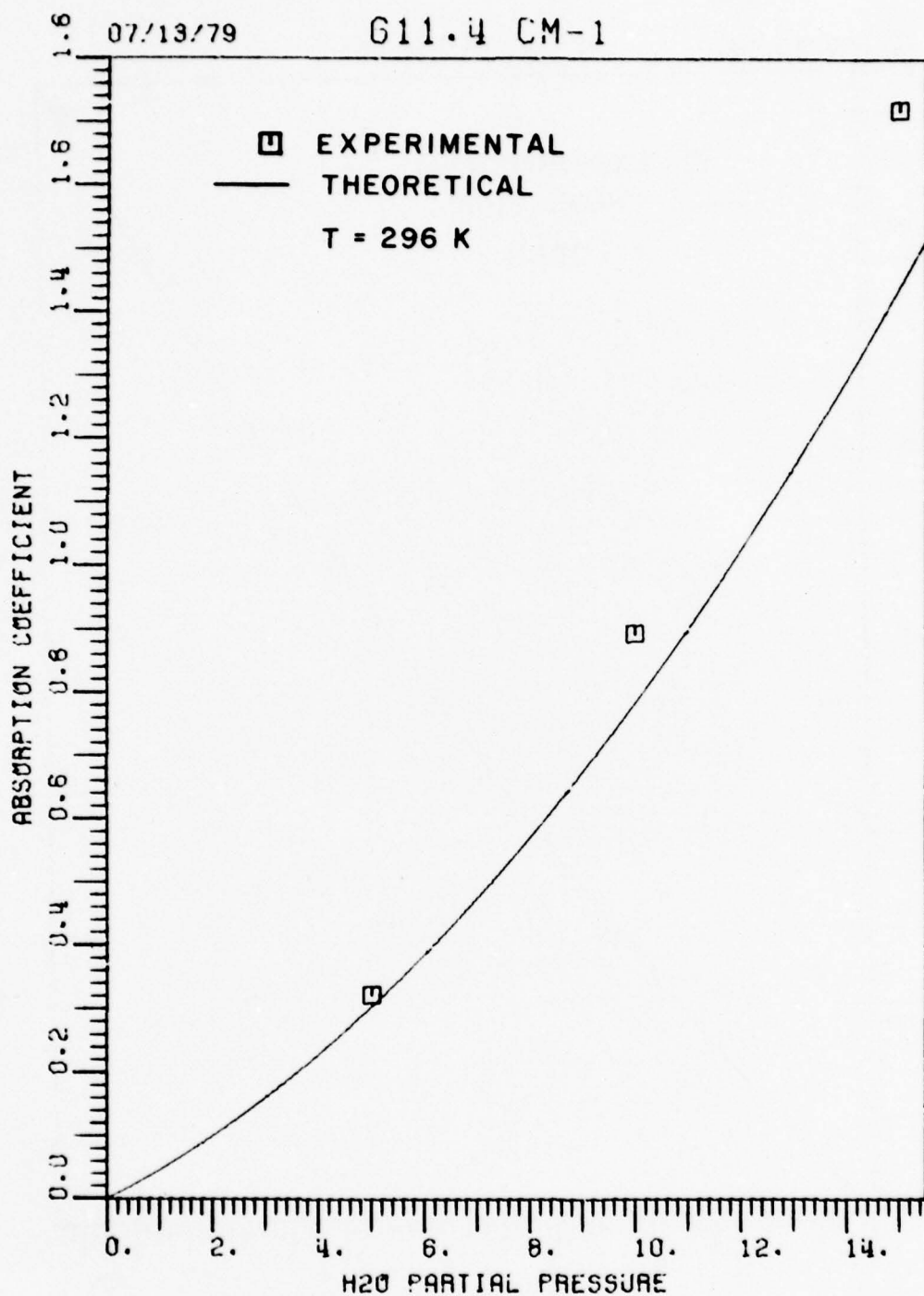


Figure 35. Comparison of experimental and theoretical H₂O partial pressure dependence at 611.4 cm⁻¹.

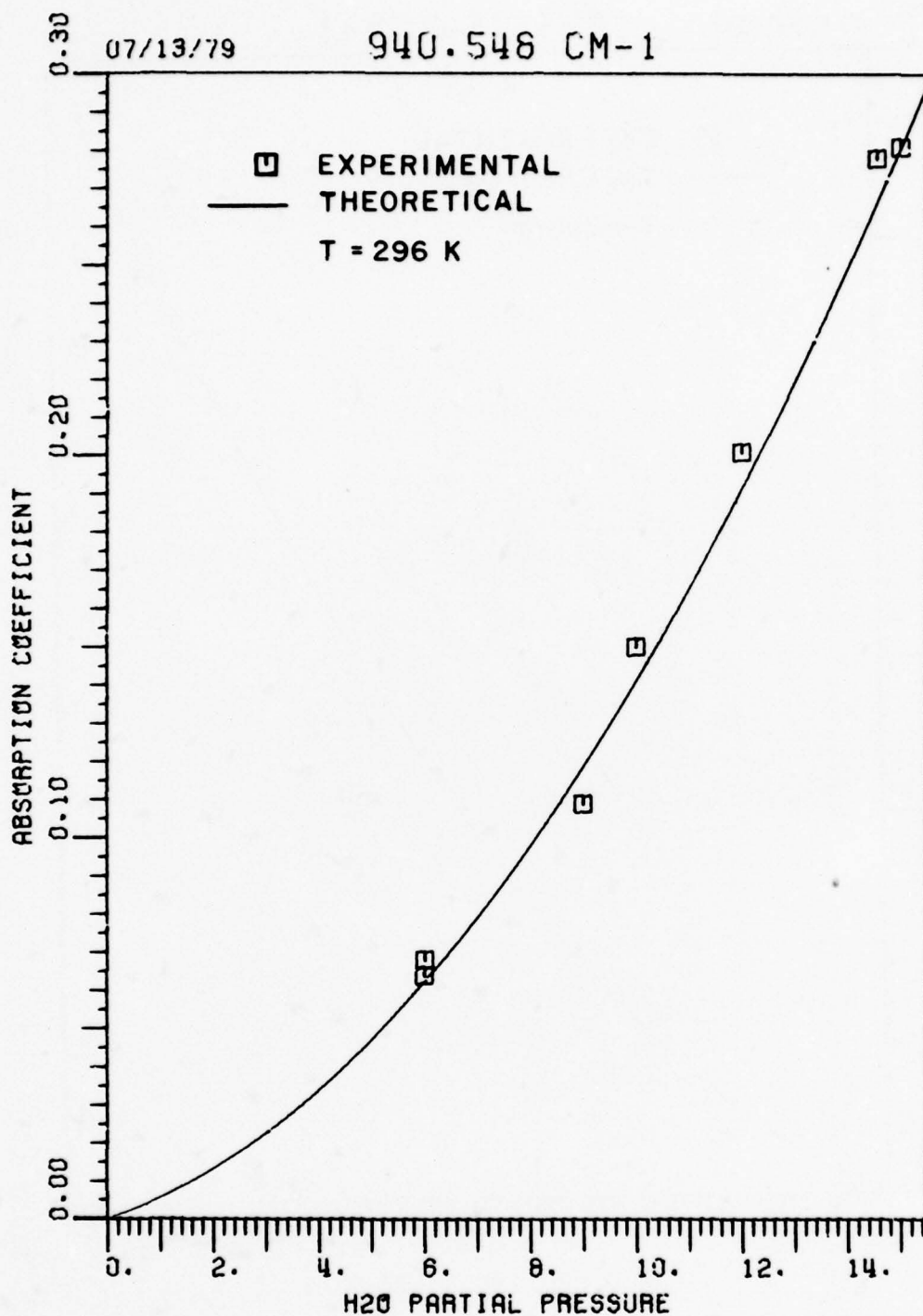


Figure 36. Comparison of experimental and theoretical H₂O partial pressure dependence at 940.548 cm⁻¹.

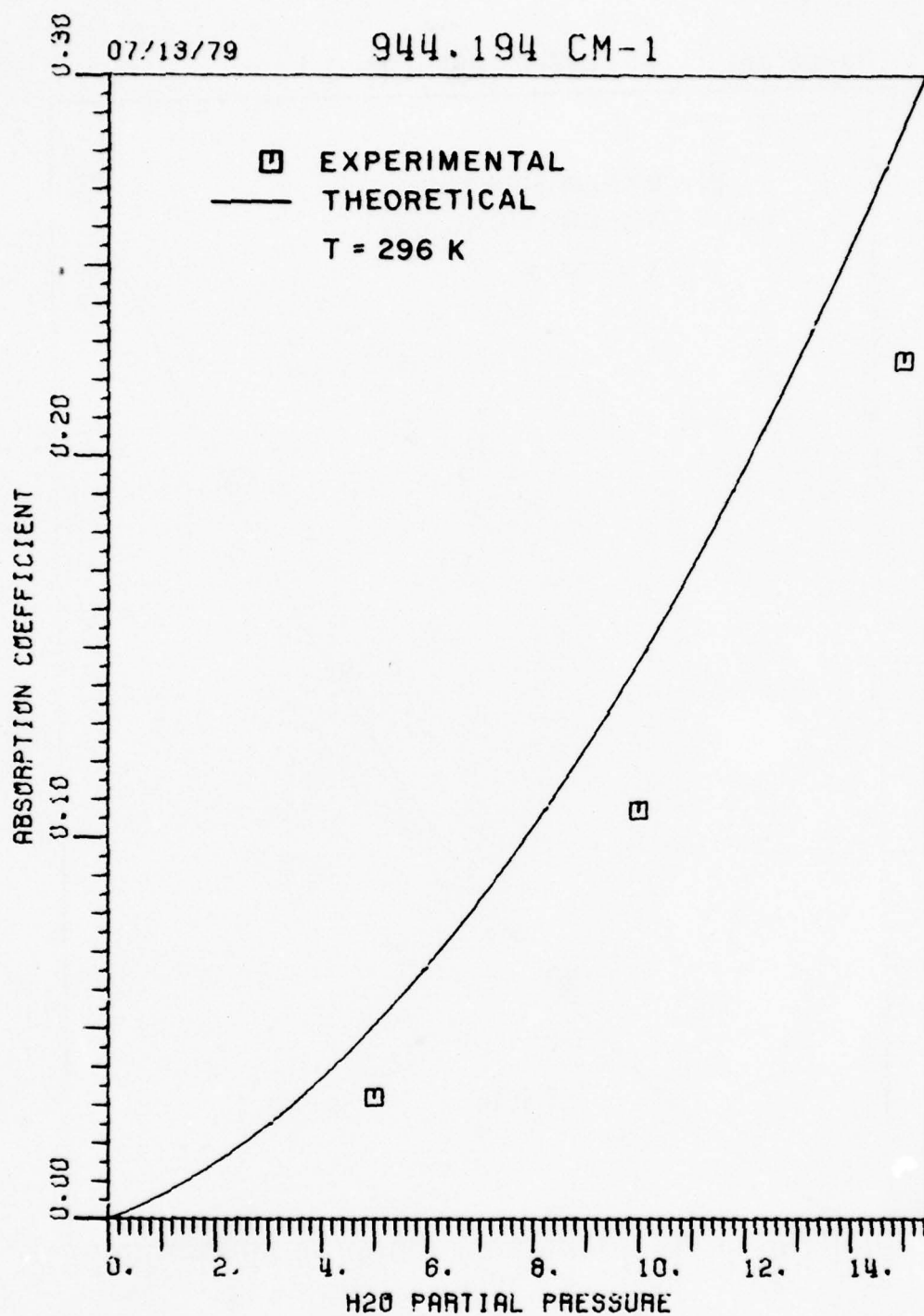


Figure 37. Comparison of experimental and theoretical H₂O partial pressure dependence at 944.194 cm⁻¹.

07/13/79

970.547 CM-1

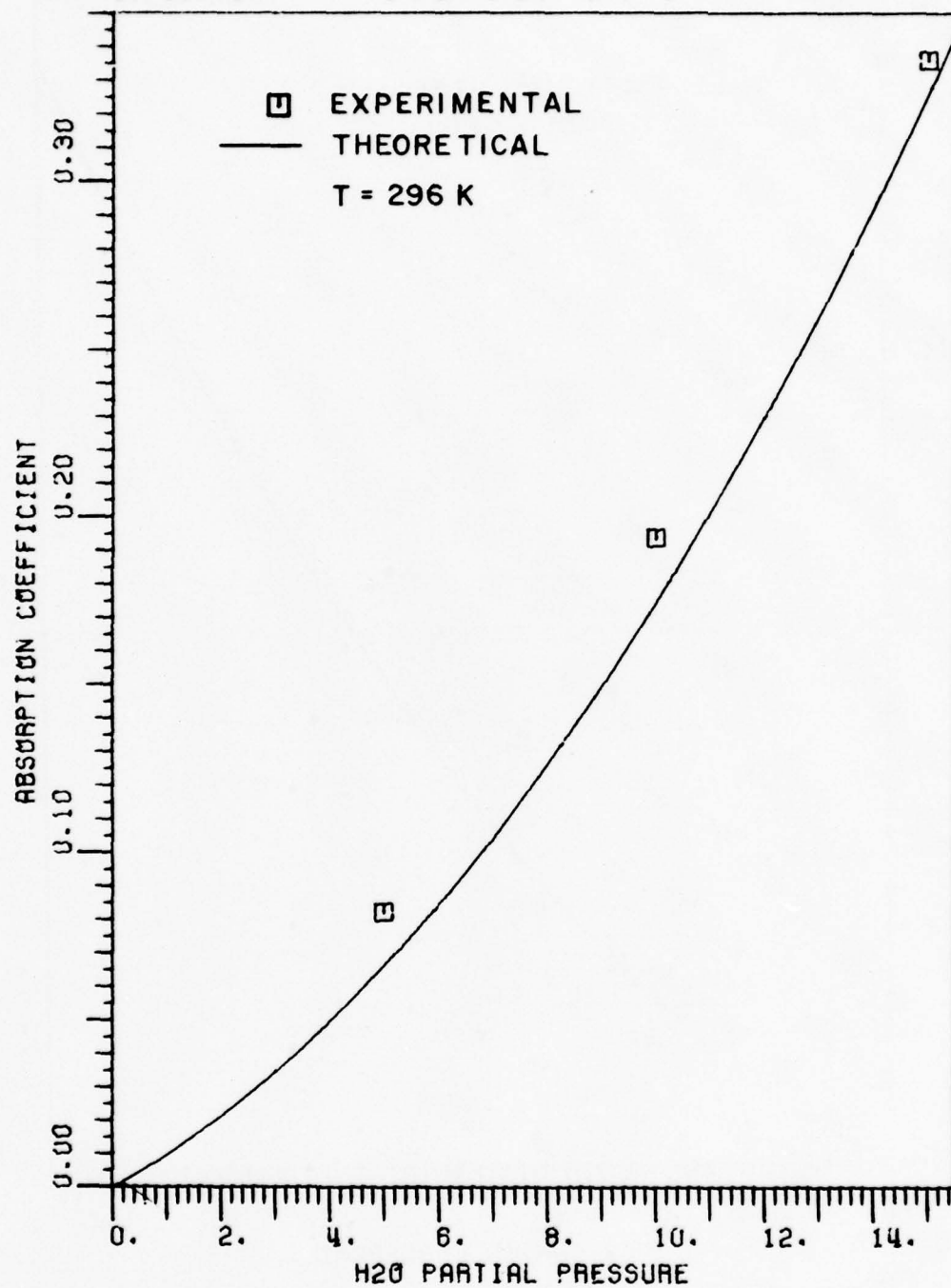


Figure 38. Comparison of experimental and theoretical H_2O partial pressure dependence at 970.547 cm^{-1} .

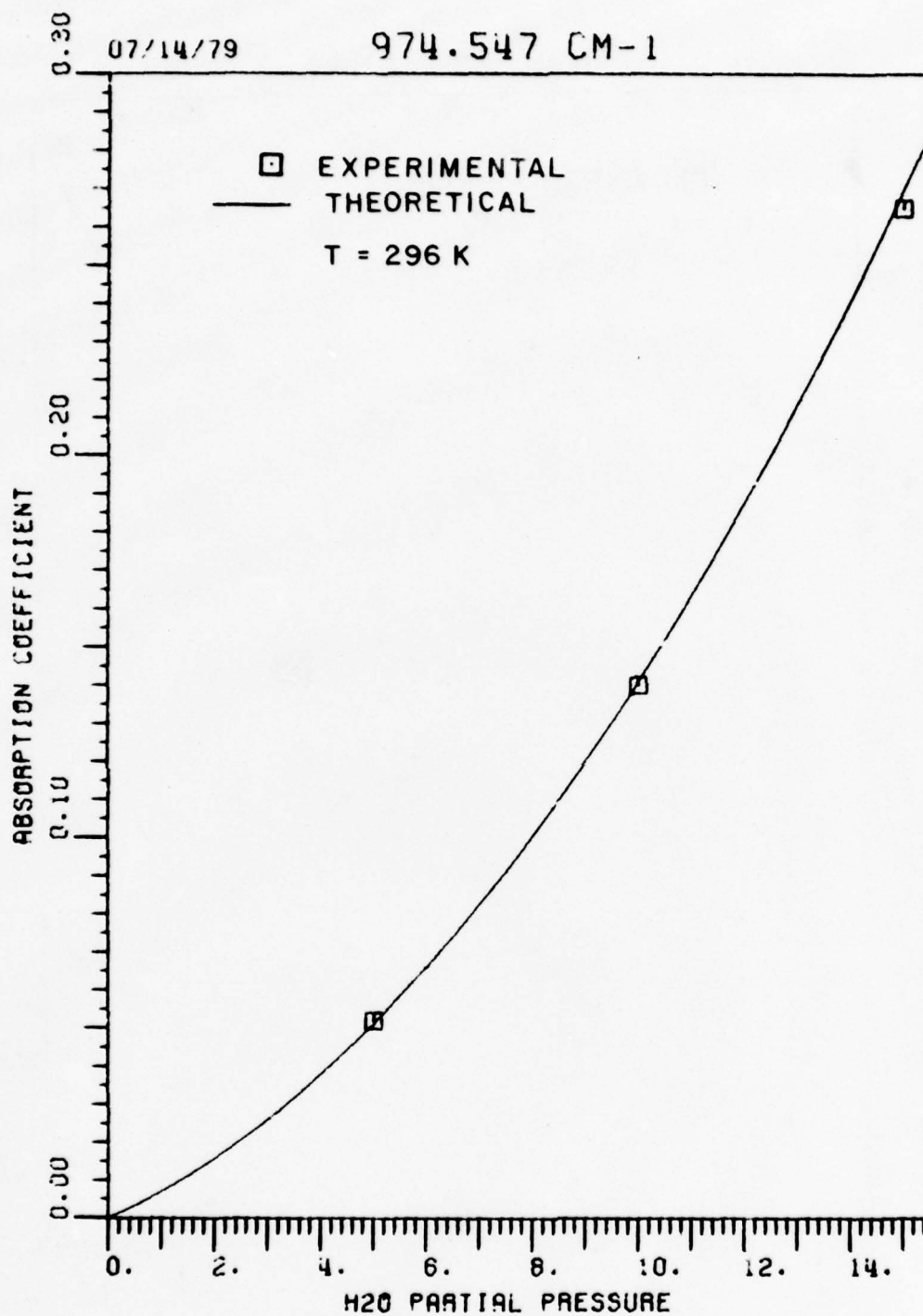


Figure 39. Comparison of experimental and theoretical H₂O partial pressure dependence at 974.547 cm⁻¹.

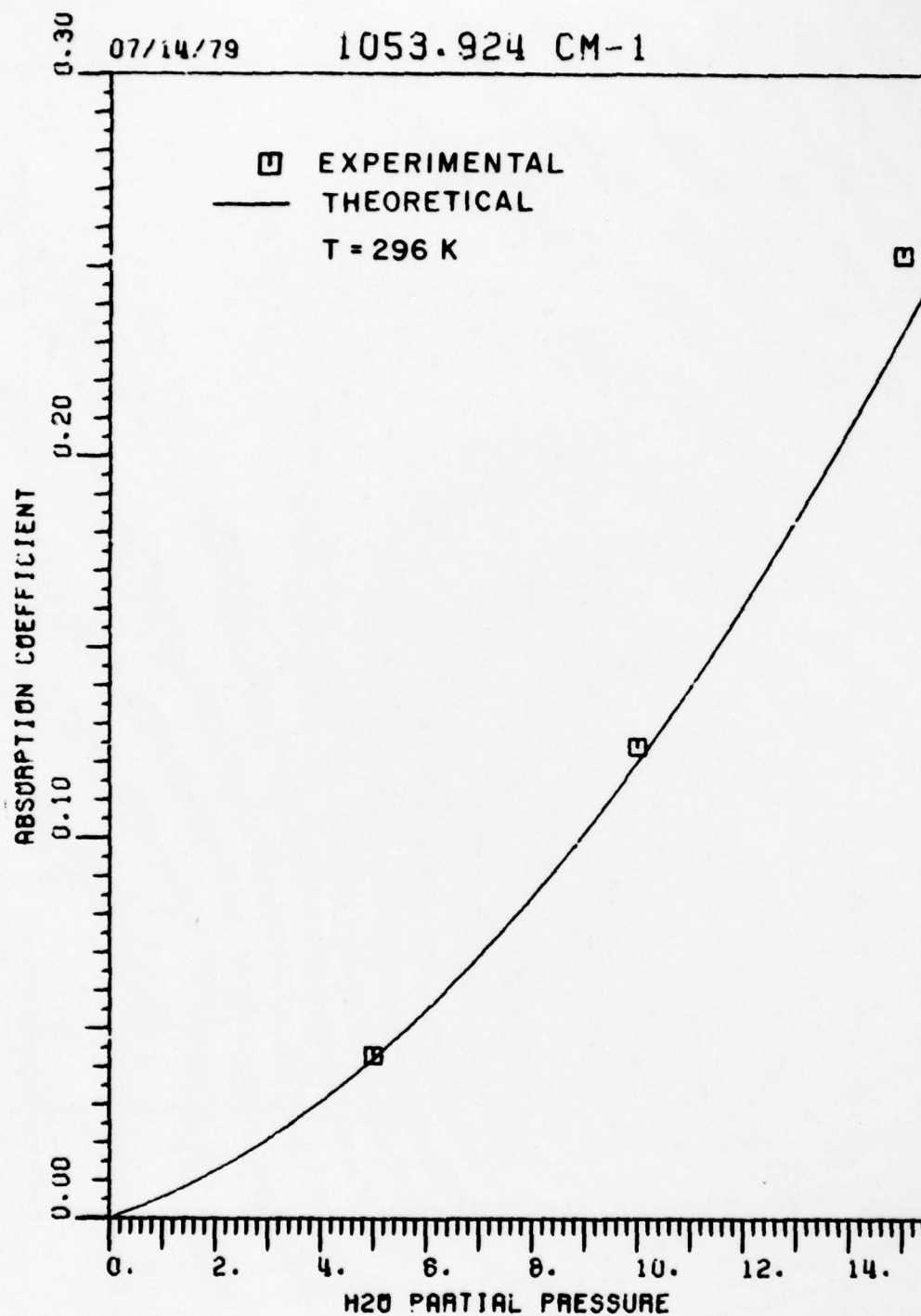


Figure 40. Comparison of experimental and theoretical H₂O partial pressure dependence at 1053.924 cm⁻¹.

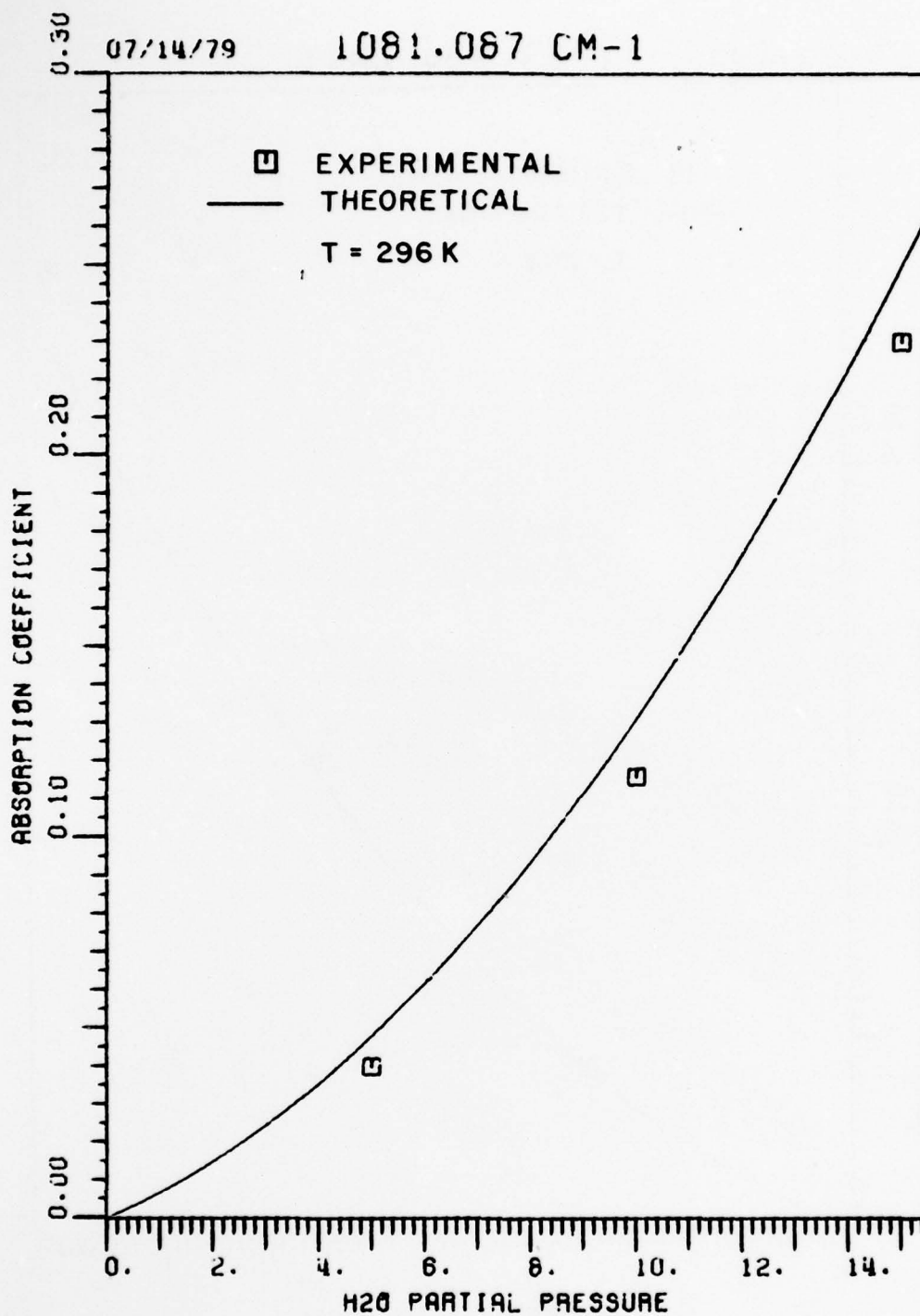


Figure 41. Comparison of experimental and theoretical H₂O partial pressure dependence at 1081.087 cm⁻¹.

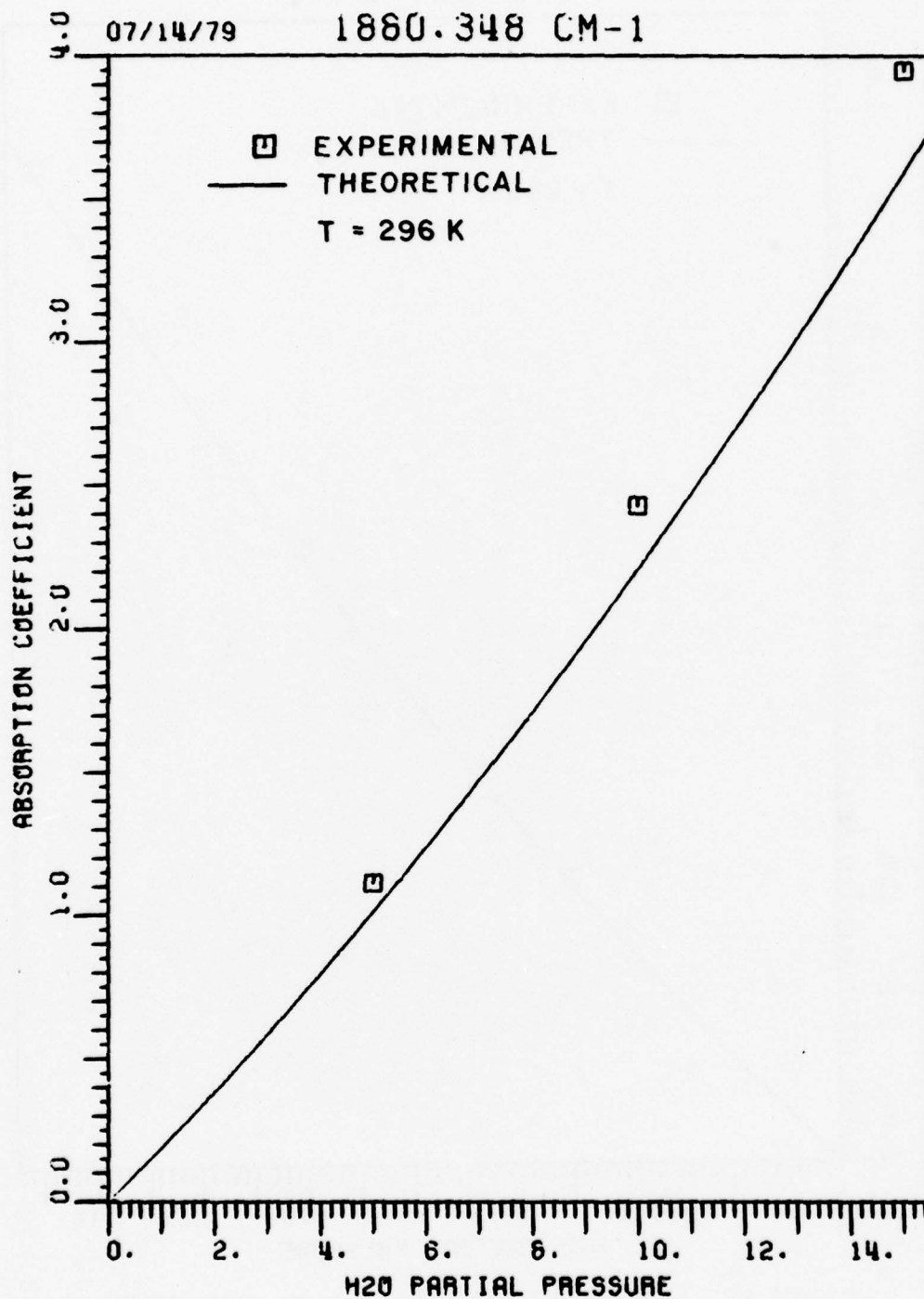


Figure 42. Comparison of experimental and theoretical H₂O partial pressure dependence at 1880.348 cm⁻¹.

07/14/79

1952.907 CM-1

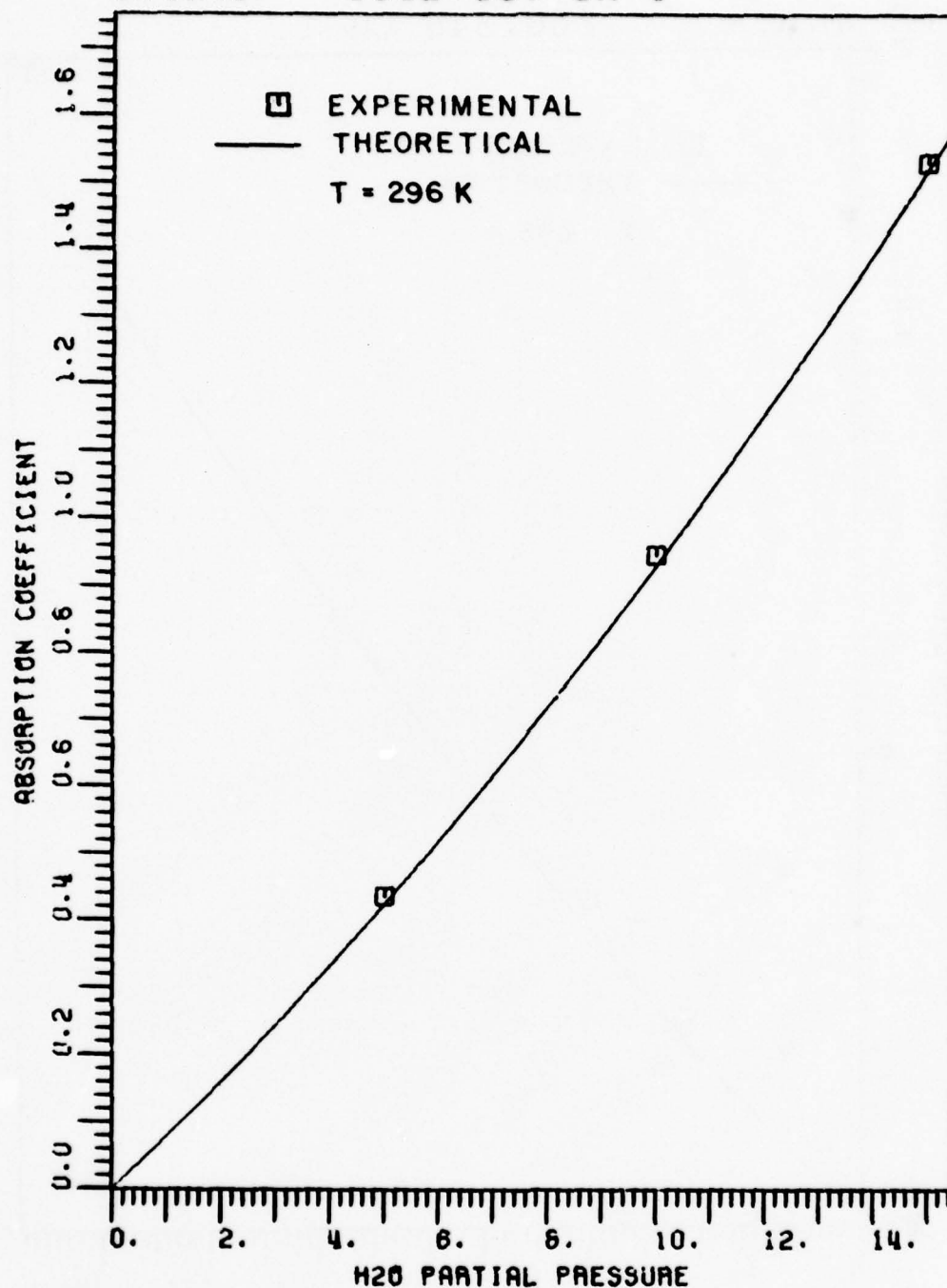


Figure 43. Comparison of experimental and theoretical H_2O partial pressure dependence at 1952.907 cm^{-1} .

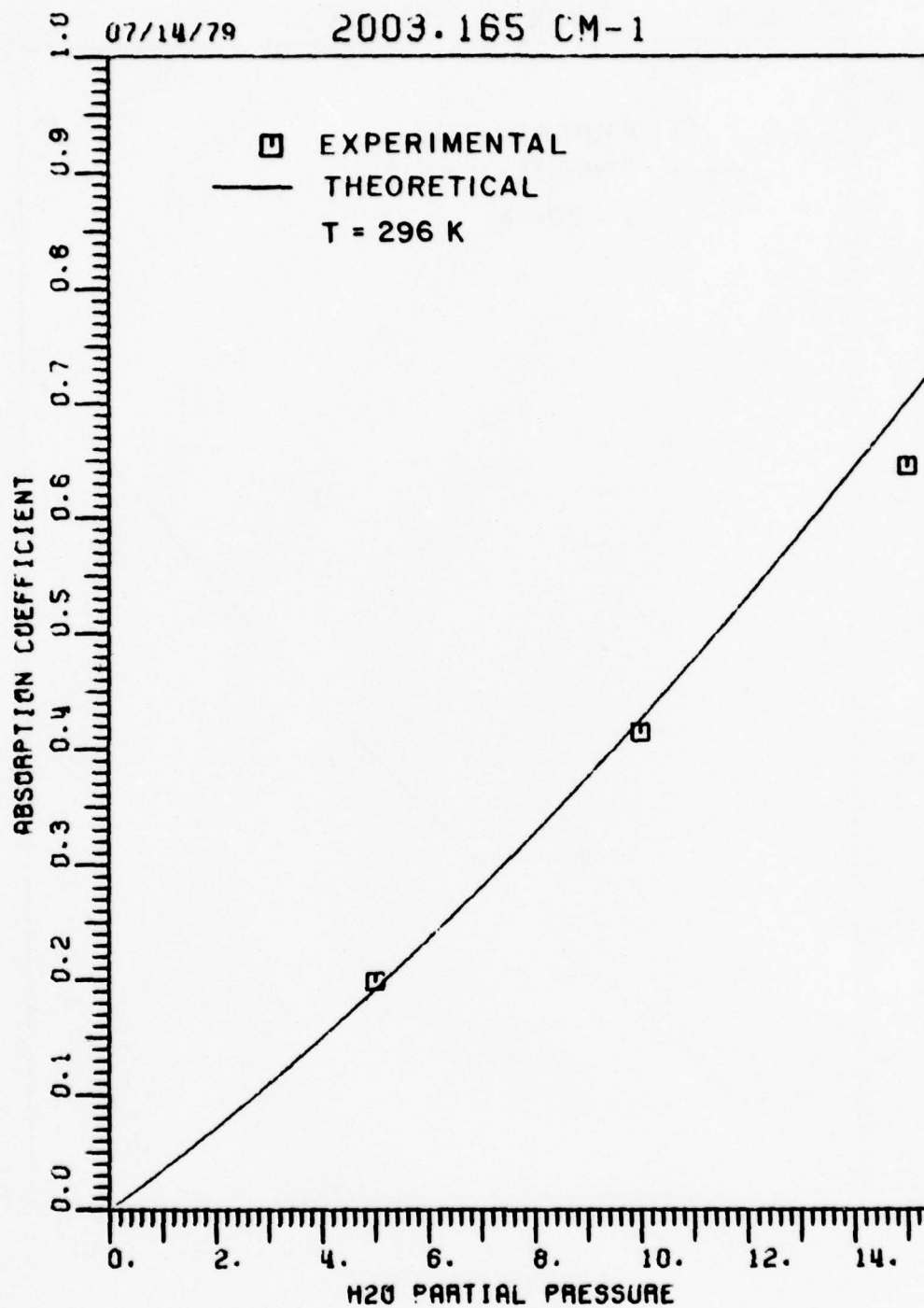


Figure 44. Comparison of experimental and theoretical H₂O partial pressure dependence at 2003.165 cm⁻¹.

07/14/79

3434.9994 CM-1

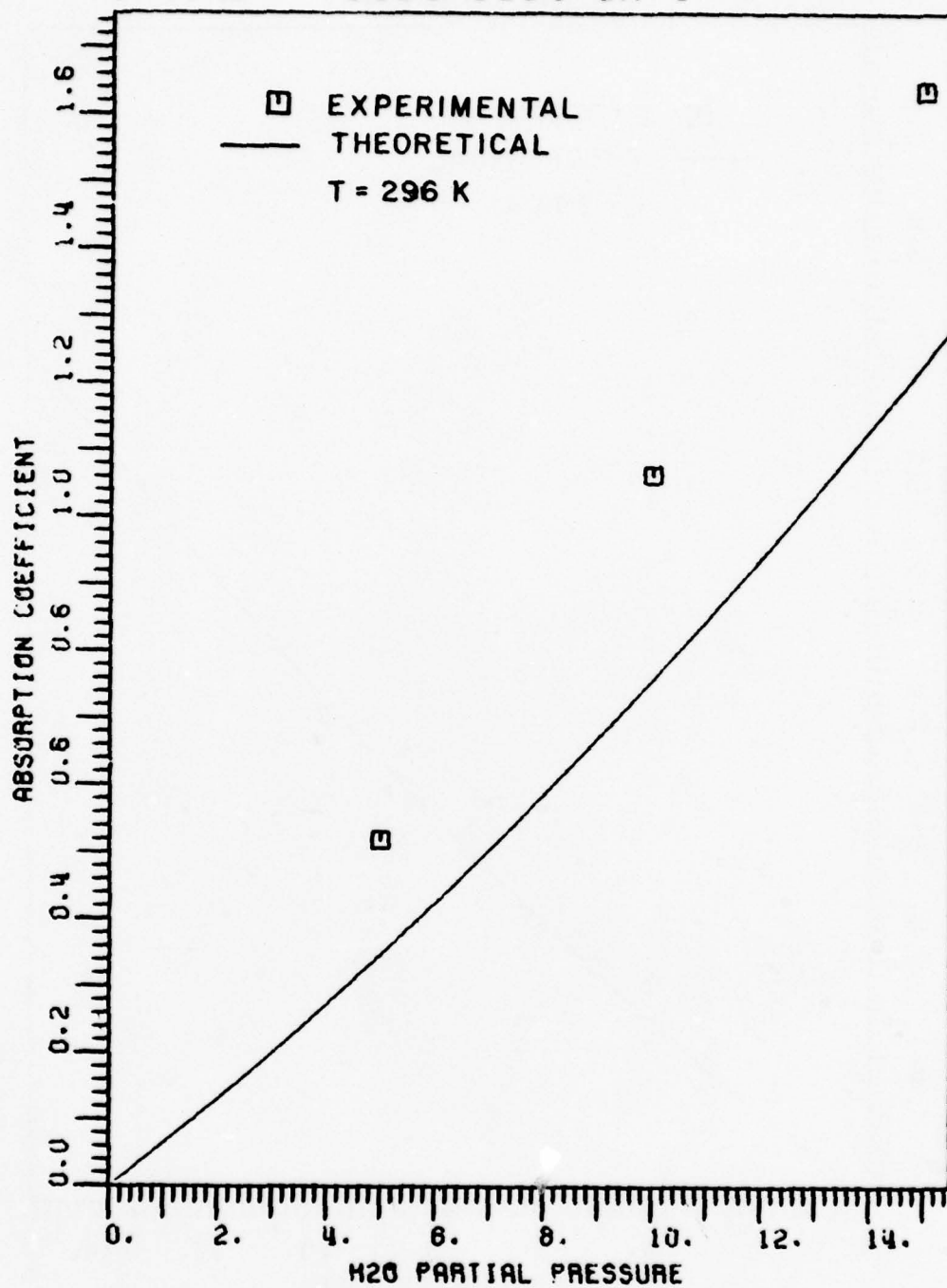


Figure 45. Comparison of experimental and theoretical H₂O partial pressure dependence at 3434.9994 cm⁻¹.

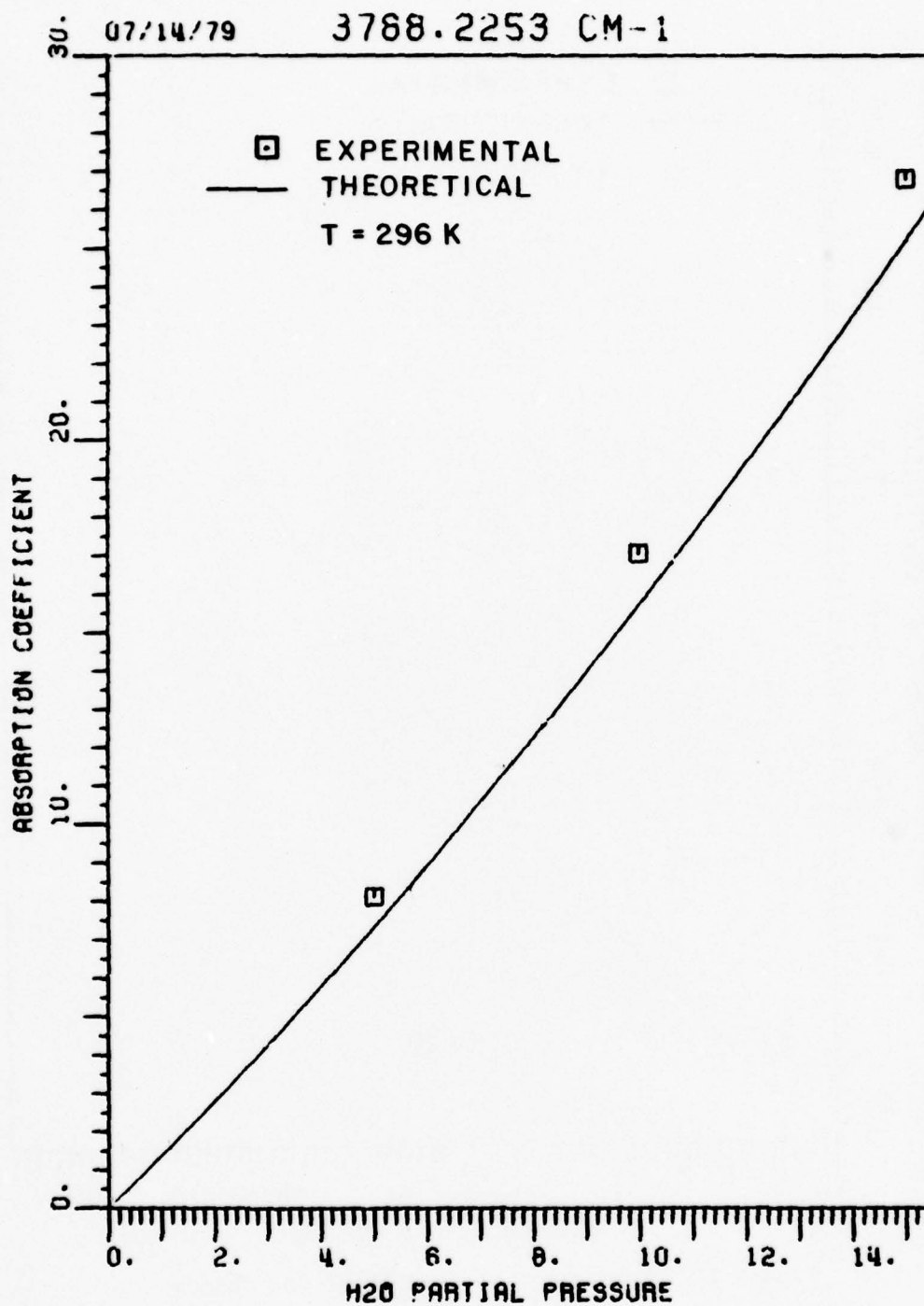


Figure 46. Comparison of experimental and theoretical H_2O partial pressure dependence at $3788.2253 \text{ cm}^{-1}$.

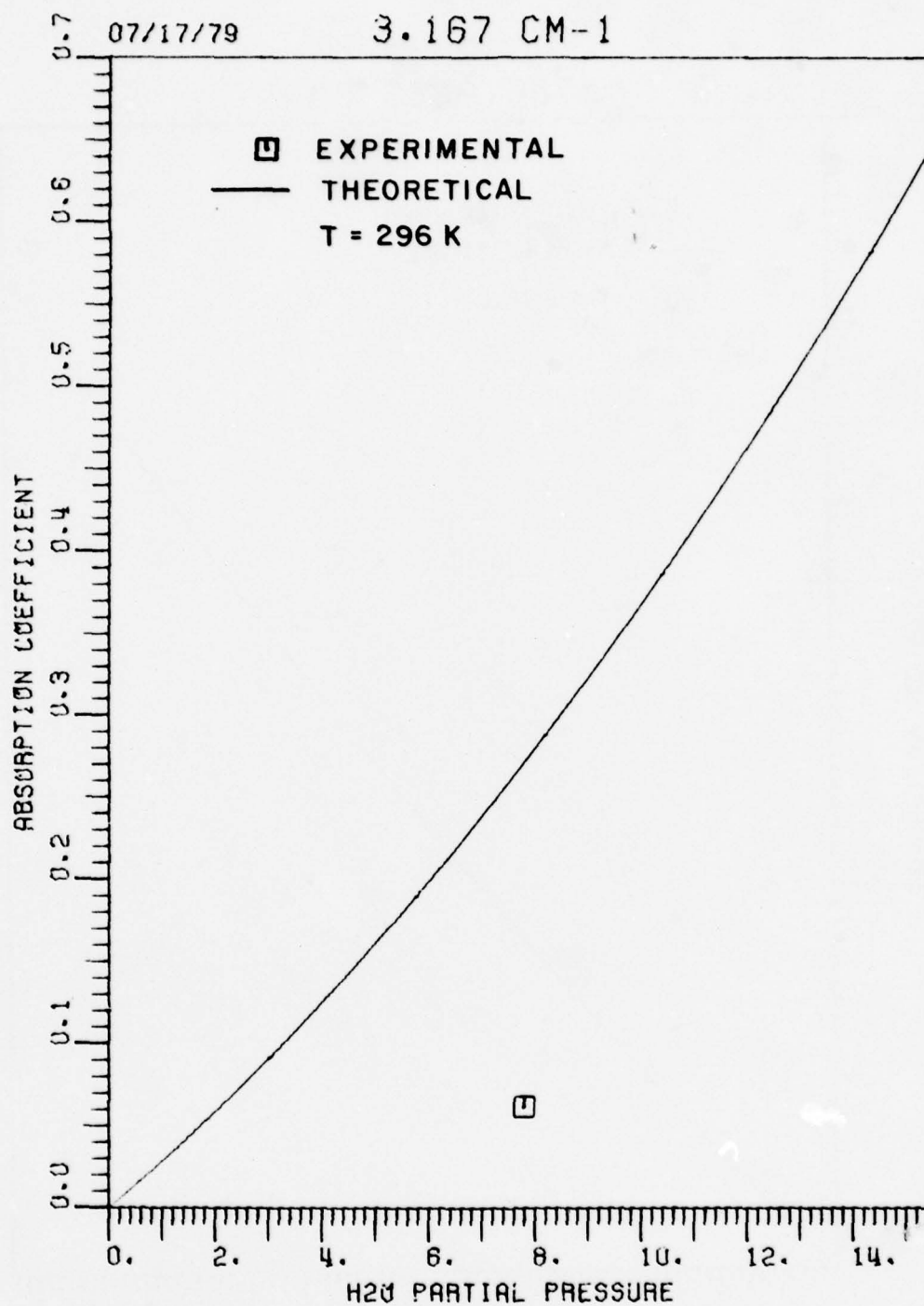


Figure 47. Comparison of experiment and theory
at 3.167 cm⁻¹.

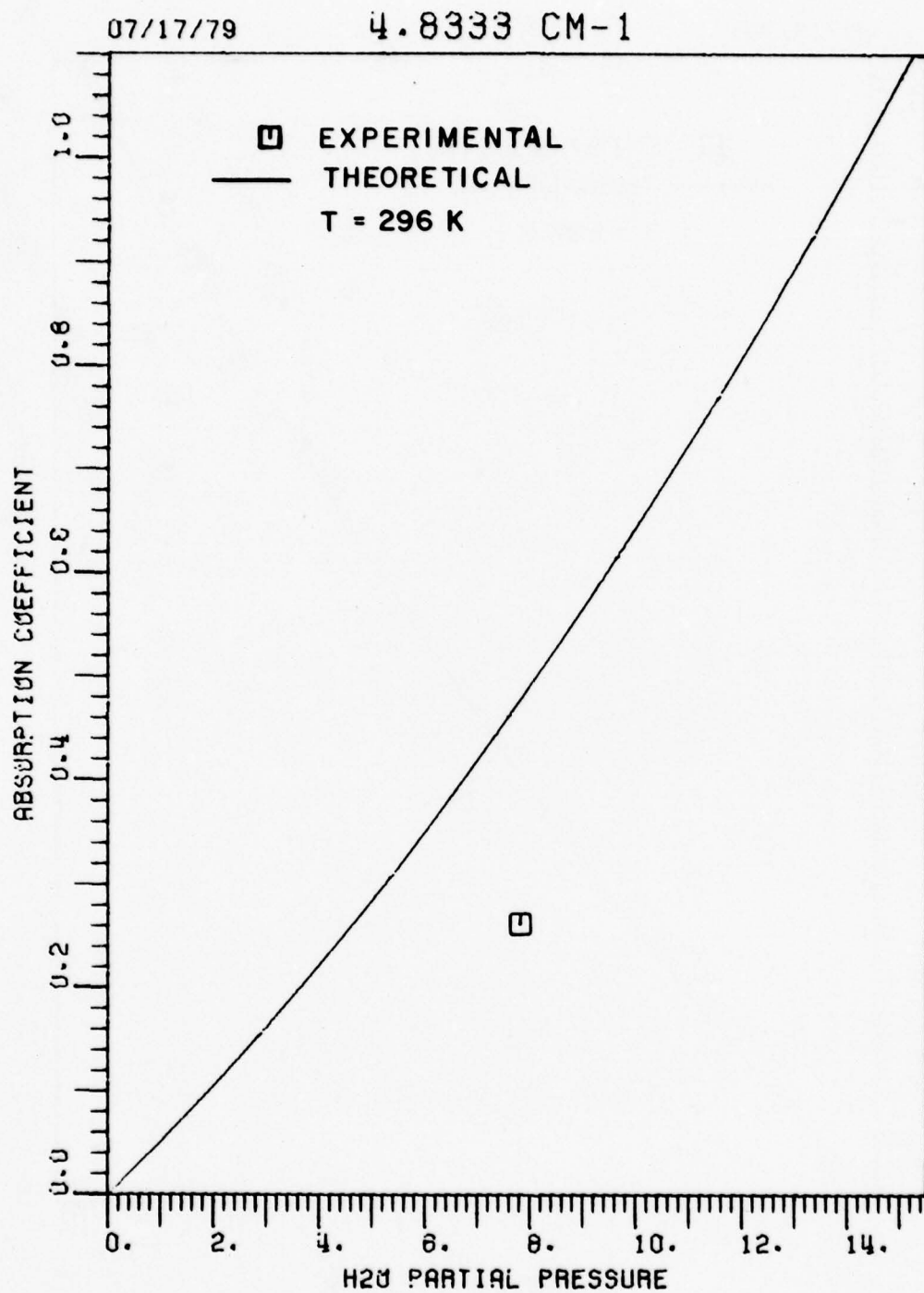


Figure 48. Comparison of experiment and theory
at 4.8333 cm⁻¹.

07/17/79

7.667 CM-1

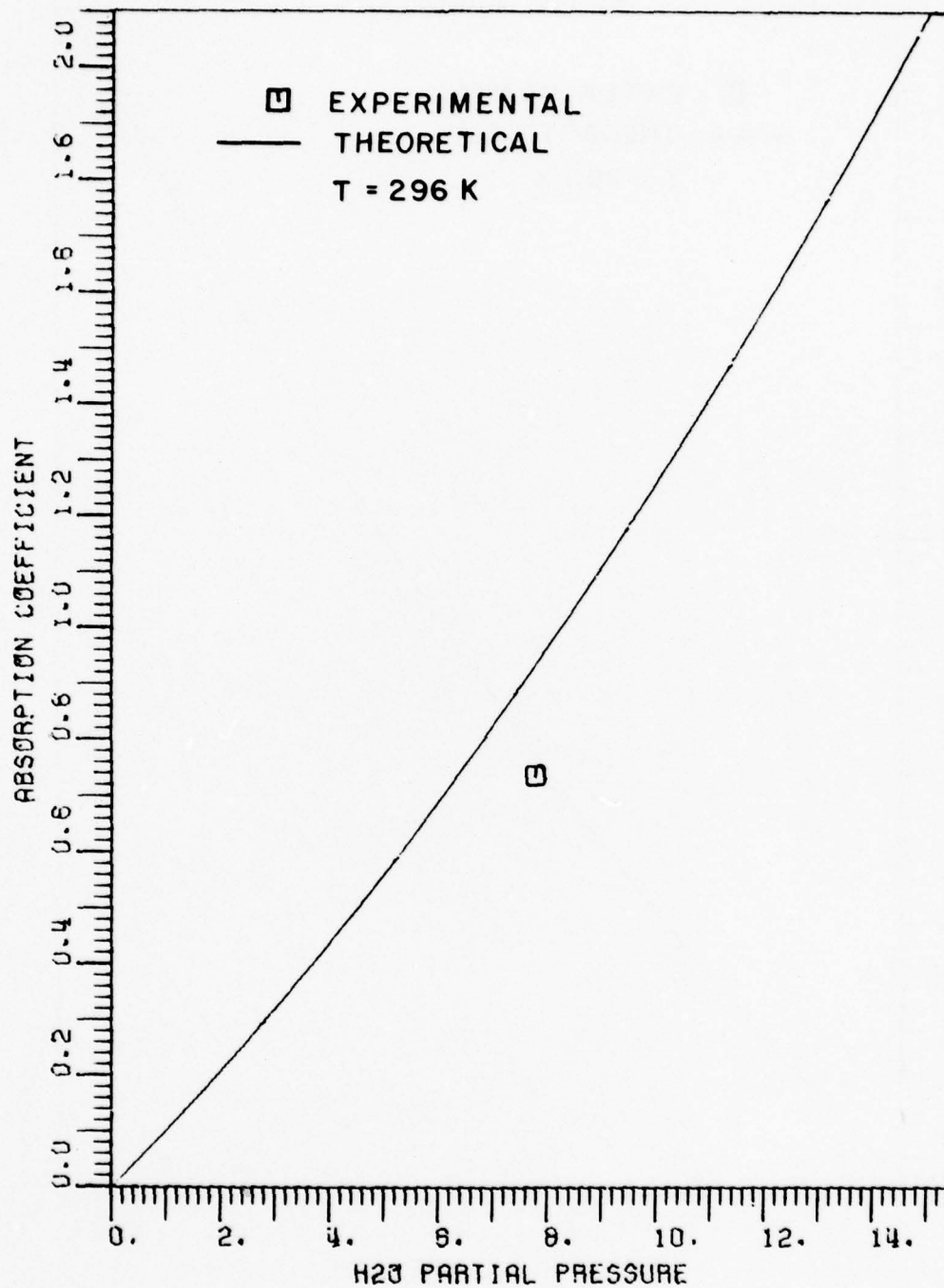


Figure 49. Comparison of experiment and theory
at 7.667 cm⁻¹.

Table 5
Nitrogen Broadened Water Vapor Window
Absorption Parameter at 430 K.

ν	$C_N/RT \times 10^5 \left(\frac{\text{km}^{-1}}{\text{Torr}^2} \right)$	B
430.0	103.1	6.9
433.7	190.5	7.0
440.1	111.6	7.8
448.8	127.6	7.9
465.4	87.4	7.8
475.1	103.1	7.6
482.6	104.3	6.6
498.0	32.5	10.9
531.6	18.3	12.3
559.2	13.0	13.1
579.0	40.7	7.0
597.0	19.2	10.3
629.0	8.5	13.0

far wing temperature dependence is not accurately represented, a correction to Equation (196) was performed. By changing the power of $\left(\frac{296}{T}\right)$ from 0.5 to 4.5 in Equation (196) a substantial improvement in modeling performance was achieved. That particular term comes from the temperature dependence of the interaction potential (see Equation (157)). Figure 50 illustrates the agreement between the calculated and experimental data. Figures 51 and 52 show the H_2O partial pressure dependence at 430 K. Excellent agreement with experimental measurements is demonstrated.

The application of the total line shape to the temperature dependence at the $00^0_1-10^0_0$ P(20) laser line is illustrated in Figure 53. The ordinate is C_s as defined in Equation (192). The two labeled solid lines represent calculations using the total line shape and the Lorentz line shape with all the absorption lines included from the rotational and ν_2 bands (i.e., no bound). The Lorentz line shape curve shows a slight positive temperature dependence and is considerably lower than the experimental data. The total line shape calculation does not show the rapid temperature dependence of the experimental data but the computed C_s does decrease with increasing temperature. The experiment 1 data points are taken from Peterson (OSU data) [18] and Arefév and Dianov-Klovov (Soviet data) [21]. High temperature measurements by Montgomery [22] at 1203 cm^{-1} exhibit an interesting effect. A negative temperature

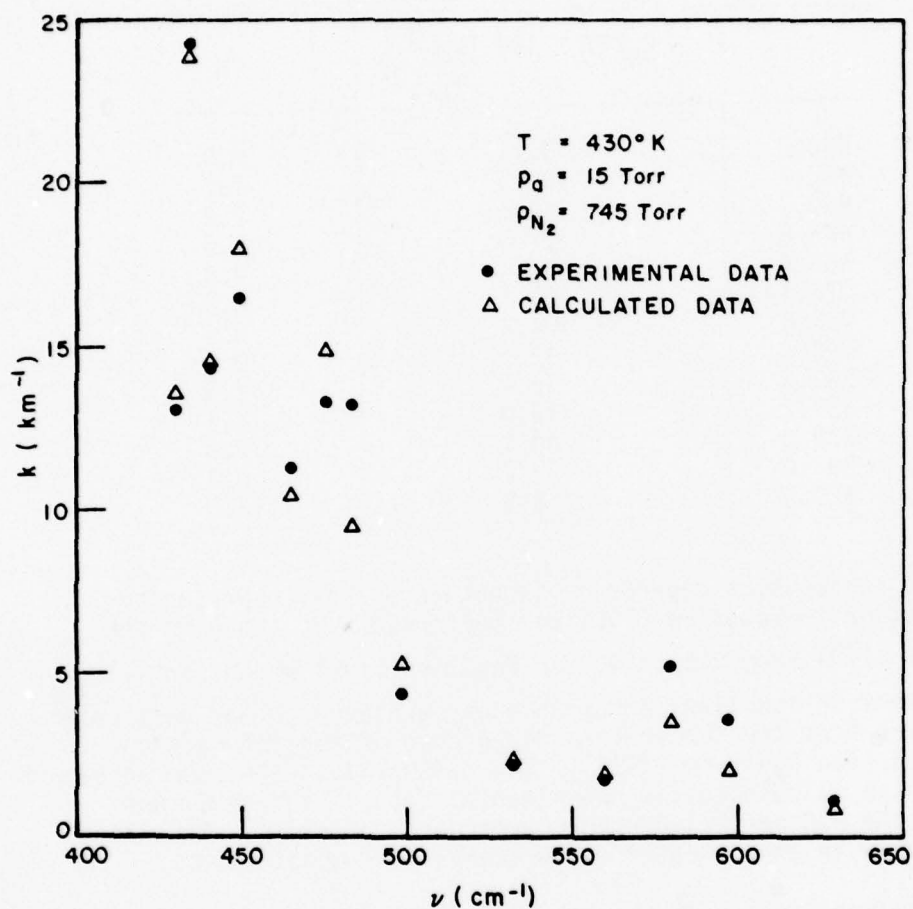


Figure 50. Comparison of experimental and theoretical frequency dependence of the absorption coefficient from 400 cm^{-1} to 650 cm^{-1} at 430 K .

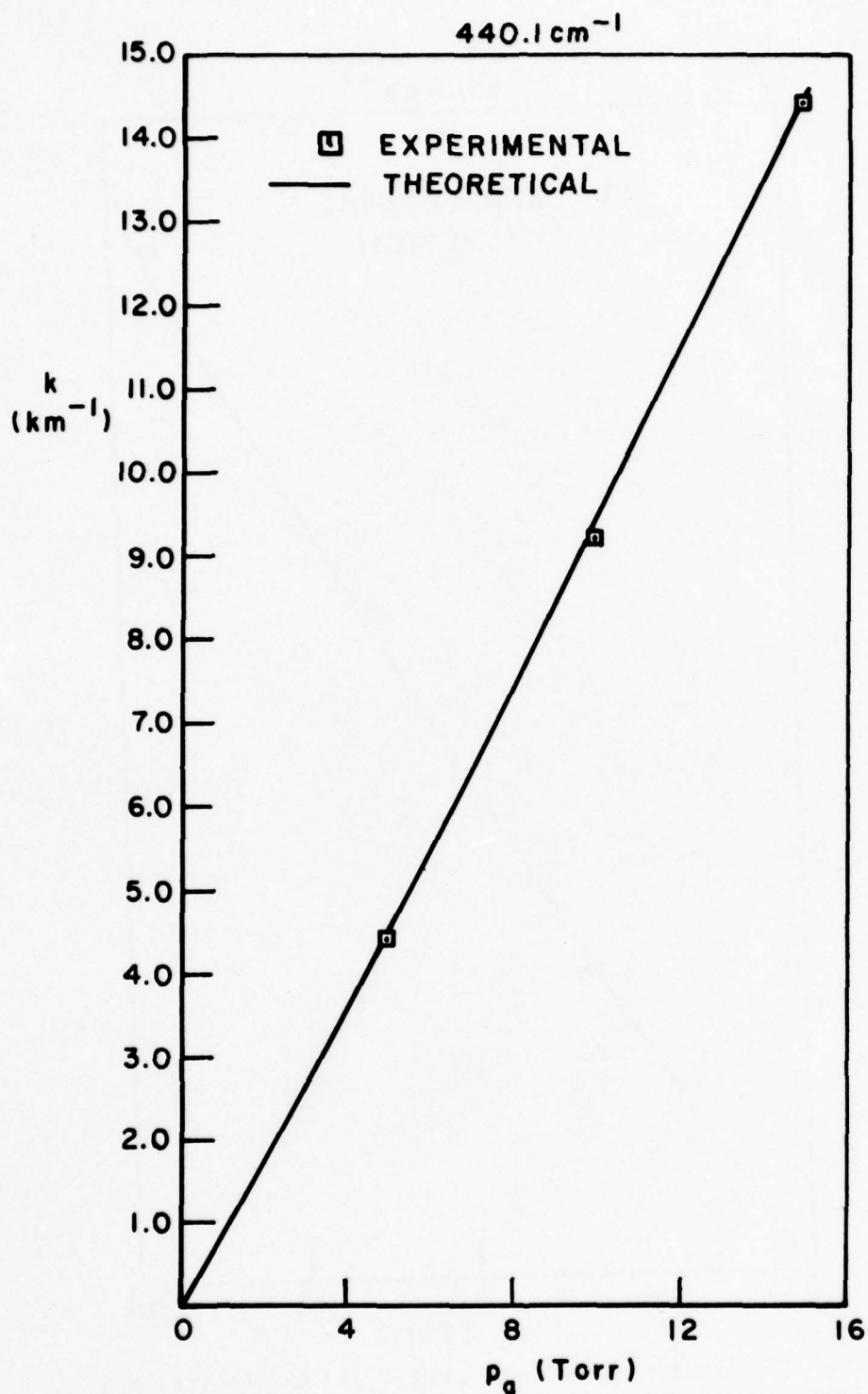


Figure 51. Comparison of experimental and theoretical H_2O partial pressure dependence at 440.1 cm^{-1} at 430 K .²

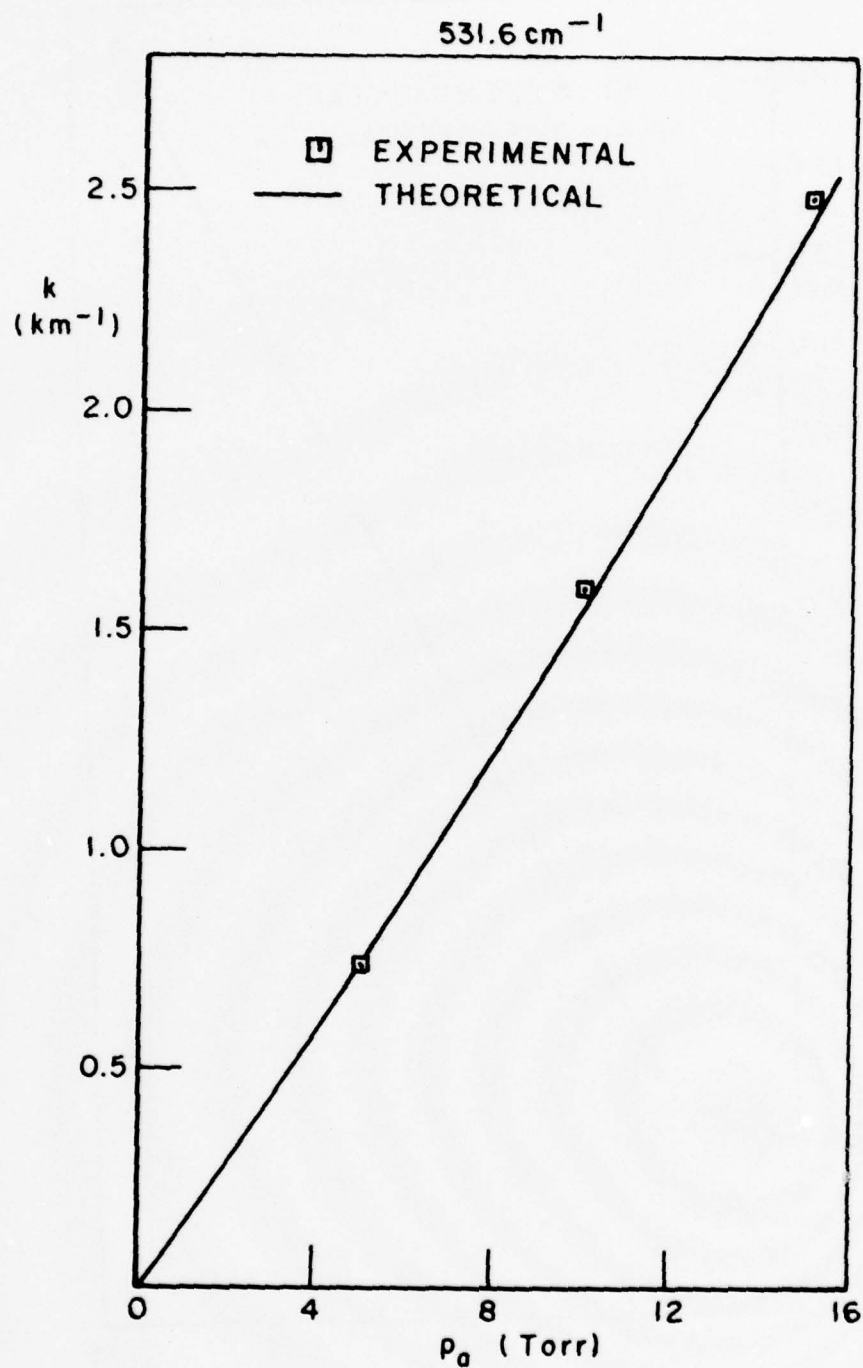


Figure 52. Comparison of experimental and theoretical H_2O partial pressure dependence at 531.6 cm^{-1} at 430 K .²

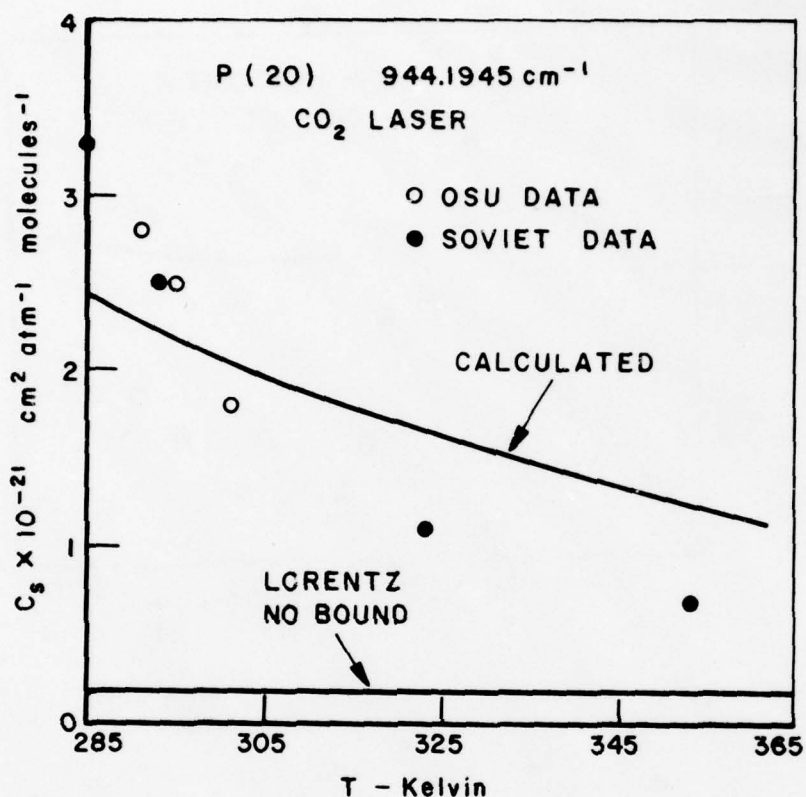


Figure 53. Comparison of experimental and theoretical temperature dependence of C_s at 944.1945 cm⁻¹.

dependence of C_s is observed from 290K to 400K, then a positive dependence appears above 400K. A minimum occurs around 400K. Figure 54 shows a comparison between Montgomery's data and calculations using the total line shape formula developed in Chapter II. The general trends of the temperature dependence are modeled. However the magnitude of the temperature dependence is not closely modeled.

Burch, [15] indicates a decrease in C_s from 296K to 430K at 2600 cm⁻¹ by a factor of 3. The total line shape model predicts a factor of 1.2 decrease.

Continuum modeling by far wings of Lorentz or Van Vleck-Weisskopf line shapes indicate a positive temperature dependence in C_s . This fact has been used to discredit far wing models in general. The important result of this section is that a properly

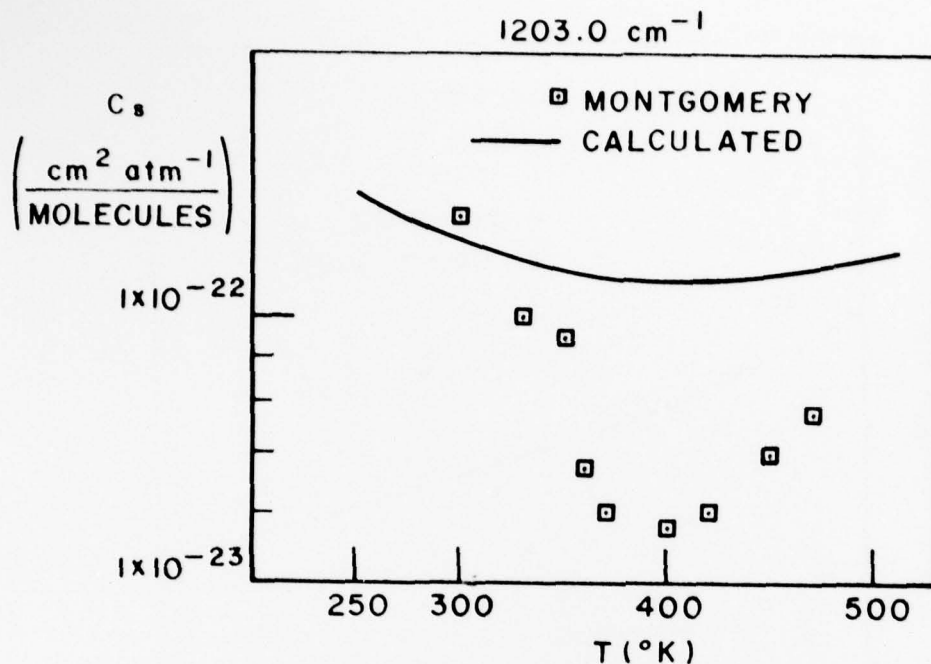


Figure 54. Comparison of experimental and theoretical temperature dependence of C_s at 1203.0 cm^{-1} .

developed total line shape does predict a negative temperature dependence in continuum regions. The success of dimer and cluster theories [25,27] in describing the temperature dependence at $10 \mu\text{m}$ as mentioned in Chapter I is related to the nature of the intermolecular potentials in forming and breaking bonds between molecules. As emphasized in Chapter II these same intermolecular potentials of close molecular encounters determine the nature of the far wings. Thus as the line shape and intermolecular potential models are improved they will also characterize the temperature dependences of the absorption coefficient more accurately.

CHAPTER V CONCLUSIONS

Attenuation of infrared radiation in the troposphere is dominated by water vapor absorption. Most past work on the spectroscopy of water vapor has been on the analysis of the rotational and vibrational bands. As a result a thorough listing of line positions, line strengths and halfwidths exists today. Because of the weak "continuum" absorption in the water vapor windows centered at 10 and 4 microns, efforts to measure and model the continuum have not been as successful as efforts in the analysis of the bands. Yet a precise understanding of continuum absorption is important for long path energy transmission. For this reason the study of the water vapor windows has had a long and speculative history.

The purpose of this study is to demonstrate the importance of far wing phenomena in characterizing H_2O continuum absorption. A total line shape for water vapor-nitrogen interactions valid under tropospheric conditions is derived. The model is tested using a set of experimental room temperature H_2O continuum measurements of high quality. Using this data base parameters of the far wing component of the total line shape are determined from near band experimental data. Grating spectrometer measurements from 300 to 650 cm^{-1} are used to determine unknown far wing parameters of the pure rotational band of H_2O . CO and HF laser measurements taken in the 5 micron and 3 micron regions are used to determine the far wing parameters of the ν_2 and ν_1, ν_3 fundamental bands, respectively.

The total line shape model is applied to the millimeter, 10 μm , and 4 μm absorption windows with encouraging success. A significant increase in the self-broadening ability of H_2O over N_2 is predicted in the far wing. This allows the proper modeling of the absorption coefficient versus H_2O partial pressure dependence in all window regions. A negative temperature dependence is predicted by the model in the continuum. The observed rate of the temperature decrease is not predicted by the model, however the failings are related to approximations made on the interaction potentials and perturbation expansion of the Hamiltonians. Although the total line shape model has limitations, it does demonstrate the importance of considering far wings of absorption lines in continuum absorption.

Included in the study are spectra of H_2O in the $10\text{ }\mu\text{m}$, $5\text{ }\mu\text{m}$ and $4\text{ }\mu\text{m}$ window regions obtained with a Fourier transform spectrometer. The resolution is 0.05 cm^{-1} . The spectral plots are presented in Appendix B.

Future efforts to improve the total line shape model should concentrate on the statistical line shape part. The phase shift approximation which is used does not adequately describe the nature of the statistical far wings. The level shift correction term is an important factor in the far wing equations. A more general solution including phase and level shifts of the stationary states should be attempted. Also future investigations of the molecular interactions important in far wing physics must solve the problem of strong interaction energies (greater than kT).

The theoretical development in Chapter II presents a complete characterization of the molecular absorption problem. However approximations made during the solution making the problem tractable have caused shortcomings in the model as previously described. The important contribution of Chapter II is the unified development of line strength and line shape in a general setting. This has allowed the description of the absorption coefficient from millimeter to the near infrared.

REFERENCES

1. H.R. Carlon, Appl. Opt., 10, 2297 (1971).
2. W.S. Benedict and R.F. Calfee, "Line Parameters for the 1.9 and 6.3 Micron Water Vapor Bands," ESSA Professional Paper 2 (June 1967) U.S. Government Printing Office.
3. D.M. Gates, R.F. Calfee, D.W. Hansen and W.S. Benedict, "Line Parameters and Computed Spectra for Water Vapor Bands at 2.7 μ ," National Bureau of Standards Monograph 71 (1964), U.S. Government Printing Office.
4. C. Camy-Peyret and J.M. Flaud, Molecular Physics 32, 523 (1976).
5. R.A. McClatchey, W.S. Benedict, S.A. Clough, D.E. Burch, R.F. Calfee, K. Fox, L.S. Rothman and J.S. Garing, "AFCRL Atmospheric Absorption Line Parameters Compilation," Air Force Research Laboratories, Bedford, Mass., AFCRL-TR-73-0096 (January 1973).
6. J.H. Shaw, Ohio Journal of Science 53, 258 (1953).
7. W.M. Elsasser, "Heat Transfer by Infrared Radiation in the Atmosphere," Harvard University Press, Cambridge, Mass. (1942).
8. H.W. Yates and J.H. Taylor, "Infrared Transmission of the Atmosphere," NRL Report 5453 (AD 240-88) (1960).
9. A. Adel, Astrophys. J. 89, 1 (1939).
10. R. Anthony, Phys. Rev. 85, 674 (1952).
11. W.T. Roach and R.W. Goody, Quart. J. Roy. Meteorol. Soc. 84, 319 (1958).
12. K. Bignell, F. Saiedy and P.A. Sheppard, J. Opt. Soc. America 53, 466 (1963).
13. K. Bignell, Quart. J. Roy. Meteorol. Soc. 96, 390 (1970).

14. D.E. Burch, Aeronutronic Publication No. U-4784, "Semi-Annual Technical Report," Air Force Cambridge Research Laboratories, Contract No. F19628-69-C-0263, January 1970.
15. D.E. Burch, D.A. Gruyvnak and J.D. Pembroke, Aeronutronic Publication No. U-4897, "Investigation of the Absorption of Infrared Radiation by Atmospheric Gases: Water, Nitrogen, Nitrous Oxide," Air Force Cambridge Research Laboratories, Contract No. F19628-69-C-0263, January, 1971.
16. J.H. McCoy, D.B. Rensch and R.K. Long, Appl. Opt. 8, 1471 (1969).
17. D.E. Burch, E.B. Singleton, W.L. France and D. Williams, "Infrared Absorption by Minor Atmospheric Constituents," The Ohio State University Research Foundation, Final Report, prepared under Contract AF 19(604)-2633, December, 1960.
18. J.C. Peterson, "A Study of Water Vapor Absorption at CO₂ Laser Frequencies Using a Differential Spectrophone and White Cell," Dissertation, The Ohio State University, June 1978.
19. R.J. Nordstrom, M.E. Thomas, J.C. Peterson, E.K. Damon and R.K. Long, Appl. Opt. 17, 2724 (1978).
20. J.C. Peterson, M.E. Thomas, R.J. Nordstrom, E.K. Damon and R.K. Long, Appl. Opt. 18, 834 (1979).
21. V.N. Aref'ev and V.I. Dianov-Klokov, Opt. Spectrosc. 42, 488 (1977).
22. G.P. Montgomery, Jr., Appl. Opt. 17, 2299 (1978).
23. R.K. Long, E.K. Damon, R.J. Nordstrom, J.C. Peterson, M.E. Thomas, J.J. Sherman, "Laser Atmospheric Absorption Studies," Rome Air Development Center, Report No. RADC-TR-78-124, June 1978.
24. W.R. Watkins, K.O. White, L.R. Bower, B.Z. Sojka, "Pressure Dependence of the Water Vapor Continuum Absorption in the 3.5 to 4.0 Micrometer Region," U.S. Army Electronics Research and Development Command, Report No. ASL-TR-0017, September 1978.
25. P.S. Varanasi, S. Chou and S.S. Penner, J. Quant. Spectros. Radiat. Transfer. 8, 1537 (1968).
26. S.S. Penner, J. Quant. Spectrosc. Radiat. Transfer. 13, 383 (1973).

27. H.R. Carlon, "Final Report: Infrared Absorption by Water Clusters," Chemical Systems Laboratory, Report No. ARCSL-TR-79013, March 1979.
28. V.V. Fomin and S.D. Tvorogov, *App. Opt.*, 12, 584, (1973).
29. V.E. Zuev and V.V. Fomin, "Consideration of Continuum Absorption in the Problems of Sounding From Outer Space," Presented at the Symposium on Remote Sounding of the Atmosphere from Space, Innsbruck, Austria, June 1-3, 1978.
30. R.E. Roberts, J.A. Selby and L.M. Biberman, *Appl. Opt.* 15, 2085, (1976).
31. W. Heitler, The Quantum Theory of Radiation, Oxford University Press, (1954), 3rd Edition.
32. G. Baym, Lectures on Quantum Mechanics, W.A. Benjamin Inc., (1977).
33. H. Mergenau and N.R. Kestner, Theory of Intermolecular Forces, Pergamon Press, (1969).
34. D. Eisenberg and W. Kauzmann, The Structure and Properties of Water, Oxford University Press, (1969).
35. P.W. Anderson, *Phys. Rev.* 76, 647, (1949).
36. C.J. Tsao and B. Curnutte, *J. Quant. Spectrosc. Radiat. Transfer* 2, 41, (1962).
37. M. Barranger, Atomic and Molecular Processes, Academic Press, (1962), D.R. Bates Editor, Chapter 13.
38. A.P. Galtsev and V.V. Tsukanov, *Opt. Spectrosc. (USSR)* 42, 612, (1977).
39. E.W. Smith, J. Cooper, L.J. Roszman, *J. Quant. Spectrosc. Radiat. Transf.* 13, 1523, (1973).
40. H.R. Zaidi, *Can. J. Phys.*, 53, 76, (1975).
41. V.V. Fomin and S.D. Tvorogov, *Appl. Opt.*, 12, 584, (1973).
42. A. Einstein, *Physik. Z.*, 18, 121, (1917).
43. J.H. Van Vleck and V.F. Weisskopf, *Rev. Mod. Phys.* 17, 227, (1945).

44. R. Karplus and J. Schwinger, Phys. Rev. 73, p. 1020, (1948).
45. B. Farmer, "Extinction Coefficients and Computed Spectra for the Rotational Band of Water Vapour Between 0.7 and 1000 cm^{-1} ," E.M.I. Electronics LTD, Contract No. KH-G-5828-CB19(d)3, April 1967.
46. R.G. Breene, The Shift and Shape of Spectral Lines, Pergamon Press, 1961.
47. M. Mizushima, Phys. Rev. 83, 1061, (1951).
48. E.M. Deutchman and R.F. Calfee, "Two Computer Programs to Produce Theoretical Absorption Spectra of Water Vapor and Carbon Dioxide," AD816 369, April 1967.
49. P. Varanasi and F.K. Ko, "Intensity Measurements in the 2 μm CO_2 Bands at Low Temperatures," presented at Thirty Third Symposium on Molecular Spectroscopy, The Ohio State University, 1978.
50. H.M. Foley, Phys. Rev. 69, 616, (1946).
51. C.V. Heer, Statistical Mechanics, Kinetic Theory, and Stochastic Processes. Academic Press, 1972, Chapter 11.
52. W.S. Benedict and L.D. Kaplan, J. Chem. Phys. 30, 388, (1959).
53. W.S. Benedict and L.D. Kaplan, J. Quant. Spectrosc. Radiat. Transfer 4, 453, (1964).
54. C. Kittel, Introduction to Solid State Physics, John Wiley and Sons, 4th Edition, (1971).
55. E.U. Condon and H. Odishaw, Editors, Handbook of Physics, McGraw-Hill Book Co., 2nd Edition, (1967).
56. P. Varanasi, P.S.K. Sarangi and G.D.T. Tejwani, J. Quant. Spectrosc. Radiat. Transfer 12, 857, (1972).
57. G. Herzberg, Infrared and Raman Spectra, Van Nostrand Reinhold, (1945).
58. P. Brechignac and J.P. Martin, IEEE JQE, QE-12, 80, (1976).
59. C. Freed, "Proceeding of the Frequency Standards and Metrology Seminar," at the University Laval, Quebec, Canada, August-September, 1971.

60. N. Djeu, Appl. Phys. Lett. 23, 309, (1973).
61. W.H. Thomason, D.C. Elbers, "An Inexpensive Method to Stabilize the Frequency of a CO₂ Laser," Louisiana State University, Department of Chemistry, 1974, private communication.
62. J.W. Cooley and J.W. Tukey, Math. Comput., 19, 297, (1965).
63. R.K. Long, "Absorption of Laser Radiation in the Atmosphere," The Ohio State University ElectroScience Laboratory, Report 1579-3, May 1963; prepared under Contract AF33(657)-10824 for Air Force Avionics Laboratory. (AD 410571)
64. R.K. Long, E.K. Damon, J.C. Peterson and M.E. Thomas, "Laser Atmospheric Absorption Studies," Rome Air Development Center, Report No. RADC-TR-76-330, June 1978.
65. D. Horn and J.C. Pimentel, Appl. Opt. 10, 1892, (1971).
66. J.U. White, "Very Long Optical Paths in a Near-Confocal System," presented at 1975 Annual Meeting, Optical Society of America.
67. J.U. White, J. Opt. Soc. Amer. 32, 285, (1942).
68. G.L. Trusty, "Absorption Measurements of the 10.4 Micron Region Using a CO₂ Laser and a Spectrophone," Report 2819-4, January 1973, The Ohio State University ElectroScience Laboratory. (AFAL-TR-72-413) (AD 907549)
69. W.R. Watkins, Appl. Opt. 15, 17, (1976).
70. D.E. Burch, D.A. Gryvnak and R.R. Patty, J. Opt. Soc. Am. 57, 885, (1967).
71. G.M. Hale and M.R. Querry, Appl. Opt. 12, 555, (1973).
72. D.E. Burch, Presented at Conference on Atmospheric Transmission Models, May 22-23 1979, AFGL Hanscom Air Force Base.
73. D.A. Gryvnak and D.E. Burch, "Infrared Absorption by CO₂ and H₂O," Aeronutronic Publication U-6417, Air Force Geophysics Laboratories, Contract F19628-76-C-0302, (May 1978).
74. R.K. Long, F.S. Mills and G.L. Trusty, "Experimental Absorption Coefficients for Eleven CO Laser Lines," Contract Number F30602-72-C-0016, (1973), Advanced Research Projects Agency.

75. K.O. White, W.R. Watkins, C.W. Bruce, R.E. Meredith and F.G. Smith, Appl. Opt. 17, 2711, (1978).
76. W.R. Watkins, R.L. Spellicy, K.O. White, B.Z. Sojka and L.R. Bower, Appl. Opt. 18, 1582, (1979).
77. F.S. Mills, "Absorption of Deuterium Fluoride Laser Radiation by the Atmosphere," Dissertation, The Ohio State University, June 1978.
78. J.A. Bastin, Infra. Phys. 6, 209, (1966).

APPENDIX A NORMALIZATION INTEGRALS

The solution of the normalization constant (Equation (183)) is presented in this Appendix. This requires the integration of the total line shape (Equation (170)) and making the area underneath the line shape equal to one. The realization of this requirement resulted in the evaluation of many difficult integrals. Whenever possible an exact solution was obtained. However in many cases numerical and series expansion approaches were used.

To simplify the computation of the normalization constant for every absorption line the total line shape formula has been written for two cases $\nu_0 < 1000 \text{ cm}^{-1}$ and $\nu_0 > 1000 \text{ cm}^{-1}$ (see Equations (181) and (182)). Also the simpler expression for the case $\nu_0 > 1000 \text{ cm}^{-1}$ reduced the computer time of the program used for calculating the absorption coefficient.

A summary of the resulting expressions is presented in the following equations.

$$N = \left(\int_0^{\infty} j_{\text{CNLC}}(\nu) p(\nu) d\nu + \int_0^{\infty} j_{\text{CFW}}(\nu) (1-p(\nu)) d\nu \right)^{-1} \quad (197)$$

For $\nu_0 > 1000 \text{ cm}^{-1}$

$$\int_0^{\infty} j_{\text{CNLC}}(\nu) p(\nu) d\nu = \frac{1}{2} \exp\left(-\frac{\pi}{5} \alpha r\right) + \frac{1}{\pi} \tan^{-1} \left(\frac{5}{\alpha r} \right) \quad (198)$$

$$\begin{aligned}
& \int_0^{\infty} j_{\text{CFW}}(\nu)(1-p(\nu))d\nu = \\
& (0.0342 - 0.0537 G_{a6} + 0.0455 G_{a6}^2 - (0.0039 - 0.004 G_{a6} \\
& + 0.0022 G_{a6})\lambda_{a6})\lambda_{a6} + (0.0388 - 0.0575 G_{b4} + 0.047 G_{b4} \\
& - (0.0089 - 0.0075 G_{b4} + 0.0038 G_{b4}^2)\lambda_{b4})\lambda_{b4} + \\
& (0.1821 e^{-G_{a6}^5} + 0.5627 G_{a6} + 0.4072 G_{a6} \ln(G_{a6}) \\
& - 0.9104 G_{a6}^2 + 0.509 G_{a6}^3)\lambda_{a6} + ([0.1100 - 0.4920 G_{b4} \\
& - 2.2004 G_{b4}^2] e^{-G_{b4}^{\sqrt{5}}} + 1.3041 G_{b4}^{1.5})\lambda_{b4} \quad . \quad (199)
\end{aligned}$$

For $\nu_0 < 1000 \text{ cm}^{-1}$

$$\begin{aligned}
& \int_0^{\infty} j_{\text{CNLC}}(\nu)p(\nu)d\nu = \frac{1}{2} \exp(-\frac{\pi}{5} \alpha^r) + \frac{1}{\pi} \tan^{-1} \left(\frac{5}{\alpha^r} \right) \\
& + \frac{b \alpha^r}{\pi \nu_0 (\exp(\nu_0 b) - 1)} (1.5900 - 0.9436 \alpha^r) \quad (200)
\end{aligned}$$

where $b = 0.004861 \left(\frac{296}{T} \right)$

$$\begin{aligned}
\int_0^{\infty} j_{cFW}(v)(1-p(v))dv &= \frac{.3198\lambda_{a6}}{\pi(1-\exp(-v_0b))} \left(\frac{2\exp(-G_{a6}\sqrt{5})}{\sqrt{5}} \right. \\
&- \frac{2\exp(-G_{a6}\sqrt{v_0})}{\sqrt{v_0}} + \left(\ln \frac{5}{v_0} \right) G_{a6} - 2(\sqrt{5} - \sqrt{v_0}) G_{a6}^2 \\
&- \frac{1}{2}(5-v_0) G_{a6}^3 + \frac{1}{9}(5\sqrt{5} - v_0\sqrt{v_0}) G_{a6}^4 + \frac{v_0^2}{48} G_{a6}^5 \\
&- \left. \frac{v_0^2\sqrt{v_0}}{300} G_{a6}^6 + \frac{v_0^3 G_{a6}^7}{2160} \right) + \frac{.4334\lambda_{b4}}{\pi(1-\exp(-v_0b))} \left((0.3988 \right. \\
&- 1.7833 G_{b4} - 7.9752 G_{b4}^2) \exp(-G_{b4}\sqrt{5}) + \tau \\
&- \left. \frac{1}{(.75)(v_0)^{.75}} - \frac{2.6667}{v_0^{1/4}} G_{b4} - 5.3333(v_0)^{1/4} G_{b4}^2 \exp(-G_{b4}\sqrt{v_0}) \right) \\
&- \frac{0.3198\lambda_{a6}}{\pi(\exp(v_0b)-1)} \left(2\exp(-bc_a^2) \left[\frac{1}{\sqrt{5}} \exp(be_a^2) \right. \right. \\
&- \frac{1}{\sqrt{v_0}} \exp(bd_a^2) + 2b(d_a - e_a) + \frac{b}{3}(d_a^3 - e_a^3) \\
&+ \frac{b^2}{10}(d_a^5 - e_a^5) + \frac{b^3}{42}(d_a^7 - e_a^7) + \frac{b^4}{216}(d_a^9 - e_a^9) \Big) \\
&- \left. G_{a6} \left(\frac{1}{2} \ln\left(\frac{v_0}{5}\right) + b \left[\frac{1}{2}(v_0 - 5) + \frac{2}{a} \ln\left(\frac{v_0}{5}\right) - 2c_a(d_a - e_a) \right] \right) \right)
\end{aligned}$$

$$\begin{aligned}
& - \frac{0.4334 \lambda_{b4}}{\pi(\exp(v_0 b) - 1)} \left(2 \exp(-bc_b^2) \left[\frac{\exp(b e_a^2)}{(1.5)(5) \cdot 75} - \frac{\exp(b d_a^2)}{(1.5)(v_0) \cdot 75} \right. \right. \\
& \left. \left. + \frac{b}{75} \left(2 \left[(v_0) \cdot 25 \sum_{p=0}^4 B_p \sum_{k=0}^{2p} \varepsilon_k (-1)^k \left(\frac{d_b}{2c_b} \right)^k - (5) \cdot 25 \sum_{p=0}^4 B_p \sum_{k=0}^{2p} \varepsilon_k (-1)^k \left(\frac{e_b}{2c_b} \right)^k \right] \right) \right. \right. \\
& \left. \left. - \frac{G_{b4} \exp(b e_b^2)}{1.5 \left(\frac{2}{5} \right)^{1/4}} - \frac{\exp(b d_b^2)}{2(v_0)^{1/4}} + 2G_{b4} \left[(v_0) \cdot 5 \sum_{p=0}^4 B_p \sum_{k=0}^{2p+1} \varepsilon_k (-1)^{k+1} \left(\frac{d_b}{2c_b} \right)^k \right. \right. \right. \\
& \left. \left. \left. - (5) \cdot 25 \sum_{p=0}^4 B_p \sum_{k=0}^{2p+1} \varepsilon_k (-1)^{k+1} \left(\frac{e_b}{2c_b} \right)^k \right] \right] \right) \right) \\
& + 0.1018 \lambda_{a6} (0.3363 - 0.0386 \lambda_{a6} - G_{a6} (0.5274 - 0.0393 \lambda_{a6})) \\
& + G_{a6}^2 (0.4472 - 0.0217 \lambda_{a6}) + 0.1379 \lambda_{b4} (0.2810 \\
& - 0.0645 \lambda_{b4} - G_{b4} (0.4165 - 0.0541 \lambda_{b4}) + G_{b4}^2 (0.3410 - 0.0279 \lambda_{b4})) \\
& + 0.1018 \lambda_{a6} \left[0.8944 \exp(-\sqrt{5} G_{a6}) + 2.7638 G_{a6} + 2G_{a6} \ln G_{a6} - 4.4722 G_{a6}^2 \right. \\
& \left. + 2.5 G_{a6}^3 + \frac{b}{(\exp(v_{0b}) - 1)} \left(\frac{2}{G_{a6}} - b \left(\frac{1}{G_{a6}} \left(5 + \frac{1}{G_{a6}} (4.4722 + \frac{2}{G_{a6}}) \right) \right) \right) \right. \\
& \left. - b \left(\frac{1}{G_{a6}} \left(8.3333 + \frac{1}{G_{a6}} \left(74.5367 + \frac{1}{G_{a6}} \left(20 + \frac{1}{G_{a6}} \left(17.8888 \right. \right. \right. \right. \right. \right. \right. \right. \\
& \left. \left. \left. \left. \left. \left. + \frac{8}{G_{a6}} \right) \right) \right) \right) \right) \right) \exp(-\sqrt{5} G_{a6}) \right] + 0.1379 \lambda_{b4} \left[0.3988 - 1.7833 G_{b4} \right.
\end{aligned}$$

$$\begin{aligned}
& - 7.9752G_{b4}^2 \exp(-\sqrt{5}G_{b4}) + 4.7265G_{b4}^{1.5} \\
& + \frac{b}{(\exp(v_0 b) - 1)} \left(3.5449\sqrt{G_{b4}} - 8.9443 \exp(-\sqrt{5}G_{b4}) \right. \\
& \left. - 8.9165G_{b4} + 11.9628G_{b4}^2 - b \left(1.3293 \frac{1}{G_{b4}^{2.5}} - 2.9907 + 4.7765G_{b4} \right) \right) \Big] \quad (201)
\end{aligned}$$

where

$$b = 0.004861 \left(\frac{296}{T} \right)$$

$$c_a = \frac{G_{a6}}{2b}, \quad c_b = \frac{G_{b4}}{2b}$$

$$d_a = \sqrt{v_0} - c_a, \quad d_b = \sqrt{v_0} - c_b$$

$$e_a = \sqrt{5} - c_a, \quad e_b = \sqrt{5} - c_b$$

$$B_p = \frac{(bc_b^2)^p (4)^p (2p+1)!}{p! (4p+3)!!}, \quad B_p = \frac{(2p-1)!! (8c_b^2)^p}{(4p+1)!!}$$

$$\xi_k = \frac{(2k-1)!!}{k!}$$

$$T = 1.7724 (\operatorname{erf}(v_0^{.25} \sqrt{G_{b4}}) - \operatorname{erf}((5)^{.25} \sqrt{G_{b4}})) \sqrt{G_{b4}}$$

APPENDIX B
H₂O SPECTRA IN THE WINDOW REGIONS

Appendix B presents H₂O spectra in the window regions from 850 cm⁻¹ to 1282 cm⁻¹, 1800 cm⁻¹ to 2054 cm⁻¹ and 2500 cm⁻¹ to 2862 cm⁻¹. The plots represent a 12 torr water vapor sample at 296 K taken on a Nicolet 7199 Fourier transform spectrometer with a resolution of 0.05 cm⁻¹. The ordinate of the following plots is the absorption coefficient in km⁻¹ and the abscissa is frequency in cm⁻¹. The measurement was made on the 10.785 m cell with a path length of 323.6 m.

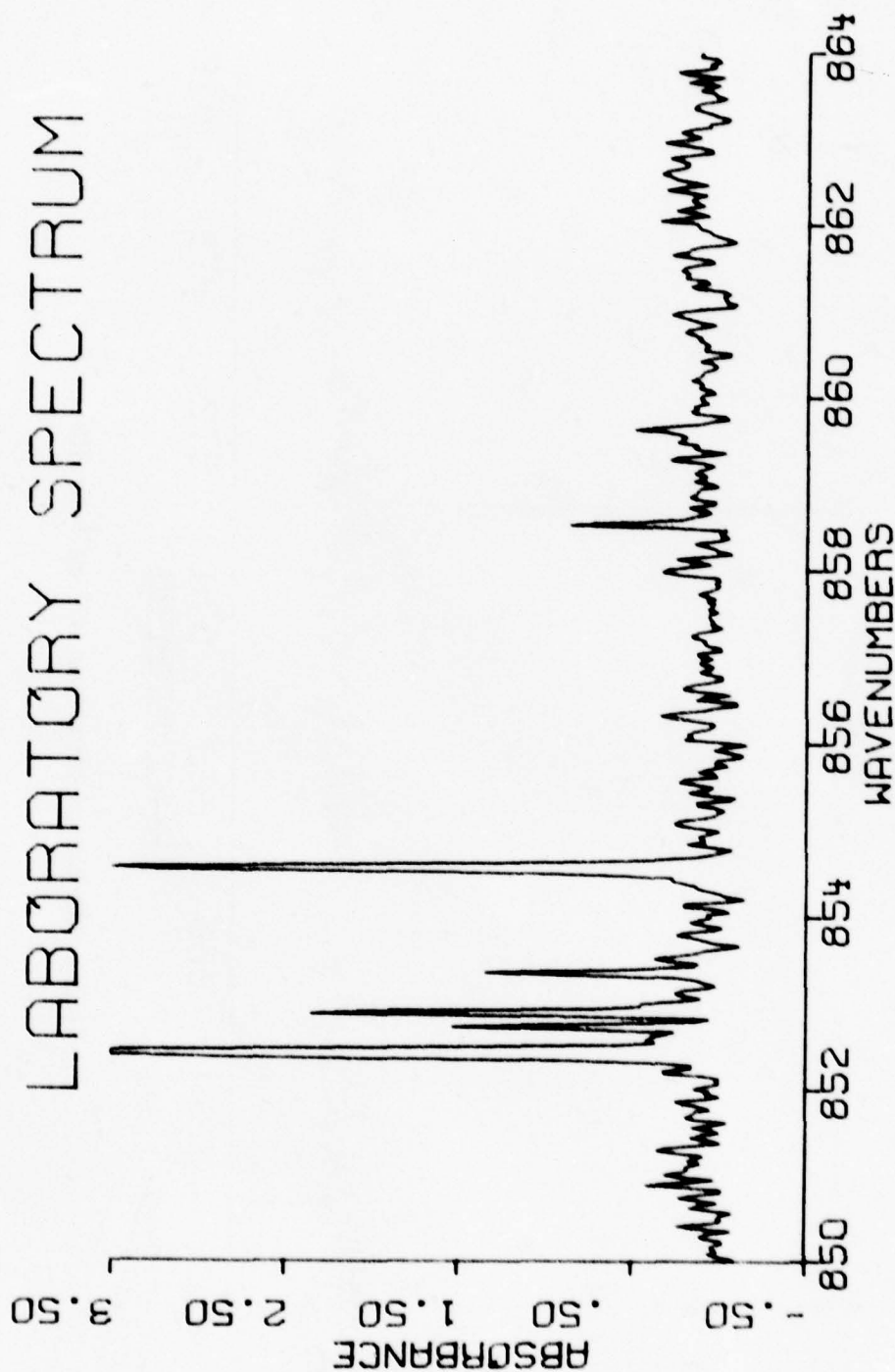


Figure 55. H_2O spectra from 330 cm^{-1} to 364 cm^{-1} .

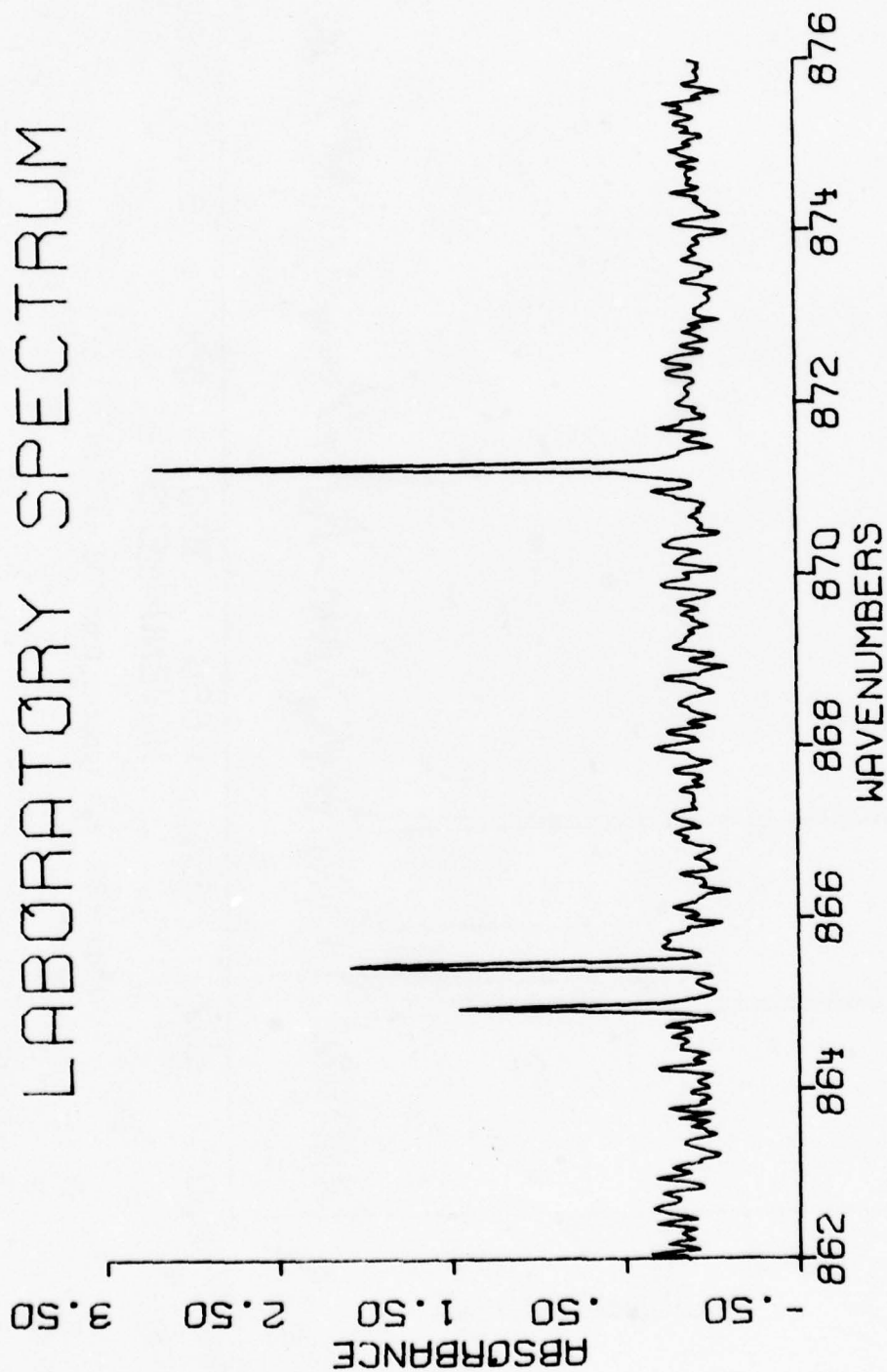


Figure 55. H_2O spectra from 362 cm^{-1} to 376 cm^{-1} .

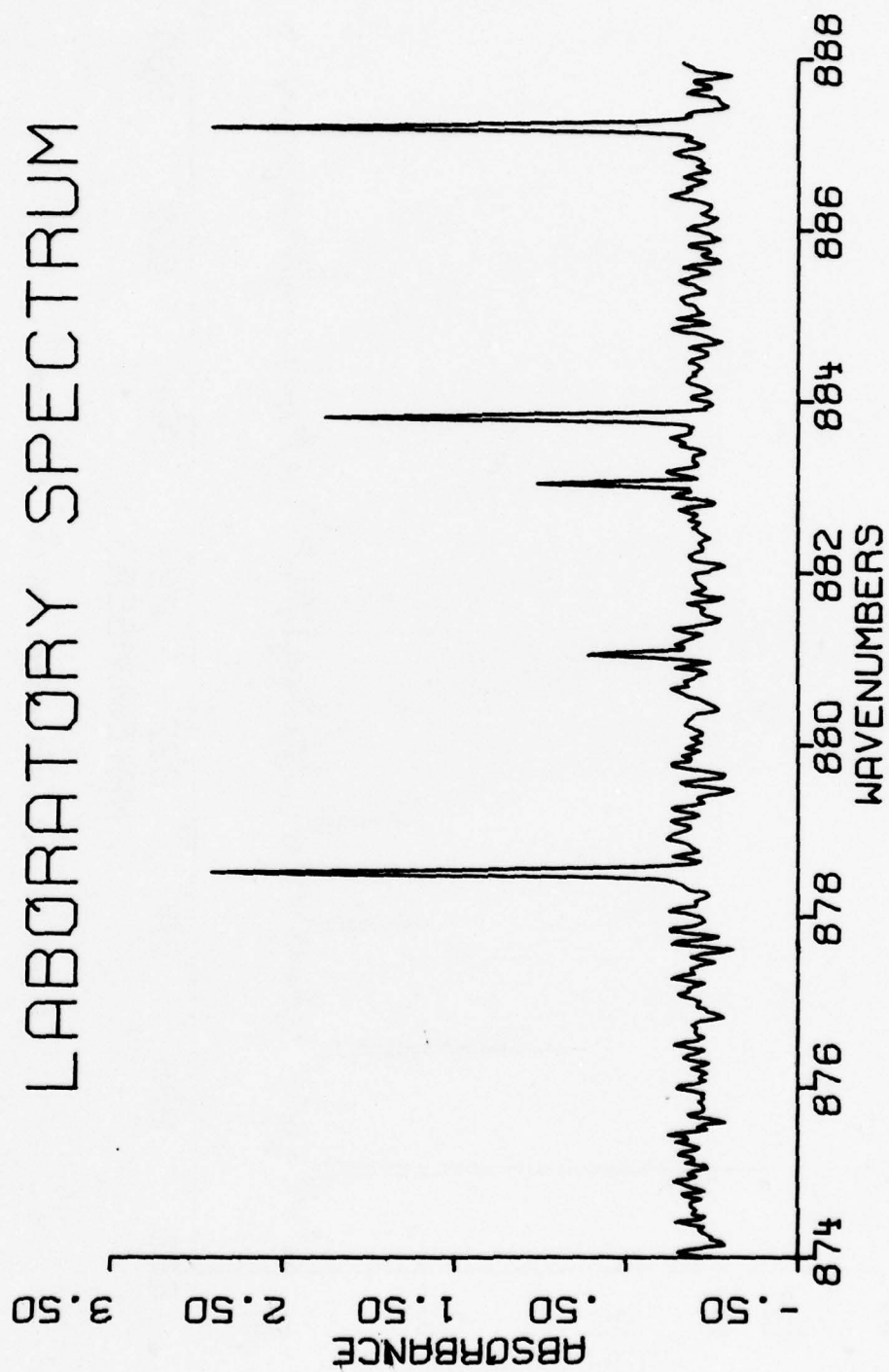


Figure 57. H₂O spectra from 874 cm⁻¹ to 888 cm⁻¹.

LABORATORY SPECTRUM



Figure 58. H_2O spectra from 886 cm^{-1} to 900 cm^{-1} .

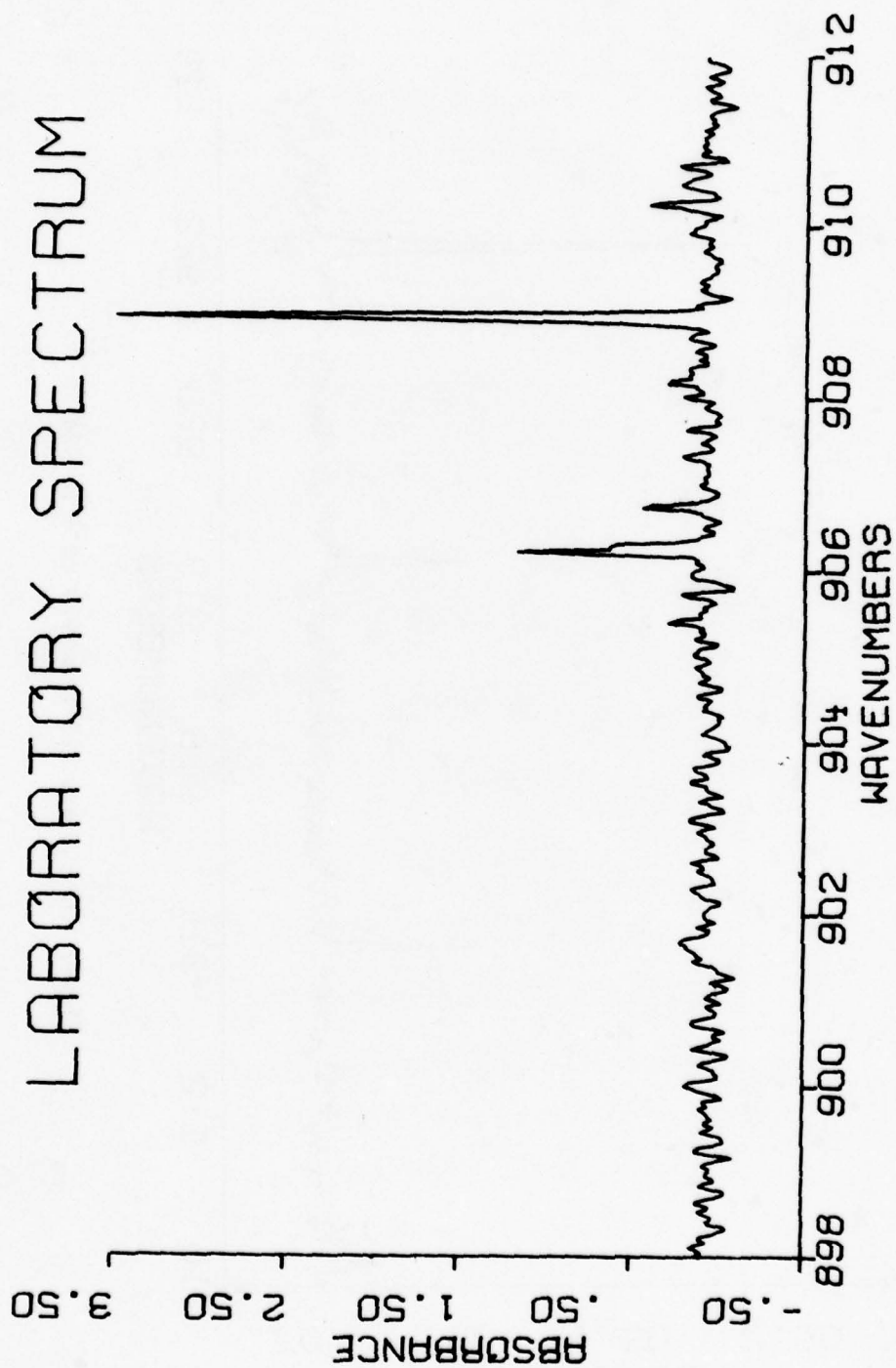


Figure 59. H_2O spectra from 898 cm^{-1} to 912 cm^{-1} .

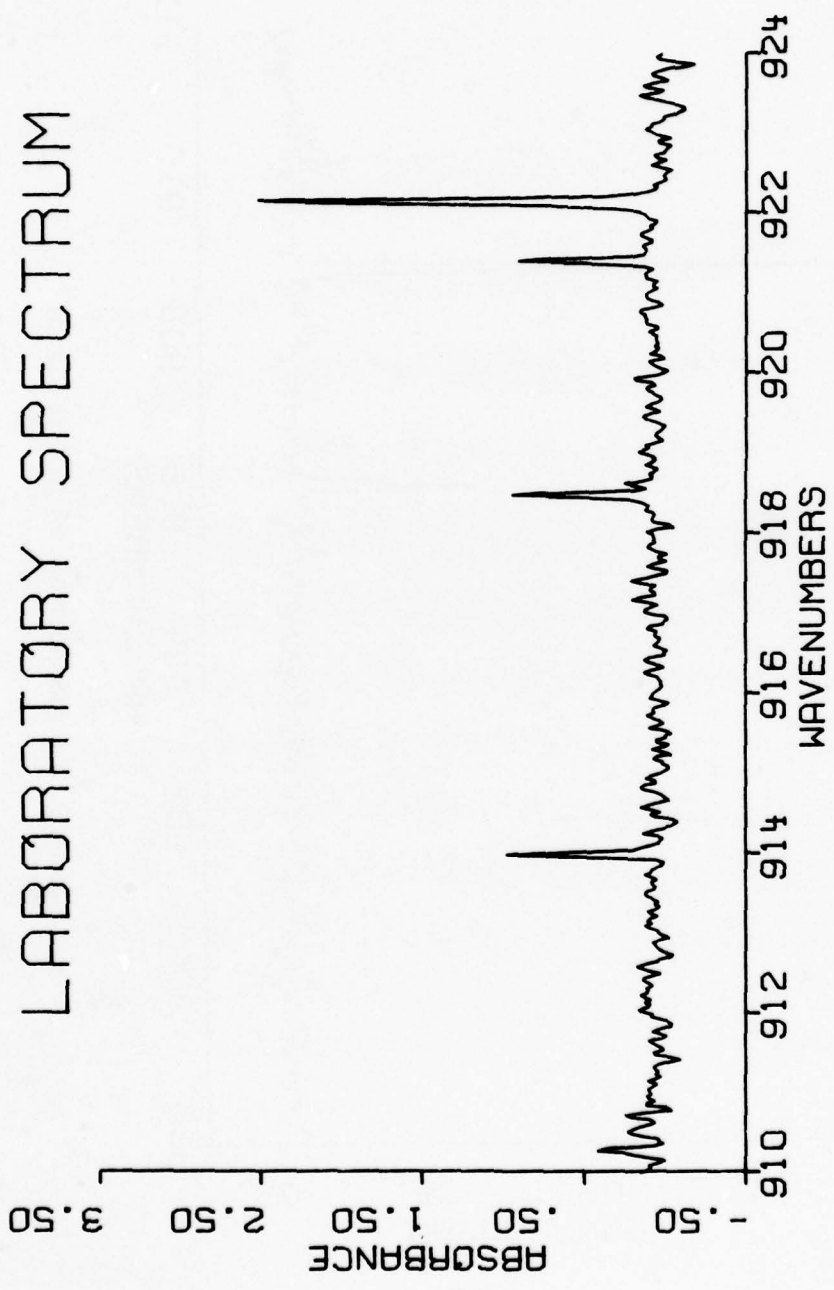


Figure 60. H_2O spectra from 910 cm^{-1} to 924 cm^{-1} .

LABORATORY SPECTRUM

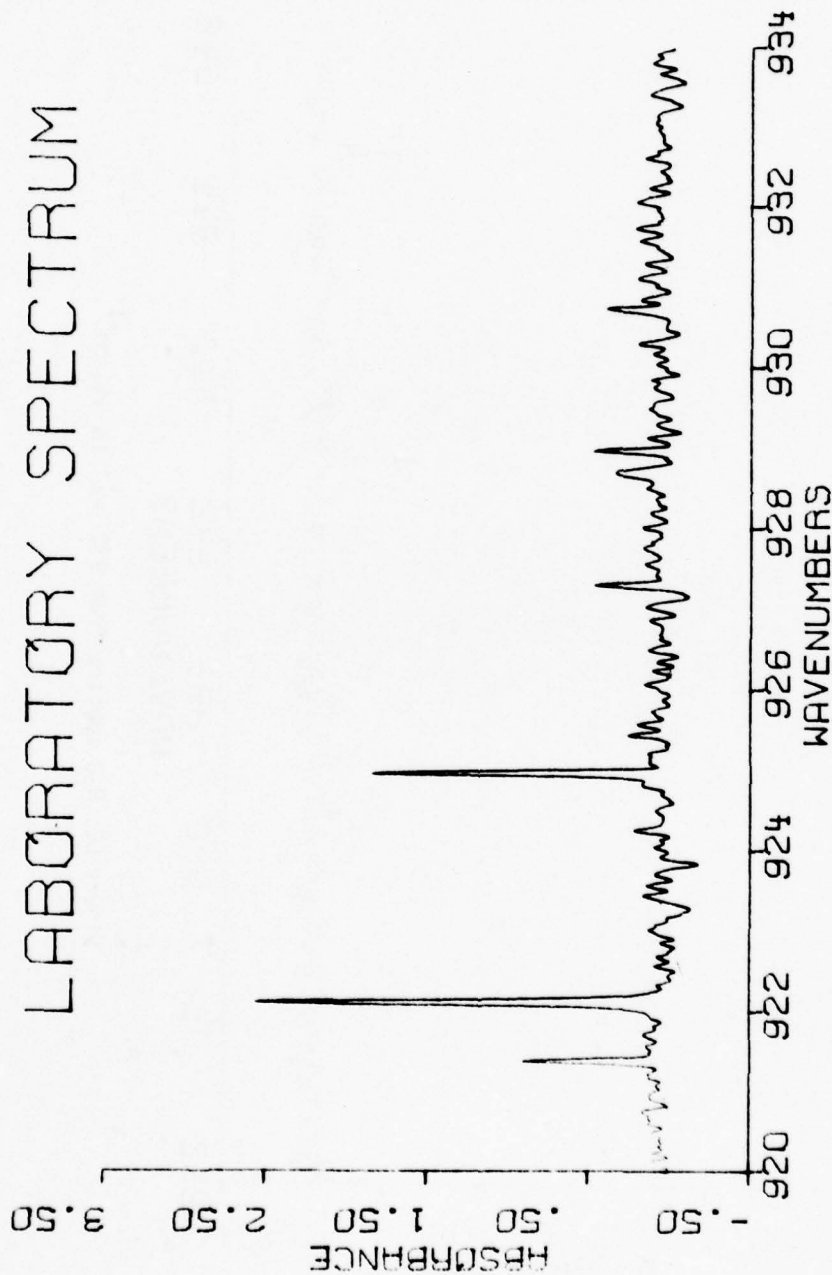


Figure 61. H₂O spectra from 920 cm⁻¹ to 934 cm⁻¹.

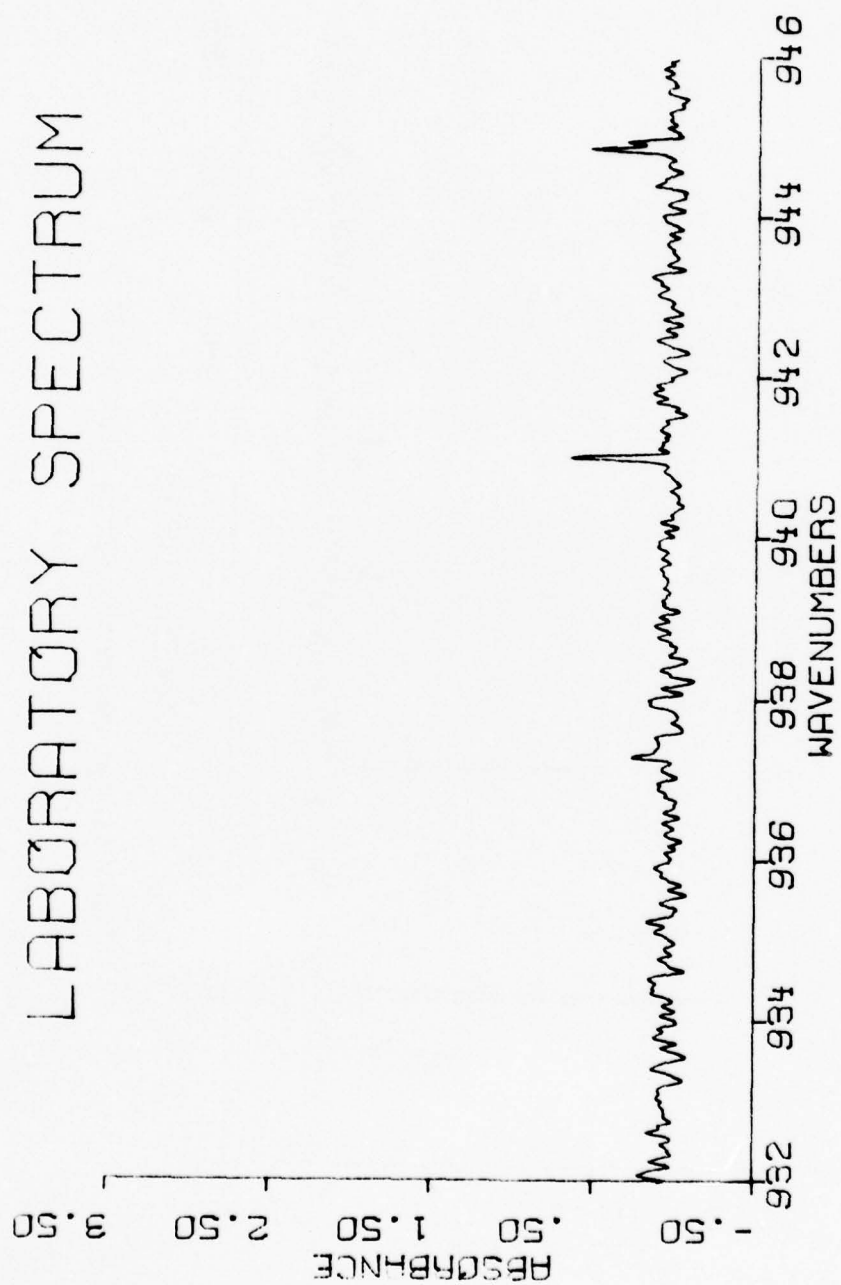


Figure 62. H_2O spectra from 932 cm^{-1} to 946 cm^{-1} .

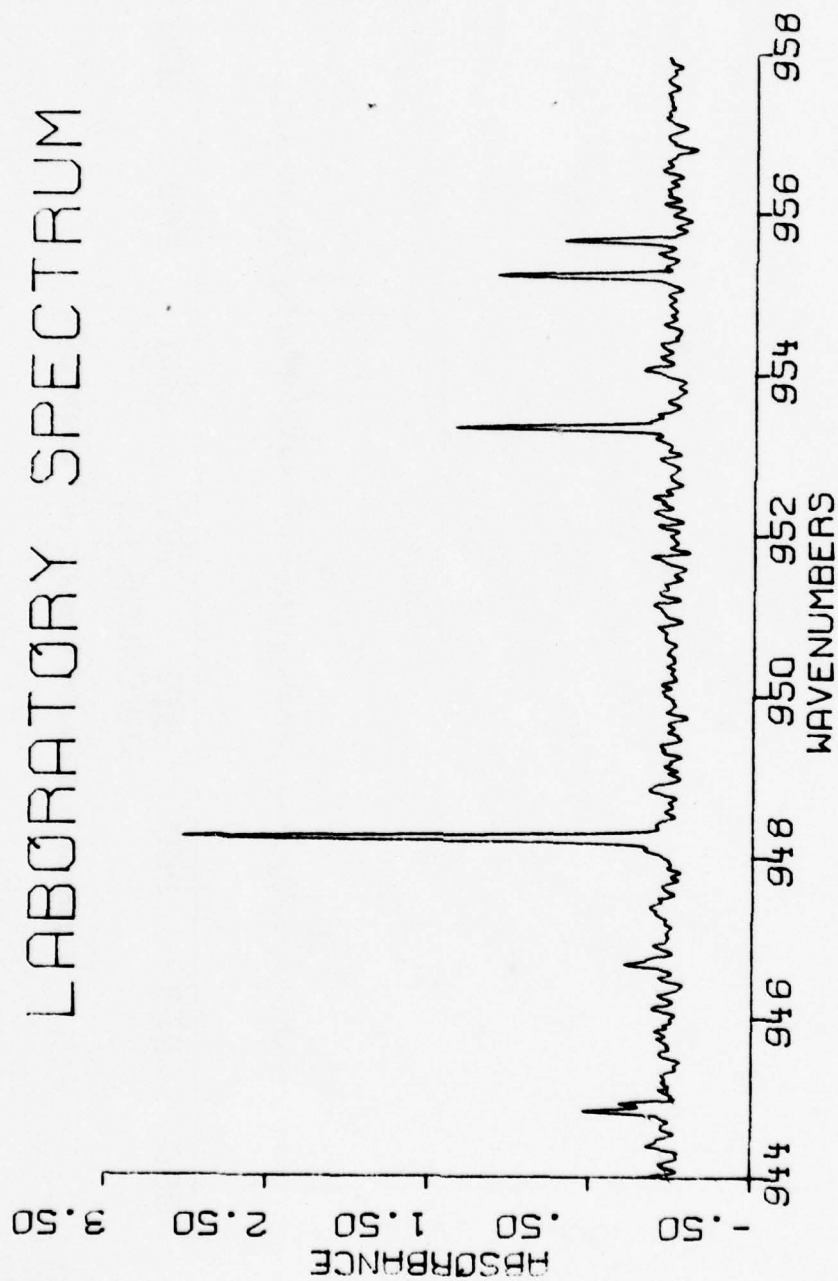


Figure 63. H₂O spectra from 944 cm⁻¹ to 958 cm⁻¹.

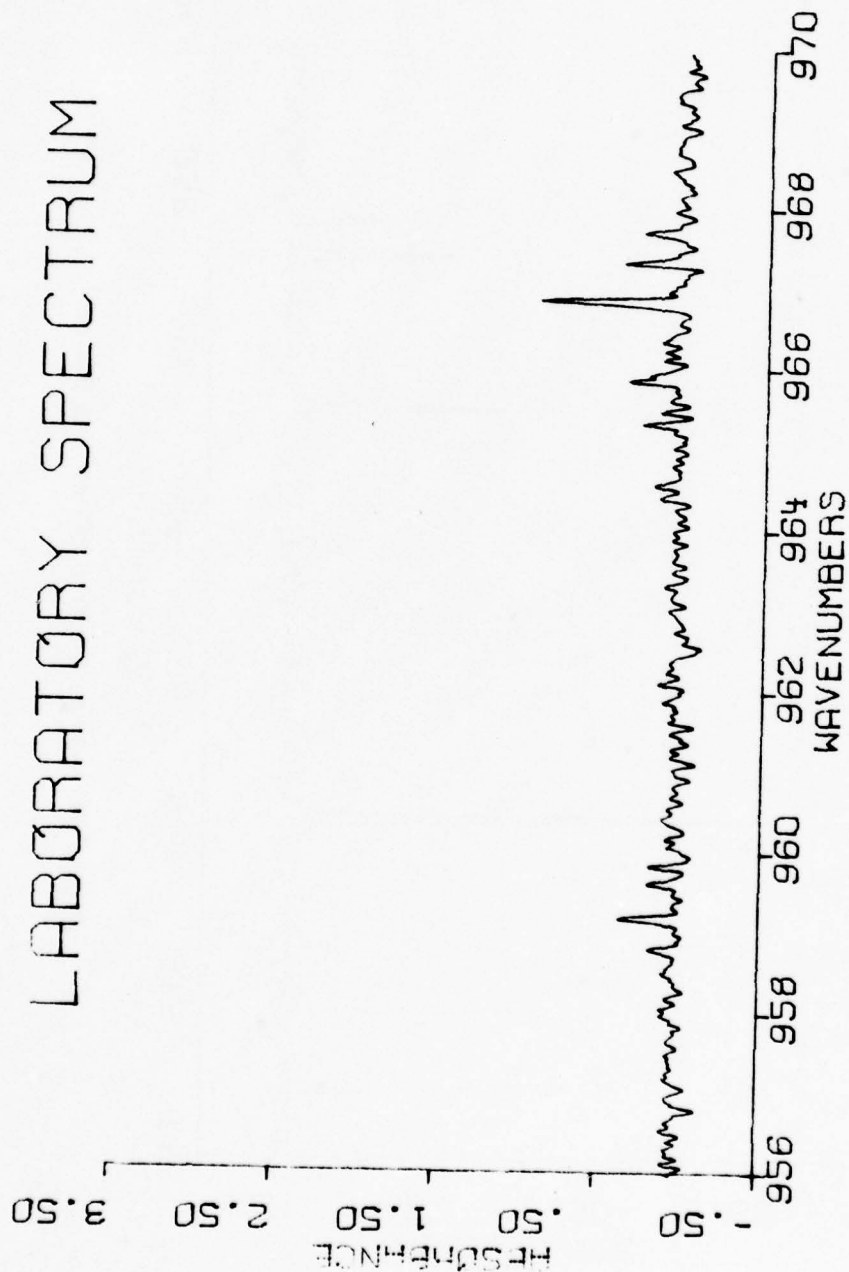


Figure 64. H₂O spectra from 956 cm⁻¹ to 970 cm⁻¹.

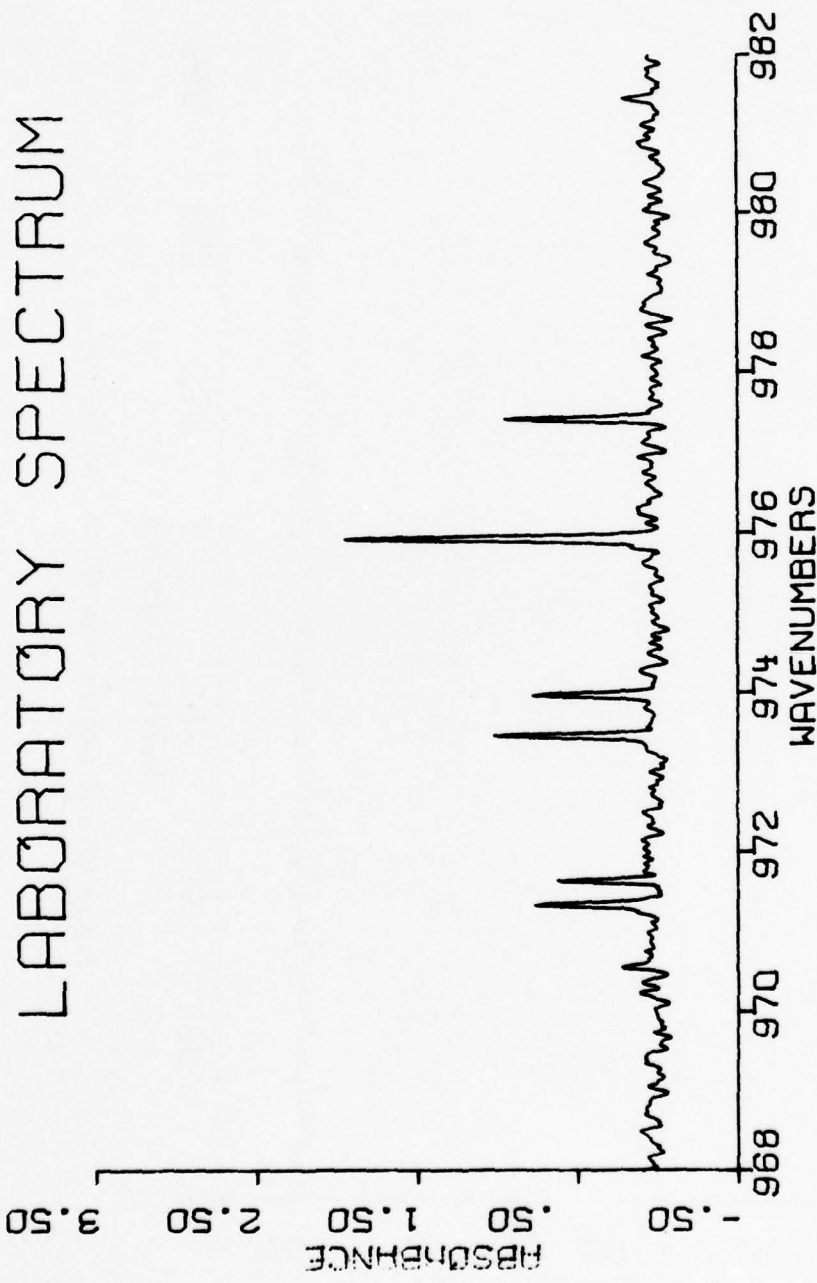


Figure 65. H₂O spectra from 968 cm⁻¹ to 982 cm⁻¹.

LABORATORY SPECTRUM

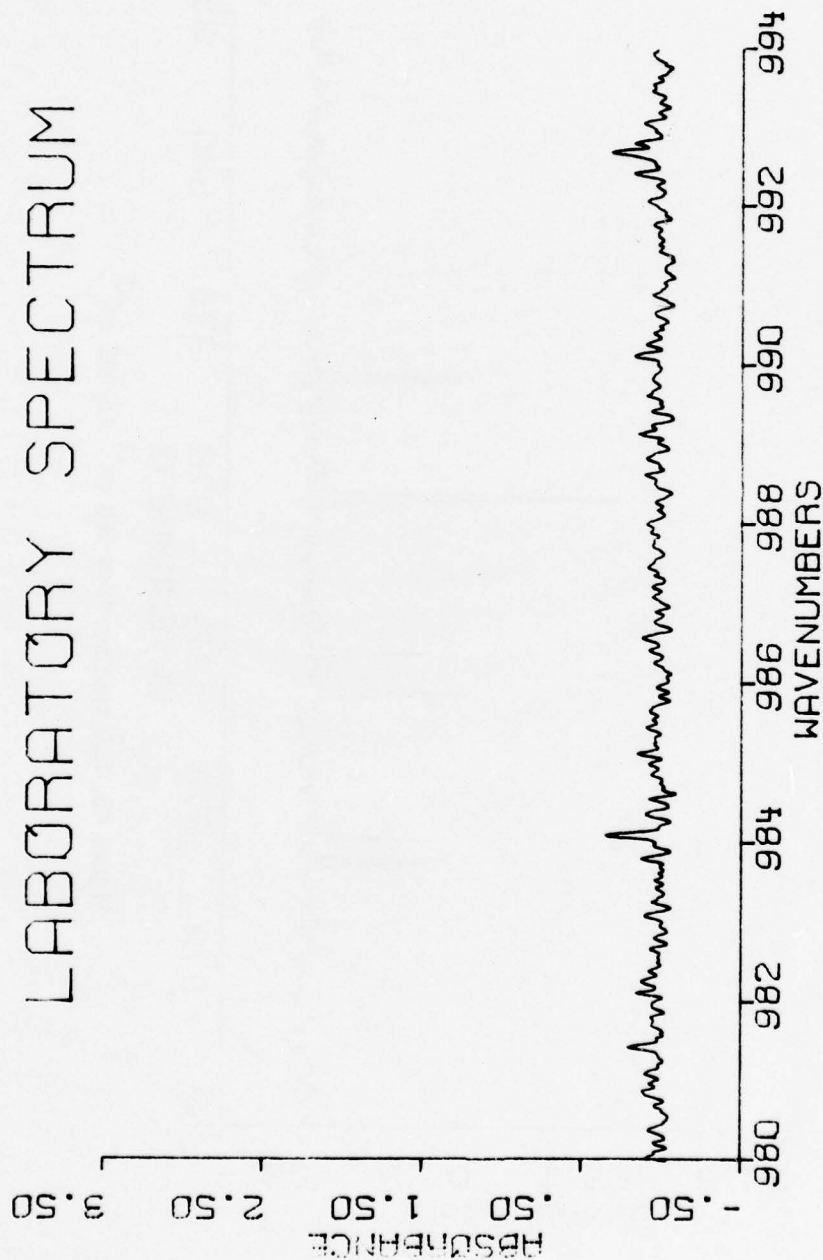


Figure 66. H₂O spectra from 980 cm⁻¹ to 994 cm⁻¹.



Figure 67. H_2O spectra from 992 cm^{-1} to 1006 cm^{-1} .

LABORATORY SPECTRUM



Figure 68. H_2O spectra from 1004 cm^{-1} to 1018 cm^{-1} .

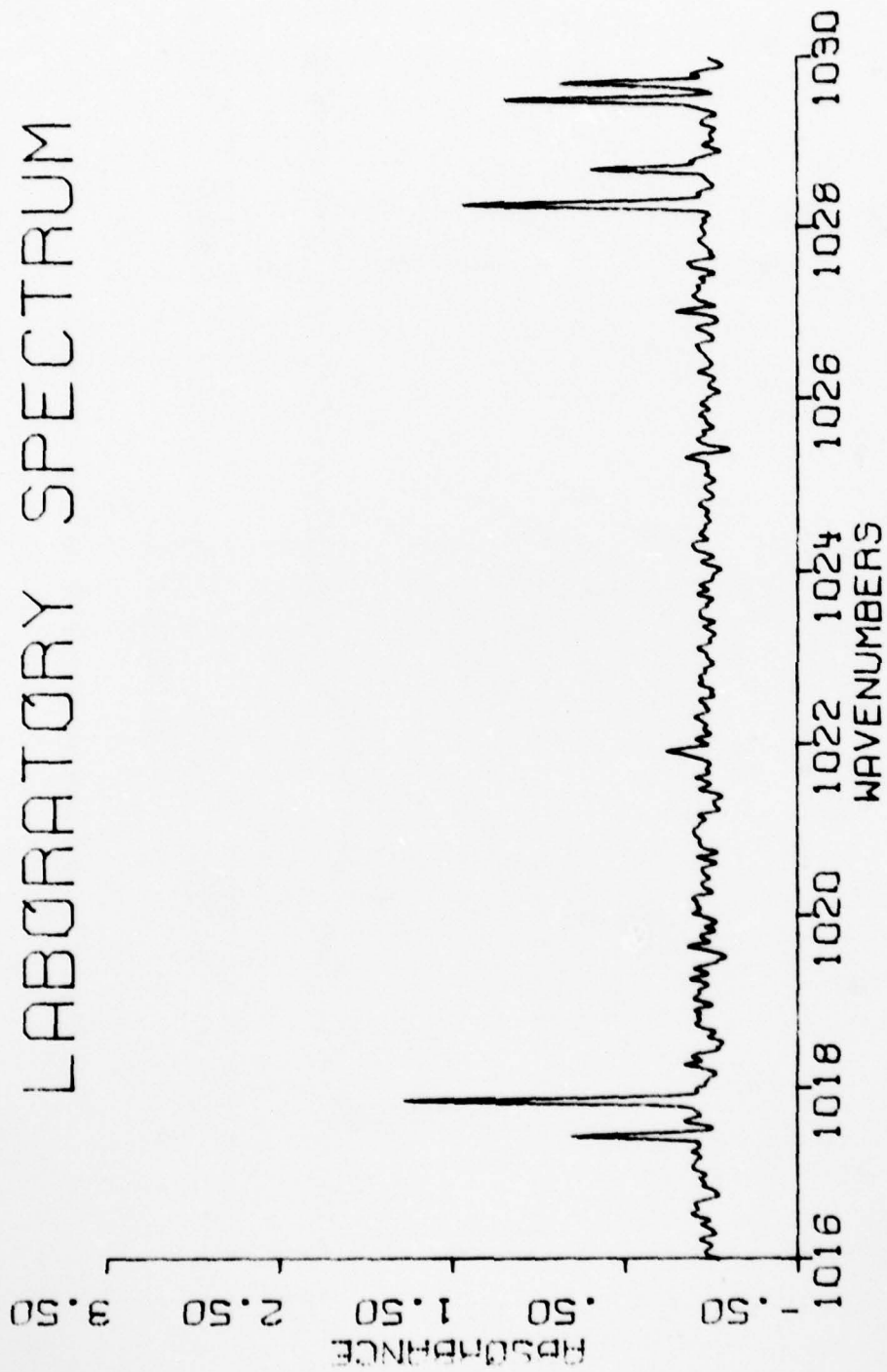


Figure 69. H_2O spectra from 1016 cm^{-1} to 1030 cm^{-1} .

LABORATORY SPECTRUM



Figure 70. H₂O spectra from 1028 cm⁻¹ to 1042 cm⁻¹.



Figure 71. H_2O spectra from 1040 cm^{-1} to 1054 cm^{-1} .

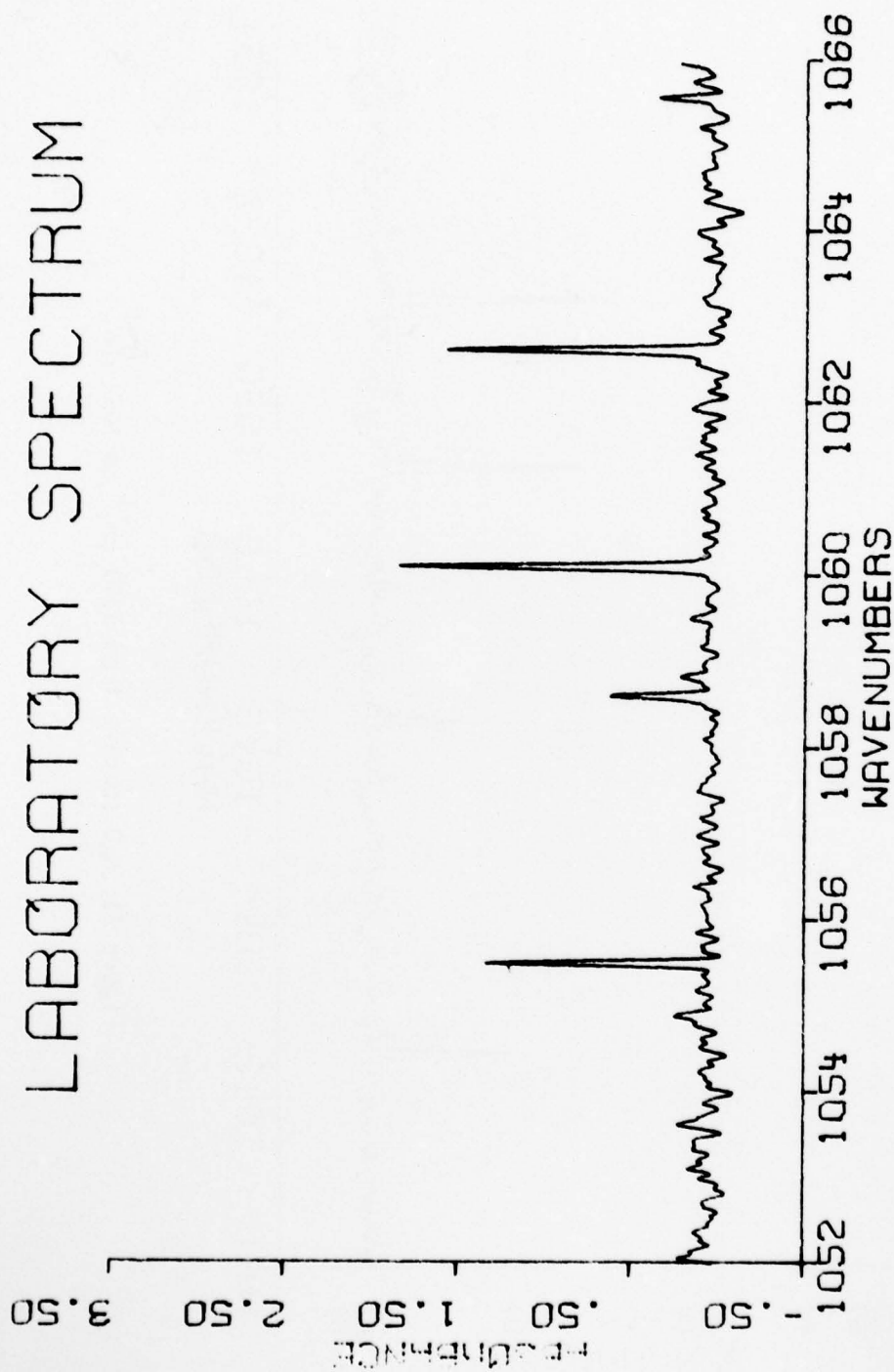


Figure 72. H_2O spectra from 1052 cm^{-1} to 1066 cm^{-1} .

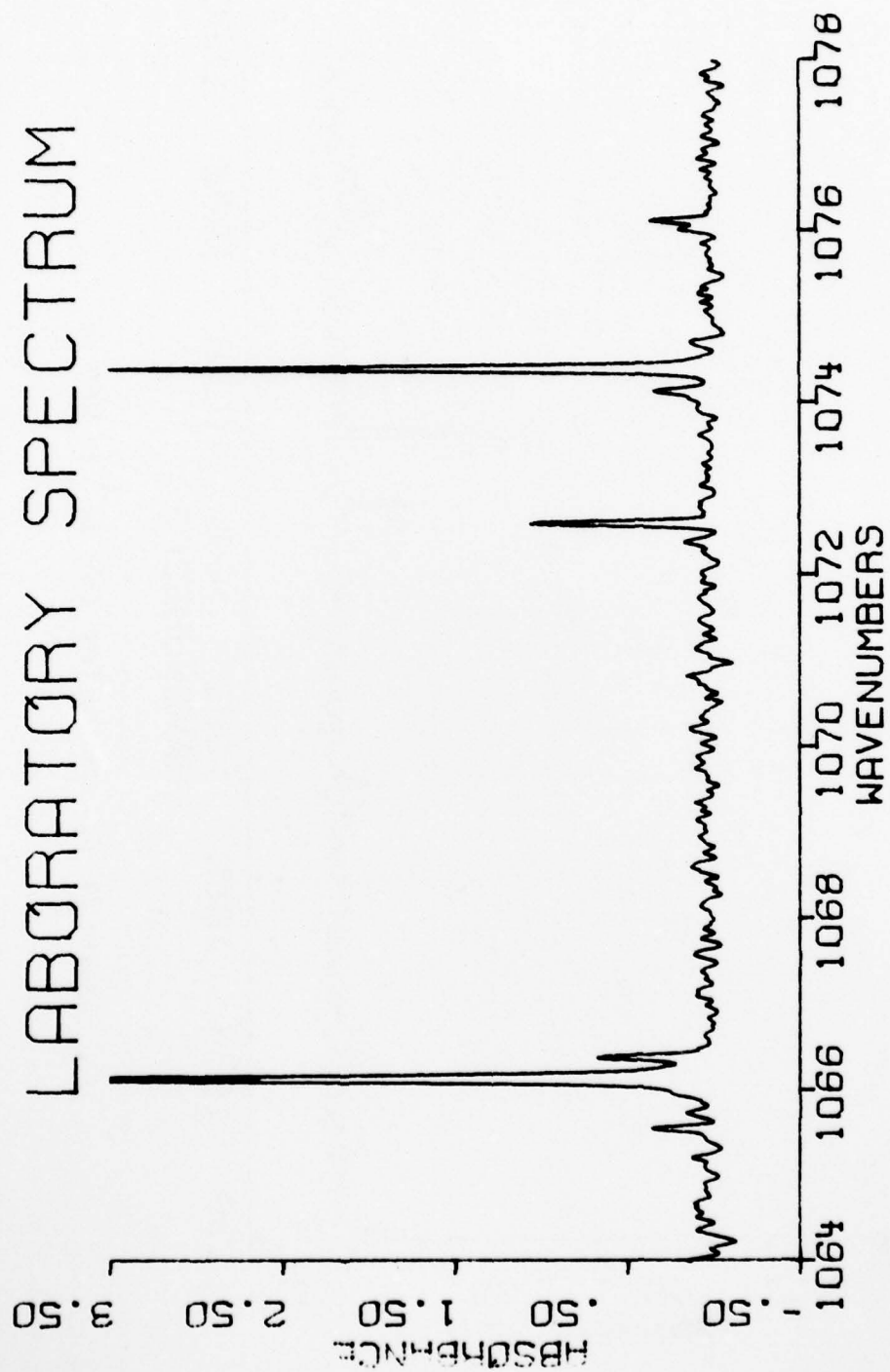


Figure 73. H_2O spectra from 1064 cm^{-1} to 1073 cm^{-1} .

LABORATORY SPECTRUM

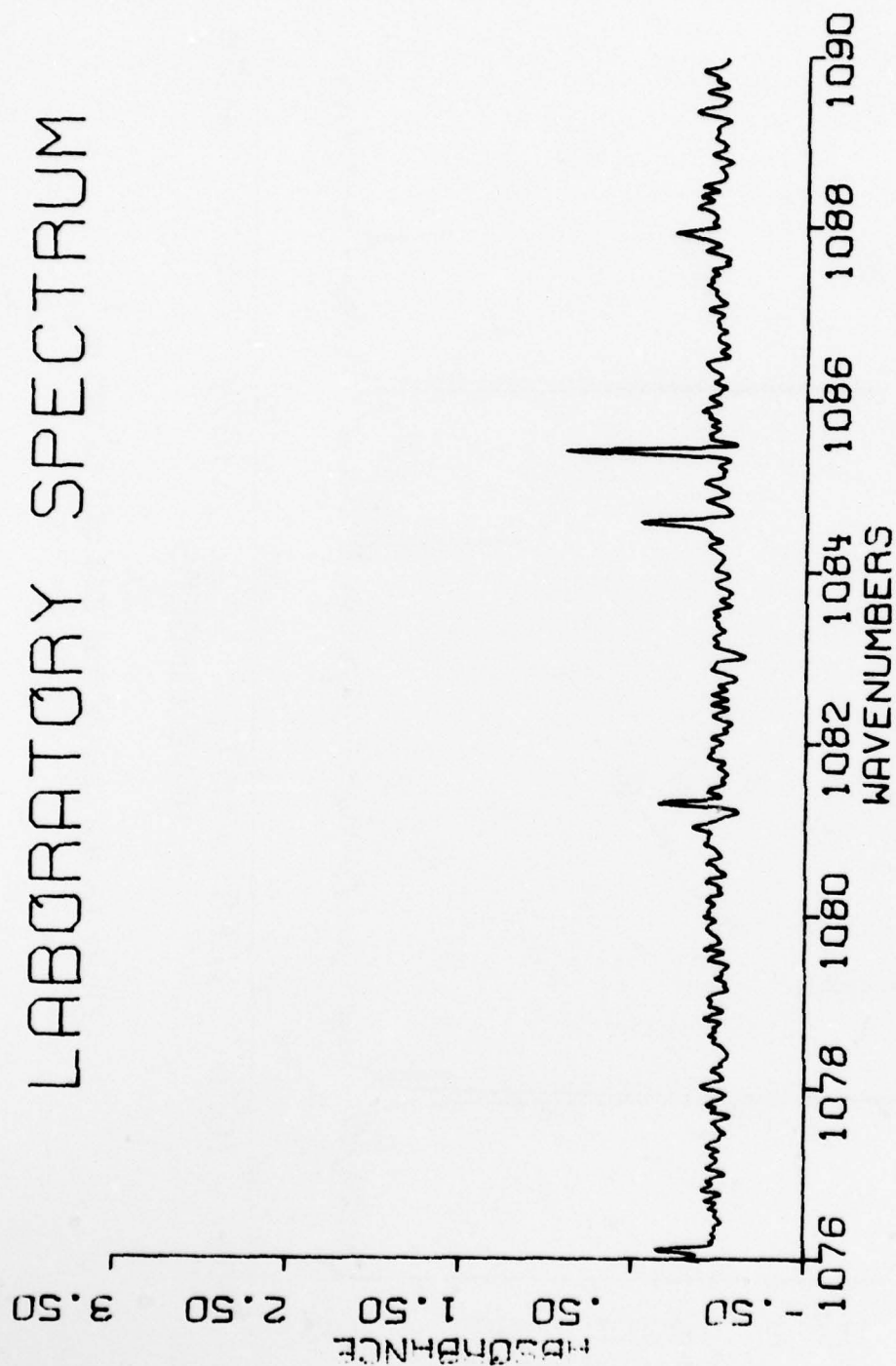


Figure 74. H₂O spectra from 1076 cm⁻¹ to 1090 cm⁻¹.

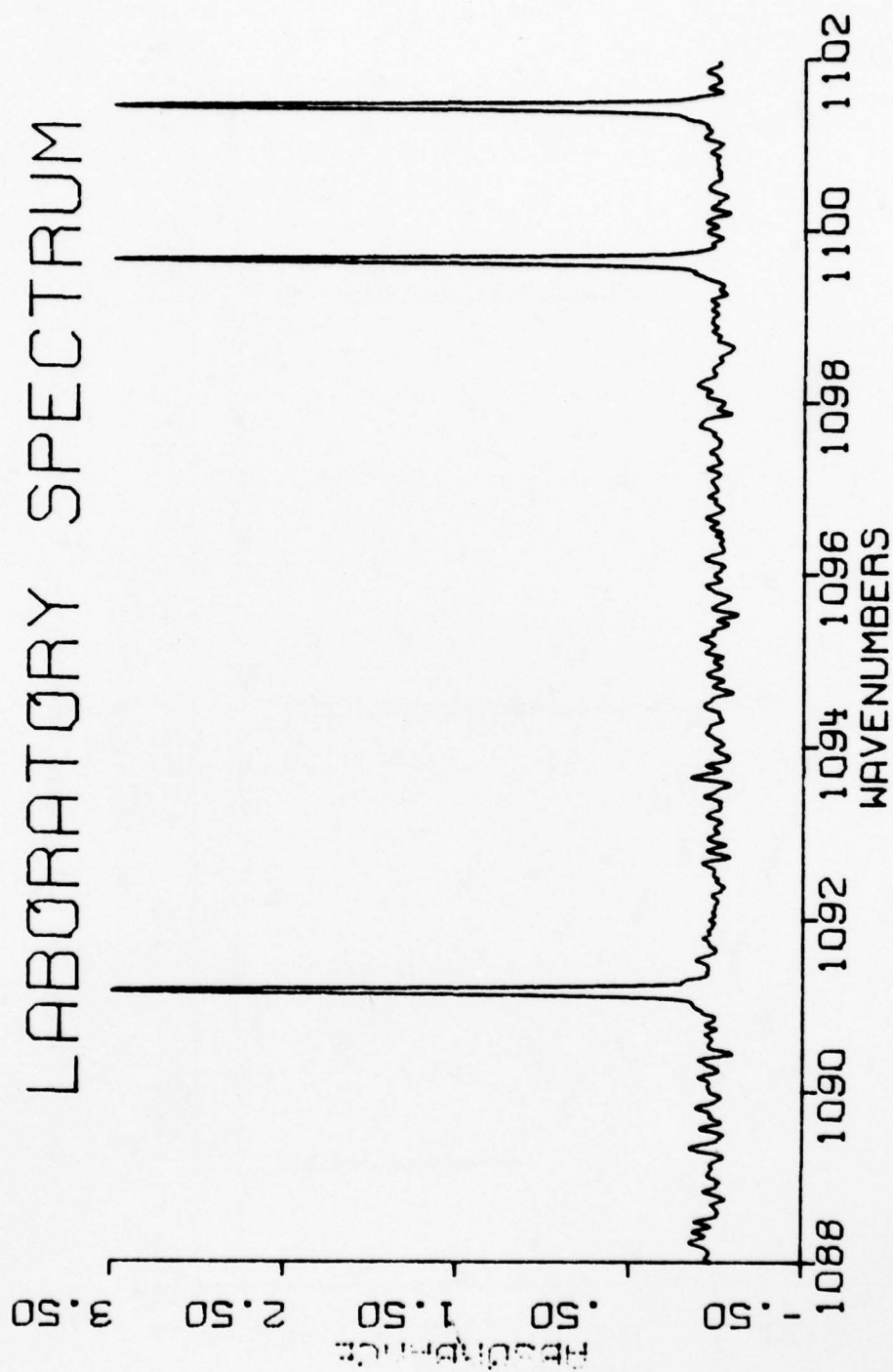


Figure 75. H_2O spectra from 1088 cm^{-1} to 1102 cm^{-1} .

LABORATORY SPECTRUM

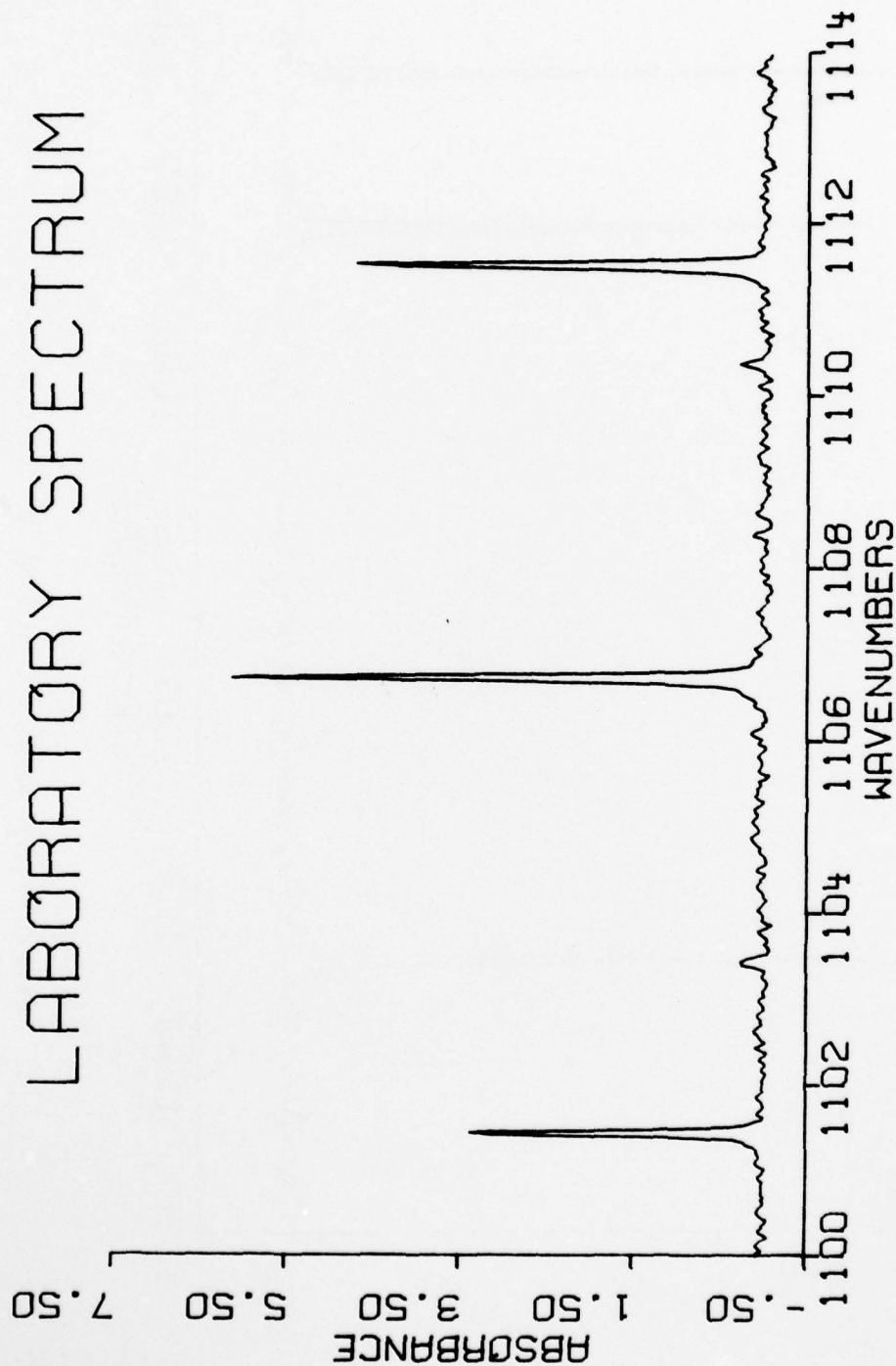


Figure 76. H_2O spectra from 1100 cm^{-1} to 1114 cm^{-1} .

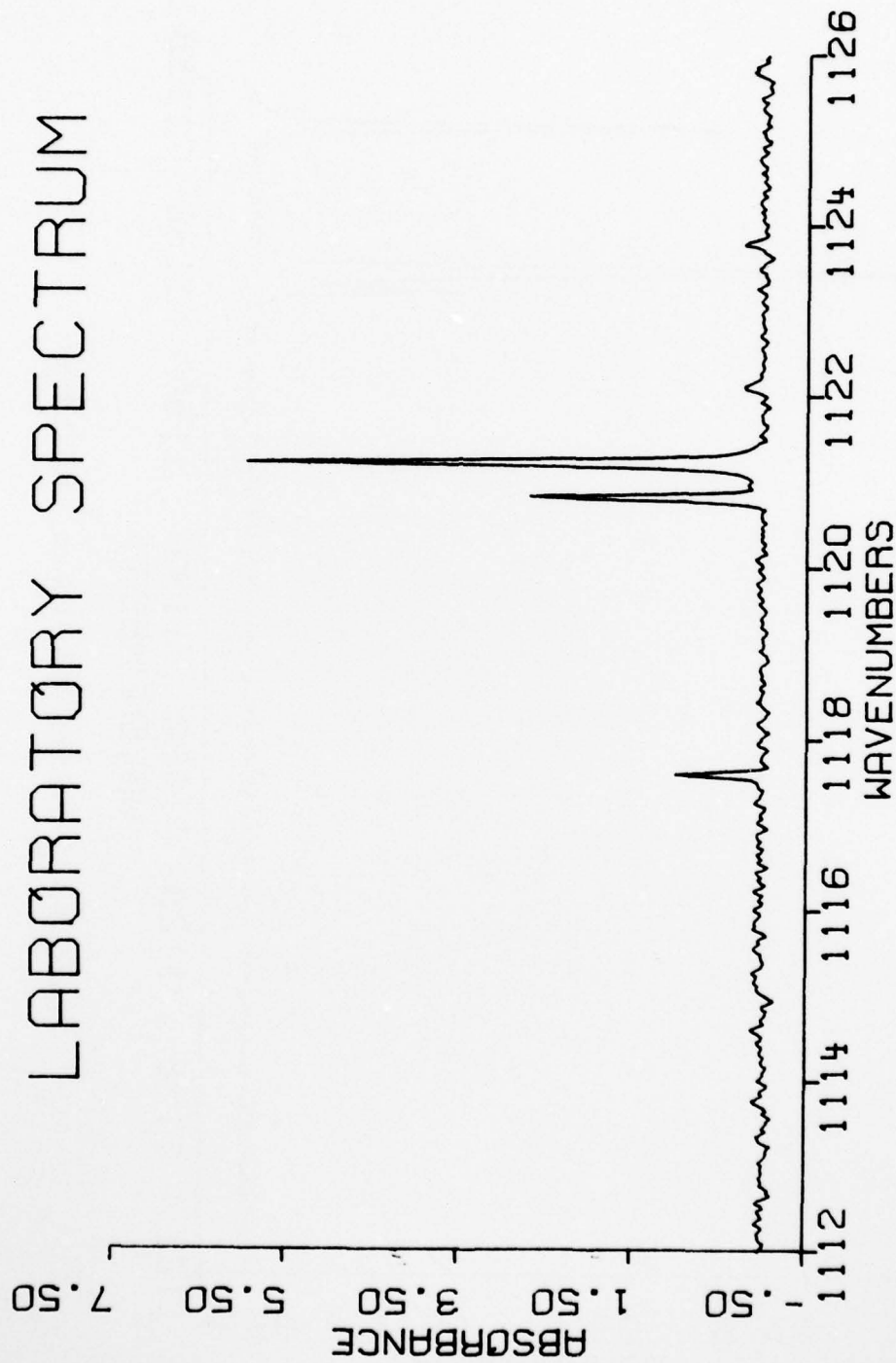


Figure 77. H_2O spectra from 1112 cm^{-1} to 1126 cm^{-1} .

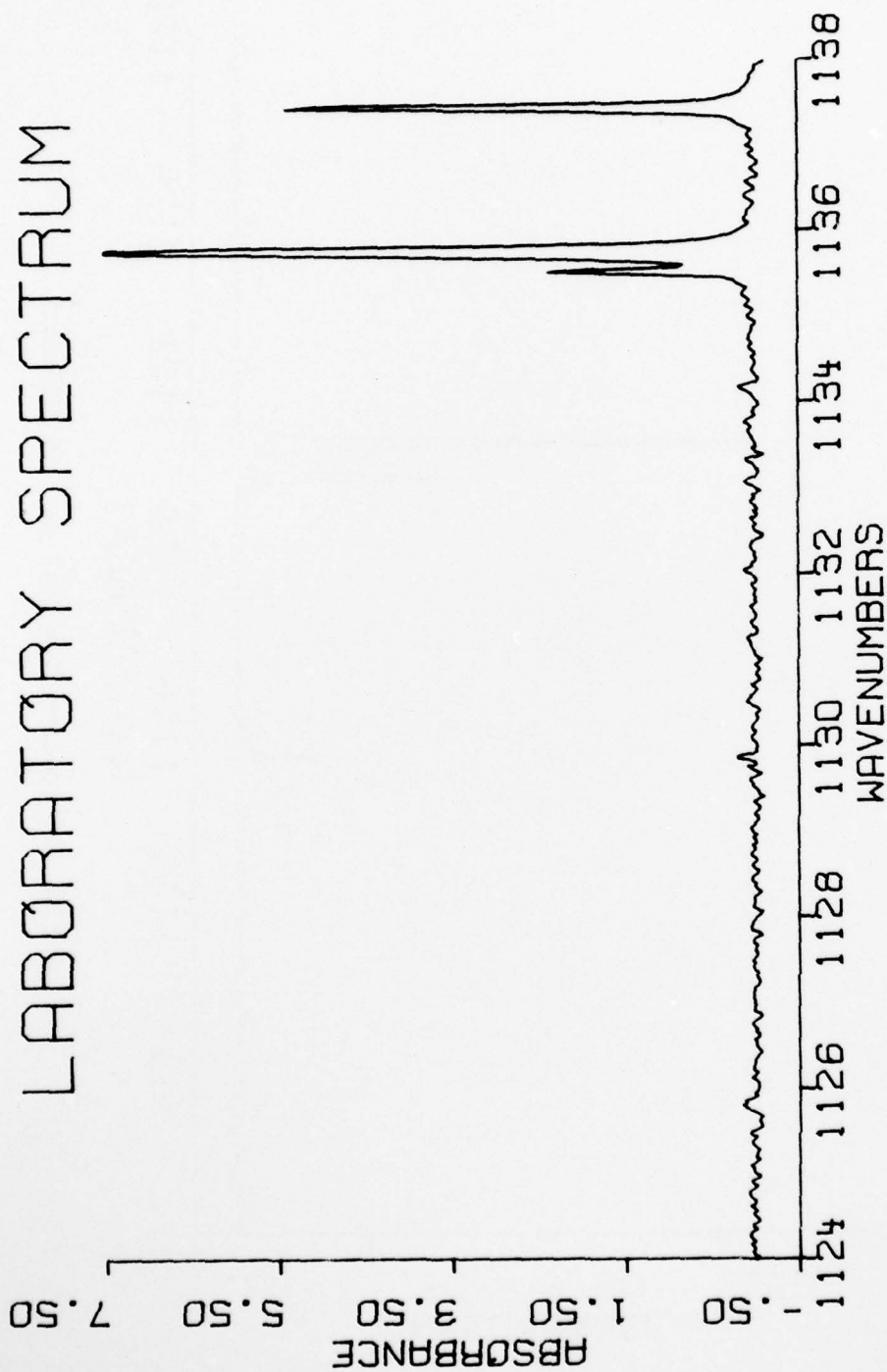


Figure 78. H₂O spectra from 1124 cm⁻¹ to 1138 cm⁻¹.

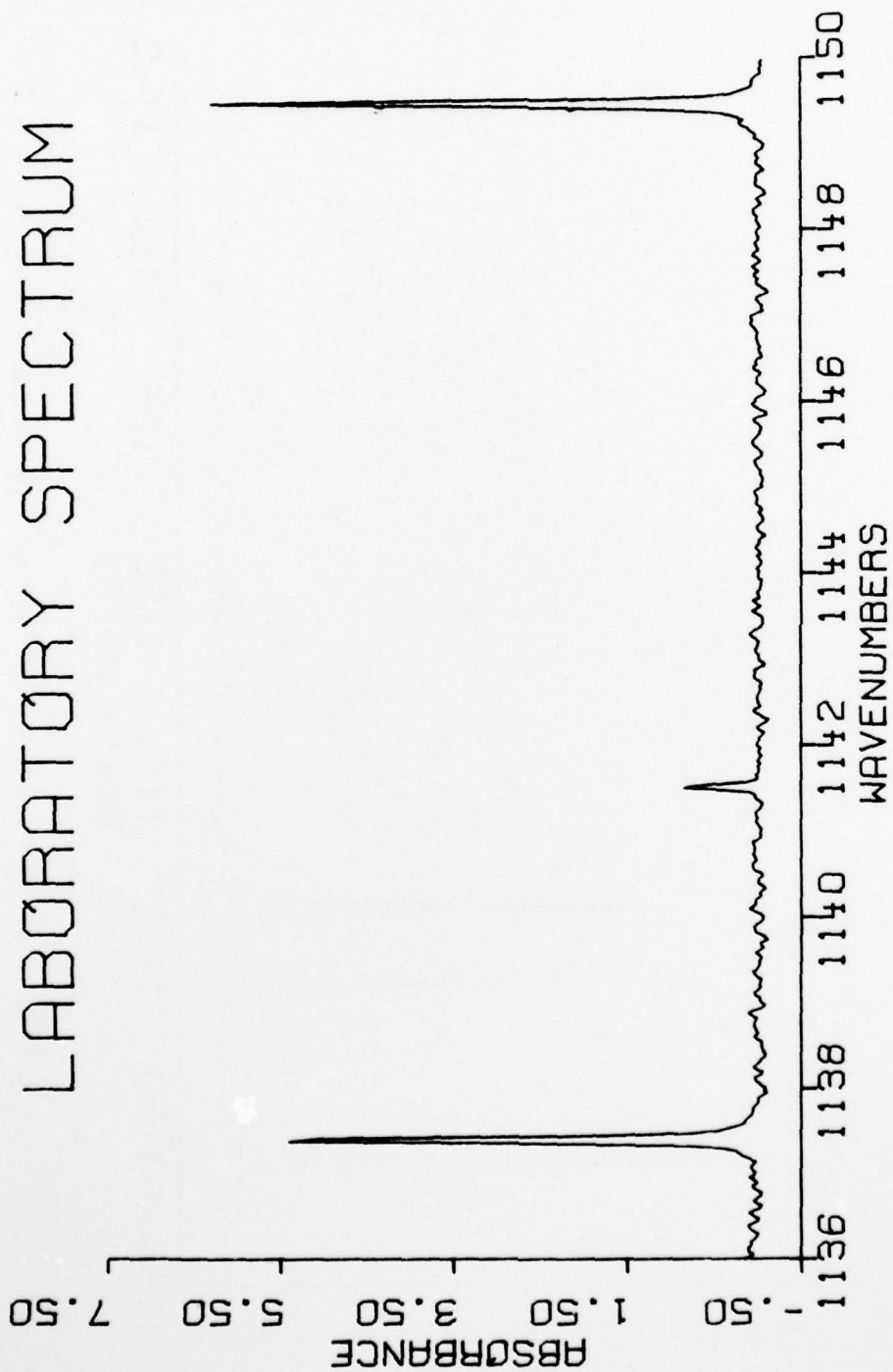


Figure 79. H_2O spectra from 1136 cm^{-1} to 1150 cm^{-1} .

LABORATORY SPECTRUM

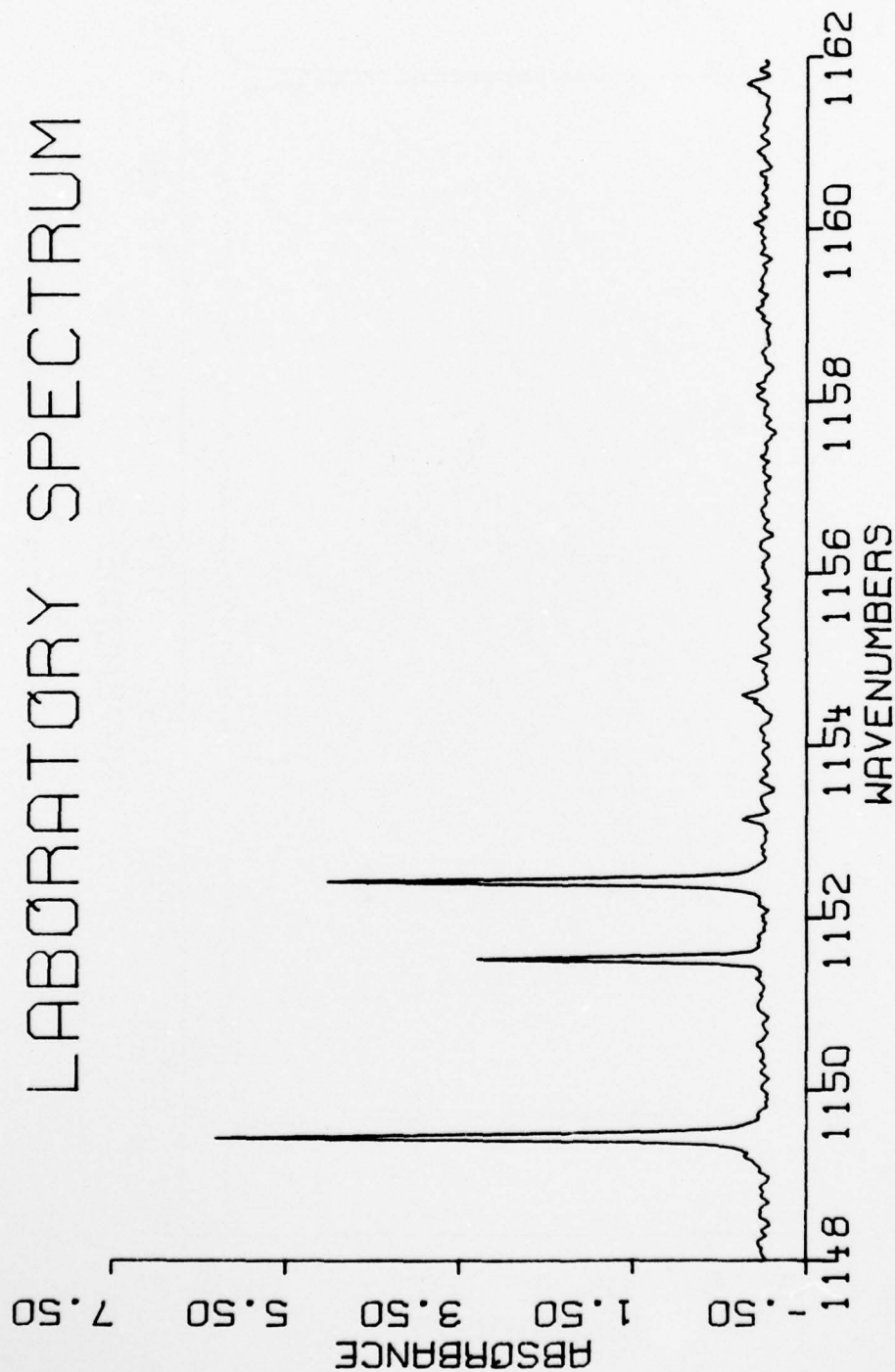


Figure 80. H_2O spectra from 1148 cm^{-1} to 1162 cm^{-1} .



Figure 81. H_2O spectra from 1160 cm^{-1} to 1174 cm^{-1} .

AD-A076 267

OHIO STATE UNIV COLUMBUS ELECTROSCIENCE LAB

F/G 4/1

TROPOSPHERIC WATER VAPOR ABSORPTION IN THE INFRARED WINDOW REGI--ETC(U)

AUG 79 M E THOMAS

DAAG29-77-C-0010

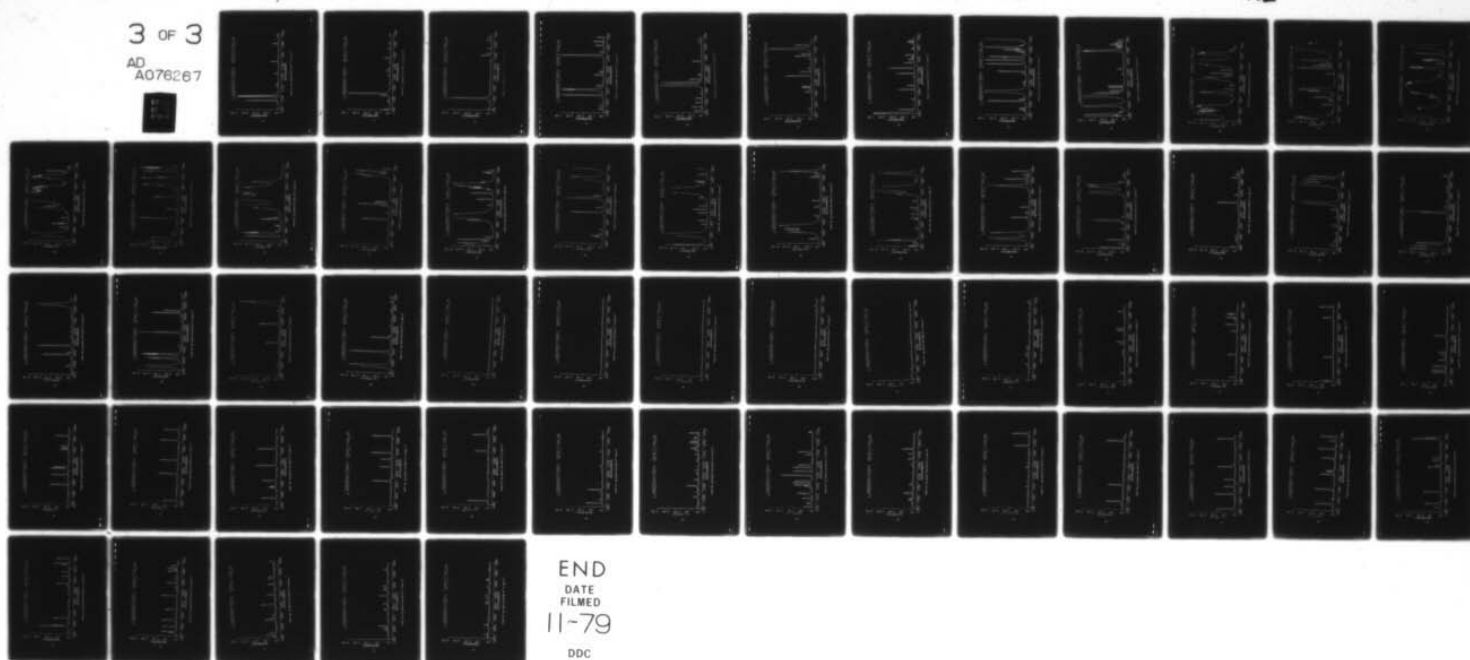
UNCLASSIFIED ESL-784701-5

ARO-14702.4-6S

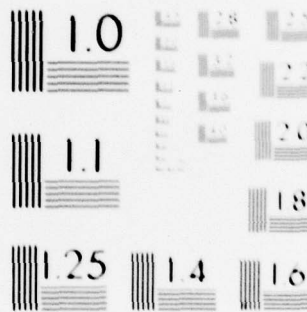
NL

3 OF 3

AD
A076267



END
DATE
FILMED
11-79
DDC



MICROCOPY RESOLUTION TEST CHART
NATIONAL BUREAU OF STANDARDS-1963-A

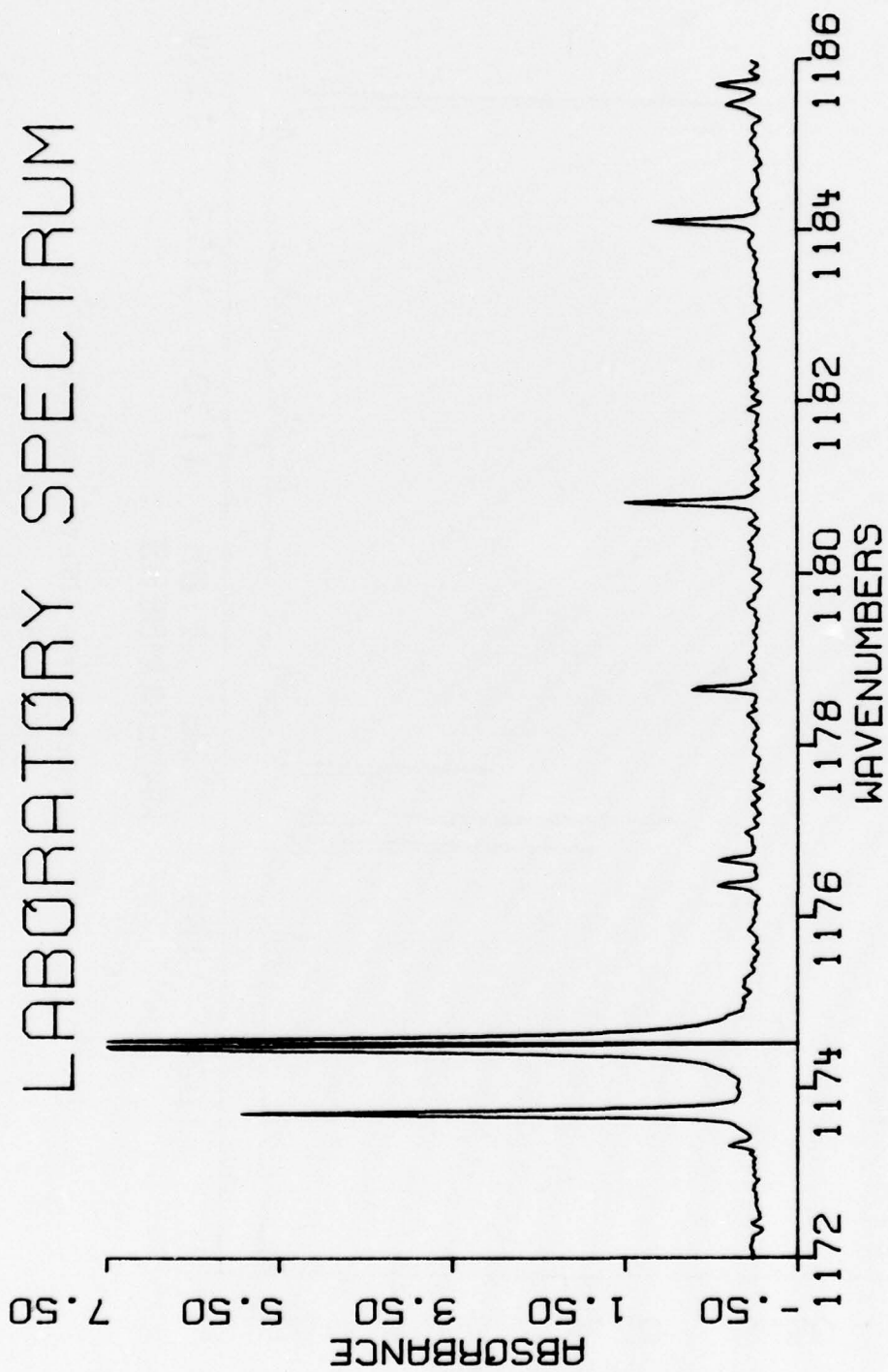


Figure 32. H_2O spectra from 1172 cm^{-1} to 1186 cm^{-1} .

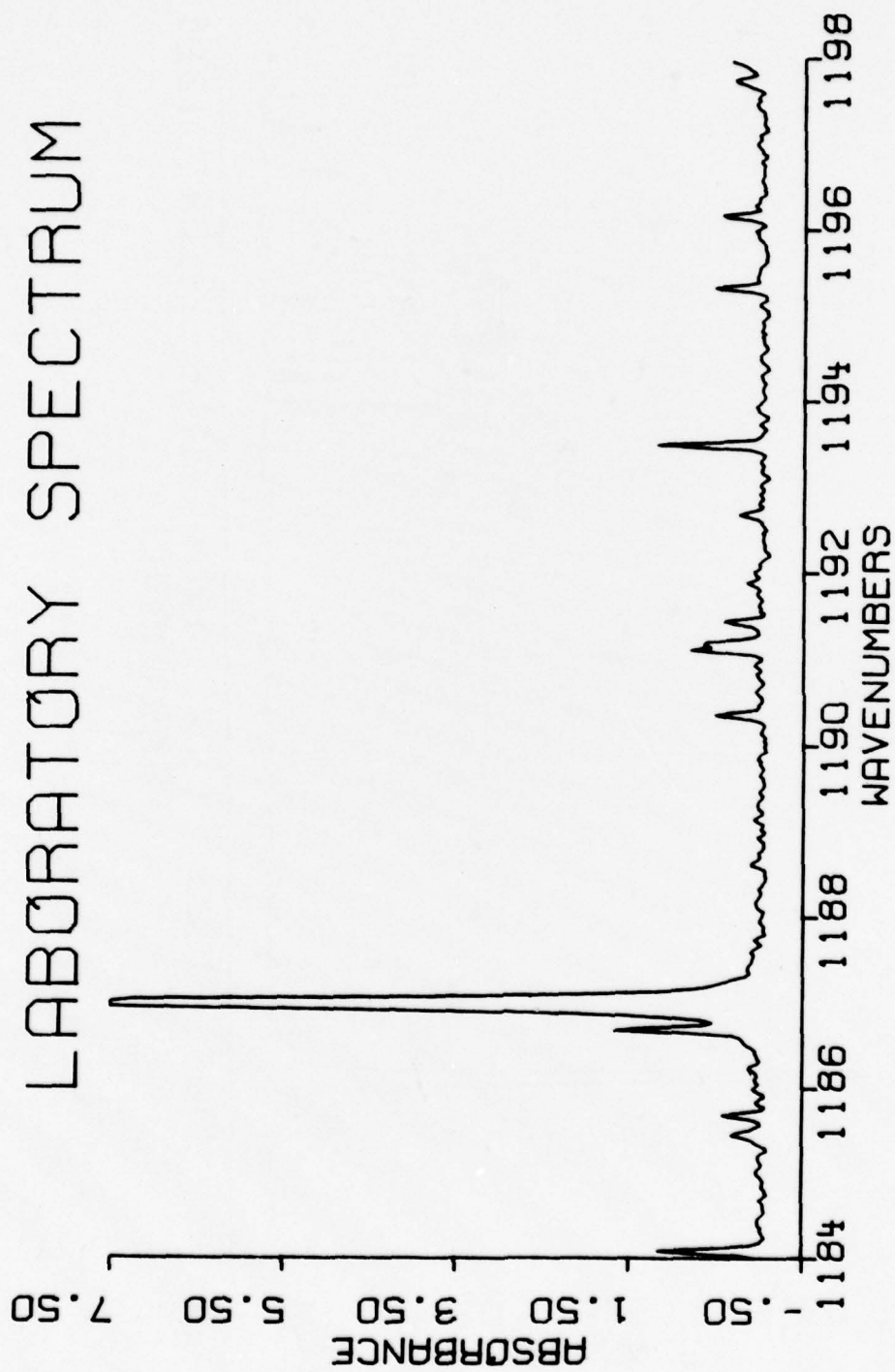


Figure 83. H_2O spectra from 1184 cm^{-1} to 1198 cm^{-1} .

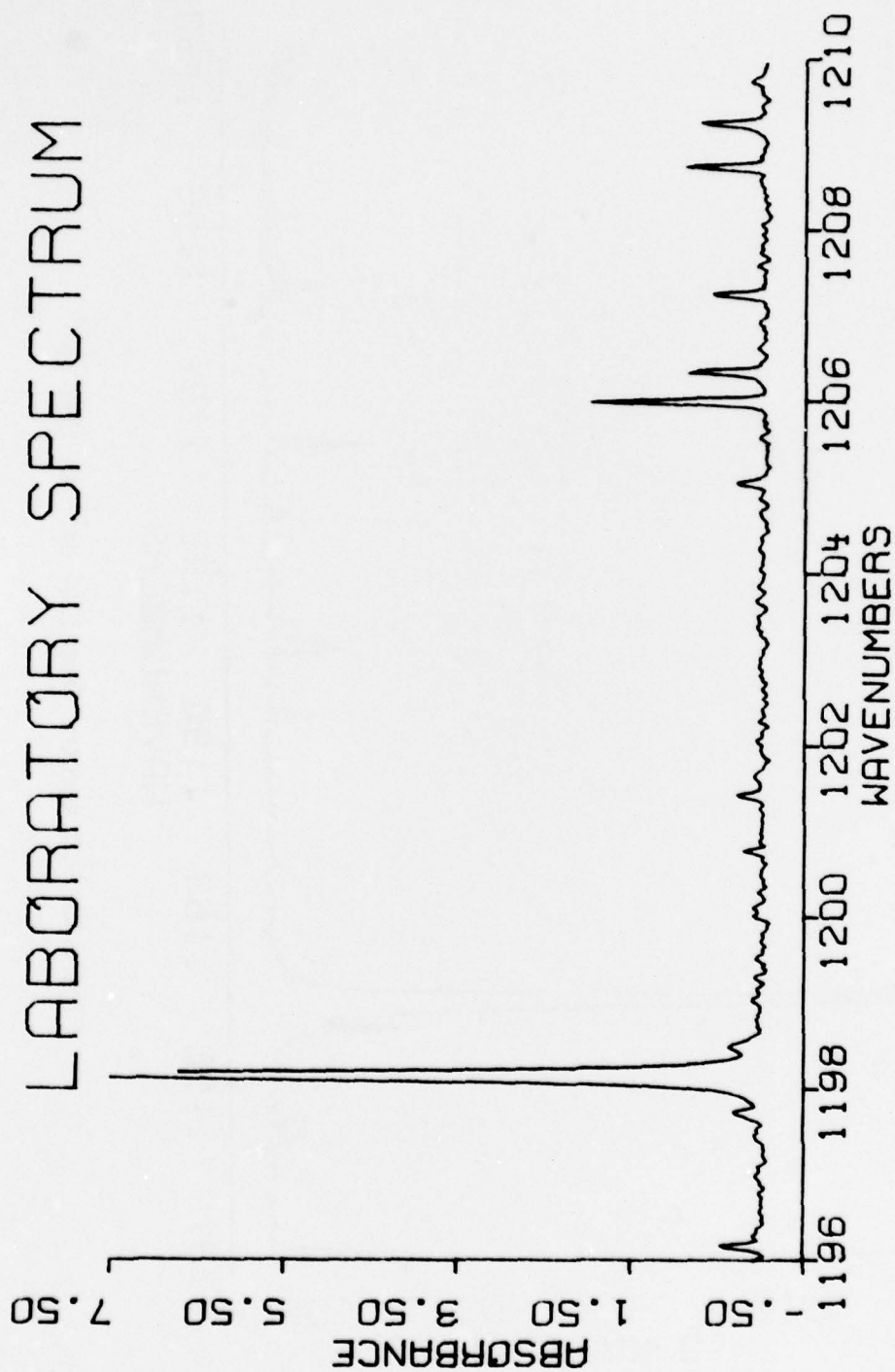


Figure 34. H_2O spectra from 1196 cm^{-1} to 1210 cm^{-1} .

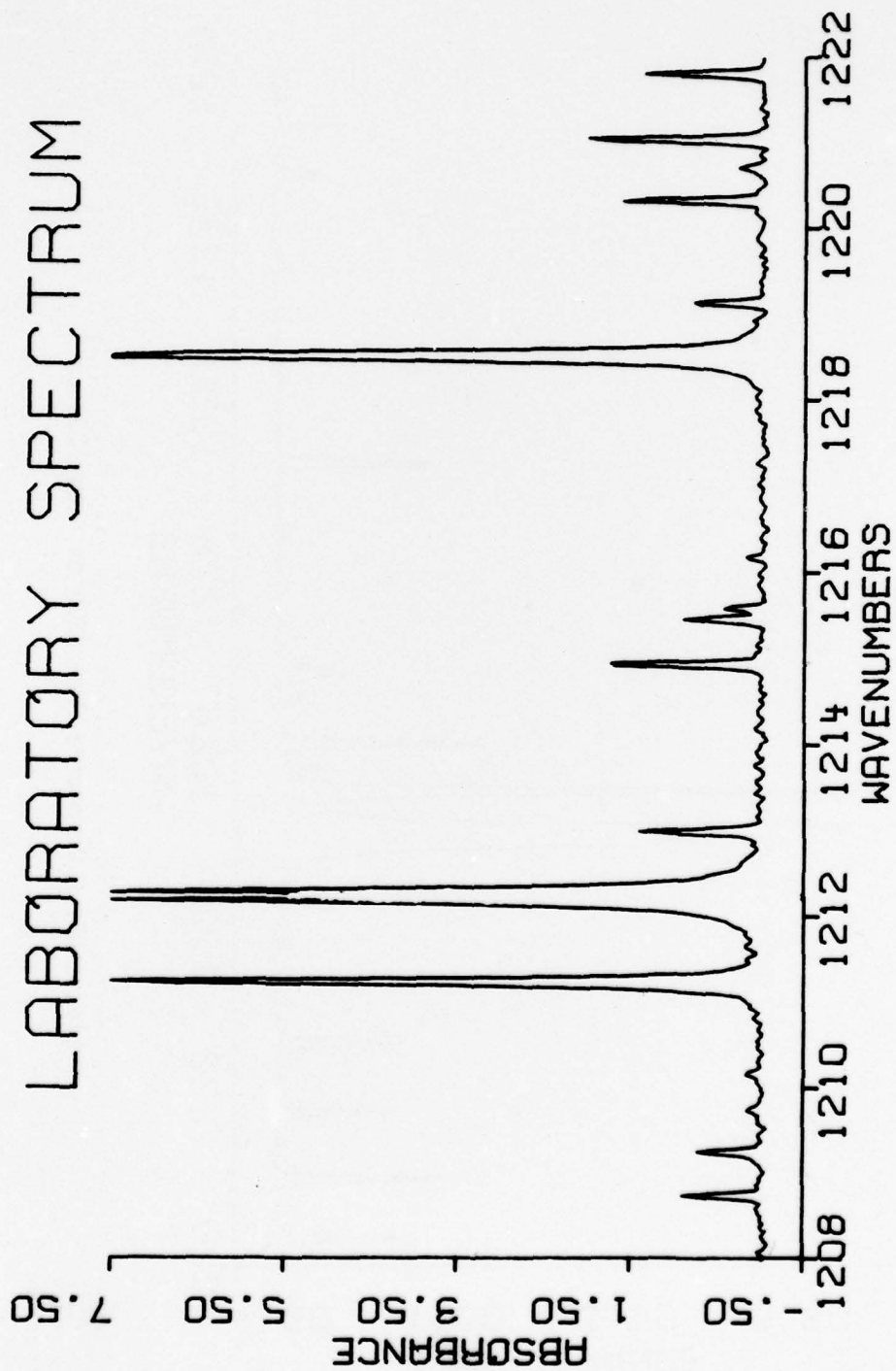


Figure 35. H_2O spectra from 1203 cm^{-1} to 1222 cm^{-1} .

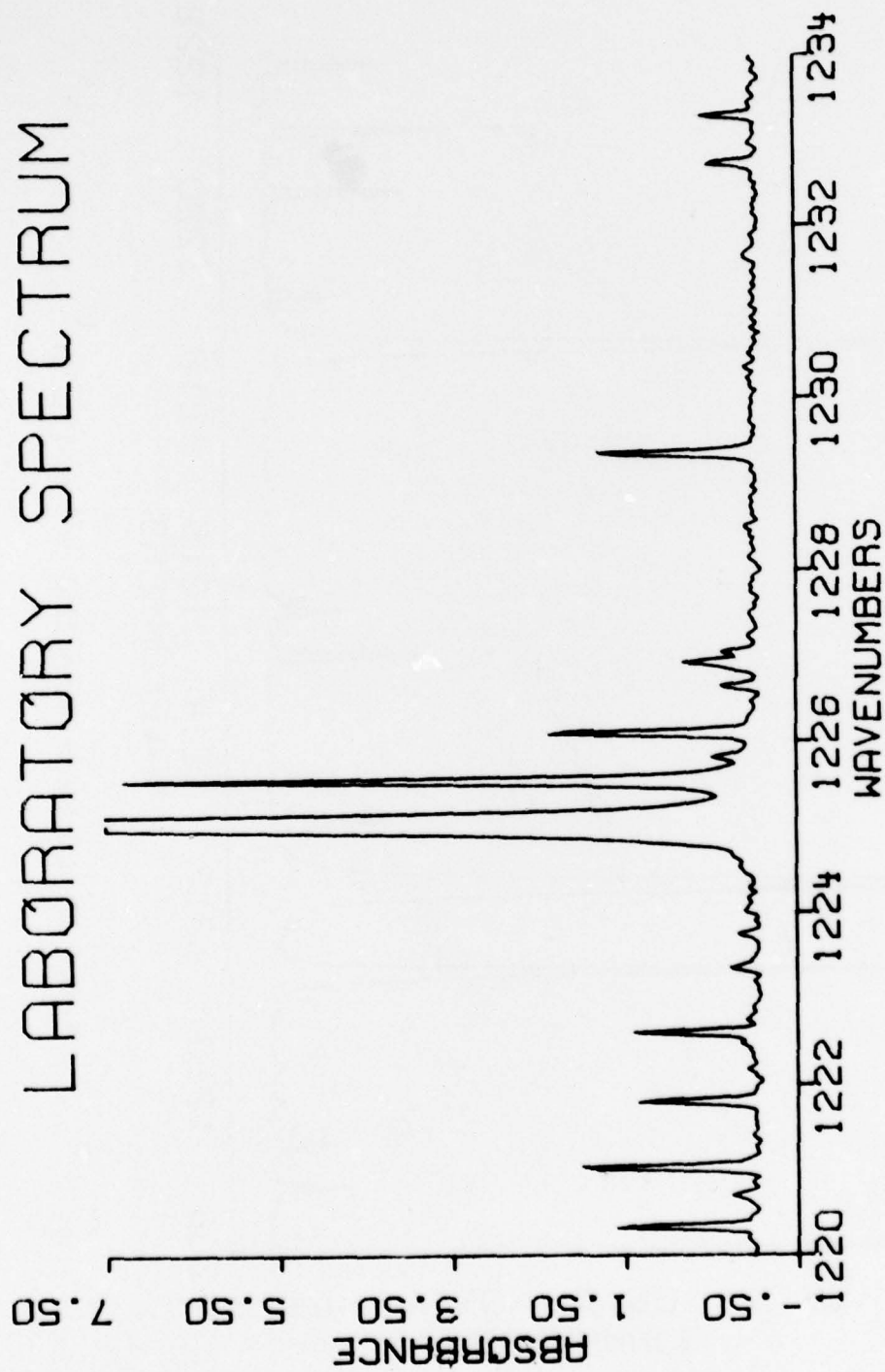


Figure 36. H_2O spectra from 1220 cm^{-1} to 1234 cm^{-1} .

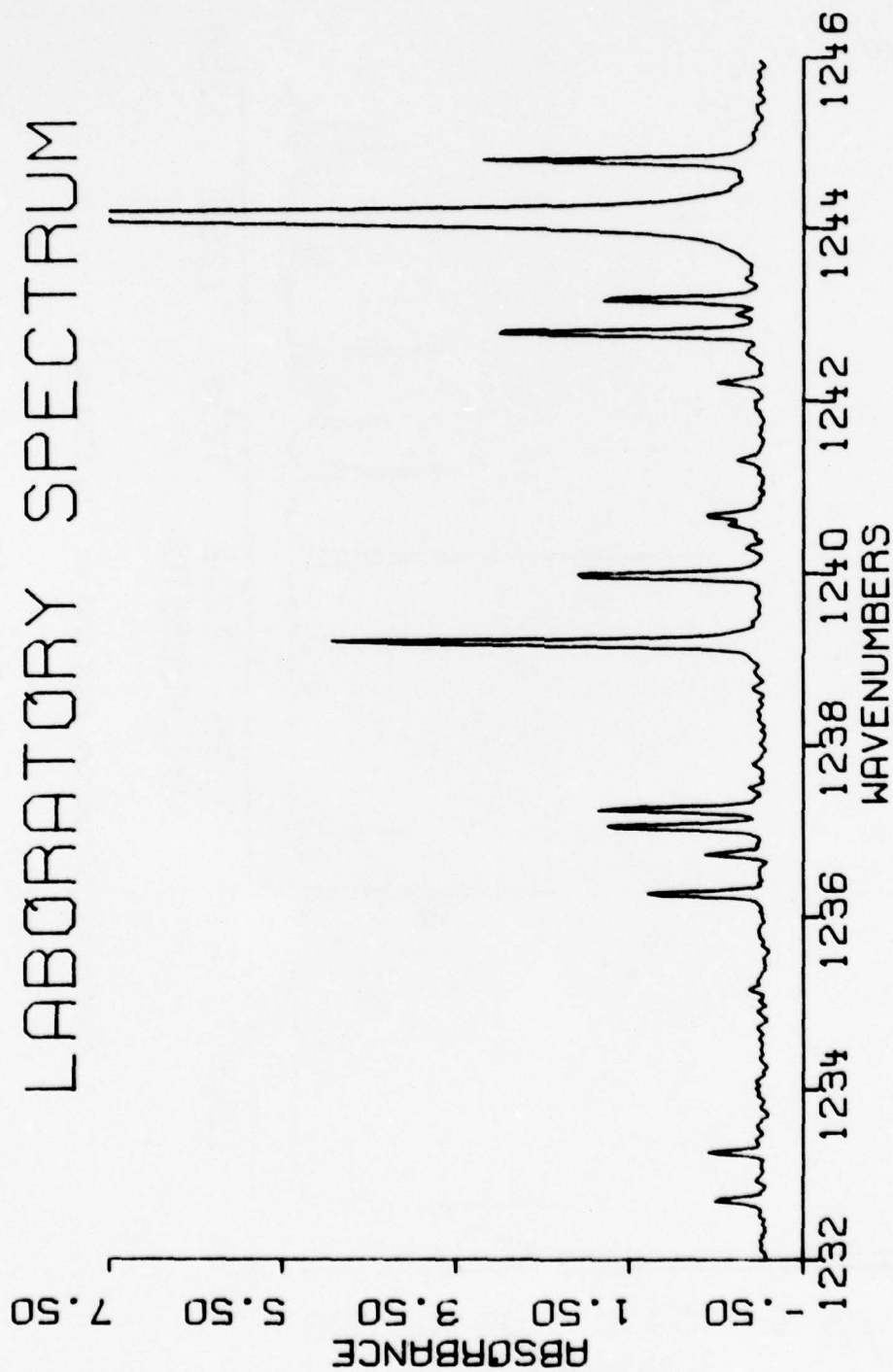


Figure 37. H₂O spectra from 1232 cm⁻¹ to 1246 cm⁻¹.

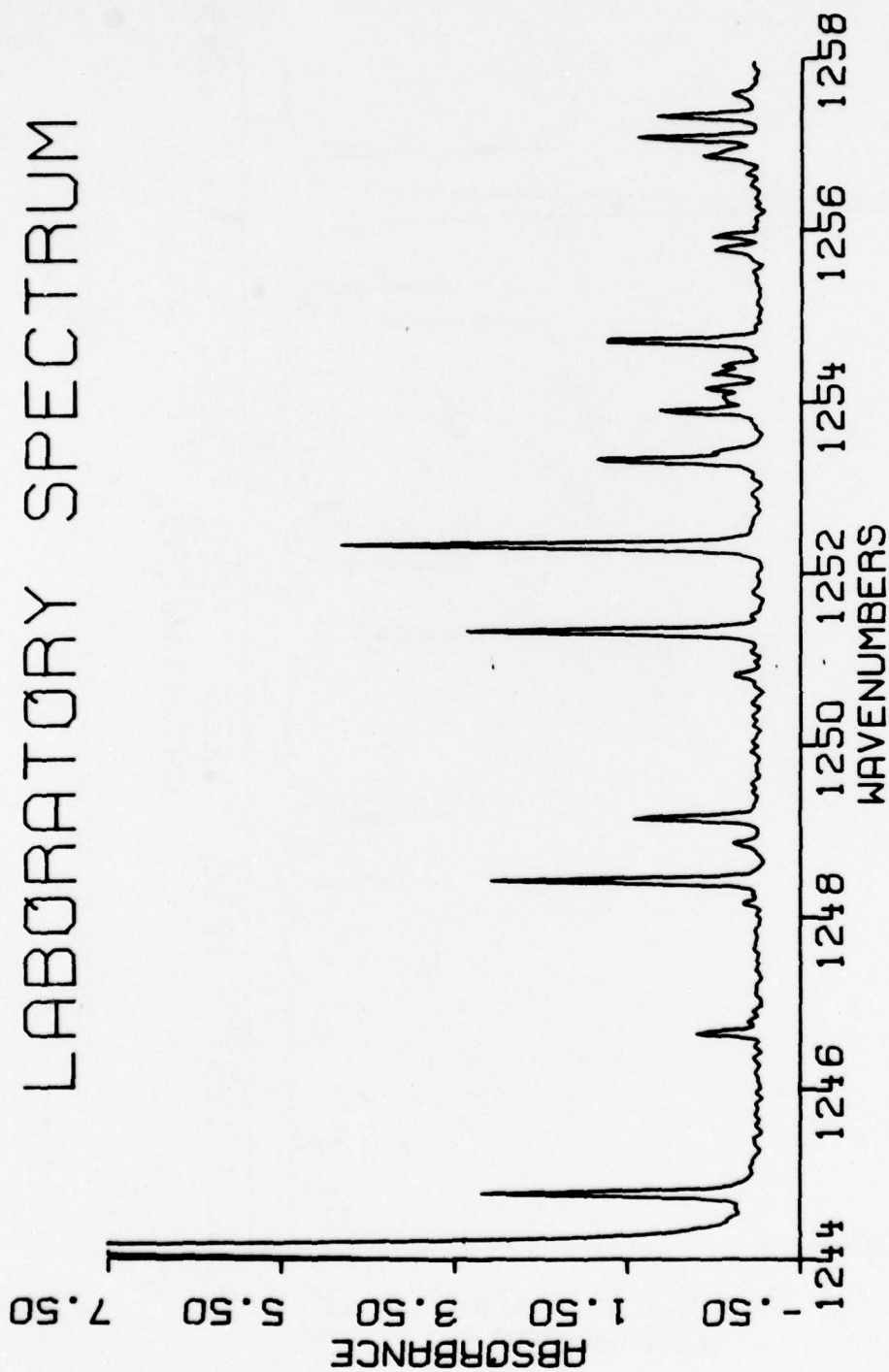


Figure 38. H_2O spectra from 1244 cm^{-1} to 1258 cm^{-1} .

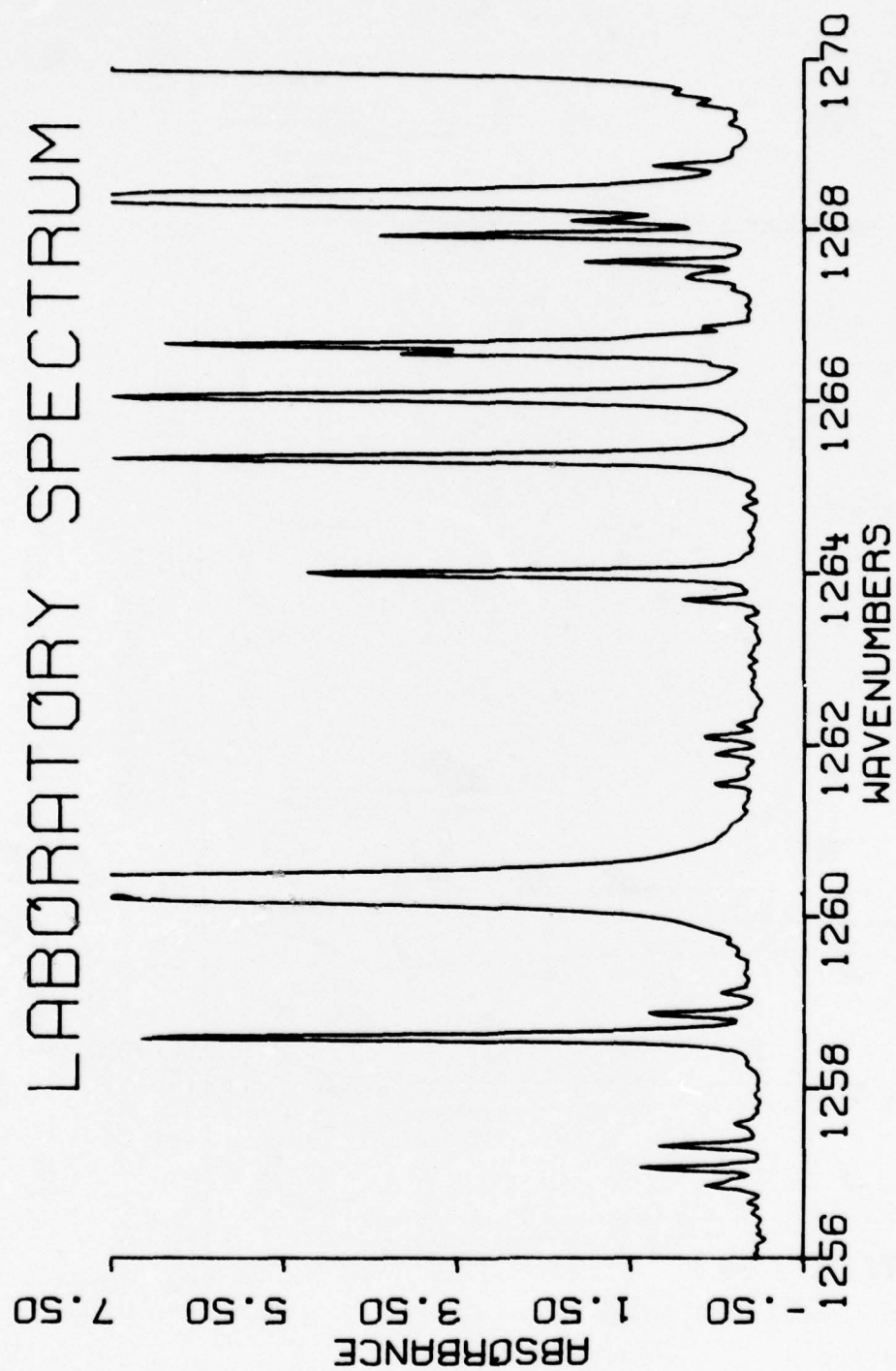


Figure 89. H_2O spectra from 1256 cm^{-1} to 1270 cm^{-1} .

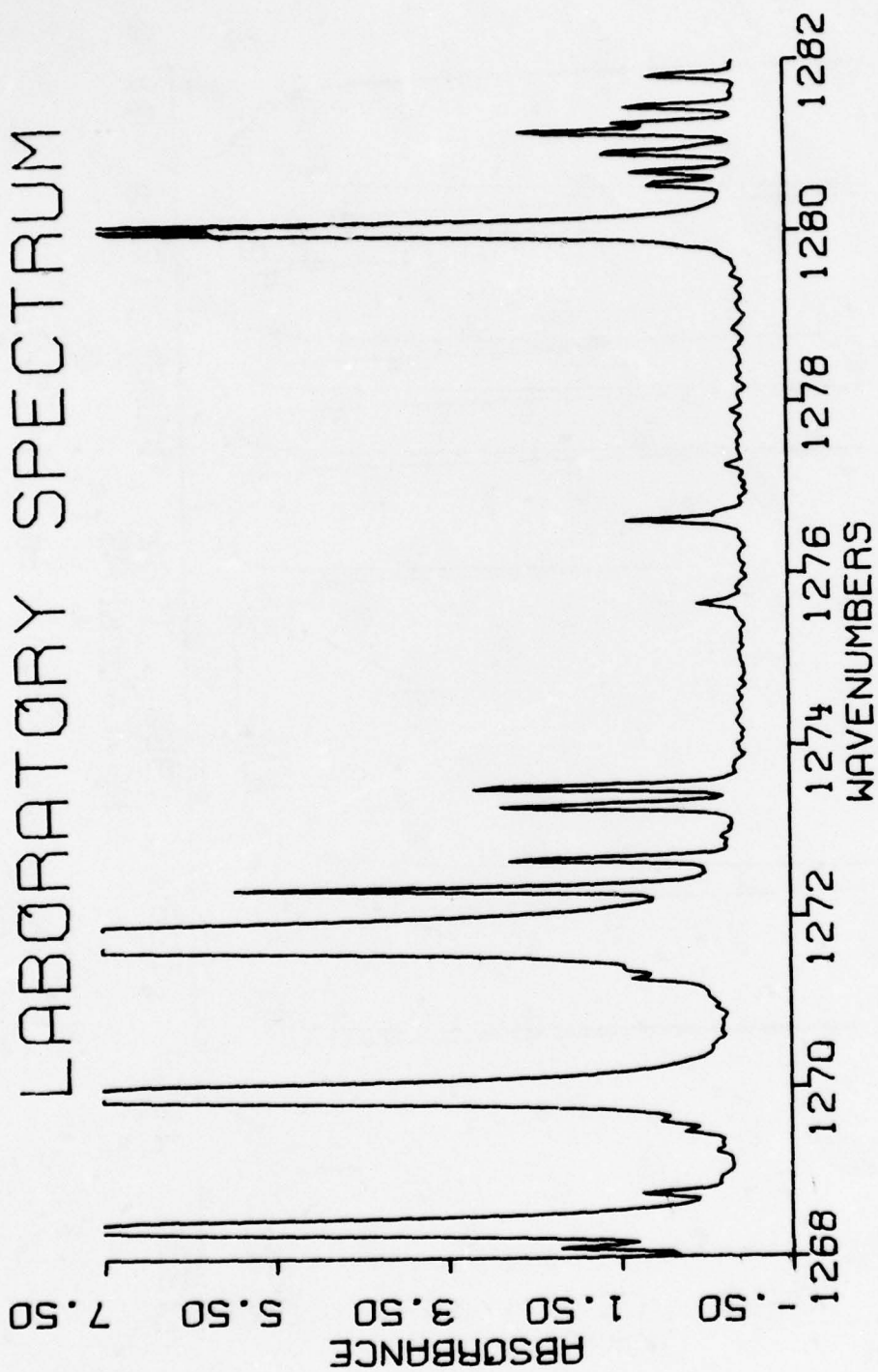


Figure 90. H_2O spectra from 1263 cm^{-1} to 1282 cm^{-1} .

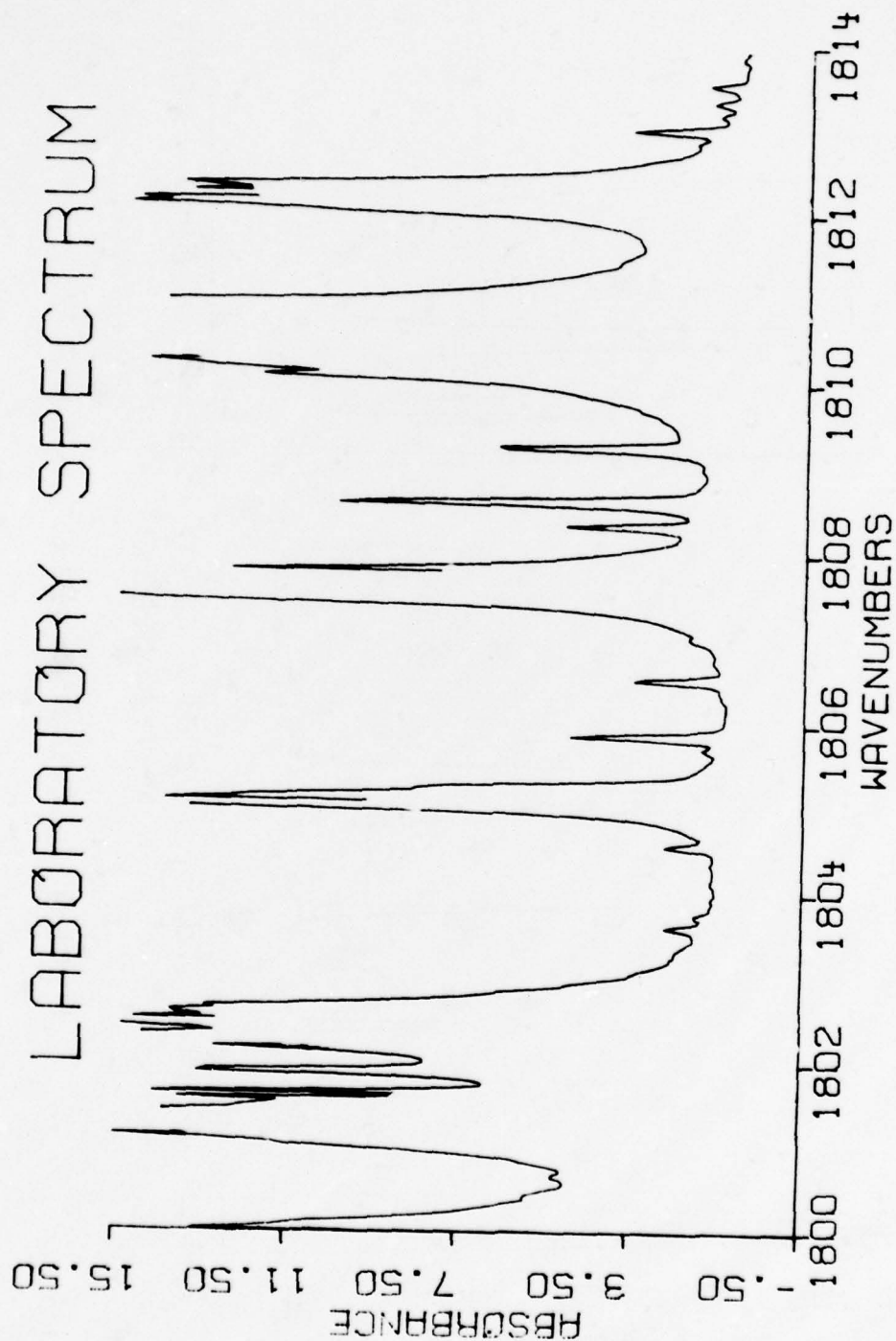


Figure 91. H_2O spectra from 1800 cm^{-1} to 1814 cm^{-1} .

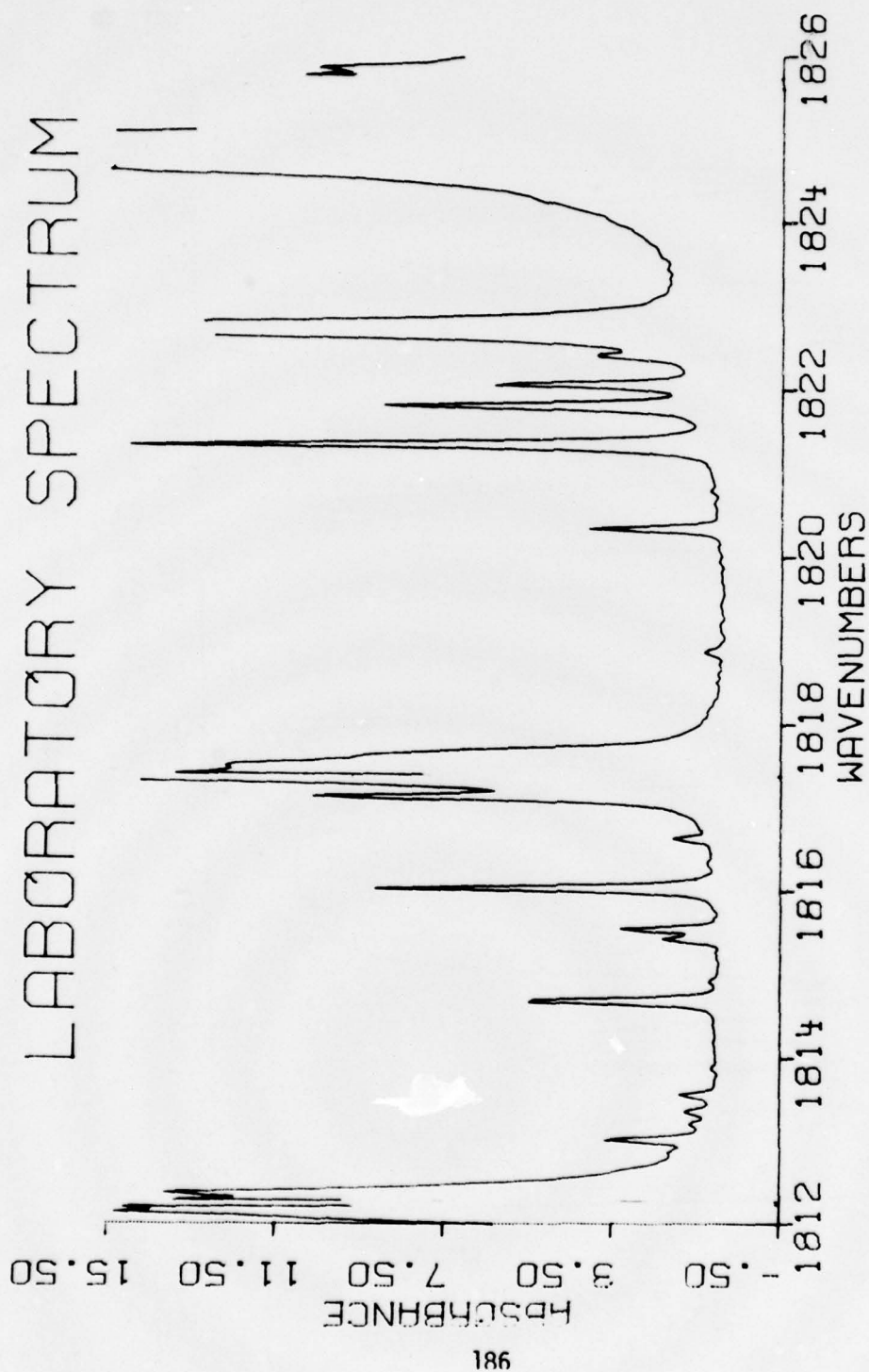


Figure 92. H_2O spectra from 1812 cm^{-1} to 1826 cm^{-1} .

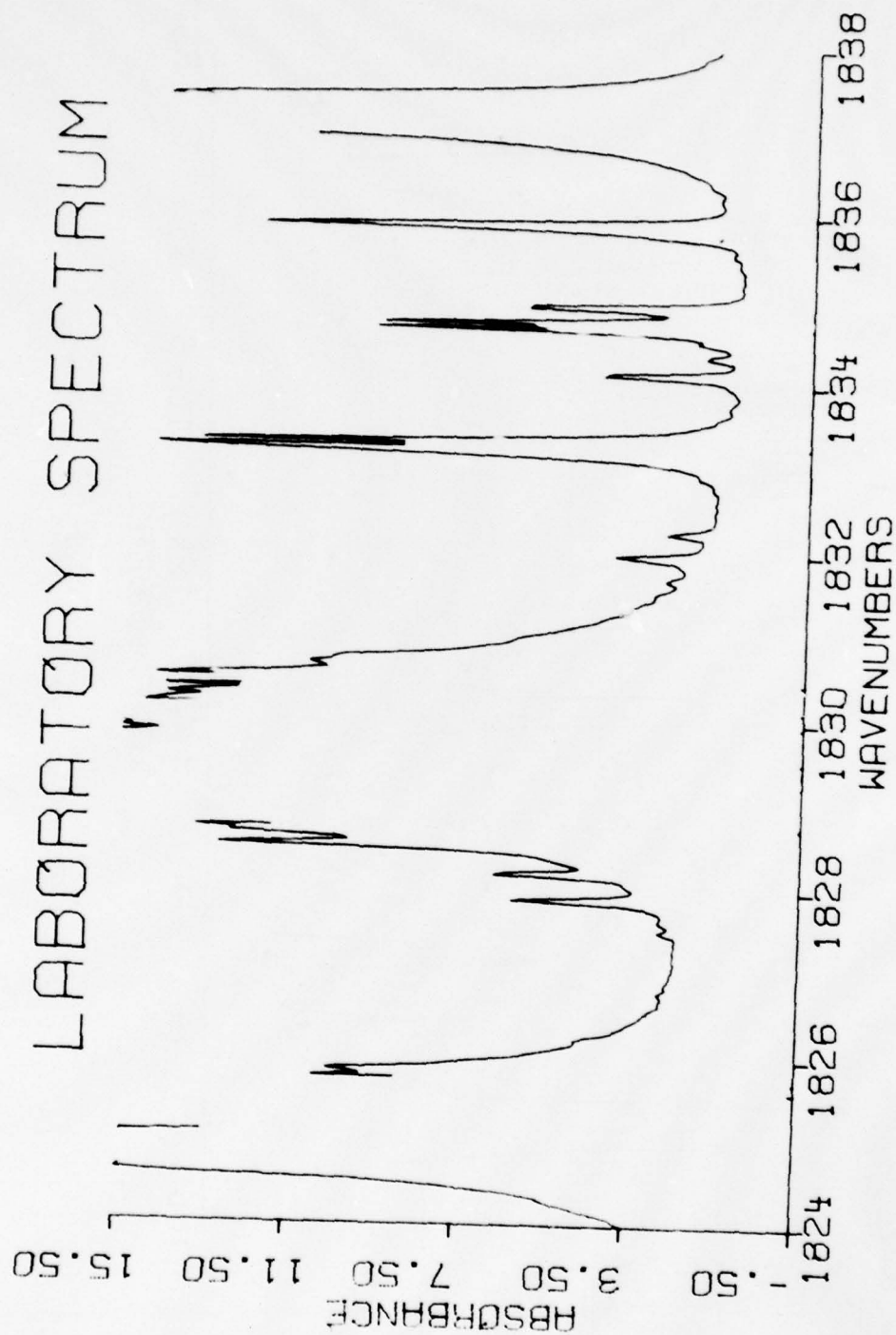


Figure 93. H_2O spectra from 1824 cm^{-1} to 1833 cm^{-1} .

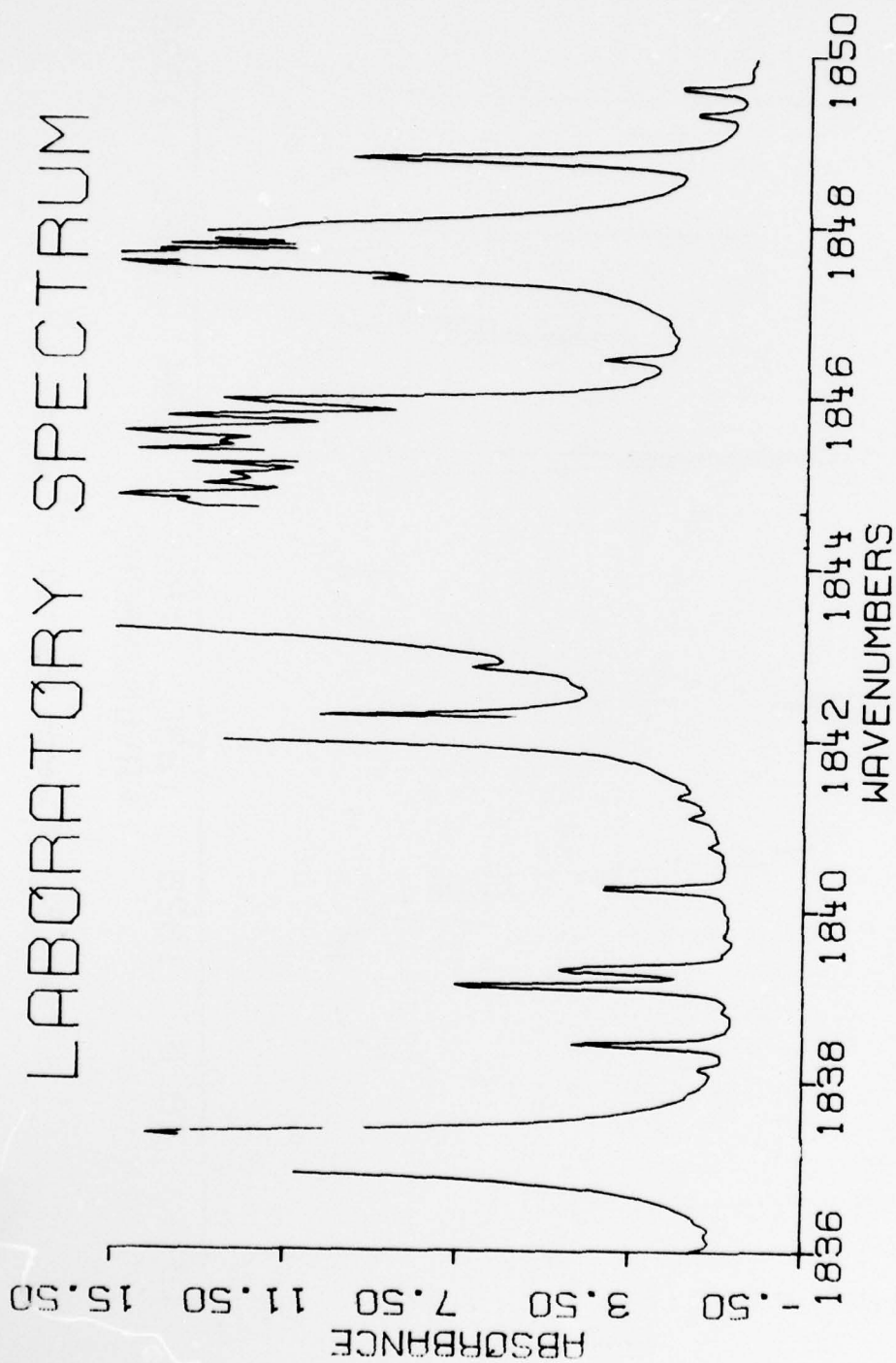


Figure 94. H_2O spectra from 1836 cm^{-1} to 1850 cm^{-1} .

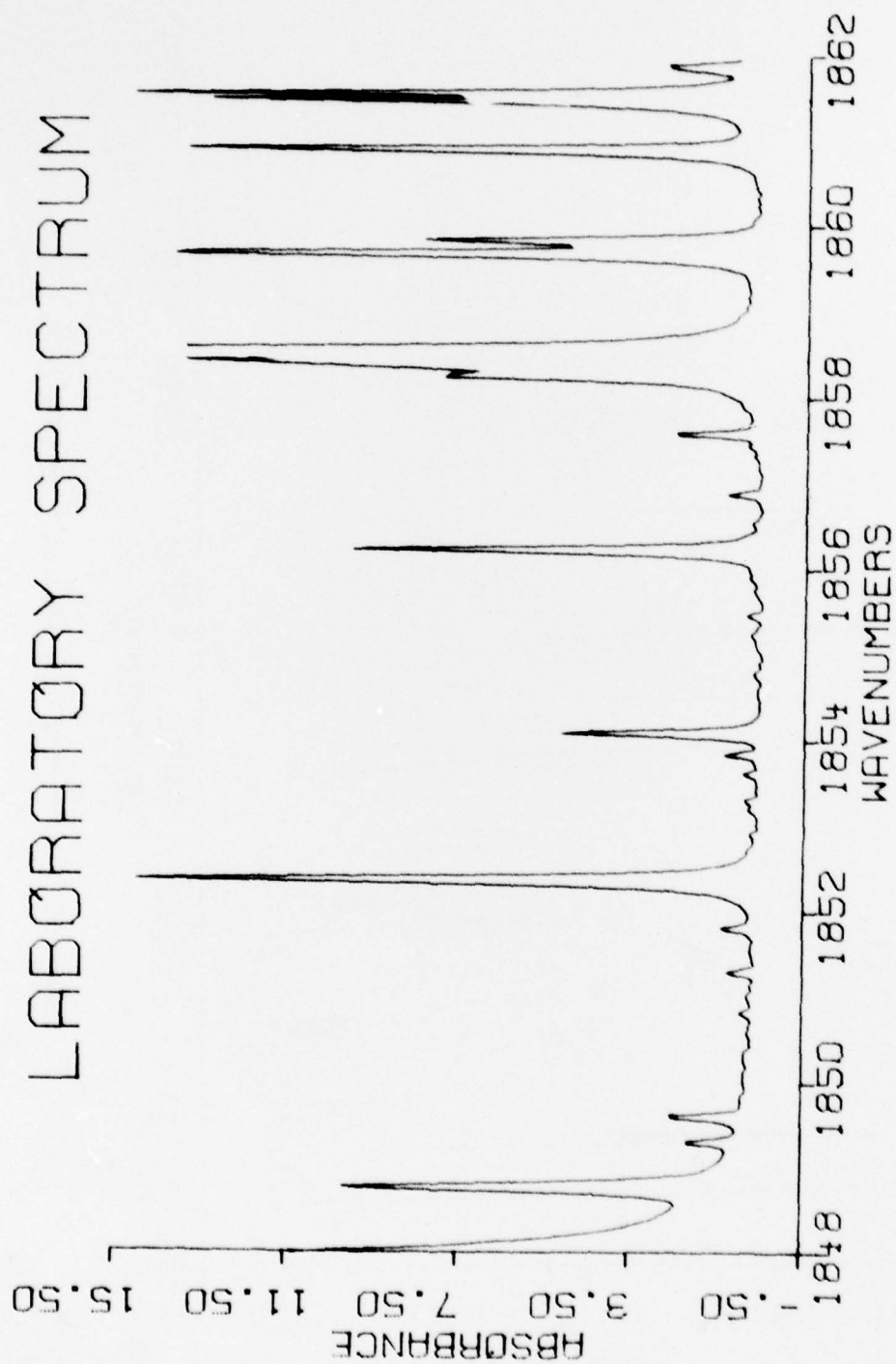


Figure 95. H_2O spectra from 1848 cm^{-1} to 1862 cm^{-1} .

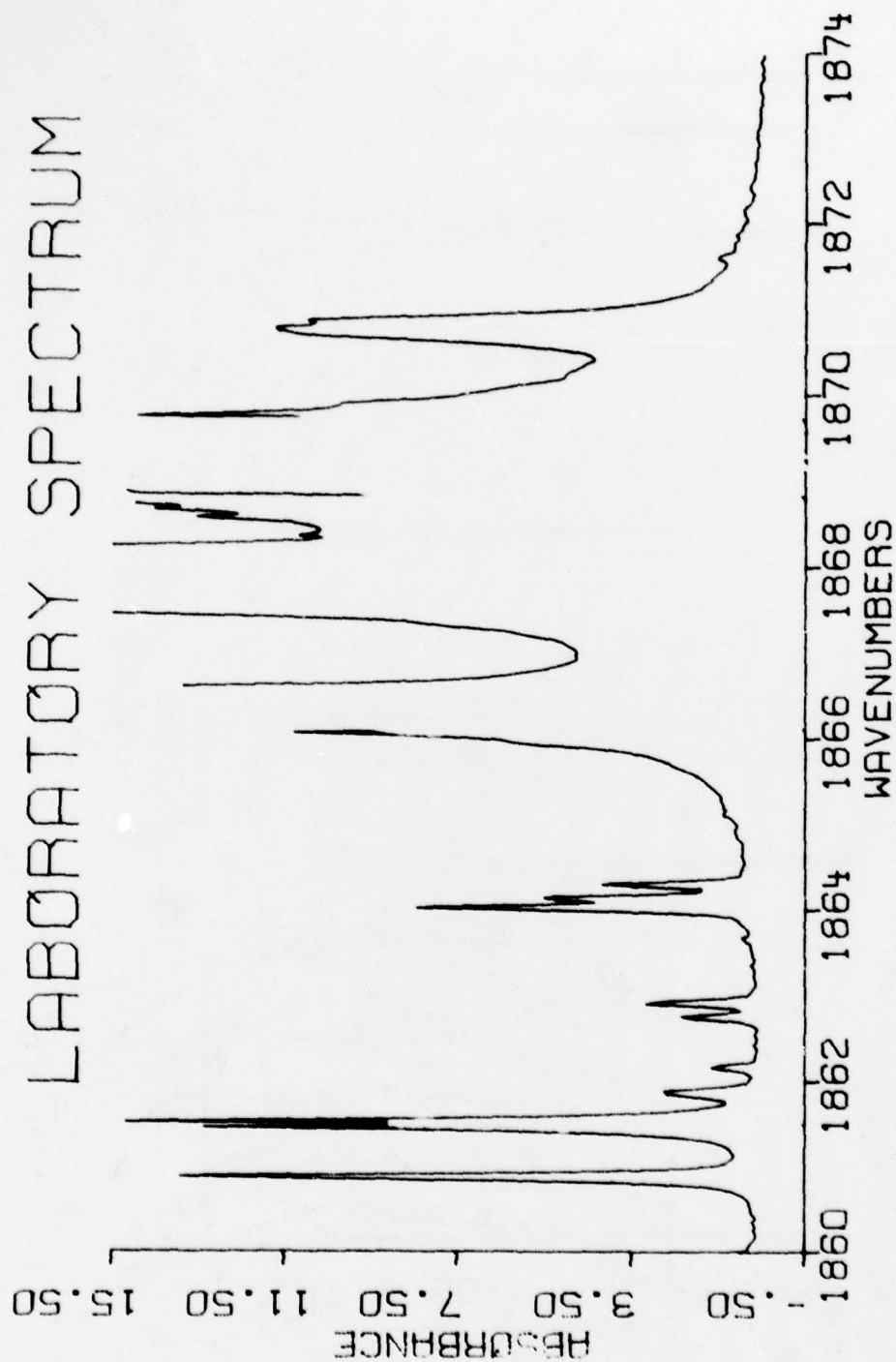


Figure 96. H_2O spectra from 1860 cm^{-1} to 1874 cm^{-1} .

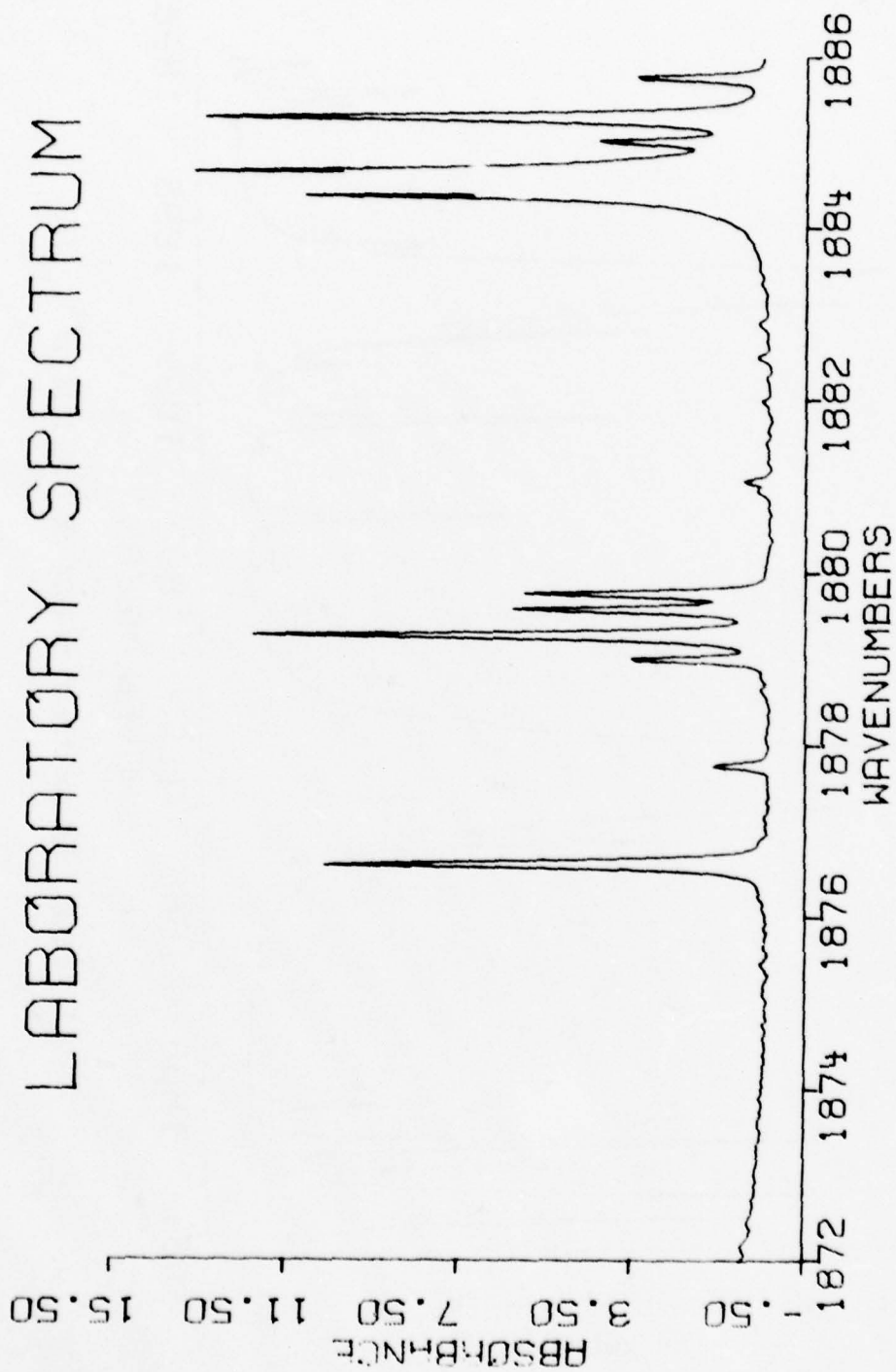


Figure 97. H₂O spectra from 1872 cm⁻¹ to 1886 cm⁻¹.

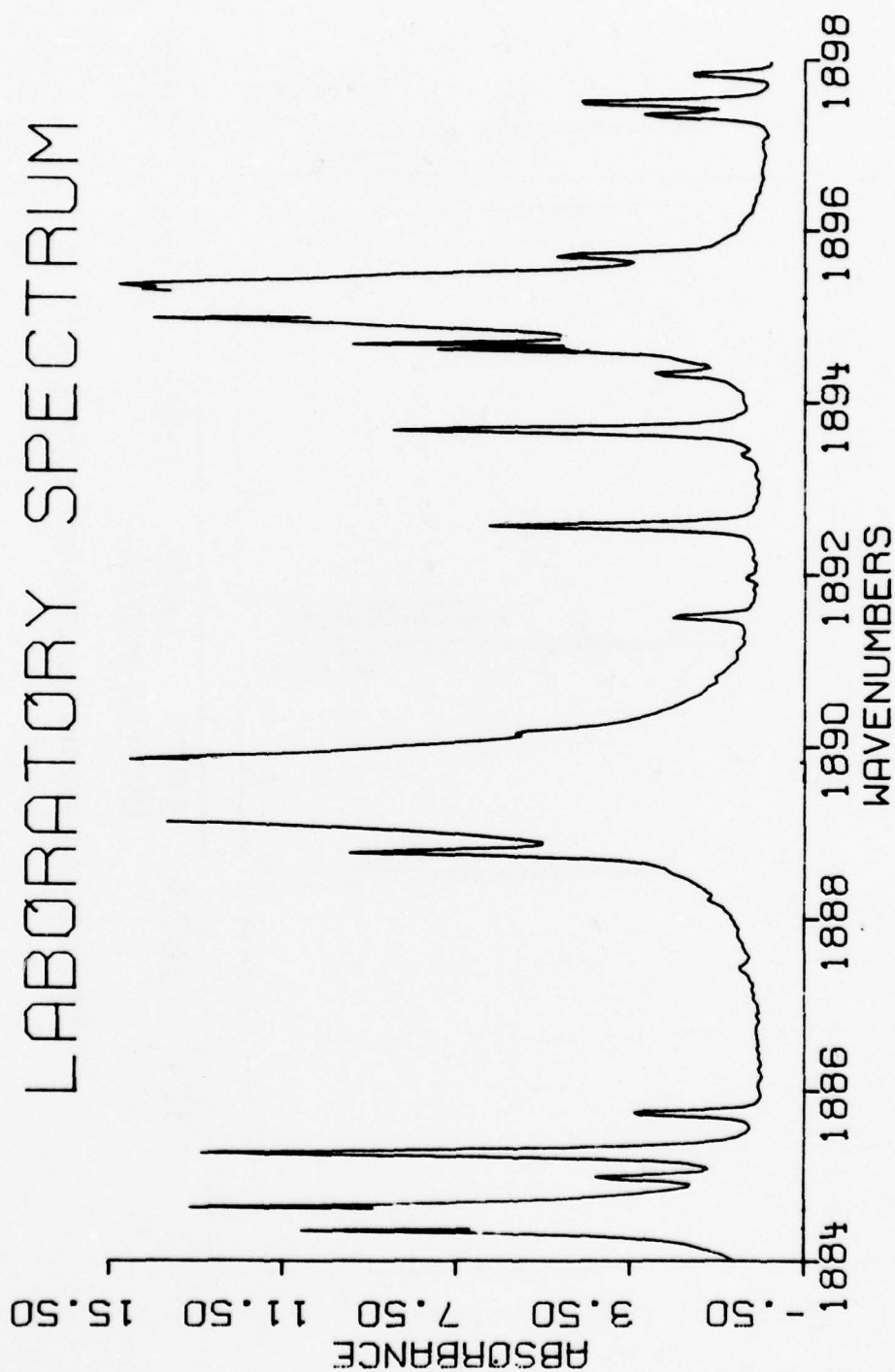


Figure 38. H_2O spectra from 1884 cm^{-1} to 1898 cm^{-1} .

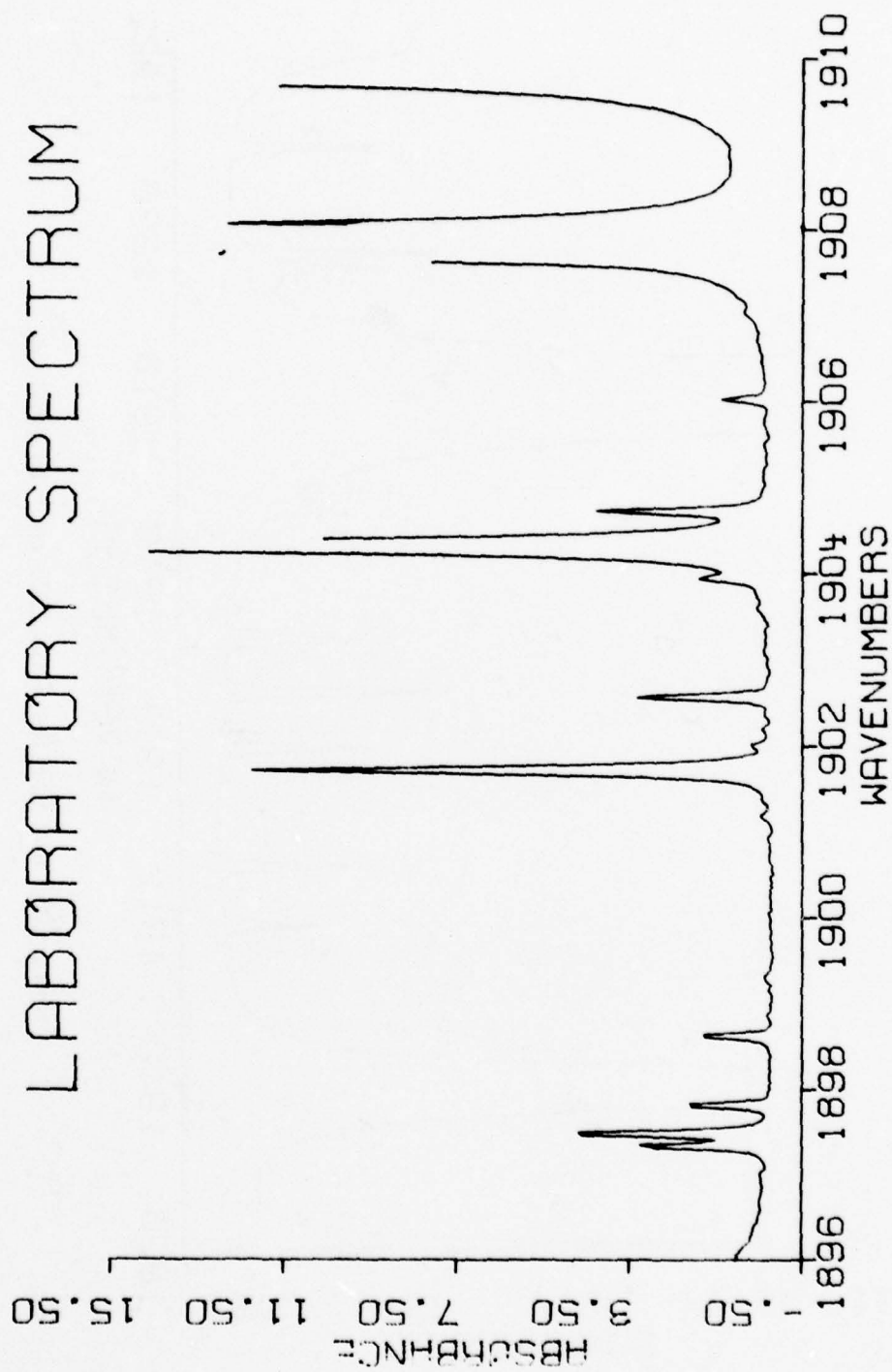


Figure 39. H_2O spectra from 1896 cm^{-1} to 1910 cm^{-1} .

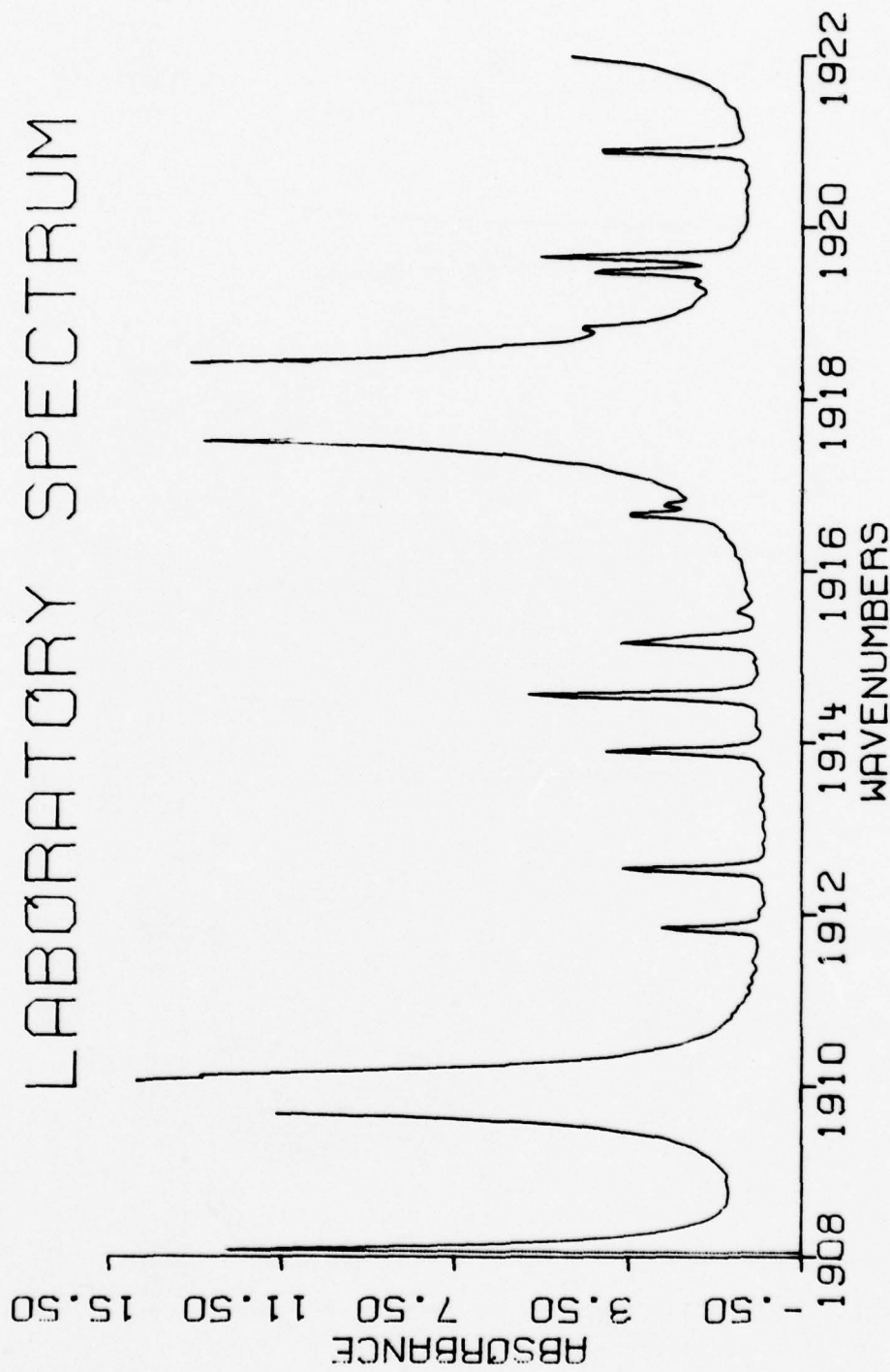


Figure 100. H_2O spectra from 1903 cm^{-1} to 1922 cm^{-1} .

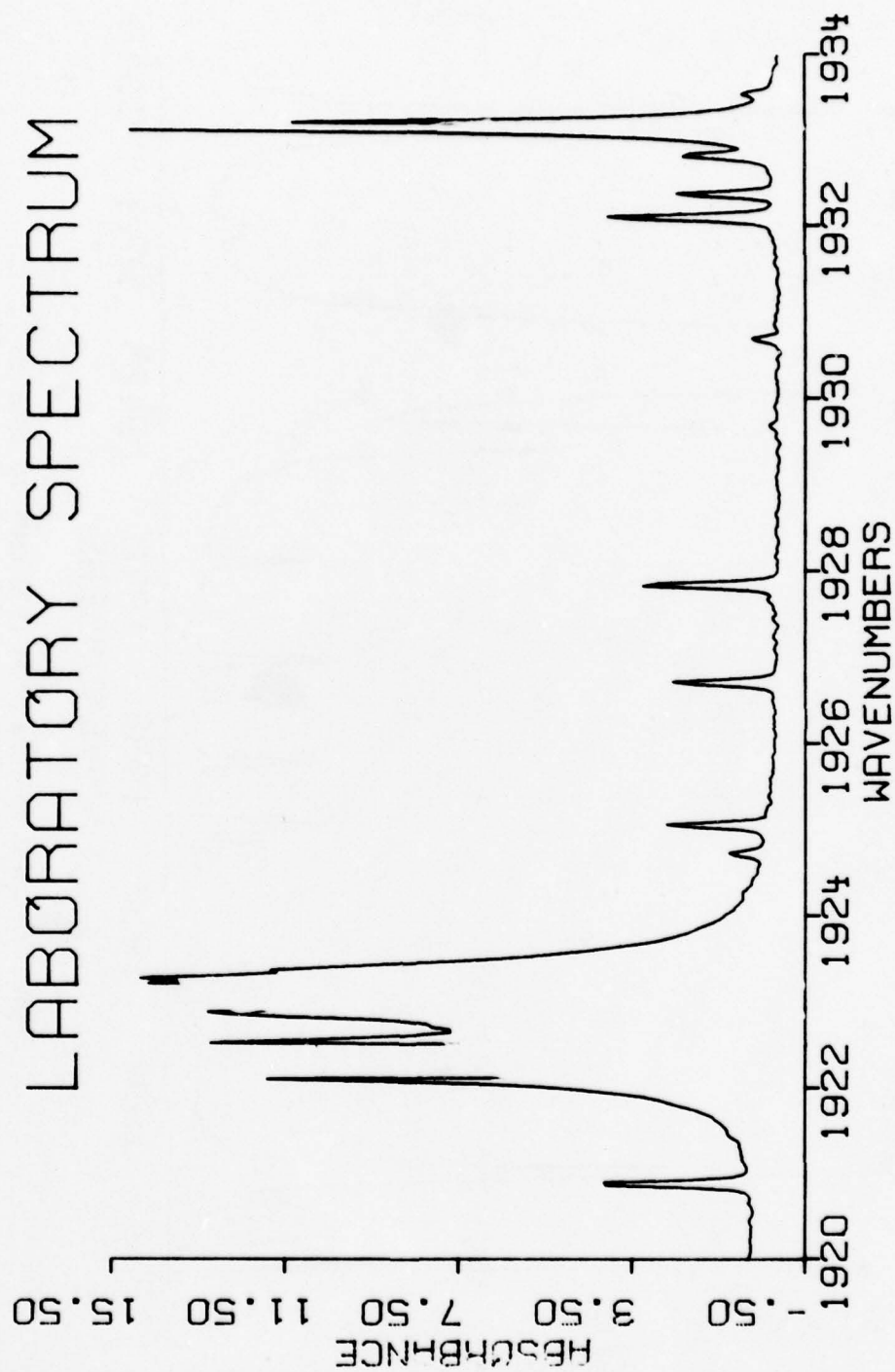


Figure 101. H_2O spectra from 1920 cm^{-1} to 1934 cm^{-1} .

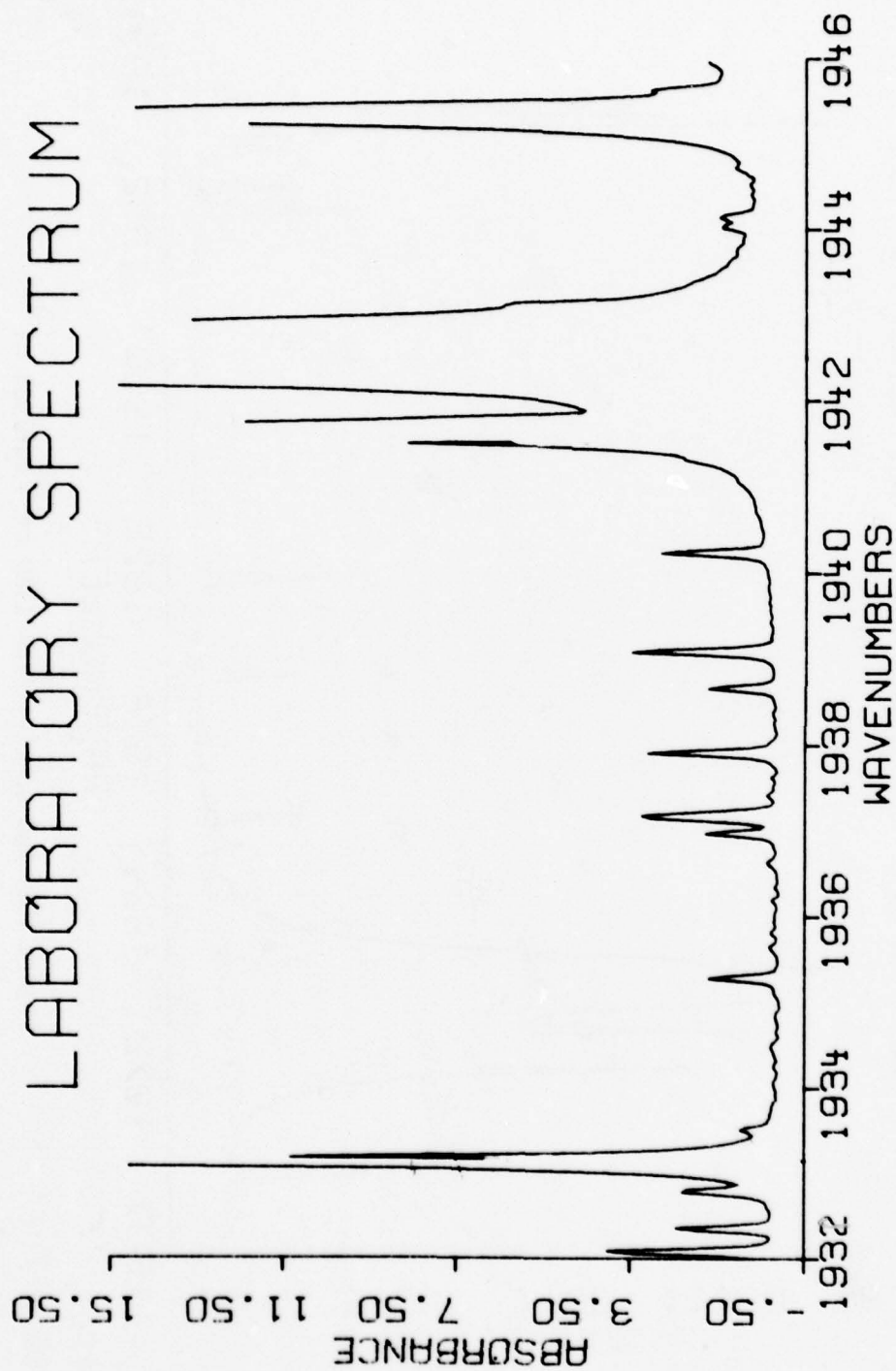


Figure 102. H_2O spectra from 1932 cm^{-1} to 1946 cm^{-1} .

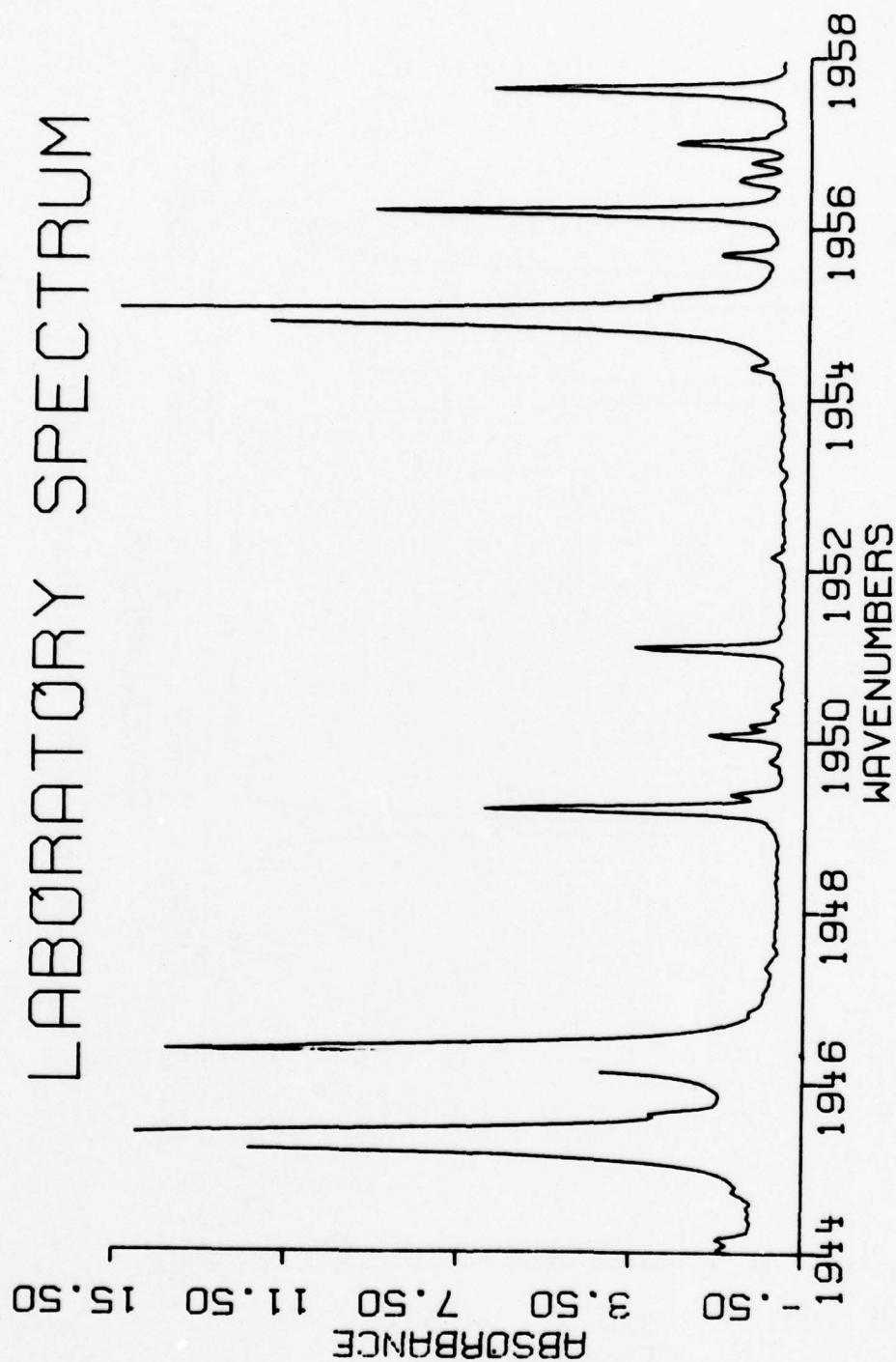


Figure 103. H₂O spectra from 1944 cm⁻¹ to 1958 cm⁻¹.

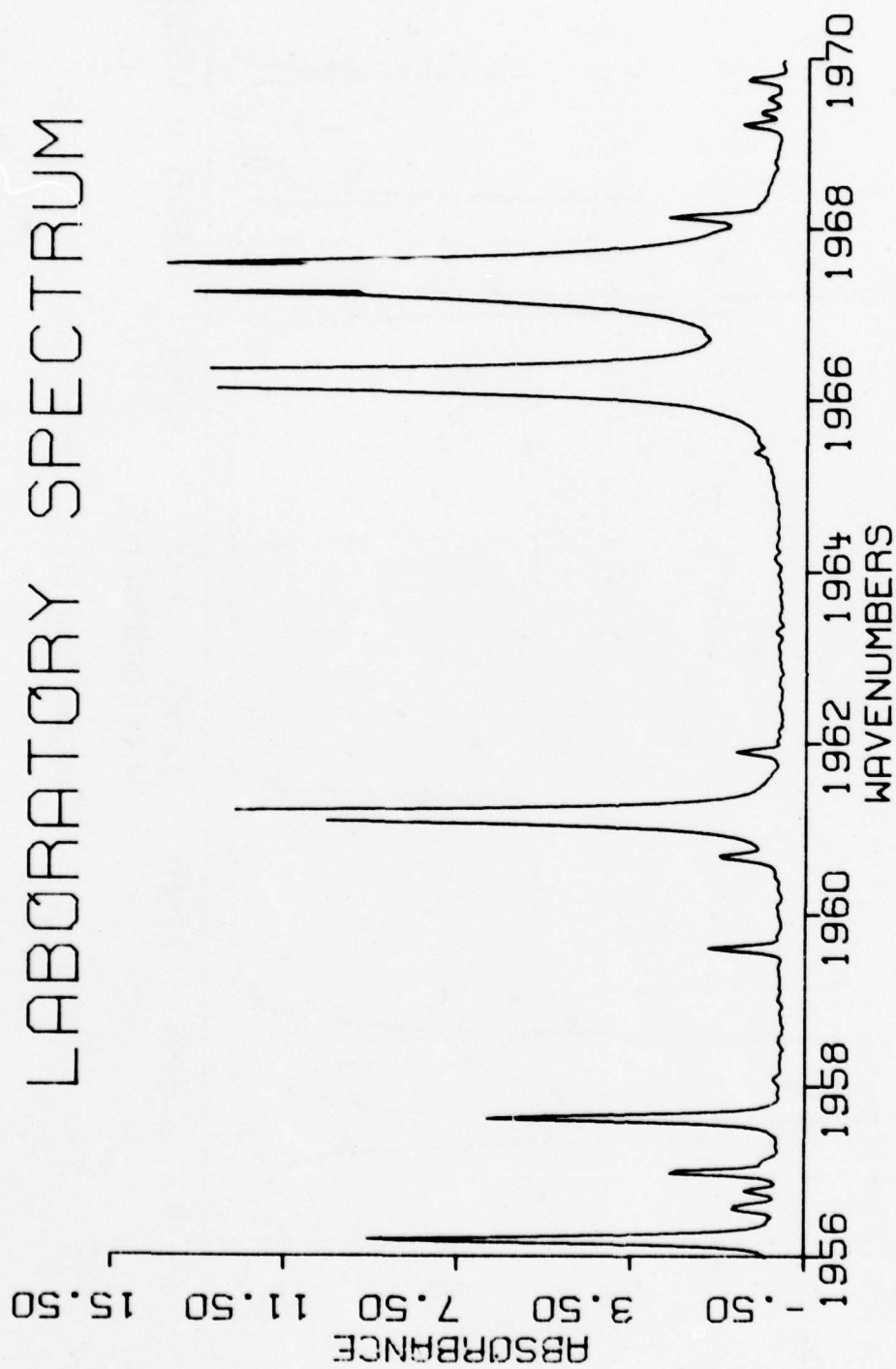


Figure 104. H_2O spectra from 1956 cm^{-1} to 1970 cm^{-1} .

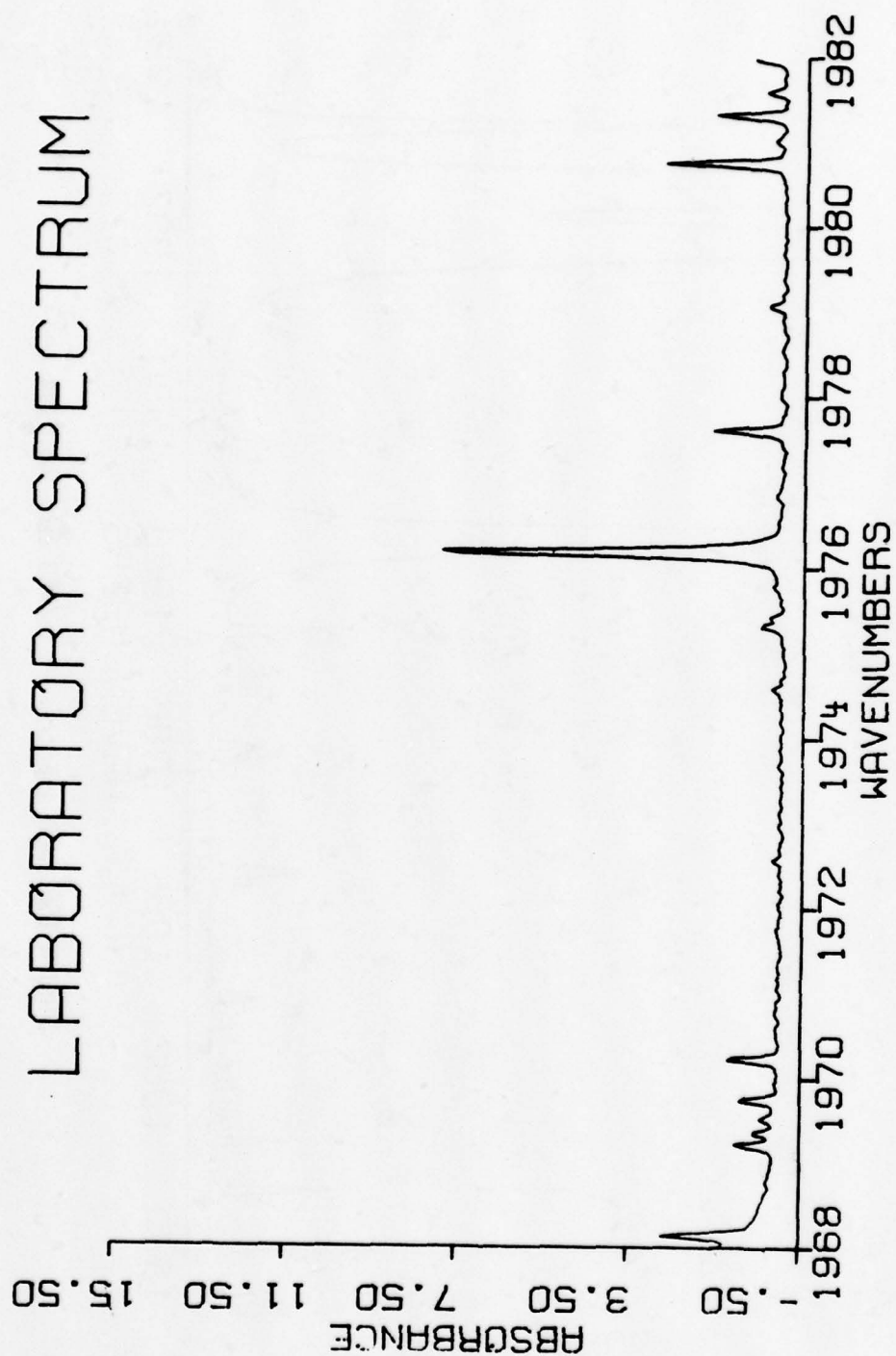


Figure 105. H_2O spectra from 1963 cm^{-1} to 1982 cm^{-1} .

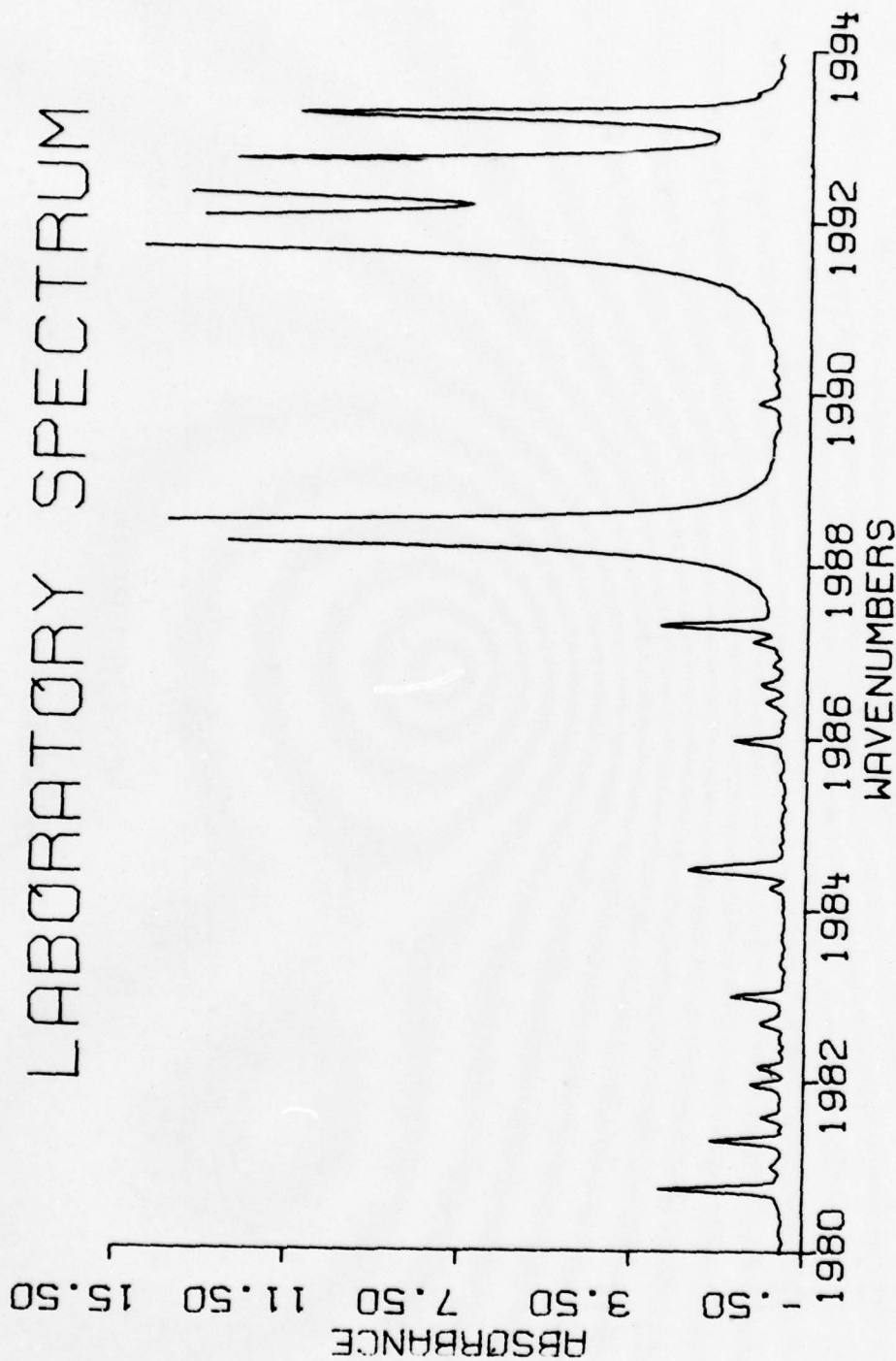


Figure 106. H_2O spectra from 1980 cm^{-1} to 1994 cm^{-1} .

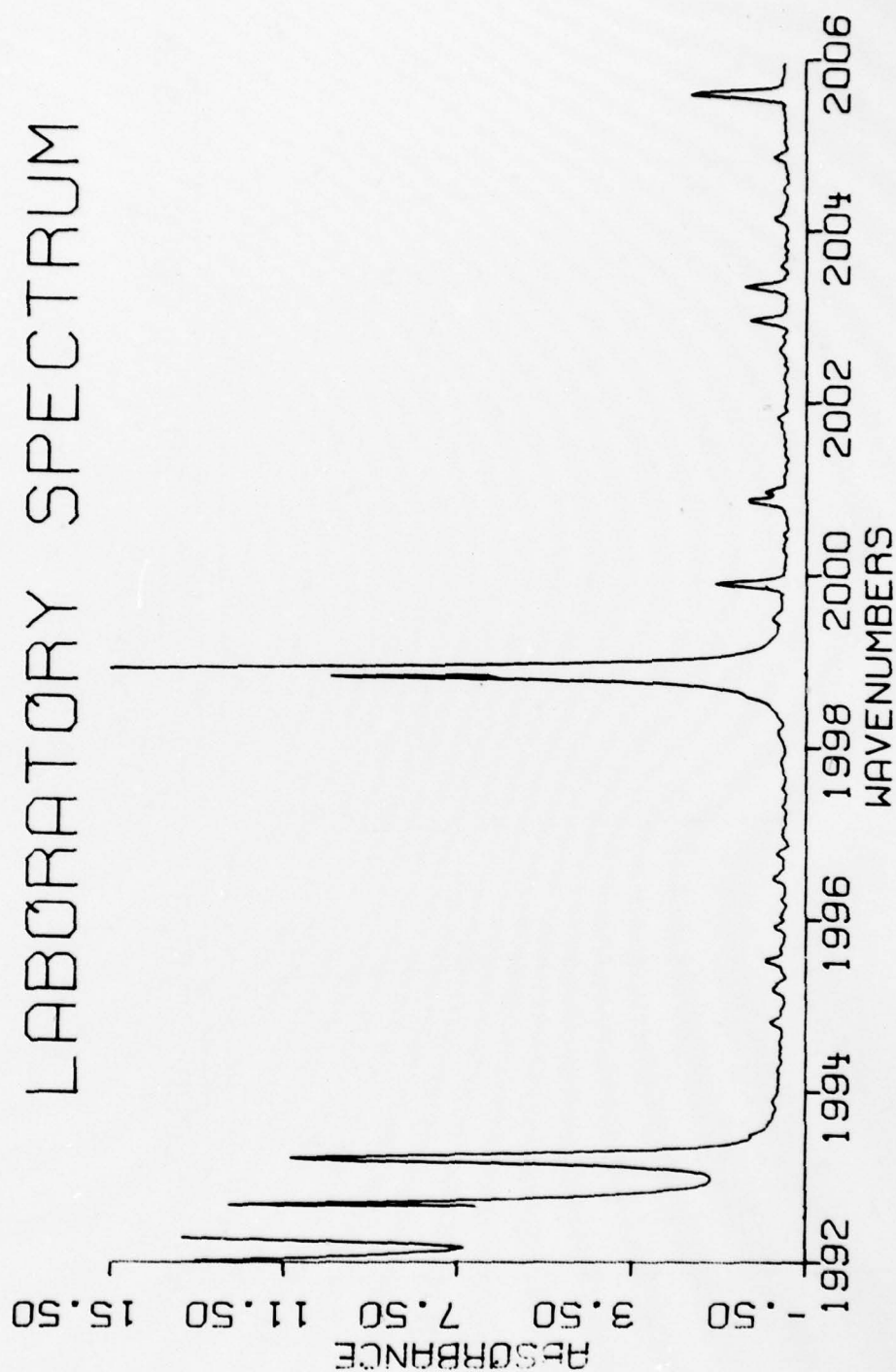


Figure 107. H_2O spectra from 1992 cm^{-1} to 2006 cm^{-1} .

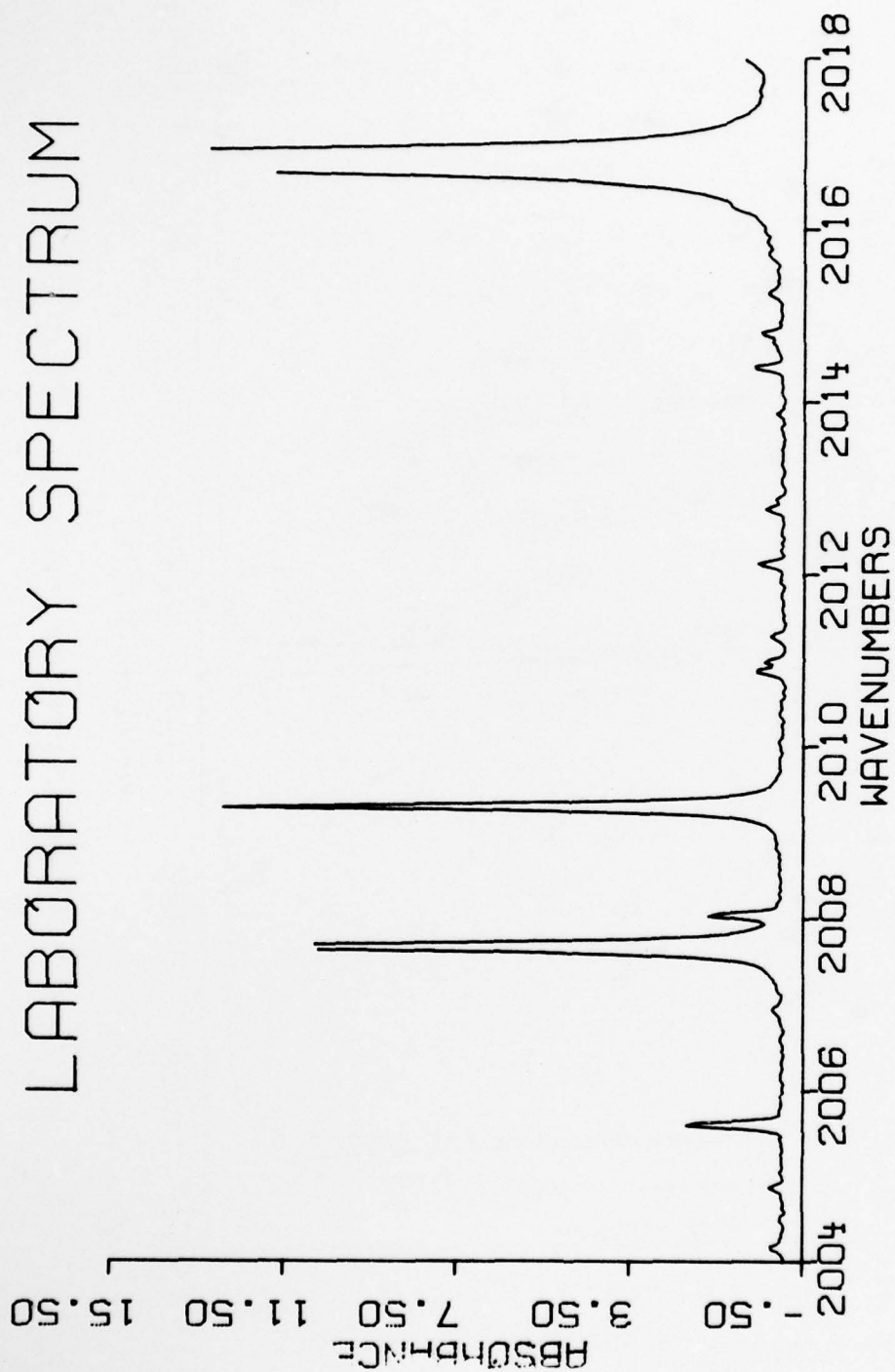


Figure 108. H_2O spectra from 2004 cm^{-1} to 2018 cm^{-1} .

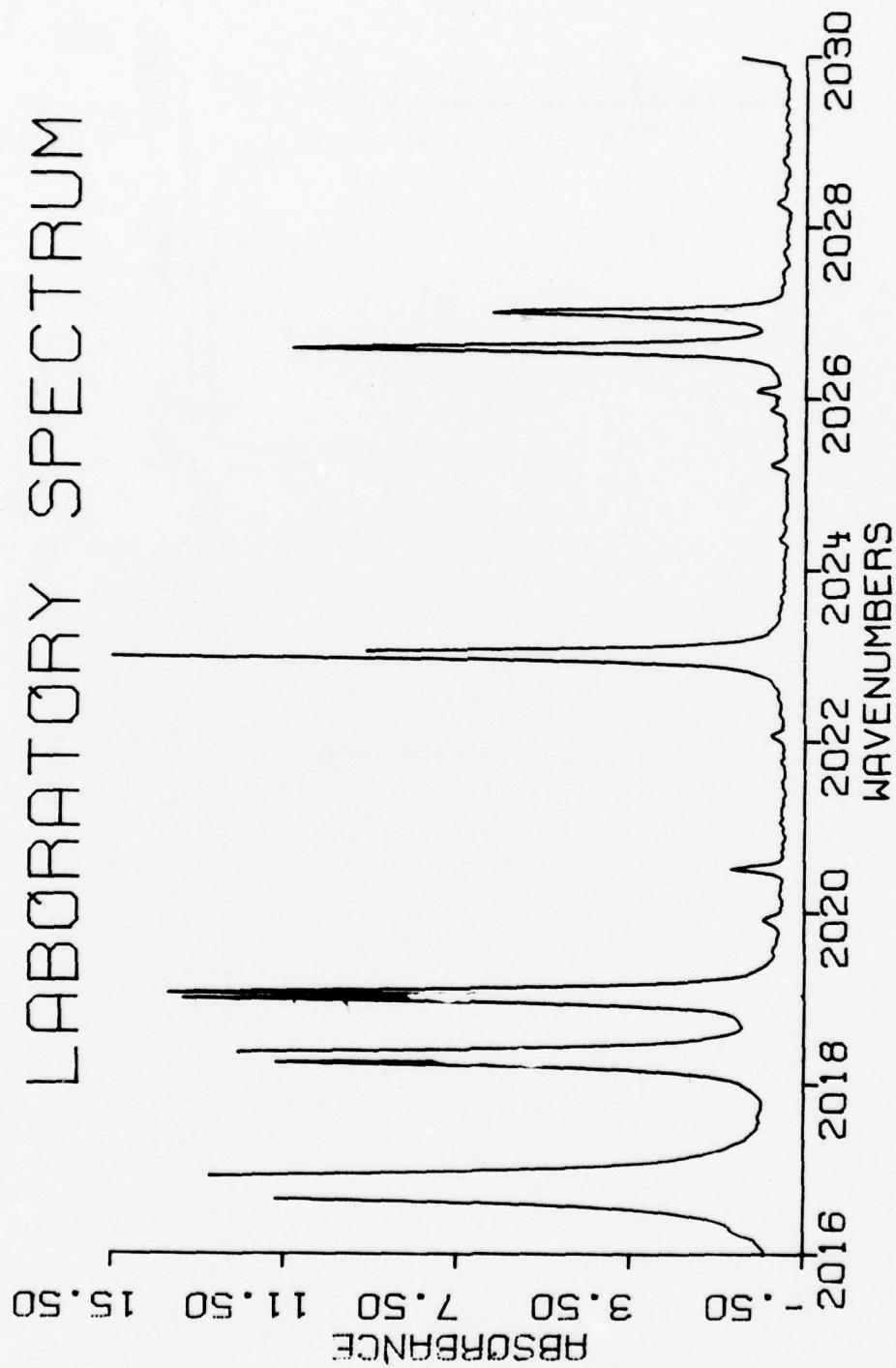


Figure 109. H_2O spectra from 2016 cm^{-1} to 2030 cm^{-1} .

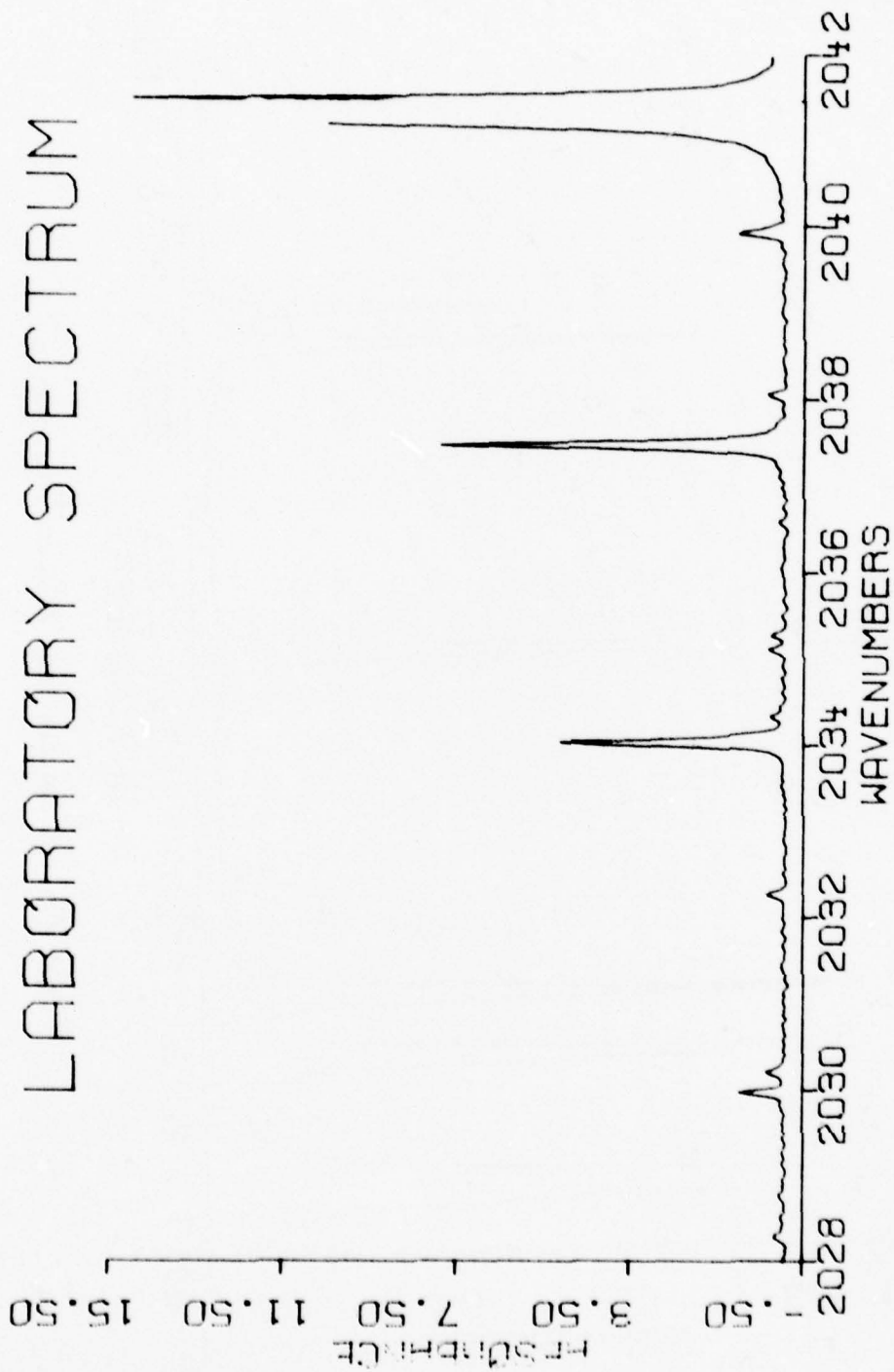


Figure 110. H_2O spectra from 2028 cm^{-1} to 2042 cm^{-1} .

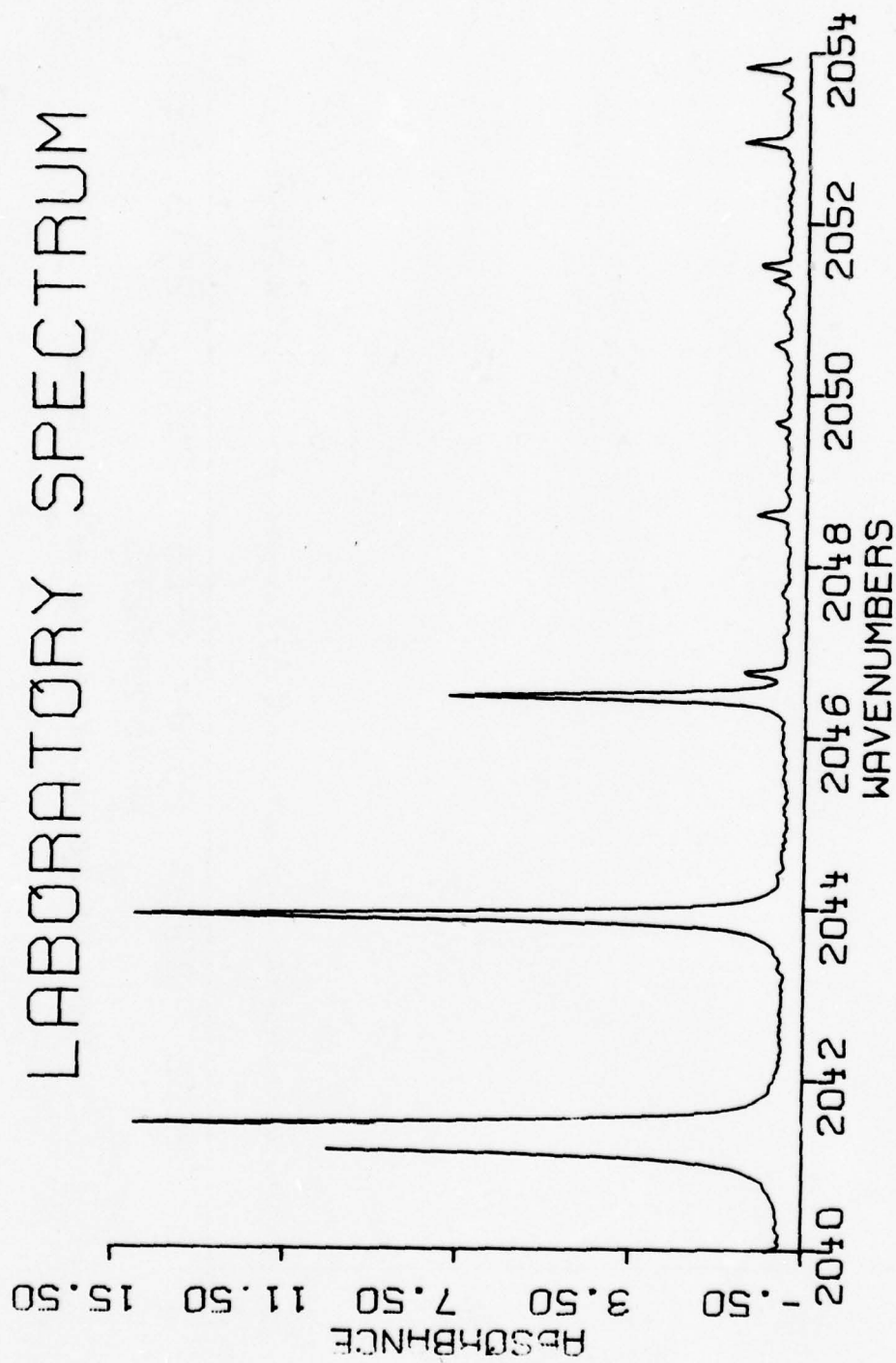


Figure 111. H₂O spectra from 2040 cm⁻¹ to 2054 cm⁻¹.



Figure 112. H_2O spectra from 2500 cm^{-1} to 2514 cm^{-1} .



Figure 113. H₂O spectra from 2512 cm⁻¹ to 2526 cm⁻¹.



Figure 114. H_2O spectra from 2524 cm^{-1} to 2538 cm^{-1} .



Figure 115. H_2O spectra from 2536 cm^{-1} to 2550 cm^{-1} .

LABORATORY SPECTRUM



Figure 116. H₂O spectra from 2548 cm⁻¹ to 2562 cm⁻¹.



Figure 117. H_2O spectra from 2560 cm^{-1} to 2574 cm^{-1} .

LABORATORY SPECTRUM

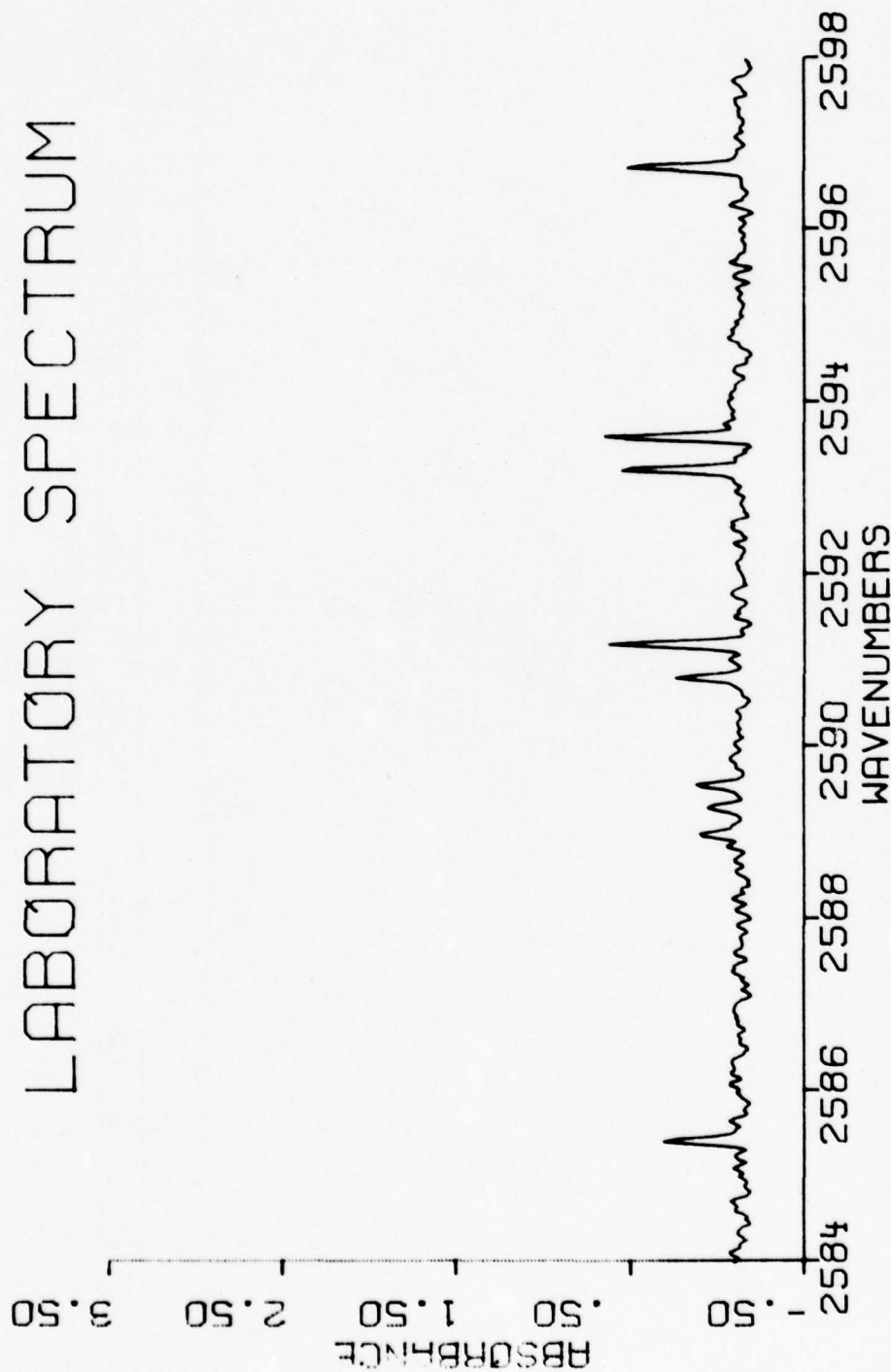


Figure 113. H_2O spectra from 2584 cm^{-1} to 2598 cm^{-1} .

LABORATORY SPECTRUM

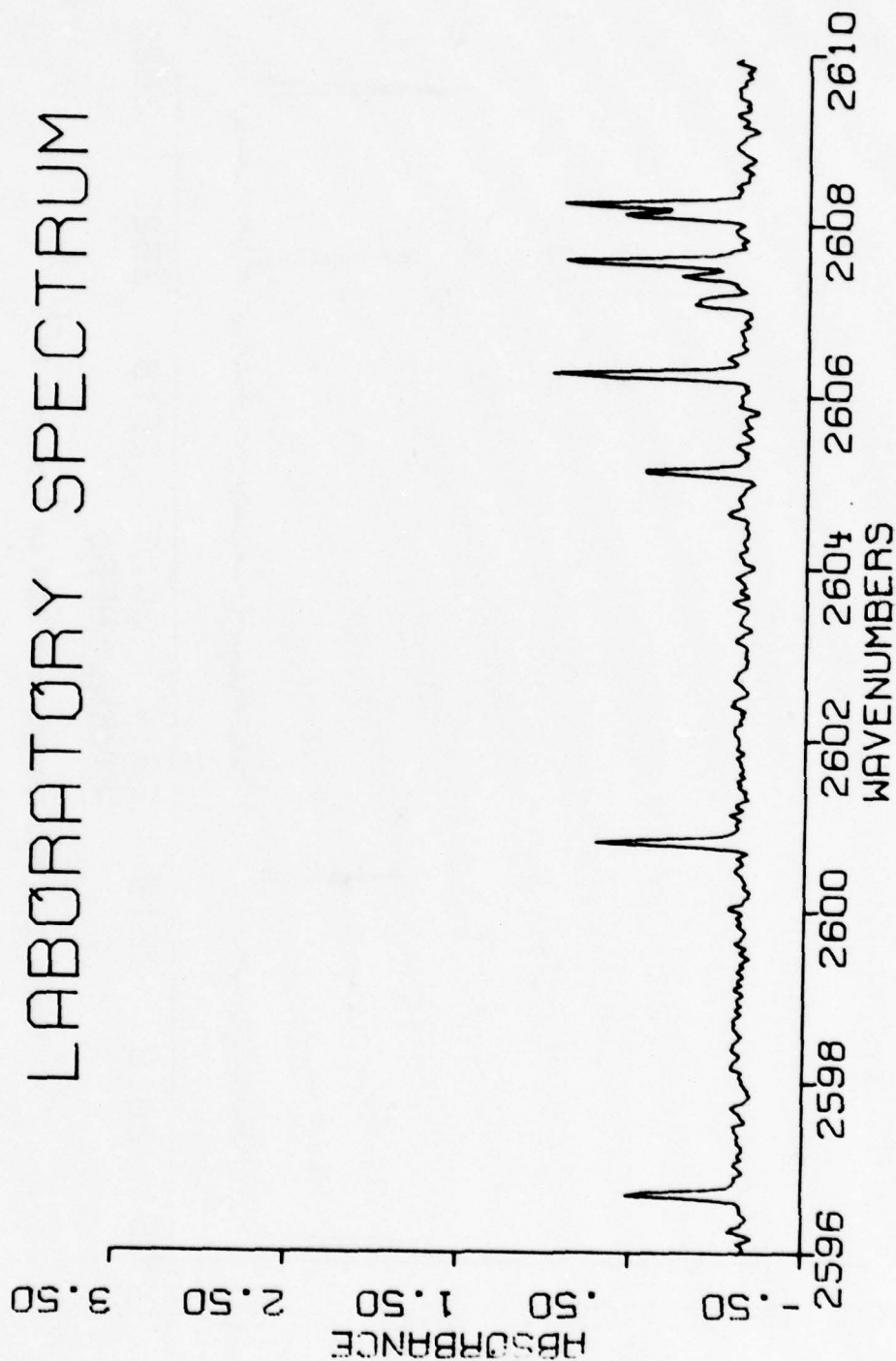


Figure 119. H_2O spectra from 2596 cm^{-1} to 2610 cm^{-1} .

LABORATORY SPECTRUM



Figure 120. H_2O spectra from 2608 cm^{-1} to 2622 cm^{-1} .

LABORATORY SPECTRUM



Figure 121. H_2O spectra from 2620 cm^{-1} to 2634 cm^{-1} .

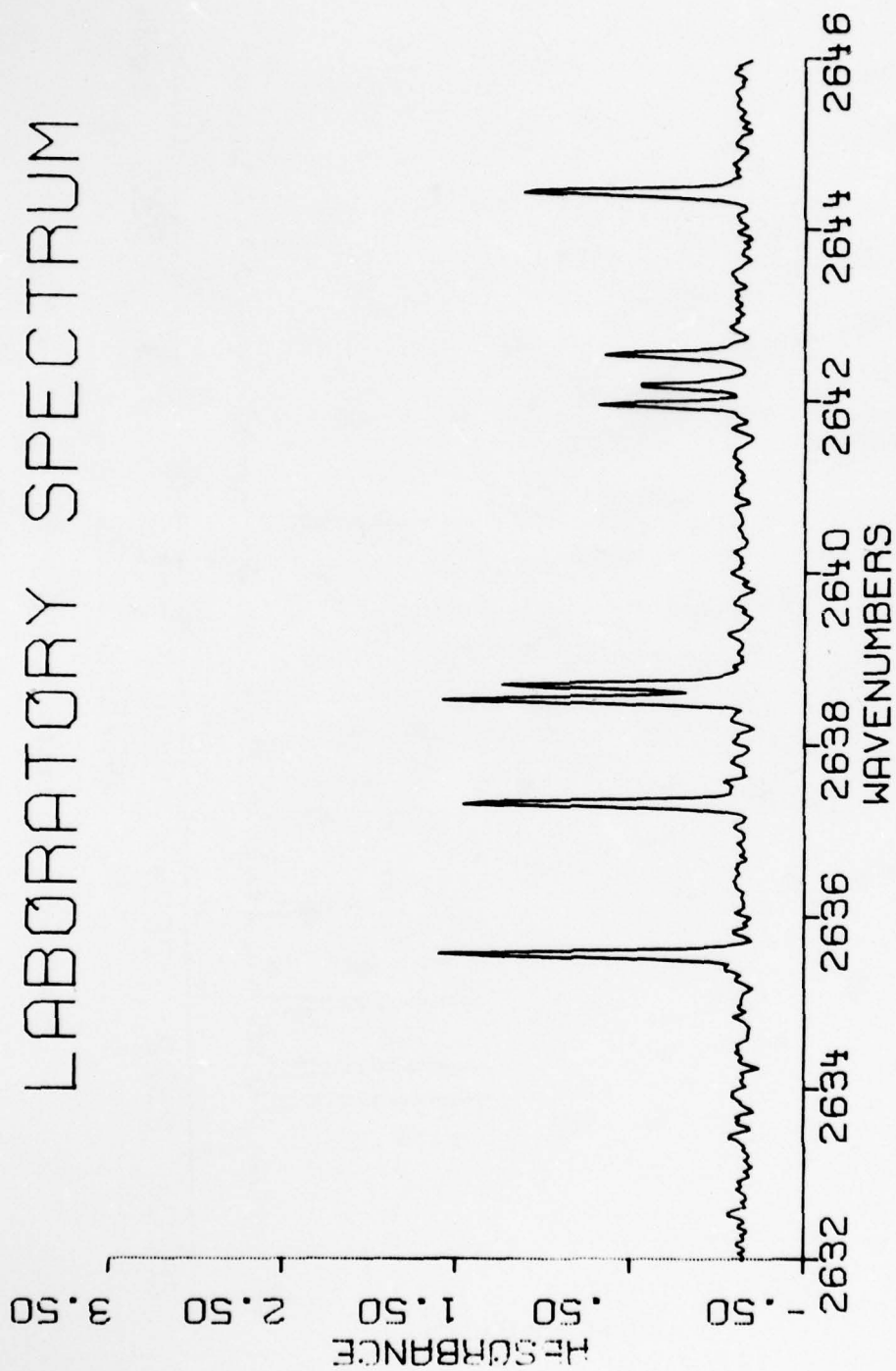


Figure 122. H_2O spectra from 2632 cm^{-1} to 2646 cm^{-1} .

LABORATORY SPECTRUM

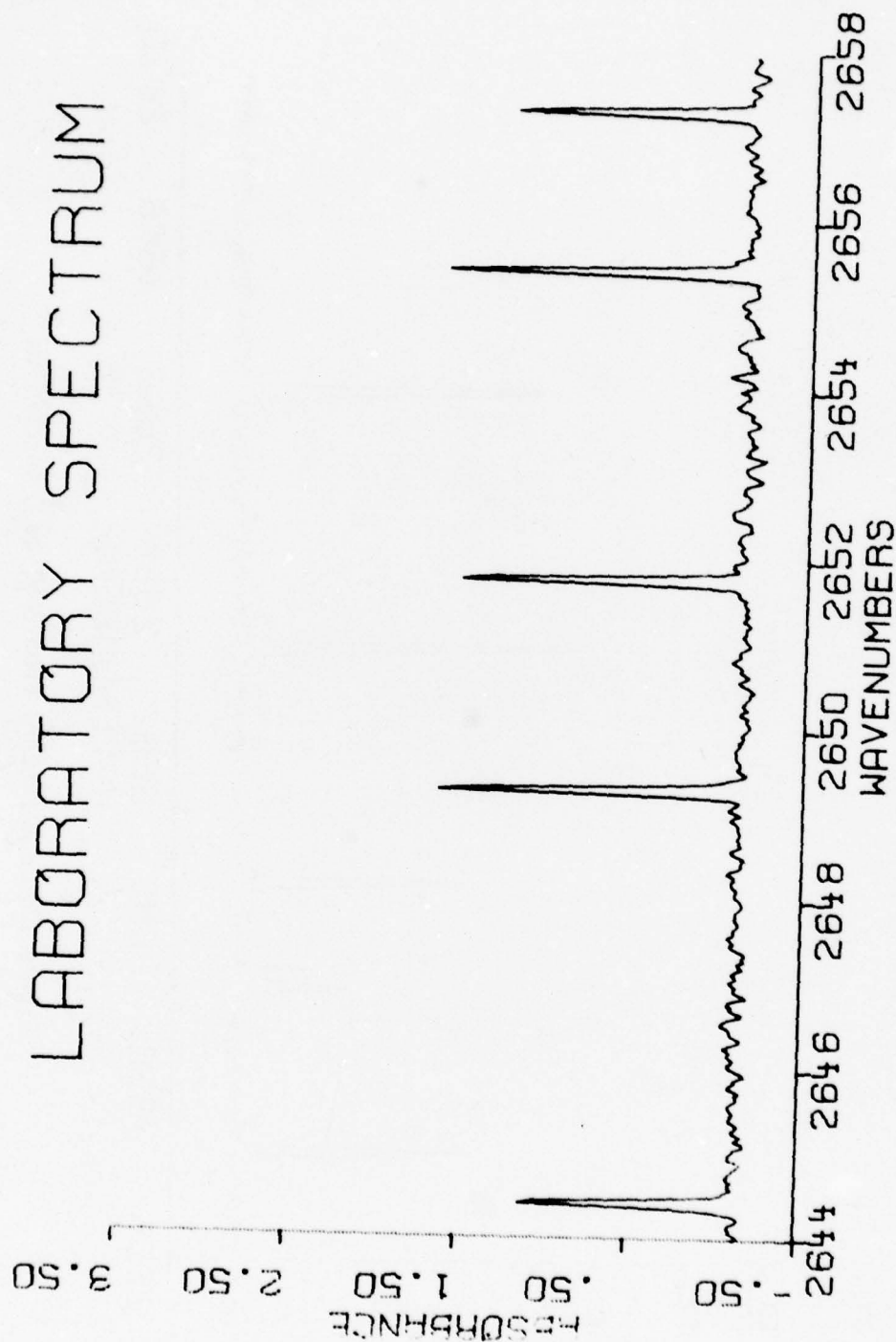


Figure 123. H₂O spectra from 2644 cm⁻¹ to 2658 cm⁻¹.

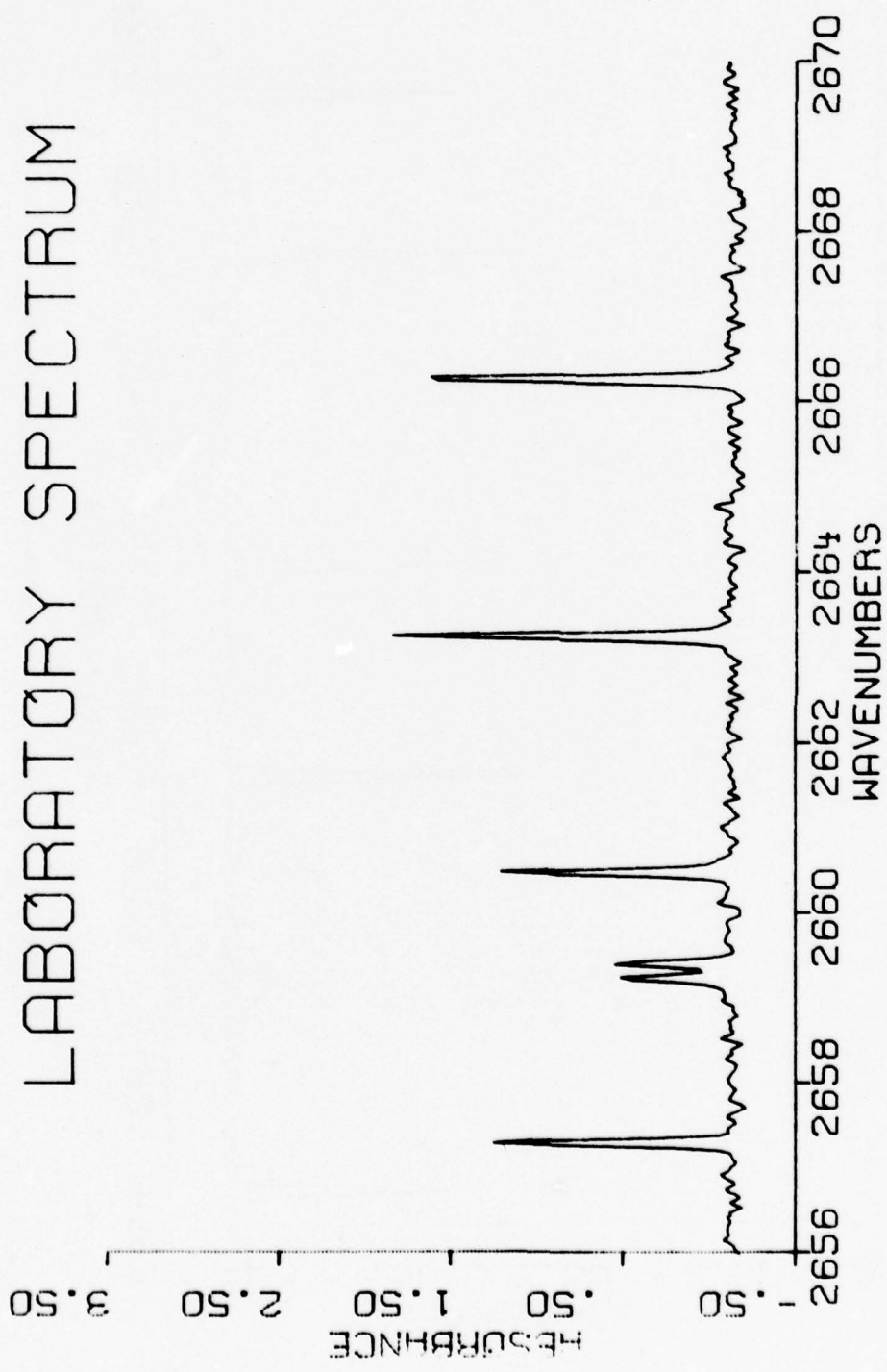


Figure 124. H_2O spectra from 2656 cm^{-1} to 2670 cm^{-1} .

LABORATORY SPECTRUM

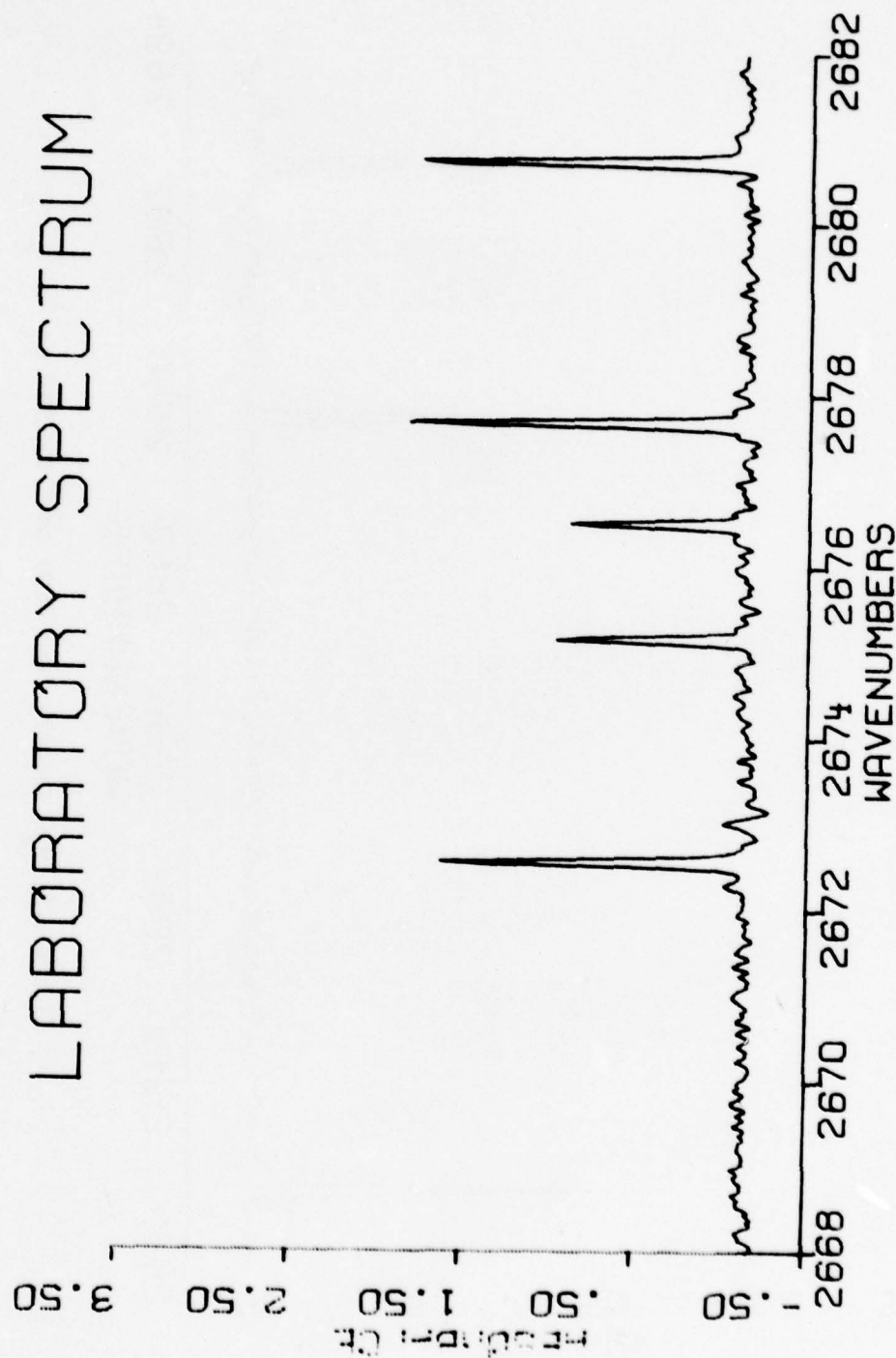


Figure 125. H_2O spectra from 2668 cm^{-1} to 2682 cm^{-1} .

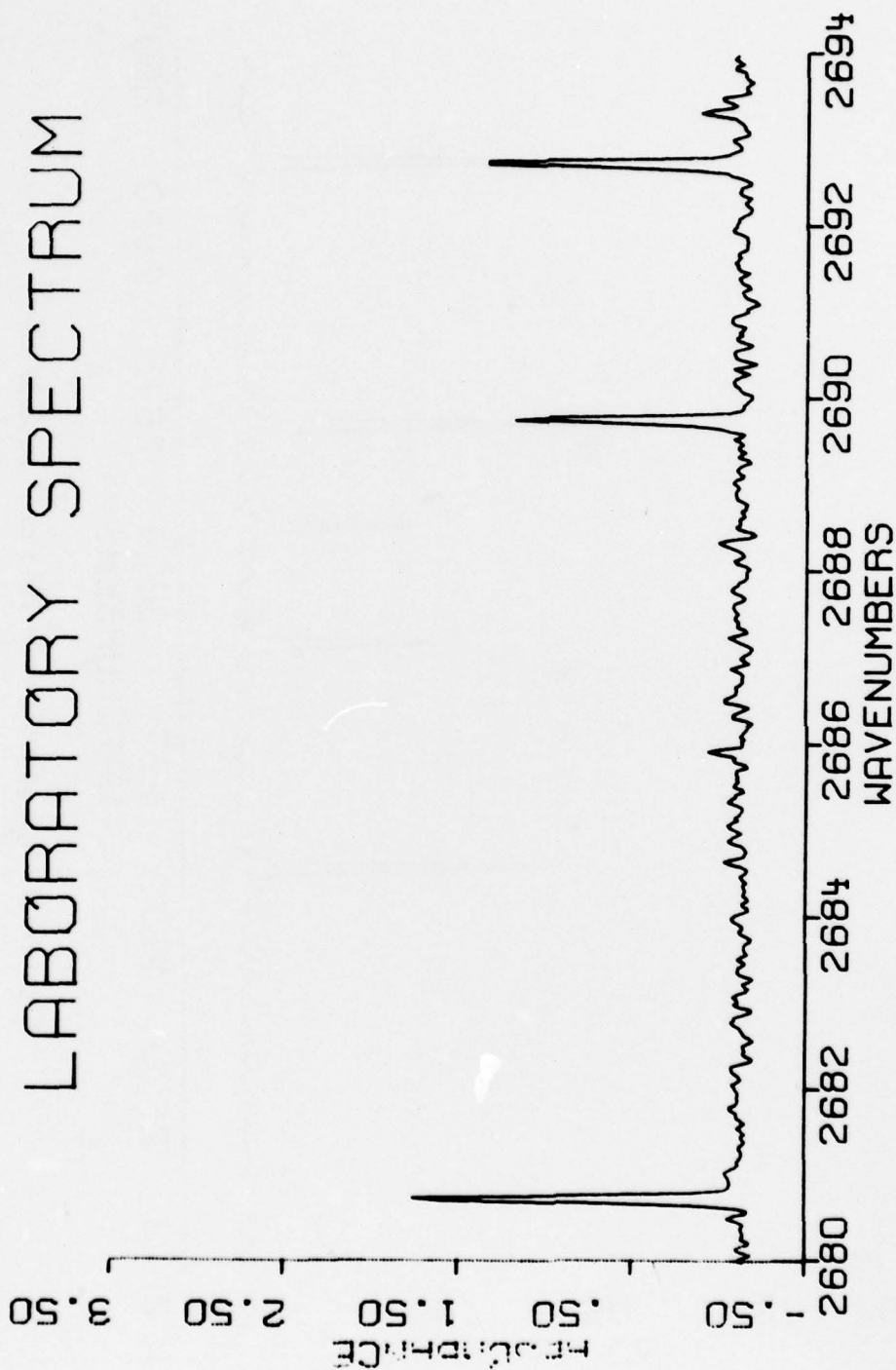


Figure 126. H_2O spectra from 2680 cm^{-1} to 2694 cm^{-1} .

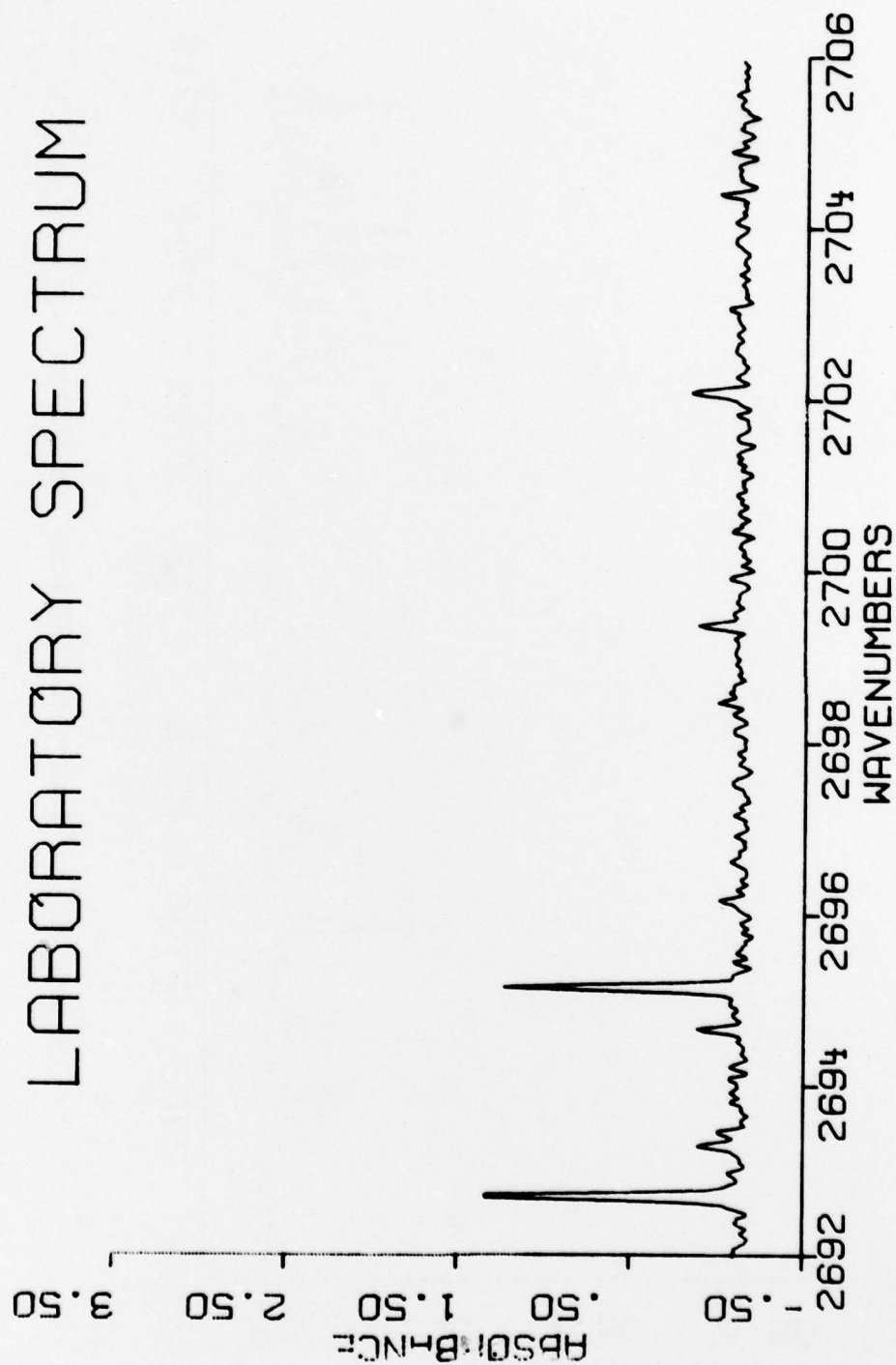


Figure 127. H_2O spectra from 2692 cm^{-1} to 2706 cm^{-1} .

LABORATORY SPECTRUM



Figure 128. H_2O spectra from 2704 cm^{-1} to 2718 cm^{-1} .

LABORATORY SPECTRUM



Figure 129. H_2O spectra from 2716 cm^{-1} to 2730 cm^{-1} .

LABORATORY SPECTRUM



Figure 130. H_2O spectra from 2728 cm^{-1} to 2742 cm^{-1} .

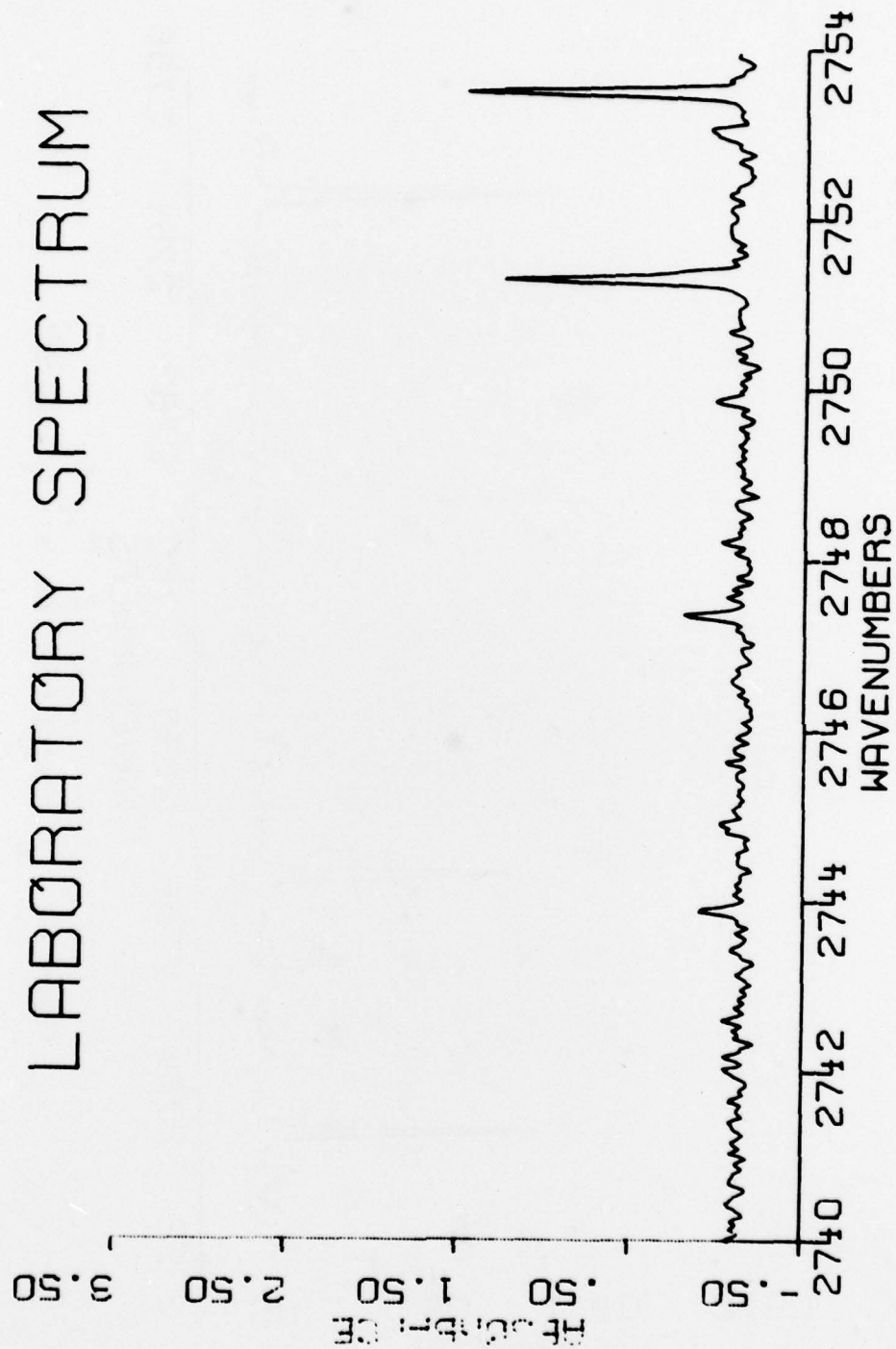


Figure 131. H_2O spectra from 2740 cm^{-1} to 2754 cm^{-1} .

LABORATORY SPECTRUM

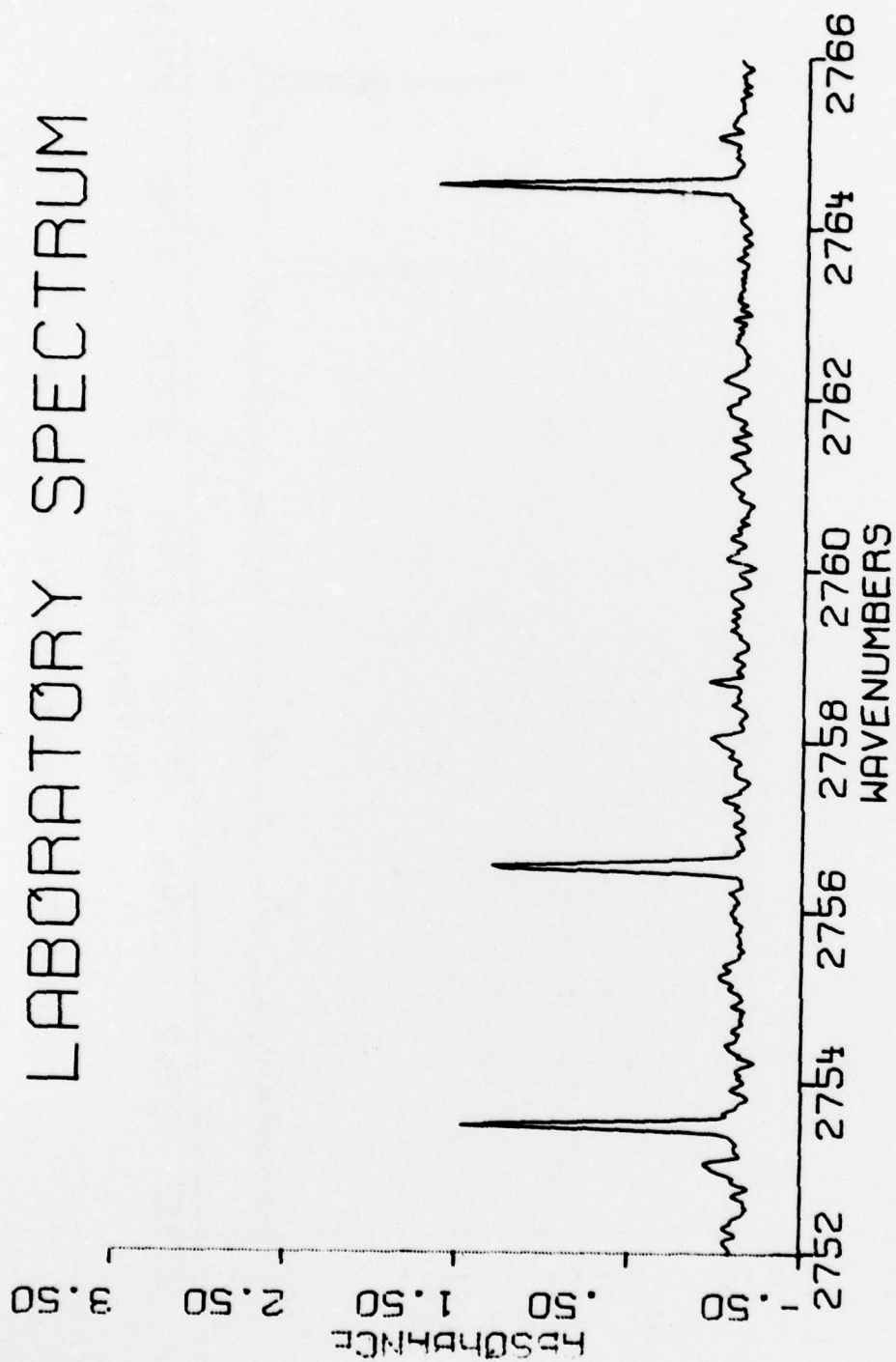


Figure 132. H_2O spectra from 2752 cm^{-1} to 2766 cm^{-1} .

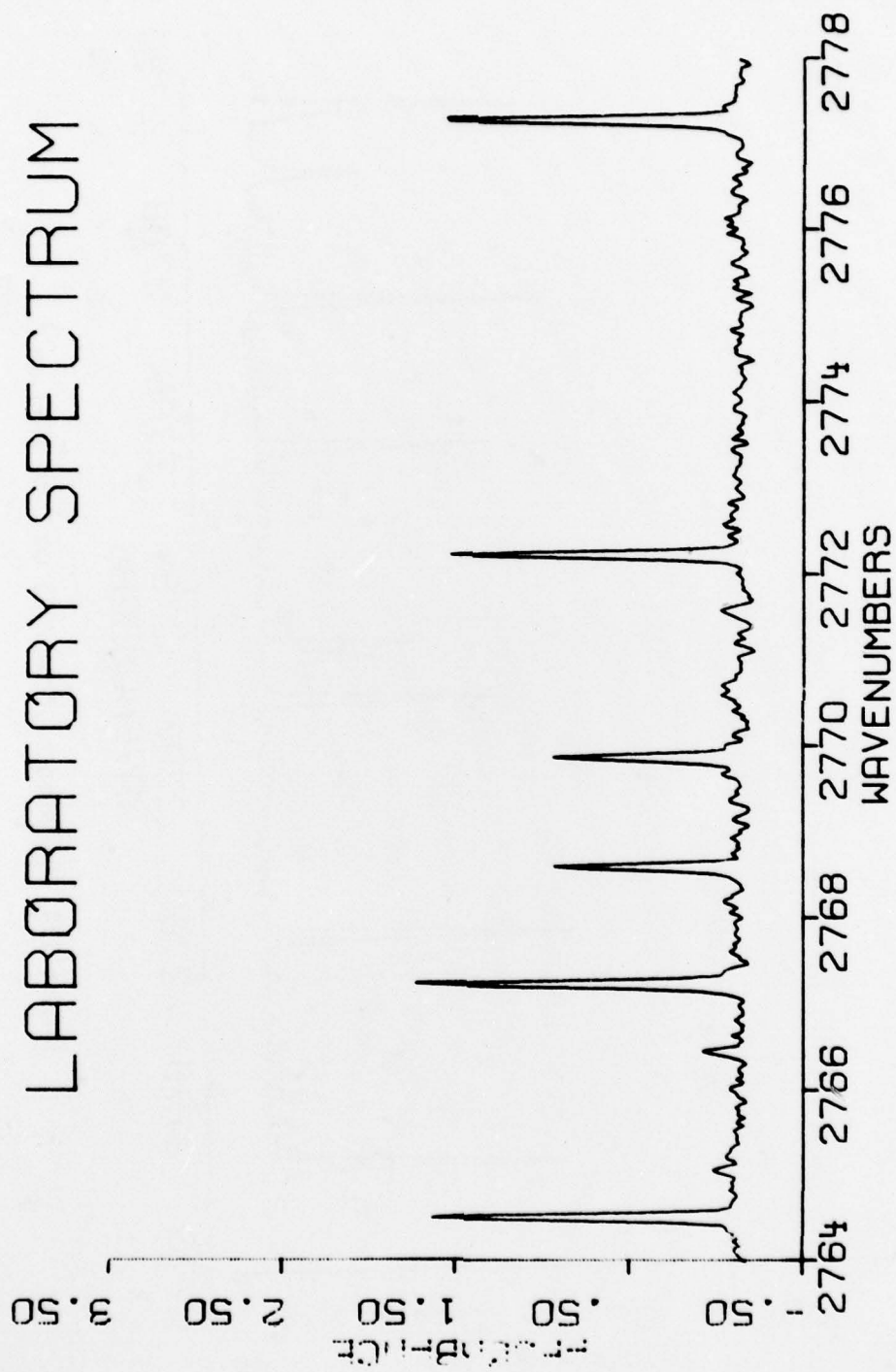


Figure 133. H_2O spectra from 2764 cm^{-1} to 2778 cm^{-1} .

LABORATORY SPECTRUM



Figure 134. H_2O spectra from 2776 cm^{-1} to 2790 cm^{-1} .

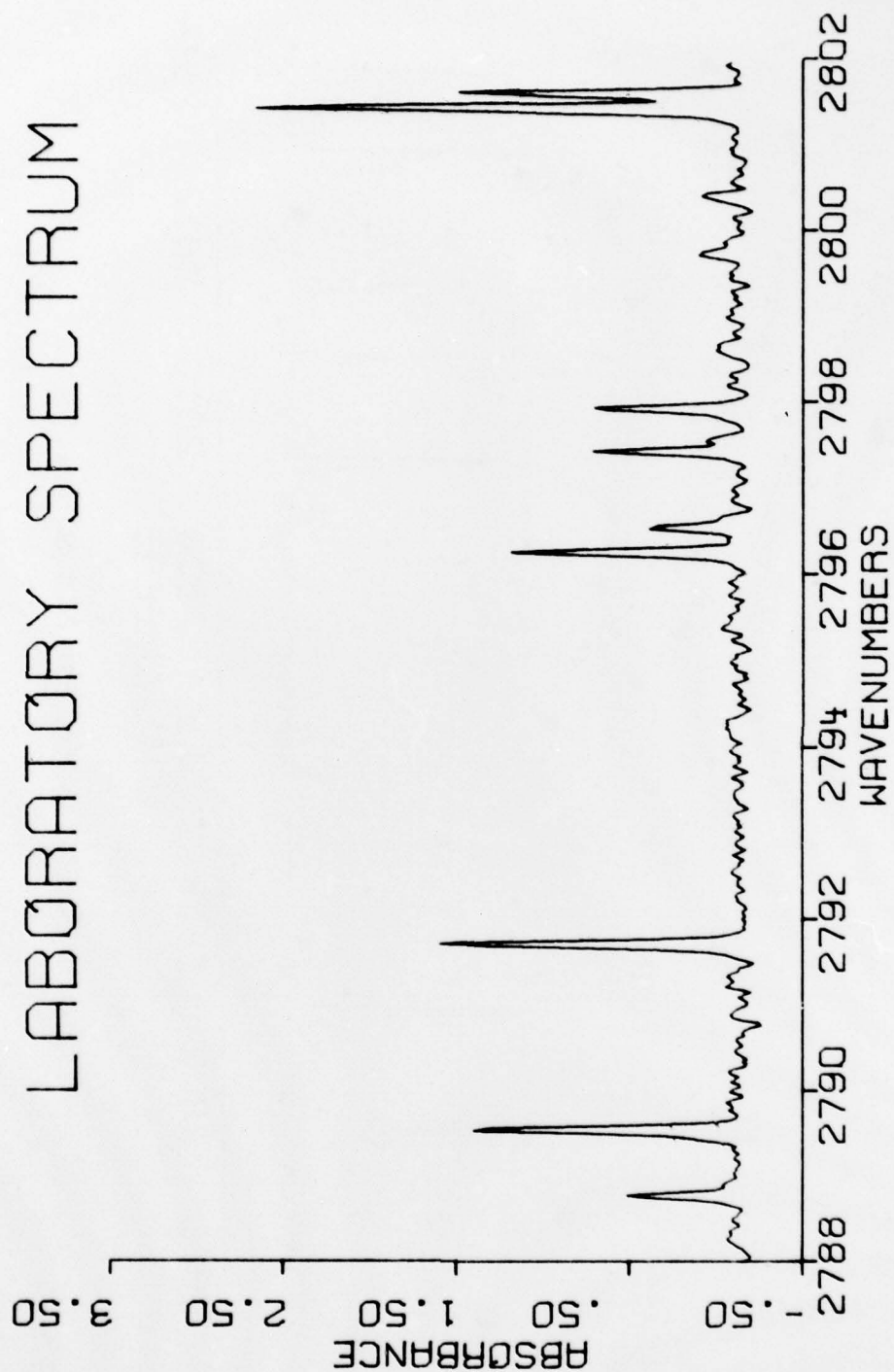


Figure 135. H_2O spectra from 2788 cm^{-1} to 2802 cm^{-1} .

LABORATORY SPECTRUM



Figure 136. H_2O spectra from 2800 cm^{-1} to 2814 cm^{-1} .

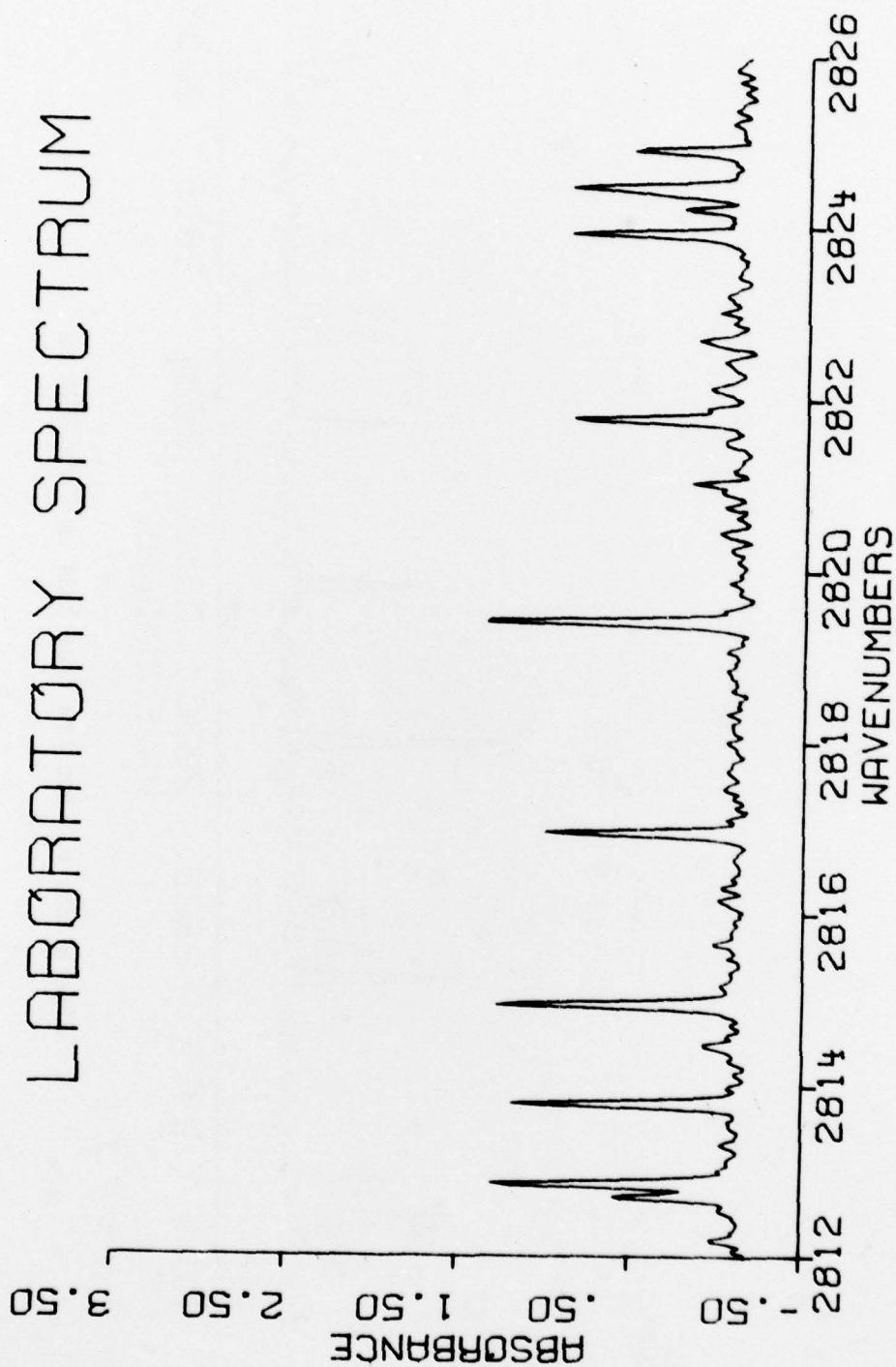


Figure 137. H_2O spectra from 2812 cm^{-1} to 2826 cm^{-1} .

LABORATORY SPECTRUM

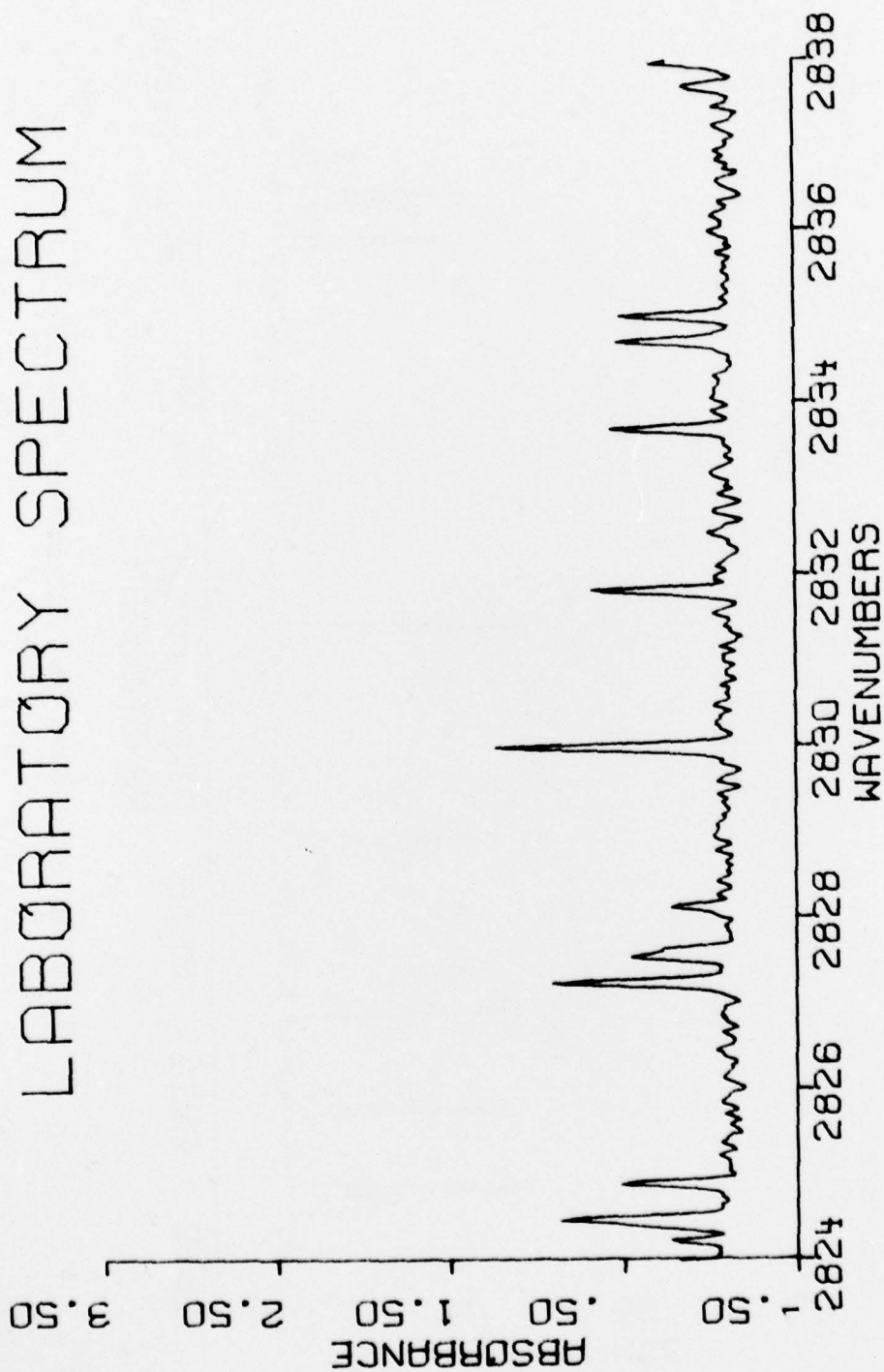


Figure 138. H_2O spectra from 2824 cm^{-1} to 2838 cm^{-1} .

LABORATORY SPECTRUM



Figure 139. H_2O spectra from 2836 cm^{-1} to 2850 cm^{-1} .



Figure 140. H₂O spectra from 2848 cm⁻¹ to 2862 cm⁻¹.